Offshore surveys of Birds, Bats and Marine Mammals for Offshore Wind Farms in Danish Waters, North Sea I for Year 2

Birds – Baseline surveys 2024-2025

Energinet Eltransmission A/S

Date: 20. October 2025

Contents

Preface 4
Declaration 4
List of key terms 5
Summary 6
1. Introduction and project objectives 8
1.1 Objectives 9
1.2 Survey area 9
2. Survey methods 11
2.1 Aerial surveys 11
2.1.1 Data collection 11
2.1.2 Data analysis 12
2.2 Ship-based surveys 18
2.2.1 Data collection 19
2.2.2 Visual bird flight data analysis 22
3. Survey results 25
3.1 Aerial surveys 25
3.1.1 Red-throated diver/black-throated diver (*Gaviidae*) 26
3.1.2 Northern gannet (*Morus bassanus*) 43
3.1.3 Common scoter (*Melanitta nigra*) 60
3.1.4 Little gull (*Hydrocoloeus minutus*) 62
3.1.5 Black-legged kittiwake (*Rissa tridactyla*) 76
3.1.6 Gulls (Larus sp.) 93
3.1.7 Terns (Sterna sp.) 95
3.1.8 Razorbill/common guillemot (*Alca torda/Urea aalge*) 97
3.2 Ship-based surveys 113
3.2.1 Migration magnitude 114
3.2.2 Flight altitude 118
3.2.3 Species composition 134
3.2.4 Vertical radar counts 140
3.2.5 Spatial results 143
4. Data and knowledge gaps 145
4.1 Bird abundance and distribution 145
4.2 Bird flight data 145

5. Discussion and conclusion 146
5.1 Aerial surveys 146
5.2 Ship-based surveys 147
5.2.1 Migration magnitude 148
5.2.2 Flight altitude 148
5.2.3 Species composition 149

References 150

Appendix 1 152
Appendix 2 157
Appendix 3 163
Appendix 4 166
Appendix 5 169

Rev. no.	Date	Description	Done by	Verified by	Approved by
2.0	20.10.2025	Survey of Birds for Offshore Wind Farms in Danish Waters – North Sea I, Year 2	Ib Krag Petersen (DCE) Heidi Maria Thomsen (DCE) Lindesay Scott-Hayward (CREEM) Saana Isojuuno (CREEM) Monique Mac Kenzie (CREEM) Klara Johanna Grethen (DCE) Claus Lunde Pedersen (DCE) Rune Sø Neergaard (NIRAS) Troels Eske Ortvad (DCE) Rasmus Due Nielsen (DCE) Jacob Sterup (DCE)	Tony Fox (DCE) Camilla Uldal (DCE) Rune Sø Neergaard (NIRAS)	Søren Granskov (NIRAS)

Preface

This report was commissioned by Energinet. It describes results obtained from the bird survey program in connection with the planned construction of the offshore wind farms in the North Sea I (NSI) survey area off the west coast of Jutland.

The report builds upon data collected during the second year of surveys under this project and analysis of those data. The report has five main chapters. Chapter 1 provides the Introduction and establishes the objectives for the report. Chapter 2 describes the data collection methods and the data analysis methods. Chapter 3 describes the results of this project. Chapter 4 outlines the knowledge gaps, and Chapter 5 provides discussions and conclusions from the work.

Front page illustration: An adult northern gannet in flight, photographed by Yann Kolbeinsson, Iceland.

Declaration

NIRAS was contracted by Energinet to conduct baseline studies on birds concerning North Sea I in collaboration with Aarhus University and the Danish Centre for Environment and Energy (DCE) as a subcontractor. DCE subcontracted to the University of St. Andrews (CREEM) to assist with parts of the data analysis.

Aarhus University (DCE) has designed and conducted the data collection for this project and analysed the data for all parts of the work. The University of St. Andrews (CREEM) conducted the distance sampling analyses and the spatial models for selected bird species in Chapter 0.

From Aarhus University, Dept. of Ecoscience: Ib Krag Petersen (responsible for field work, report writing of bird surveys and final editing), Heidi Maria Thomsen (data analysis of ship-based data, report writing of ship-based surveys), Klara Johanna Grethen (data analysis of flight altitude information from vertical radar), Lindesay Scott-Hayward, Saana Isojuuno and Monique Mac Kenzie (Scott-Hayward, Isojuuno and Mac Kenzie from CREEM, Univ. of St. Andrews were responsible for the Distance sampling and spatial modelling analyses of data from aerial surveys), Claus Lunde Pedersen (GIS work), Rasmus Due Nielsen, Jacob Sterup and Troels Eske Ortvad (fieldwork aerial surveys and ship-based surveys).

From NIRAS, Rune Sø Neergaard assisted with coordination, planning and report review.

The report was peer-reviewed by Tony Fox of Aarhus University and quality assured by Camilla Uldal at DCE, Aarhus University, and Rune Sø Neergaard of NIRAS. Søren Granskov, NIRAS, gave final approval for publication of the report by NIRAS.

Energinet commented on both the first and second drafts of the report before the final version was published. The comments and author replies can be found here:

https://dce.au.dk/udgivelser/oevrige-dce-udgivelser/eksterne-udgivelser/2025

The report is published by the Danish Energy Agency as part of the tender for offshore wind farms in North Sea I.

The report and associated surveys were financed by Energinet. Energinet wrote the initial section of the Introduction chapter. Aarhus University, DCE and CREEM were responsible for the remaining part of the report.

List of key terms

A list of terms (in English and Danish) and their explanations concerning the present North Sea I report.

Table 0-1 Terminology including Danish and English terms as well as explanations.

English (abbreviation)	Danish	Explanation
North Sea I	Nordsø 1 forundersøgelsesområdet	North Sea I pre-investigation area
OWF	Havvindmøllepark	Offshore Wind Farm
HR3 OWF	Horns Rev III havvindmøllepark	Horns Rev 3 Offshore Wind Farm
Pre-investigation area	Forundersøgelsesområde	The area covered by the survey permit for North Sea I and the geographical scope of the technical baseline reports.
Bird survey area	Undersøgelsesområde for fugle, inkluderende en 20 km zone omkring forundersøgelsesområdet	The pre-investigation area and a 20 km buffer zone around that. This area was surveyed for birds using aerial surveys.
Distance sampling	Distance sampling	Distance sampling is a method used to estimate animal population density and, thereby, total abundance by classifying distances between an observer and detected animals.
Detection function	Detektionsfunktion	Modelling the declining probability of detecting an individual or cluster of individual birds with increased distance from the observer to the object.
Spatial modelling	Rumlig modellering	A method to produce avian distribution maps from sampled data. On the background of these uncertainty related to the estimates can be derived.
Alcid or Auk	Artsgruppen "Alkefugle" omfattende lomvie, alk, lunde, tejst og søkonge.	The species group of alcids comprised razorbills, common guillemots, puffins, black guillemots and little auks.
Y1	Første survey år	The first survey year. Includes all surveys conducted between April 2023 and March 2024.
Y2	Andet survey år	The second survey year. Includes all surveys conducted between April 2024 and March 2025.

Summary

In 2024 and 2025, the second year (Y2) of ornithological studies were conducted to provide baseline data for the Environmental Impact Assessment (EIA) of future offshore wind farms in the NSI area, located in the eastern part of the Danish North Sea. These surveys are continuations of the first survey year (Y1) conducted from April 2023 to March 2024 and aimed to gather background data for future environmental impact assessments related to upcoming offshore wind farm projects.

The ornithological studies consisted of two main components. The first component aimed to provide data on bird species abundances and distributions across the pre-investigation area and a 20 km buffer zone around it, referred to as the survey area, over the course of a year. To achieve this, eight aerial surveys were conducted during Y2. During these surveys, a total of eight species groups and 27 species of birds were observed in the North Sea I area. Each survey was performed using two aircraft and employed the distance sampling survey method. This approach allowed for the modelling of total abundances and distributions of selected bird species. Based on these modelled estimates, a persistency map for the survey area was created, highlighting areas of high or low importance for specific species or species groups across all surveys. These persistence models were performed for combined Y1 and Y2 data sets in this report. Data from each of the eight surveys from Y2 were used to derive information about the abundances and distributions of the following species/species groups: red-throated/black-throated diver, northern gannet, little gull, black-legged kittiwake, and razorbill/common guillemot. The maximum bird numbers per survey were 4,401 divers, 4,145 northern gannets, 4,869 little gulls, 11,659 black-legged kittiwakes, and 26,953 razorbills/common guillemots. When comparing Y1 and Y2 aerial surveys, overall patterns of species distribution were broadly consistent, with core areas of use for key species persisting across years. However, Y2 benefited from more favourable weather conditions, improved visibility, and greater spatial coverage, resulting in higher data quality and fewer survey gaps. These factors contributed to increased detection rates for several species and provided a more complete seasonal representation of bird presence and distribution. While some differences in abundance between years may reflect genuine ecological changes, such as shifts in migration patterns or local environmental conditions, others are likely influenced by the enhanced survey effort and improved observation conditions in Y2.

The other part aimed to describe the movements characterise the movements of flying birds within the NSI pre-investigation area. Observations from Y1 and Y2 provided data on species composition, migration patterns, and flight altitude distributions for selected species and species groups. Bird migration through the area was seasonally structured, with considerable variability between years and observation positions. Migration intensity peaked during autumn (September to October), particularly in the second survey year, indicating that inter-annual differences may be influenced by large-scale environmental factors or shifts in population dynamics and species composition. A consistent diurnal pattern was evident, with peak migration activity occurring shortly after sunrise. Directional movements generally followed expected sea-sonal trends, with northward migration in spring and southward in autumn. However, local variations were observed, likely driven by weather conditions and coastal topography, with some birds adopting east-southeast or southwest trajectories, especially during autumn. Furthermore, most diurnal flights occurred at low altitudes, with over 75% of individuals flying below 100 meters, particularly among auks, divers, and sea ducks. In contrast, gulls and terns displayed a broader vertical range and were the only groups frequently recorded flying above 100 meters. Species composition varied by season, year, and observation position. Spring was dominated by lesser black-backed gulls, red-throated divers, and common terns, while autumn and winter saw greater auk diversity and increased numbers of common guillemots and great black-backed gulls. Notable inter-annual changes, such as a decline in razorbills and an increase in little gulls, further highlight the dynamic and variable nature of seabird migration through the area.

Data from a vertical radar provided information on flight magnitude and altitude both day and night during Y2. The radar records objects that can be a single bird or a group of birds. Neither species nor group size can be inferred

from data from the radar. There was both annual and diurnal variation in the bird flight activity. The movement of flying birds showed much higher flight activity in September and October 2024 than in any other month, relating to bird autumn migration.

1. Introduction and project objectives

To accelerate the expansion of Danish offshore wind production, the Finance Act for 2022 and the subsequent *Climate Agreement on Green Power and Heat* of 25 June 2022 established the framework for developing a minimum of 9 GW of offshore wind capacity in Danish waters.

To realize these political commitments and significantly increase offshore wind energy production, the Danish Energy Agency has prepared a development plan for offshore wind farms in three designated areas: the North Sea, the Kattegat, and the Baltic Sea. As part of this process, the Agency has initiated a wide range of feasibility studies in the areas, some of which are reported in this report.

The North Sea I area covers approximately 1,400 km2, divided into three sub-areas designated for offshore wind development. Located 20-80 km off the coast of West Jutland, each of the three sub-areas will be connected to the onshore grid through designated export cable corridors.

In May 2025, the Danish Parliament adopted the tender framework agreement, which determined that two of the three sub-areas in North Sea I – specifically *Nordsøen I Midt* and *Nordsøen I Syd* – will be included in the first tender round. The third sub-area, *Nordsøen I Nord*, will remain in a pool of potential future tender sites.

Figure 1-1 shows the location of the two sub-areas - *Nordsøen I Midt* and *Nordsøen I Syd* – which will be tendered for in autumn 2025 (Source: ens.dk/energikilder/nordsoeen-i-syd-og-midt-havvindmoelleparker/). The area *Nordsøen I Nord* is north of *Nordsøen I Midt*, whereas the darker blue area to the west is for future development of offshore wind.

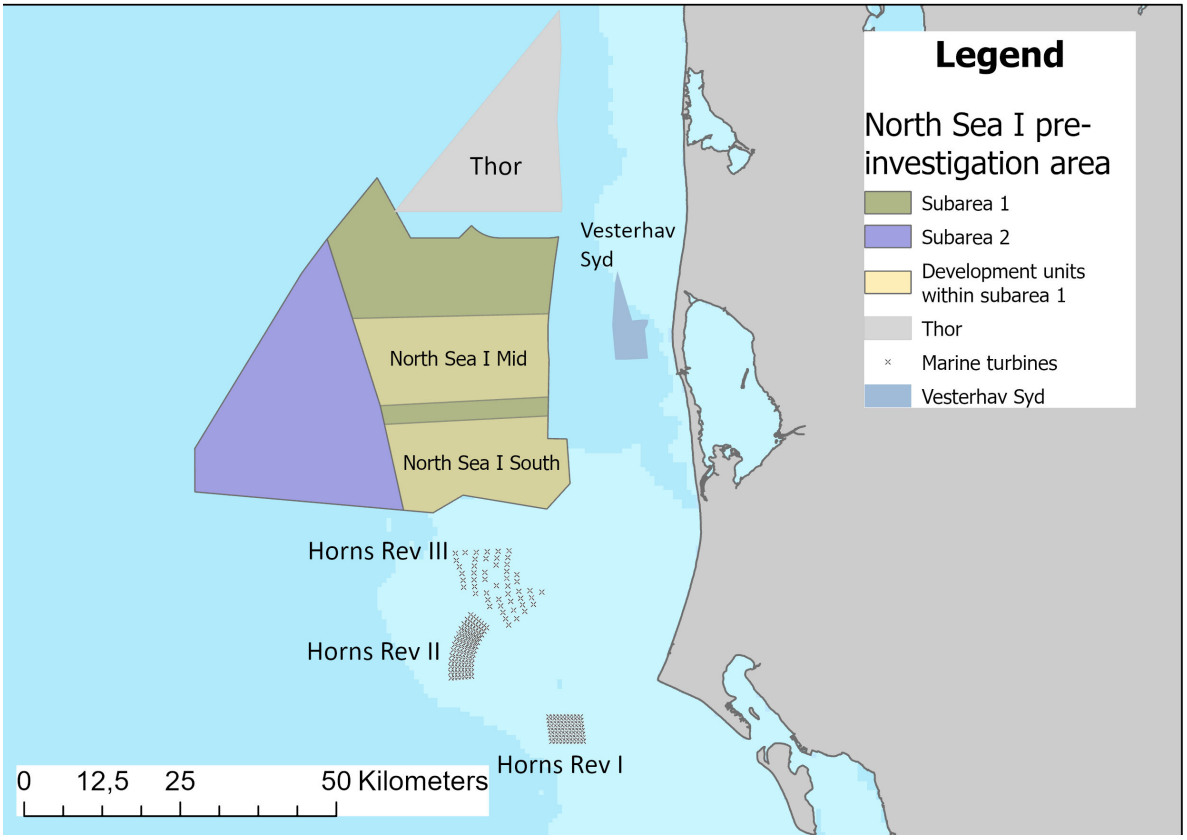

Figure 1-1. Map showing the North Sea I pre-investigation area, with an indication of subdivisions. The "Nordsøen I – Midt" and "Nordsøen I – Syd" are indicated. Wind farms at Horns Rev, Vesterhav Syd and Thor are also indicated.

The tendering process for *Nordsøen I Midt Offshore Wind Farm (OWF)* and *Nordsøen I Syd OWF* will commence in autumn 2025. The deadline for *Nordsøen I Midt OWF* is set for spring 2026, while the deadline for *Nordsøen I Syd OWF* will follow in autumn 2027. According to the current schedule, *Nordsøen I Midt OWF* is expected to be operational by 2032, with *Nordsøen I Syd OWF* coming online in 2033.

The present report presents the results and analysis from the second year (Y2) of these bird surveys, detailing the data collected between April 2024 and March 2025. Additionally, it includes analyses of the combined ornithological data set (Y1 and Y2) from 2023 to 2025.

1.1 Objectives

The objective of the environmental pre-investigations was to collect novel baseline data and compile existing data and information for use by future concessionaires as environmental baseline information in the environmental permitting processes. One specific objective of this technical report is to present and summarise the collected data describing the abundance and distribution of selected bird species and species groups observed during the aerial surveys within the bird survey area, which comprises the North Sea I pre-investigation area surrounded by a 20 km buffer area. Another objective is to describe the species composition, flight magnitude, and altitude distributions of flying birds in the area, collected from ship-based surveys, diurnally through visual observations, and nocturnally through vertical radar.

Data from the first bird survey year (Y1) in this survey area were reported in (Petersen I. K., et al., 2024). This report primarily presents data from Y2 surveys conducted between April 2024 and March 2025, which were collected in the same survey area using the same methods. Where appropriate, a combined dataset containing data from both Y1 and Y2 is presented here.

1.2 Survey area

The North Sea I (NSI) pre-investigation area covers an area of 2,158 km^2 off the west coast of Jutland. To the south, the area extends north of Horns Rev. To the north, the area extends approximately 20 km north of an east-west line from the northern end of Ringkøbing Fjord. To the west, the area extends 80 to 60 km from the coast of Jutland, and to the east, the pre-investigations begin approximately 20 km from the coastline (Figure 1-2). The aerial surveys cover an area of 7,640 km^2 and constitute the pre-investigation area plus a 20 km buffer zone.

The NSI pre-investigation area has water depths ranging from approximately 15 to 35 meters, while the aerial survey area spans water depths from the coastline (0 m) to approximately 45 meters. The NSI pre-investigation area has a minimum distance of 7.5 km to the HR3 OWF and a minimum distance of 10 km to the Vesterhav Syd OWF site. The Thor OWF site is approximately 5 km north of the NSI pre-investigation area and is largely within the aerial survey area of this project (Figure 1-2).

The NSI pre-investigation area is adjacent to the EU Special Protection Area number 113 in the southeastern part of the area, with no overlap between the two.

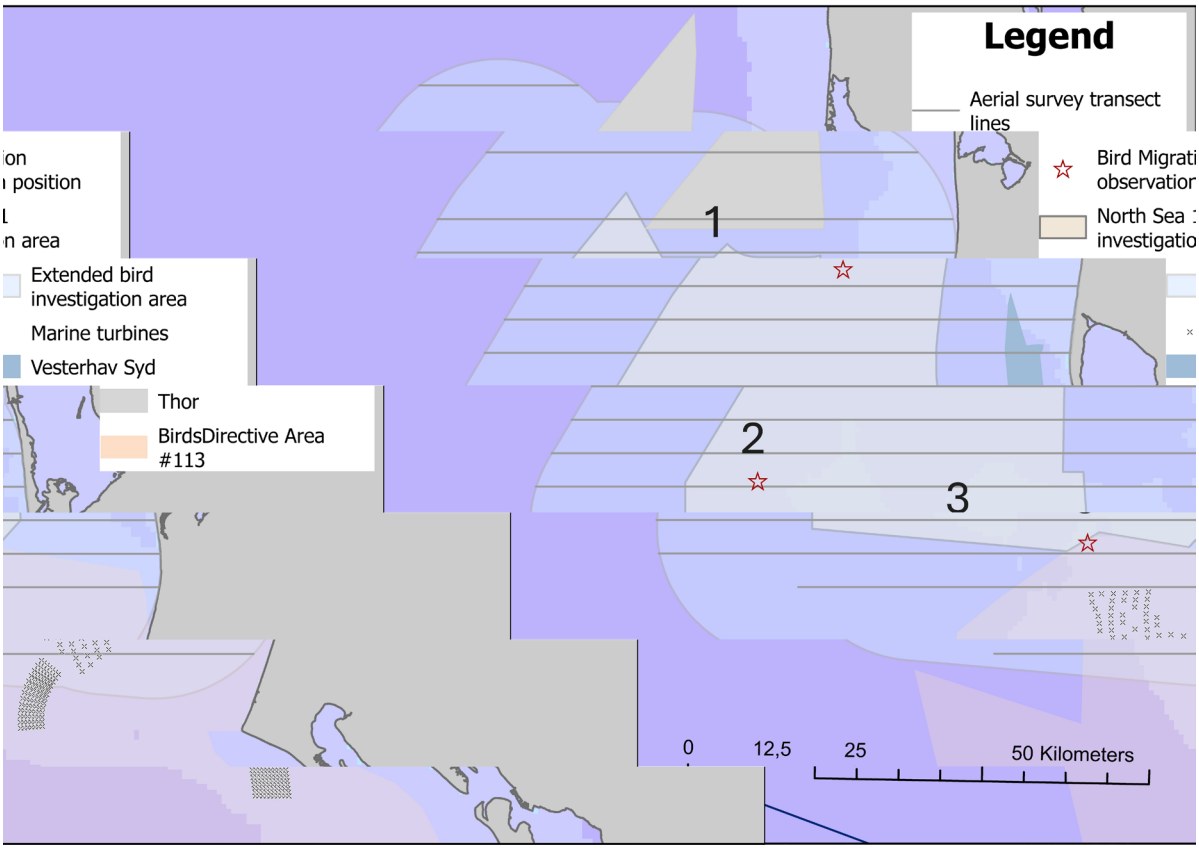

Figure 1-2. The North Sea I pre-investigation area and the survey area used for describing bird abundance and distribution. The aerial survey transect lines and ship-based bird migration observation positions are indicated. Bird migration observation positions are referred to as "North" (1), "Southwest" (2) and "Southeast" (3), Horns Rev wind turbines (marked by crosses). The Vesterhav Syd and Thor OWF sites, along with the extent of the EU Special Protection Area number 113, are also shown.

2. Survey methods

The ornithological surveys in the bird survey area were designed to provide baseline data to support the process of developing environmental impact assessments for OWFs in the area.

The bird data consists of two main parts: one that describes the abundance and distribution of bird species in the area throughout the annual cycle and another that describes bird migration, flight height and activity in the area.

Eight aerial surveys, conducted between April 2024 and March 2025 during Y2, collected data on bird abundance and distribution. These surveys employed the distance sampling method, which enables the modelling of density and fine-scale distribution of selected bird species, along with associated uncertainties.

Data on bird flight in the area were collected during eight ship-based surveys conducted between April 2024 and March 2025, during which ornithological observers recorded bird densities and flight altitudes from three predefined positions within the pre-investigation area. During the day, visual observations enabled the identification of species among the passing birds, while at night, a vertical radar recorded general bird movements and flight altitudes, but without the possibility of identifying individual tracks to specific species.

The two general survey methods are described below.

2.1 Aerial surveys

2.1.1 Data collection

Data on bird abundance and distribution were collected using standard methods. Human observers visually gathered data during aerial surveys by flying transects between designated GPS waypoints at regular speeds and altitudes (Figure 1-2). Twin-engine, high-wing aircraft, specifically the Cessna 337, the Partenavia P-68 and the Tecnam P2006T were used for the surveys. Observations were recorded within distance bands (NOVANA Technical Specification TA A188) parallel to the aircraft to allow for the modelling of differential detectability at increasing distances from the observers (Petersen & Sterup, 2019), following standard distance sampling line transect survey methods (Buckland, et al., 2001; Buckland, Rexstad, Marques, & Oedekoven, 2015).

Data were collected from a flight altitude of 76 m by two trained observers, who recorded birds on either side of the aircraft. For each record, the bird species or species group was noted with information on flock size, behaviour, and perpendicular distance from the survey track and time. The perpendicular distance for each record was classified into predefined distance bands, with increasing distance from the survey track line, extending 1.5 km on either side of the aircraft (Figure 2-1).

The survey transect lines were designed as parallel, east-west-oriented lines covering the survey area. The 15 transect lines were separated by 5 km for most transects, although in parts of the area outside of the pre-investigation area, the distance between transects was 10 km (Figure 1-2). The species distribution maps in Chapter 3.1 present the precise survey track lines covered during each survey.

The data used for this assessment were derived from eight Y2 surveys conducted between April 2024 and March 2025, all of which were completed on a single day (Table 2-1). Due to unfavourable weather conditions in January 2025, the scheduled survey for that month was performed on 1 February 2025. The length of total transect length covered on 19 March 2025 was shorter than the rest because one transect was left unsurveyed by mistake.

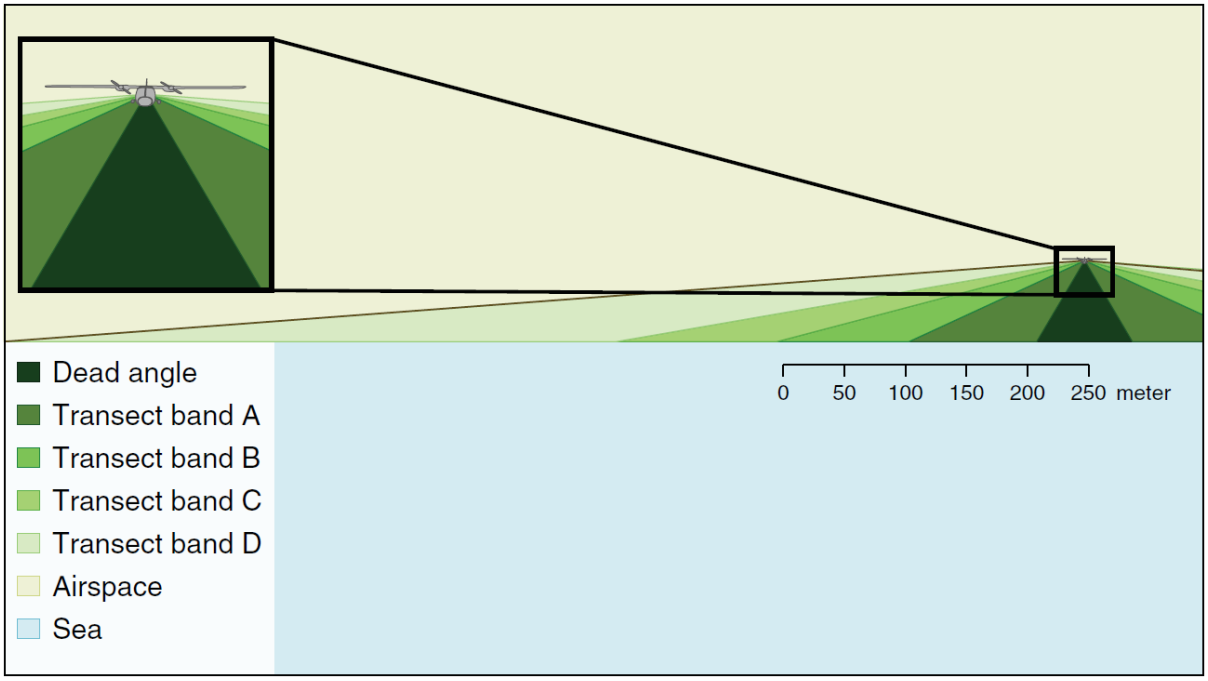

Figure 2-1. The transect band definitions for aerial line transect surveys. From the survey altitude of 76 m, there is a dead angle of 44 on each side of the survey track that the observers could not cover.

Table 2-1. Overview of the eight aerial surveys conducted between April 2024 and March 2025 in Y2. The total transect length covered in the survey area is given for each survey.

Date	Transect length (Km)	Aircraft type
17-04-2024	1,240.8	Tecnam P2006T & Cessna 337
12-07-2024	1,252.5	Partenavia P-68
18-09-2024	1,243.6	Partenavia P-68 & Cessna 337
07-11-2024	1,199.3	Partenavia P-68 & Cessna 337
12-12-2024	1,206.6	Partenavia P-68 & Cessna 337
01-02-2025	1,250.7	Partenavia P-68
14-02-2025	1,252.9	Tecnam P2006T 8 & Cessna 337
19-03-2025	1,107.0	Tecnam P2006T 8 & Cessna 337

2.1.2 Data analysis

2.1.2.1 Distance sampling analysis

All survey data were collected using visual aerial methods, and correction for declining detectability with increasing distance from the plane was accounted for using the Distance Sampling methodology (Multiple Covariate Distance Sampling, MCDS) (F. F. C. Marques and Buckland, 2004; T. A. Marques et al., 2007; Buckland et al., 2001). Analyses were conducted for each of the modelled species or species group datasets by pooling the information across all Y2 surveys. The distance sampling analysis models the decreased probability of detecting a bird or group of birds with increasing distance from the track line of the survey aircraft, incorporating relevant covariates.

To account for other factors affecting the detectability of birds (aside from distance from the observer), additional covariates were included in the distance sampling model. The candidate variables trialled were bird behaviour, observer, sun glare and sea state (see Table 2-2). For observers with too few observations for the estimation of an observer-specific detection function, their observations were combined with those of the next fewest. Observations gathered with a sea state greater than four were removed from the analysis. Sea state is a measure of wave activity (Table 2-2). Greater wave activity increases the difficulty of detecting birds at increased distances away from the survey track line. Both half-normal and hazard rate detection functions were trialled (allowing for different steepness and shapes of the decline in detectability with distance), and the best of all competing models was chosen using the Bayesian Information Criterion (BIC). Further details on the distance sampling analysis can be found in Appendix 2. The effects of glare and any mitigations resulting from them were analysed in a dedicated study (see below).

Table 2-2. Table detailing the covariates used in the detection function fitting.

Covariates	Values
Behaviour	S (sitting or diving) and F (flying or flushing)
Observer	8 Observers
Glare	1 (full sun), 2, 3 (cloudy), 9 (changeable)
Sea state	0, 0.5, 1, 1.5, 2, 2.5, 3, 3.5 (calm to rough)

2.1.2.2 Mitigating the effects of glare

Sighting conditions, such as sun glare and sea state, can affect the detection of seabirds during aerial surveys. Data to describe sighting conditions is usually collected in situ. However, when this is absent, alternative methods are required to identify (and adjust for) heterogeneity in the detection probability. Accounting for such heterogeneity is particularly important for distance sampling, where near-perfect detection at the track line is often a required assumption.

Detection information from band A was used to identify transect lines on the left-hand and right-hand sides of the aircraft, where likely poor sighting conditions were present. For all species except flying northern gannets and black-legged kittiwakes, which are much easier to see even in the presence of glare, observations were removed from the side affected by glare (i.e., returning a one-sided transect).

The effects of glare and any mitigations resulting from this were analysed using a dedicated approach. The analysis was designed to quantify the extent to which directional sun glare can lead to bias in counts on either the left-hand or right-hand side of a single transect line with the same direction of travel. Specifically, it was assumed that the proportion of left or right sightings in band A should be 0.5 and follow a binomial distribution. The proportions for each transect were then compared to a critical value calculated as the quantile of the binomial $(n, p = 0.5)$ distribution at three standard errors greater than the mean and where n equals the number of observations on the transect. This is a common measure in extreme value theory (Leys, Ley, Klein, Bernard, & Licata, 2013). Any transects with values greater than the critical value had the observations from the smaller side removed and the coverage reduced to a single side.

2.1.2.3 Spatial analysis framework

The outputs from the detection function analysis provide a detectability-corrected count (abundance) in a small area (approximately 500 m segment). Spatial models are used to transform these distance-corrected counts along transect lines into spatial distribution maps while accounting for data characteristics and modelling assumptions. The spatial modelling process was undertaken using a spatially adaptive Generalised Additive Model framework (GAM) with an error family suitable for count per unit area response data, the Tweedie distribution. The effort associated with each observation varied depending on the associated segment length and width. Segment area was therefore included as a log-scale offset term in the model. For a more detailed description of the methods, see Appendix 2.

2.1.2.3.1 Modelling summary

Each survey was analysed separately, and the candidate variables for inclusion in the spatial model included a set of one-dimensional (1D) terms: water depth (Figure 2-2) and distance to coast (Figure 2-3), which were permitted to change linearly or non-linearly with the response, and a two-dimensional (2D) term using geographic coordinates to account for surface patterns, which could be a result of unmodelled environmental variability. The flexibility of any smooth functions (1D or 2D) and the choice between competing models (inclusion or exclusion of variables) was determined using a five-fold cross-validation procedure to minimise overfitting.

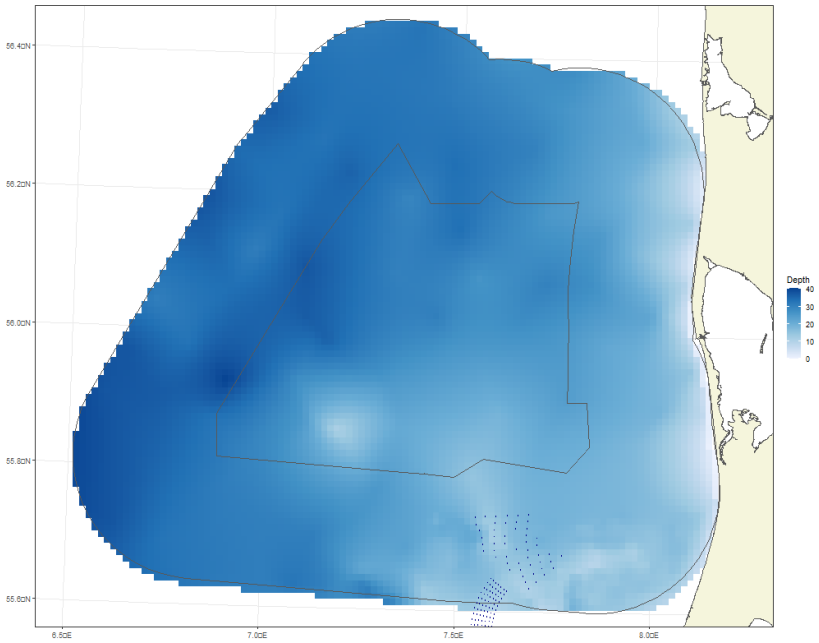

Figure 2-2. Visual representation of bathymetry (water depth).

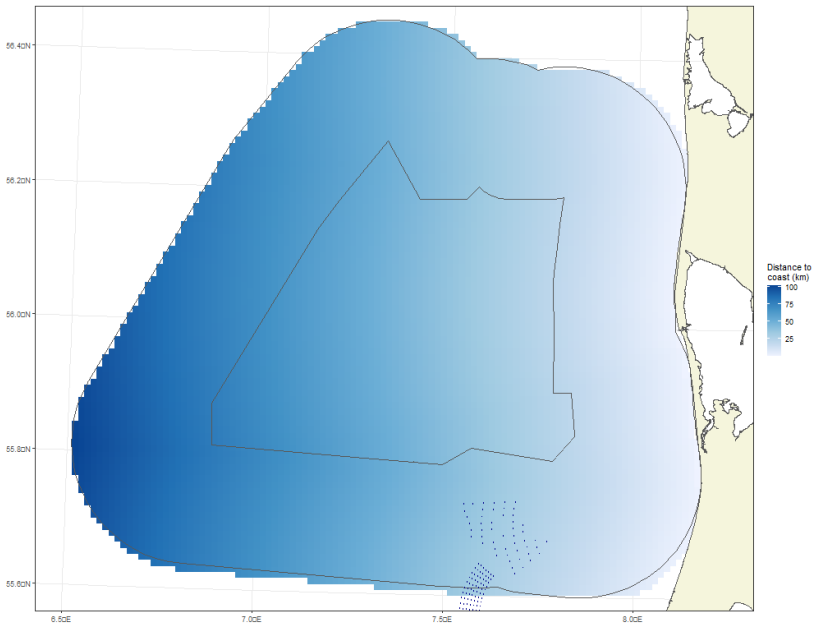

Figure 2-3. Visual representation of distance to the coast (DC).

The response data were collected along survey lines in sequence, so consecutive observations were likely to be correlated in space and time. With a spatial term included, any resulting temporal autocorrelation in model residuals was accounted for by using robust standard errors as part of the modelling framework. These essentially inflate the standard errors concerning the positive correlation observed within pre-specified blocks (here, transects) of residuals to more realistically represent uncertainty in model predictions.

Uncertainty in the outputs was estimated using the detection and spatial models combined as part of a 'bootstrapping' process. This involves repeatedly sampling from the parameter distributions assumed under each model and obtaining a new set of predicted abundances across the spatial grid. From this process, we have 500 sets of plausible predictions for every grid cell. These may be used in a variety of ways to estimate uncertainty and answer questions such as "Does the spatial distribution vary between two surveys or phases" in each geo-referenced location.

All models were fitted using the ***MRSea R*** package (Scott-Hayward, Mackenzie, & Walker, 2023; R Core Team, 2024) and subjected to various diagnostic checks (e.g. assessment of the assumed mean-variance relationship, a key assumption check).

Further methodological details on model specification, fitting, and diagnostics are available in Appendix 2

2.1.2.3.2 Model specifics

More specifically, the MRSea package uses CReSS-SALSA-based spatially adaptive generalized additive models with targeted flexibility to allow for non-linear relationships between the one-dimensional and two-dimensional covariates and the response (Scott-Hayward, Mackenzie, Donovan, Walker, & Ashe, 2014; Scott-Hayward, Mackenzie, & Walker, 2023; Walker, Mackenzie, Donovan, & O'Sullivan, 2010). CReSS is a complex-region spatial smoother, while SALSA is a Spatially Adaptive Local Smoothing Algorithm, both developed to examine animal survey data for signs of changes in animal abundance and distribution following marine renewable energy development. However, the methods are suitable for a wide range of applications.

The 1D smooth terms (for depth or distance to the coast) were specified to be either a quadratic (degree 2) *B*-spline (*df* = 3,4,5) or a natural cubic spline (*df* = 2,3,4). In cases where these degrees of freedom boundaries were reached, however, a broader range of parameters were trialled instead. The degrees of freedom for these terms determine the flexibility of these smooth (and nonlinear) relationships - the more degrees of freedom, the more flexible the relationship can be.

The spatial patterns in each analysis were based on a two-dimensional CReSS-based (Complex Region Spatial Smoother) surface using a Gaussian radial basis function (*df* = [2,100]) (Scott-Hayward, Mackenzie, Donovan, Walker, & Ashe, 2014). The flexibility of both the spatial and 1D elements constituted part of the model selection procedure and, for each survey, was determined using SALSA and the BIC measure of fit.

Uncertainty about model parameter estimates proceeded via robust standard errors due to the nature of the survey procedure (consecutive observations are likely to be correlated in space and time). These essentially work by inflating the standard errors (normally obtained under traditional approaches) concerning the positive correlation observed within pre-specified blocks of residuals. In cases where this residual correlation is minimal, the adjustments are small, and when the correlation is more extreme, the inflation is larger.

A transect-based blocking structure was used to reflect potential correlation within blocks while independence (i.e., no correlation) between blocks was assumed. To ensure this assumption was realistic, the decay of any residual correlation to zero (i.e., independence) with the distance between points (within blocks along transects) was assessed visually. Specifically, transects in each survey were used as the blocking structure.

2.1.2.3.3 Modelling diagnostics

For all modelling, assumptions are made, and the violation of these can lead to spurious results. To assess the adequacy of model fit and assumptions, a range of diagnostic measures were used.

1) ACF plot: a blocking structure was used to account for potential residual non-independence for each model, and a robust standard error approach was based on unique transects. Figure 2-4 shows an example ACF plot with the temporal correlation within each transect shown in grey and the average in red. The plot shows a mean lag one correlation of approximately 0.25 followed by a reassuring decay to zero. This indicates that robust standard errors were necessary for this model (no residual correlation is indicated by a lag-1 correlation of near zero) and that the blocking structure is appropriate.

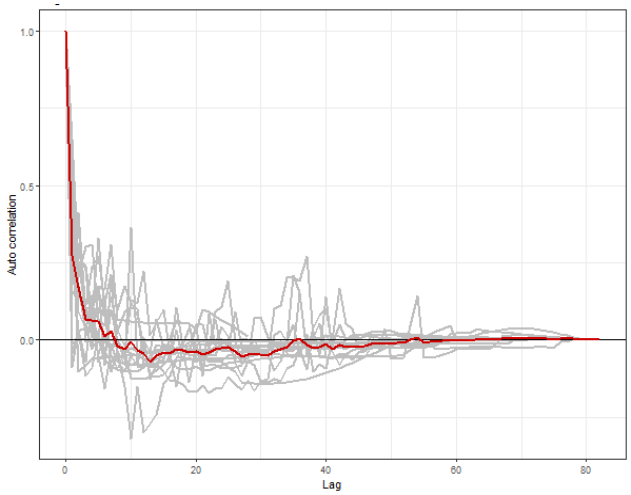

Figure 2-4. Example ACF plot. The grey lines represent the residual correlation observed in each transect, and the red line is the average of these values across transects.

2) Mean-Variance Plot: the assumed mean-variance relationship under the model was assessed visually using plots of the model's fitted values against the variance of the residuals. In this analysis, Tweedie models were employed, which assume a nonlinear mean-variance relationship. Figure 2-5 shows an example plot. The observed residual variance is calculated in bins relating to quantiles of the fitted values (hence the irregular spacing). These are plotted as black dots, and the agreement between these data and the assumed relationship (Tweedie, dotted blue line) indicates that the mean-variance assumption is appropriate. As the Quasi-Poisson and Poisson families are special cases of the Tweedie family, they are included in the plot for comparison.

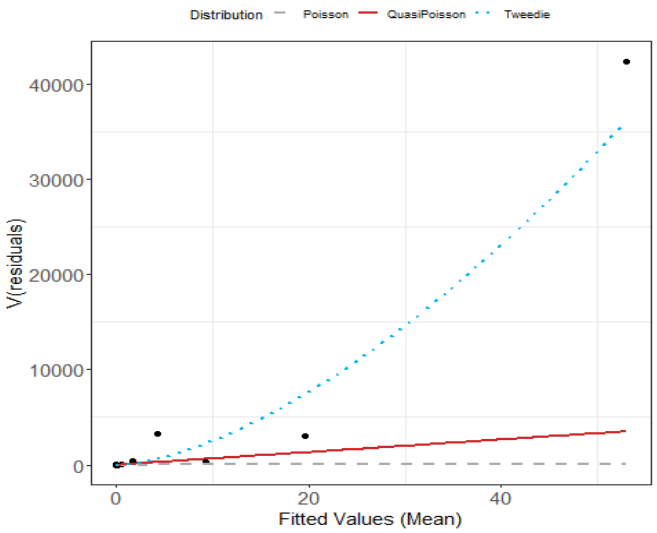

Figure 2-5. Plot showing the estimated Tweedie mean-variance relationship (blue dashed line). The red line represents the $V(\mu) = \phi\mu$ relationship, and the grey line represents the 1:1 relationship. The black dots are the observed residual variances.

3) DHARMa diagnostic plots: QQ plots and residual plots against predicted values were assessed to ascertain the level of agreement between the data and the model. These plots were created using the DHARMa R package and using simulated residuals. Figure 2-6 shows examples of these plots. Given these outputs, we would expect that a correctly specified model shows:
    a. A straight 1-1 line and no compelling evidence against the null hypothesis of a correct overall residual distribution, as indicated by the p-values for the associated tests in the QQ plot.
    b. Visual homogeneity of residuals in both the vertical and horizontal directions, in the residuals against predictor plot.

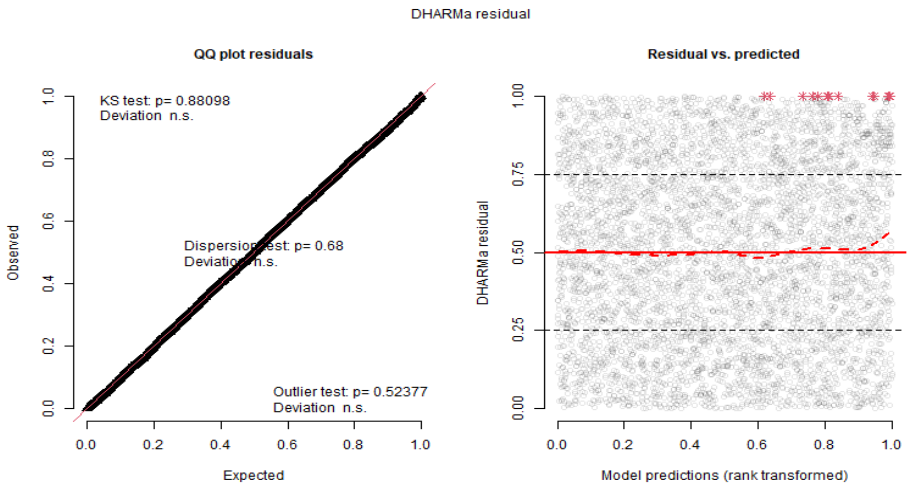

Figure 2-6. Example DHARMa plots with QQ plot (left) and residuals against predicted values (right). The red stars are outliers, and the red line represents a smooth spline fit to the mean of the residuals.

4) Pearson residuals for each model were also spatially visualised to ensure that no areas of consistent bias existed across the survey area. This would be indicated by clusters of negative or positive residuals in spatially similar locations.

2.1.2.3.4 Model predictions and estimates of uncertainty

Based on each selected model, predictions of counts were made to a grid of points (each point representing a 1 km^2 grid cell) across the survey area. Additionally, abundances within the survey-based prediction region were obtained by summing the grid cell counts across the relevant areas.

The uncertainty in the detection function was reflected using a parametric bootstrap ($\boldsymbol{n = 500}$) of the fitted distance sampling model. This generated new estimated numbers for each segment. The selected spatial model was then re-fitted to each of the new datasets to obtain a new set of parameter estimates for the model. The final output of this process was a parametric bootstrap procedure using the robust variance-covariance matrix from each parametric bootstrap model. These were used to calculate 500 sets of model predictions, which generated 95% percentile-based intervals and allowed for the calculation of a coefficient of variation for each grid cell. If it was impossible to fit a spatial model to the data, the abundance estimates for the survey were calculated using the parametric bootstraps from the distance analysis.

2.1.2.3.5 Additional Outputs

A calculation of 'persistence' was also undertaken across Y1 and Y2 surveys using the geo-referenced estimates of density (abundance per associated area) across the survey area. Distributional persistence enables the reader to gauge intra- and inter-annual variability across multiple surveys. For example, there may be areas of consistent usage despite survey-to-survey variability, which can provide context for detecting post-construction changes. Persistence scores were calculated for every grid cell as follows. Each bootstrap replicate was allocated a binary value based on whether the estimate in each location was above the mean estimated density (1) throughout the survey area or below this mean estimated density (0). This was performed for all 500 sets of plausible predictions in each grid cell (based on the bootstrap replicates), and the proportion of these bootstrap predictions above the mean (indicated by the value of 1) was calculated for each grid cell to give a persistence score for that location. The scores range between 0 and 1, where 1 indicates that the density in that grid cell was estimated to be above average in every bootstrap replicate in every survey (so uniformly above the mean; high persistence/consistent usage), while a value of 0.1 indicates that just 10% of the estimates were above the estimated mean, and thus indicates low persistence in that location. A zero would result from the density in every survey and every bootstrap being below average.

2.2 Ship-based surveys

Ship-based bird surveys were conducted during Y1 (April 2023 to March 2024) and Y2 (April 2024 to March 2025), within the NSI pre-investigation area. The surveys were conducted from three fixed observation positions: North, Southeast, and Southwest (Figure 1-2), strategically selected to provide broad and representative spatial coverage of the area. The results from Y1 are published in Petersen et al. (2024).

Across the two years (Y1 and Y2), a total of 16 surveys were completed (Table 2-3). Surveys were timed to coincide with peak migration periods and were designed to capture variation in seabird abundance, species composition, flight behaviour, and migration dynamics. In total, the Y1 and Y2 surveys accounted for 87 observation days and 1,045.4 hours of active bird monitoring. While both years followed the same consistent methodological framework, Y2 included a higher number of observation days (17.5%) and hours (14.6%), thereby enhancing the overall temporal resolution of the dataset.

Table 2-3. Overview of the 16 ship-based surveys conducted in the NSI pre-investigation area during Y1 (S01-S08) and Y2 (S09-S16). The table shows the start and end dates of each survey, along with the number of observation days (N = 87) and hours (N = 1,045.4)

for each survey. An overview of the survey effort at each observation position is provided in Table 0-2 and Table 0-3 in 3B4BAppendix 3.

Survey ID	Start date	End date	Obs. days	Obs. hours
S01	2023-04-27	2023-04-30	4	60.5
S02	2023-05-18	2023-05-22	5	82
S03	2023-06-13	2023-06-18	6	104
S04	2023-08-11	2023-08-16	6	82.6
S05	2023-09-15	2023-09-22	7	63.4
S06	2023-10-08	2023-10-10	3	33
S07	2023-12-03	2023-12-08	6	42.5
S08	2024-02-08	2024-02-10	3	19.2
S09	2024-04-18	2024-04-23	6	83.6
S10	2024-05-17	2024-05-22	6	97.8
S11	2024-06-12	2024-06-15	4	55.9
S12	2024-08-13	2024-08-19	7	90.8
S13	2024-09-17	2024-09-22	6	73.9
S14	2024-10-24	2024-10-29	6	61.7
S15	2024-12-10	2024-12-14	5	32.3
S16	2025-02-25	2025-03-03	7	62.3

Overall, the observation effort was distributed evenly across the three observation positions, with each position visited multiple times during both survey years. On average, each ship-based survey comprised 1.9 (±0.6 SD) observation days at the North, 1.8 (±0.2 SD) at the Southeast, and 1.8 (±0.7 SD) at the Southwest positions (Table 0-2, 3B4BAppendix 3). The observation hours per survey were similarly distributed, with averages of 21.8 (±9.6 SD) hours at the North, 21.5 (±9.5 SD) at the Southeast, and 22 (±10.3 SD) at the Southwest positions (Table 0-3, 3B4BAppendix 3).

The following sections detail the specific methodologies used for the ship-based surveys.

2.2.1 Data collection

2.2.1.1 Transect counts

To quantify bird abundance, standardised visual transect surveys were conducted from a stationary vessel using a fixed 1500-meter horizontal detection range. Each survey consisted of a 15-minute continuous observation period, during which a single trained observer recorded all birds crossing a transect line extending 1,500 meters outward from the vessel. These sessions were followed by 15-minute breaks, during which the transect orientation shifted from East-West to North-South. The specific direction within each axis (e.g., East vs. West) was chosen by the observer based on environmental conditions, including wind direction, sun position, and visibility, to optimise detectability.

Observations were conducted from an elevated platform, 2-8 meters above sea level, depending on the vessel type, and typically lasted up to two hours. Surveys spanned daylight hours, from sunrise to sunset, and were limited to periods of favourable observation conditions. These were defined as visibility exceeding 1500 meters and sea state with wave heights below 2.5 meters. Surveying was suspended during heavy precipitation, even if visibility remained within the threshold, to ensure data quality.

During each 15-minute transect count, only birds actively crossing the transect line were recorded. Individuals flying near the vessel were included only once per observation period, regardless of the number of times they crossed. For each observation, observers systematically recorded information about transect orientation, species (or species group, if specific identification was not possible), number of individuals, and flight direction (in 45° sectors). The latter was inferred using a combination of vessel orientation, solar angle, and prevailing wind direction.

To ensure consistency and reduce motion-induced errors during observations, observers used handheld binoculars (8× magnification; 130-150 meters field of view) mounted on a monopod (FINNSTICK FF VM15). This stabilisation enabled continuous scanning throughout each session. For enhanced species identification and documentation, a tripod-mounted telescope and a digital camera equipped with a 300-800 mm telephoto lens were used when required.

2.2.1.2 Altitude recordings

Flight altitude and horizontal distance were measured alongside transect counts using a combination of precise measurements and visually calibrated estimates. The primary instrument used for measurements was a laser rangefinder (Vectronix Vector 21 Aero), capable of capturing both distance and inclination angle to determine altitude by triangulation. The rangefinder was employed whenever conditions allowed stable use, typically during calm sea states and steady vessel positioning. Where possible, multiple measurements (typically 2-5) were taken to capture variation in flight altitude, particularly for birds exhibiting undulating or variable flight patterns. All repeated measurements were linked by a shared observation ID, allowing for the analysis of within-flight variation in altitude.

In cases where sea conditions prevented the use of the rangefinder, flight altitude was estimated visually. Observers continuously compared visual estimates with rangefinder measurements during the survey period to maintain accuracy and consistency over time. This method has previously been shown to lead to estimates that do not significantly deviate from rangefinder measurements (Petersen I. K., et al., 2024).

Altitude data were recorded for both individual birds and flocks. When flocks were observed, both group size and representative flight altitudes were recorded. Observations were primarily conducted while the vessel was stationary at an observation position; however, some data were collected during slow movements between positions, provided that measurement reliability could be maintained. Furthermore, observers aimed to collect altitude data at the furthest possible distance from the vessel to minimise disturbance-related bias in altitude measurements.

In addition to recordings made during transect sessions, flight altitude data were also collected opportunistically during the 15-minute breaks between transect counts. These additional records included birds flying beyond the 1,500-meter transect limit and species of special interest, such as rare or locally important taxa. Opportunistic measurements followed the same protocols and equipment standards used during transect counts to ensure consistency across all data.

2.2.1.3 Vertical radar data

2.2.1.3.1 Vertical radar data overview

Between 17 April 2024 and 3 February 2025 during Y2, 33,640 screen-grab images were collected from a vessel-borne radar system across eight collection periods. In June, the collection period lasted only four days, amounting to only half of the images compared to other periods (Table 2-4).

Table 2-4. Details of the eight radar recording sessions conducted during Y2 and included in the analysis. Pulse length is a setting on the radar system, and resolution is a setting in the screen-grab software.

Start date	End date	N days	Pulse length	Resolution	N images
2024-04-17	2023-04-24	8	Medium	1280×1024	4,636
2024-05-16	2023-05-23	8	Short	1920×1080	4,577
2024-06-12	2023-06-15	4	Short	2400×1900	2,340
2024-08-12	2023-08-19	8	Short	1920×1080	4,593
2024-09-16	2023-09-23	8	Short	2400×1900	4,656
2024-10-23	2023-10-30	8	Short	2400×1900	4,678
2024-12-09	2023-12-14	8	Short	2400×1900	3,443
2025-02-25	2024-03-03	7	Short	2400×1900	4,717

2.2.1.3.2 Echo annotation

We measured the flight altitudes of passing birds by relating their positions on the radar screen to the horizon and the sweep area of the radar beam. To extract the presence of birds in radar screen grabs, annotations were performed on all images using the VGG Image Anotator software (Dutta & Zisserman, 2019). Annotations were done by a single experienced ornithologist familiar with the vessel-borne radar systems and the annotation software. Images during bad weather (primarily rain) or strong radar artefacts (most likely reflections from features onboard the ship) were excluded from annotations. The area is visible as yellow signals in the range of 0° to 50° in Figure 2-7, lower right panel. Detected objects from annotations do not allow for species or individual identification; hence, the extracted "putative bird counts" can only serve as approximations of the actual numbers of birds (likely birds) involved.

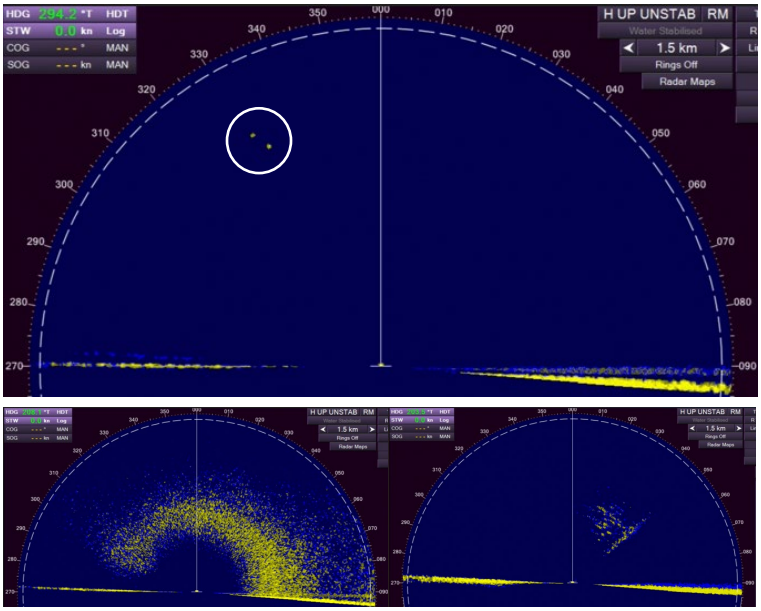

Figure 2-7. Examples of radar screengrabs. Upper panel: Radar screen dump containing two target objects. Lower left: Radar screen dump showing bad weather (typically rain or very high humidity). Lower right: Radar screen dump showing artefacts (i.e. not bird returns).

2.2.1.3.3 Computer vision approach

Using a computer vision algorithm (CVA) developed by (Petersen I. K., et al., 2024), we automatically generated putative bird counts from the radar screen grabs, in addition to the manual annotations of putative bird signals from the screen dumps, to test the robustness of the method against changes in settings and across time. The algorithm was only run on radar screen grabs, which contained a blue radar area or a detectable horizon. In screen dumps where no blue radar background area (in cases where the radar stopped temporarily) or horizon could be identified, the images were classified as missing data. Finding a horizon in the screen dump is necessary to geo-rectify the image.

After extraction, the model predictions were post-processed in three steps. First, we filtered out bird positions within a 5° angle of the shifting horizon area, as this range was frequently affected by artefacts caused by the boat's rolling. Second, we removed areas of the radar sweep that frequently presented artefacts (see 2.2.1.3.2 and Figure 2-7, lower right panel), based on quality checks from annotators and visual inspections of the angle distribution of detections. The area of artefacts shifted slightly between seasons. Specifically, the range from 0° to 50° was removed in April and May, from 15° to 40° in June, from 10° to 55° in October, and from 15° to 55° in December (see Figure 2-7). Finally, we excluded predictions based on a weather indicator that was almost exclusively due to precipitation, as indicated by the level of noise measured as "yellowness" in the image (Figure 2-7, lower left panel). If the noise level exceeded a threshold, the image was classified as containing bad weather, and a period of 30 minutes on either side was classified as the beginning and end of a bad weather period.

2.2.1.3.4 Analysis

All analyses were performed in *R* (R Core Team, 2023). To assess the flight volume of birds, we calculated both the total putative bird count per observation period and the median putative bird count per day. We aggregated putative bird counts per hour (i.e., 30 radar sweeps) to compare the performance of the CVA (see 2.2.1.3.3) with manual annotations. The two extraction methods were compared by calculating Lin's Concordance Correlation Coefficient (CCC, Lin 1989) for agreement, with values near 1 indicating strong agreement and a Pearson's correlation product.

To analyse bird numbers in space, we calculated real positions and distances of birds in meters from manual annotations across all periods. From the positions, we derived spatial densities using a density-weighted rasterization approach, where each annotation contributed a volumetrically scaled estimate of bird presence per scan. To produce comparable measurements of bird density at 50×50 m resolution, we weighed the differing depths of the 3D scan mapped into 2D space at varying distances from the sensor. This approach accounted for the geometry of the radar beam, enabling a standardized, spatially explicit estimate of bird density.

To analyse the effect of altitude on bird density, we fitted a Generalised Additive Model (GAM) with a Tweedie distribution (log link) to model the putative bird density. Included as effects were a 2D tensor product smoother to capture the interaction effect of the x- and y-positions and a univariate smoother for the distance from the radar sensor. The distance was treated separately to control for possible attraction effects of the boat on the bird's altitude. The model was fit using the gam function in the mgcv (Wood, 2011) package in R. Visual inspection of partial effects and residual diagnostics confirmed the adequacy of the smoothing terms. Smoothing parameters were estimated via REML.

2.2.2 Visual bird flight data analysis

2.2.2.1 Migration magnitude

To assess the magnitude and characteristics of diurnal migratory movements, data from the transect counts were analysed separately for Y1 and Y2. Only data collected during the standardised transect counts were included in this analysis, ensuring consistency in observation effort and methodology. To account for variability in the number and orientation of transects conducted across surveys, all directional transects (e.g., East-West and North-South) were pooled within each survey. This pooling increased the sample size and allowed for more robust comparisons across observation positions and survey years.

Three complementary metrics (explained below) were used to characterise migration magnitude. Together, these analyses provide a comprehensive assessment of migration magnitude and variability across the NSI pre-investigation area, supporting the interpretation of migratory use patterns in time and space.

2.2.2.1.1 Migration intensity

The total number of individuals recorded per survey was standardised by total survey effort (in hours) to calculate a migration intensity index (individuals per hour). This provided a comparable measure of relative abundance across different surveys and observation positions.

2.2.2.1.2 Temporal distribution

To investigate temporal variation in diurnal migration intensity, data from all surveys within each survey year were pooled across observation positions. This was necessary because sample sizes at individual positions were too small to support position-specific analyses.

To control for differences in day length across surveys, the number of individuals observed was standardised by normalising observation times relative to the day length (i.e., the period between sunrise and sunset). This normalisation allowed us to make meaningful comparisons across surveys conducted at different times of the year.

2.2.2.1.3 Directional distribution

To describe the overall directionality of migration, the flight direction of individuals recorded during transect counts was summarised for each survey year. These data were analysed separately for each observation position to assess spatial and temporal consistency in migratory pathways.

To examine potential seasonal patterns, surveys were grouped into four seasons: spring migration, summer, autumn migration and winter. The spring migration included S01 and S02 in Y1 and S09 and S10 in Y2. Summer included S03 in Y1 and S11 in Y2. Autumn migration included S04, S05, and S06 in Y1 and S12, S13, and S14 in Y2. Winter included S07 and S08 in Y1 and S15 and S16 in Y2.

2.2.2.2 Flight altitude

To provide a comprehensive overview of flight altitude distributions, data from both Y1 and Y2 surveys were combined. Furthermore, data from all three observation positions were pooled to characterise general flight patterns across the entire NSI pre-investigation area.

Where available, laser rangefinder-derived altitude records were used as the primary data source due to their higher accuracy and resolution. Visual estimates were included only in instances where rangefinder data were unavailable or returned negative altitudes, which occasionally occurred when birds flew within wave troughs. To address the issue of repeated measures within a single observation event (e.g., multiple altitude records for a flock or individual during the same observation), the mean flight altitude per observation ID was calculated and used in the analysis. This approach reduces pseudo-replication and ensures that each observation contributes equally to the analysis.

For the analysis, flight altitudes were binned into 25-meter intervals from 0 to 250 meters above sea level. For each species, the number of altitude records and the number of individuals observed within each altitude interval were summarised to describe the vertical distribution. In cases where closely related species were difficult to distinguish under field conditions (e.g., auks), data were grouped into broader taxonomic categories to improve sample size and classification reliability. Furthermore, analyses were restricted to species or species groups with a minimum of ten flight altitude records across all observation positions and both survey years, ensuring meaningful interpretation of vertical distribution patterns.

2.2.2.3 Species composition

To assess spatial and inter-annual variation in species composition, data from each survey year and each of the three observation positions were analysed separately. This approach enabled us to identify temporal trends and geographic differences in species composition across the NSI pre-investigation area.

Species composition ratios were calculated for taxonomic groups that are difficult to identify at the species level during aerial surveys. These included divers (Gaviidae), gulls (Larinae excluding kittiwakes), terns (Sterna spp.), and auks (Alcidae). Within each species group, the ratio of identified species was calculated based on the total number of individuals observed during each individual survey (i.e., per year and observation position). All types of observations were included in the analysis, regardless of the survey method, to ensure a comprehensive representation of each group's composition.

3. Survey results

3.1 Aerial surveys

A total of eight species groups and 27 species of birds were observed from the eight aerial surveys conducted in the NSI area during Y2 (Table 3-1).

Table 3-1. The bird species or species groups observed from the eight aerial surveys conducted in the survey area during Y2. The number of observed individuals per species or species group is indicated. The numbers are thus not estimations of the total abundance of birds. The total number of each species or group observed during the eight surveys is shown.

Species	Total	2024-04-17	2024-07-12	2024-09-18	2024-11-07	2024-12-12	2025-02-01	2025-02-14	2025-03-19
Red-throated diver	610	44		18	23	34	218	44	229
Diver sp.	59	21		6			16	6	10
Grebe sp.	1						1		
Fulmar	61		8	2	4	39	2		6
Gannet	793	263	48	149	21	2	4	5	301
Cormorant	24		10	4	2	1		6	1
Grey heron	1								1
Pink-footed goose	6								6
Wigeon	5			5					
Teal	10								10
Diving duck sp.	2			2					
Eider	4	2							2
Common scoter	2,841	65	48	174	815	234	232	1216	57
Velvet scooter	26					10	15	1	
Red-breasted merganser	8			6			2		
Oystercatcher	1	1							
Sanderling	10		10						
Whimbrel	1		1						
Great skua	1			1					
Little Gull	405			5	280	89	15	9	11
Black-headed gull	167		43	108	4				12
Common Gull	769	17	15	96	145	78	174	64	180
Lesser black-backed gull	146	2	123	18					3
Herring gull	1,711	367	258	387	317	54	233	25	70
Great black-backed gull	48	8	4	11	6	10	5	1	3
Herring gull/common gull	73		21				47	3	2
Gull sp.	468	2	8	50	125	47	105	4	127
Kittiwake	1,786	60	1	26	745	263	324	49	318
Sandwich tern	6		6						
Common tern	4			4					
Arctic/common tern	114	60	42	12					

Species	Total	2024-04-17	2024-07-12	2024-09-18	2024-11-07	2024-12-12	2025-02-01	2025-02-14	2025-03-19
Tern sp.	13	8	4	1					
Common guillemot	789	53	12	33	233	117	40	5	296
Razorbill/common guillemot	2,983	315	14	33	461	625	619	186	730
Razorbill	241	1			161	18	12	25	42

The following section describes the spatial and temporal distribution of selected species or species groups. For the red-throated diver/black-throated diver (diver species), northern gannet, black-legged kittiwake, little gull, and razorbill/common guillemot, distance sampling principles were used to derive total abundance estimates within the survey area. In contrast, spatial modelling principles were used to describe the fine-scale distribution of those species or groups within the survey area. These results are presented below.

3.1.1 Red-throated diver/black-throated diver (*Gaviidae*)

The only species of diver identified to species during Y2 surveys was the red-throated diver. Some divers could not be identified to species and were therefore recorded as 'diver sp.' Almost 90% of the observed divers were identified as red-throated divers (Table 3-1). Diver species were recorded during all Y2 aerial surveys except the July 2024 survey, when none were recorded. Most birds were recorded in February and March, with the fewest in July and September (Figure 3-1). A total of 669 individuals (from both diver species) were recorded across the eight surveys. The average flock size was 1.44, with a maximum of eight birds.

Diver species were primarily recorded in the eastern and southern parts of the survey area, with their occurrence being less frequent in the central and western parts of the area (Figure 3-2). In February, March and April, diver observations were more widespread in the survey area. This is a time close to migration towards the breeding grounds, which might explain the difference in distribution.

These distribution patterns were similar to the pattern found during the Y1 surveys.

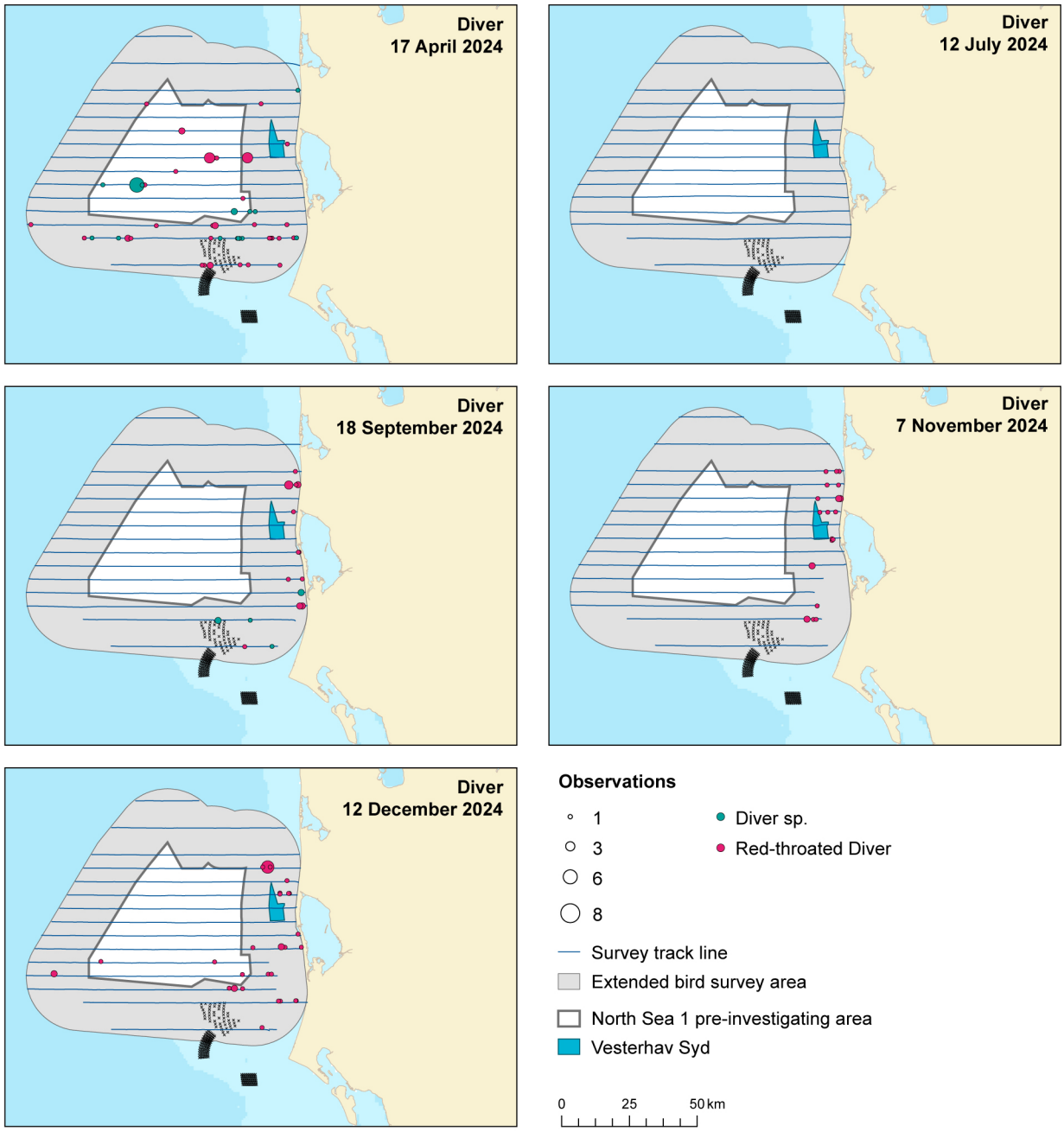

Figure 3-1. The numbers and distribution of diver species observed during five Y2 surveys in the NSI survey area.

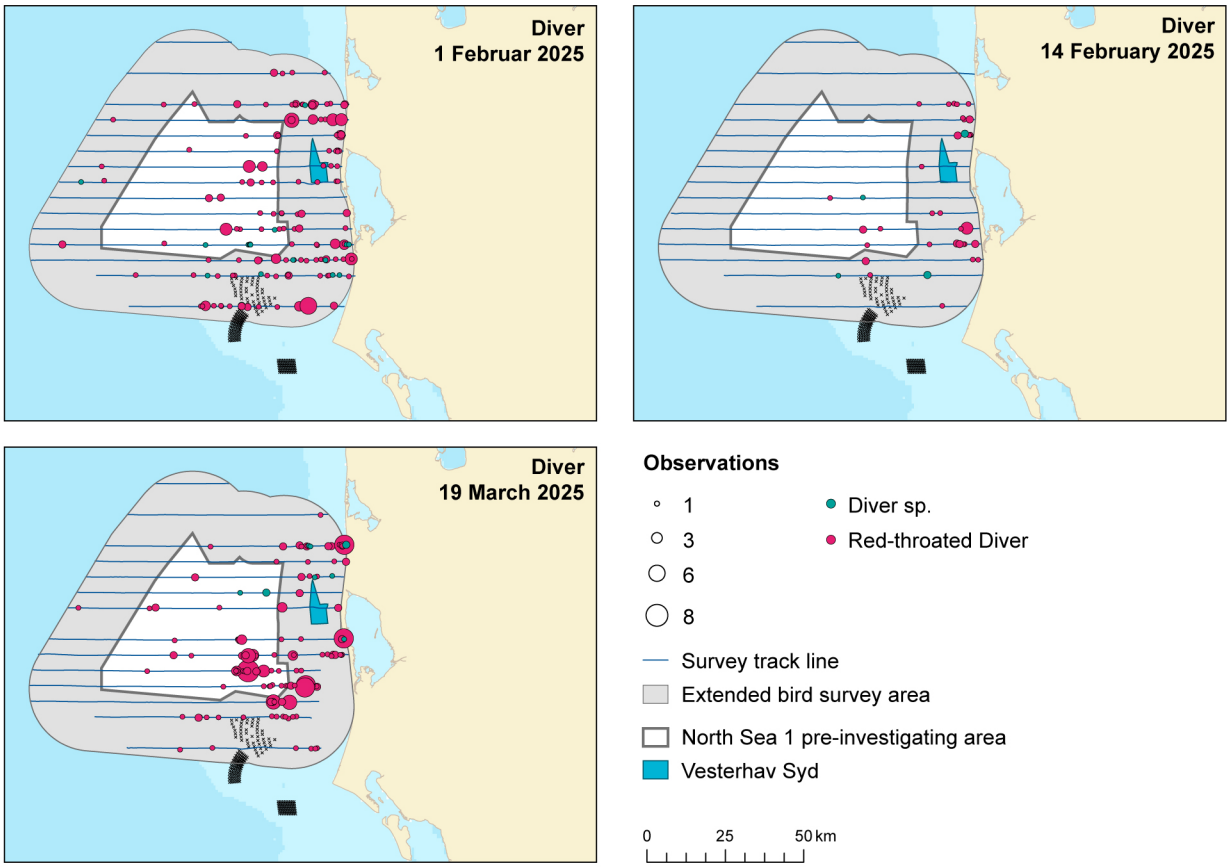

Figure 3-2. The numbers and distribution of diver species observed during three Y2 surveys in the NSI survey area.

3.1.1.1 Distance analysis

The average probability of sighting diver species was estimated to be 0.23 (Coefficient of Variation = 0.04). This probability was estimated using a half-normal detection function, and no covariates were selected. This detection function was estimated using the Y1 surveys, and this model was then used to estimate the number of birds in the eight surveys conducted in Y2. Figure 3-3 shows the estimated relationship with the data from the eight surveys in Y2.

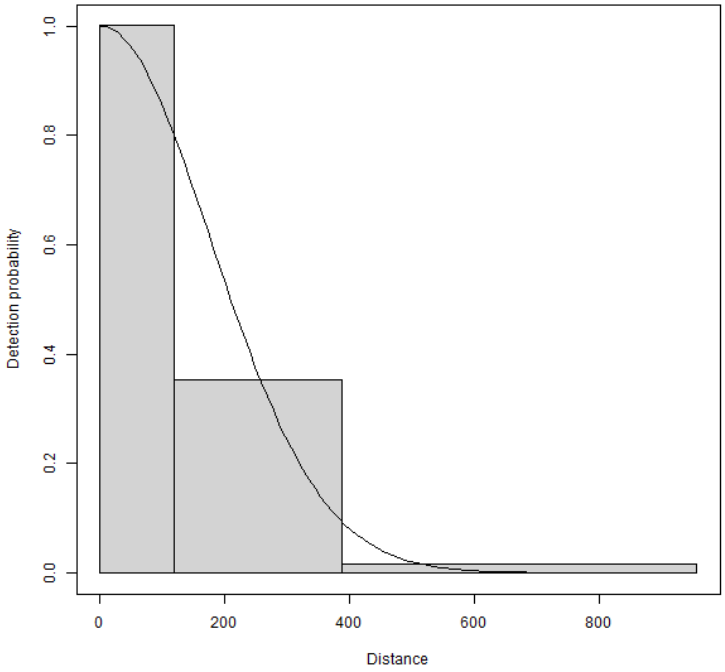

Figure 3-3. Figure showing the estimated diver detection function. The histogram represents the distances of the observed sightings.

3.1.1.2 Spatial analysis

Figure 3-4 shows the distribution of the distance-corrected counts for each of the eight Y2 surveys.

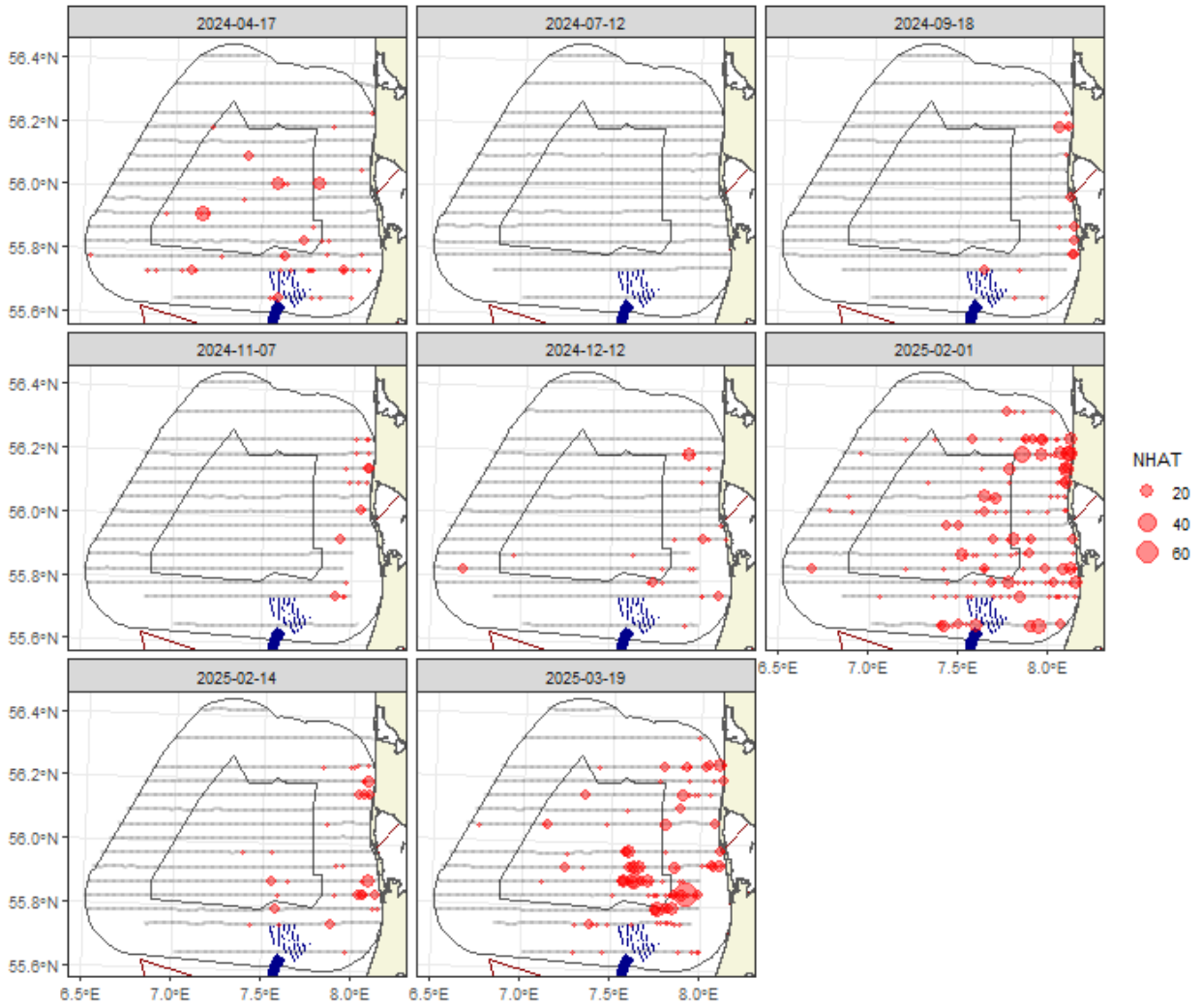

Figure 3-4. Distance-corrected counts for the diver species across the eight Y2 surveys in the NSI survey area. The red circles indicate the distance-corrected counts along the transect lines. The grey dots are segments with a count of zero.

3.1.1.3 Model selection

For one of the eight Y2 surveys, there was insufficient data to fit a credible spatial model. In all the remaining seven surveys, however, the models selected included a spatial term (of varying complexity). The depth covariate was selected as a smooth term in one model, while the distance-to-coast covariate was selected as a linear term in the other. This indicates that there was compelling evidence for non-uniform spatial patterns in most surveys. However, despite these spatial patterns, there was little evidence of relationships between depth and distance to the coast. The spatial surfaces selected ranged from eight to 11 parameters for the spatial term (Table 3-2).

Table 3-2. Model selection results for diver species for each Y2 survey. The model column represents the terms in the model.

Date	Model	Distribution	Variable 1D	Variable 2D	Number of Parameters	Dispersion parameter	Tweedie parameter
2024-04-17	2D Only	quasipoisson	NA	s(x,y, df=9)	10	9.9	NA
2024-07-12	No Model	NA	NA	NA	NA	NA	NA
2024-09-18	2D Only	quasipoisson	NA	s(x,y, df=10)	11	1.3	NA

Date	Model	Distribution	Variable 1D	Variable 2D	Number of Parameters	Dispersion parameter	Tweedie parameter
2024-11-07	2D Only	quasipoisson	NA	s(x,y, df=9)	10	0.7	NA
2024-12-12	Best 1D2D	quasipoisson	distcoast, df=1	s(x,y, df=8)	10	2.4	NA
2025-02-01	Best 1D2D	quasipoisson	s(depth, df=2)	s(x,y, df=8)	11	7.2	NA
2025-02-14	2D Only	quasipoisson	NA	s(x,y, df=10)	11	4.5	NA
2025-03-19	2D Only	quasipoisson	NA	s(x,y, df=7)	8	13.5	NA

The estimated abundances, densities, and associated 95% confidence intervals for each Y2 survey are presented in Table 3-3 and Figure 3-5. There was insufficient data to fit a spatial model for the July survey, therefore, the abundance estimates were calculated using the Horvitz-Thompson method (H-T). The estimated total abundance in the survey area varied between 0 and 4,401 individuals, equivalent to densities ranging from 0.0 to 0.6 birds/km^2. The highest abundance occurred in winter and early spring (Table 3-3 and Figure 3-5).

Table 3-3. Estimated abundance and density of diver species for each survey. The 95% confidence interval (CI) is based on percentiles.

Date	Area (km^2)	Estimator Type	Estimated Count	95% CI Count	Estimated Density	95% CI Density
2024-04-17	7833	Spatial	1106	(474, 4553)	0.1	(0.1, 0.6)
2024-07-12	7833	H-T	0	(0, 0)	0.0	(0, 0)
2024-09-18	7833	Spatial	349	(148, 972)	0.0	(0, 0.1)
2024-11-07	7833	Spatial	362	(155, 1104)	0.0	(0, 0.1)
2024-12-12	7833	Spatial	902	(479, 1923)	0.1	(0.1, 0.2)
2025-02-01	7833	Spatial	4223	(2587, 7442)	0.5	(0.3, 1)
2025-02-14	7833	Spatial	628	(338, 1370)	0.1	(0, 0.2)
2025-03-19	7833	Spatial	4401	(2477, 8648)	0.6	(0.3, 1.1)

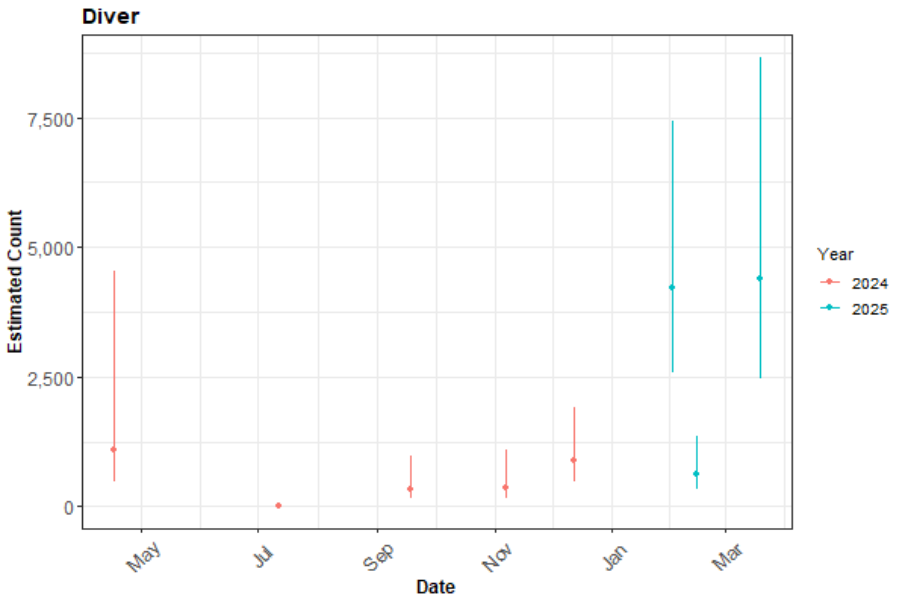

Figure 3-5. The estimated number of diver species for each Y2 survey. The 95% CI is a percentile-based confidence interval and is from a parametric bootstrap with 500 replicates.

3.1.1.4 Spatial results

Figure 3-6 shows the estimated numbers of diver species in each 1 km² grid cell for each month. Generally, the estimated abundances fitted well with the raw data, and there were no notable misalignments. In areas where the estimated numbers were systematically higher, the abundances were also relatively high, and there were no areas with large, estimated abundances that were unsupported by the data.

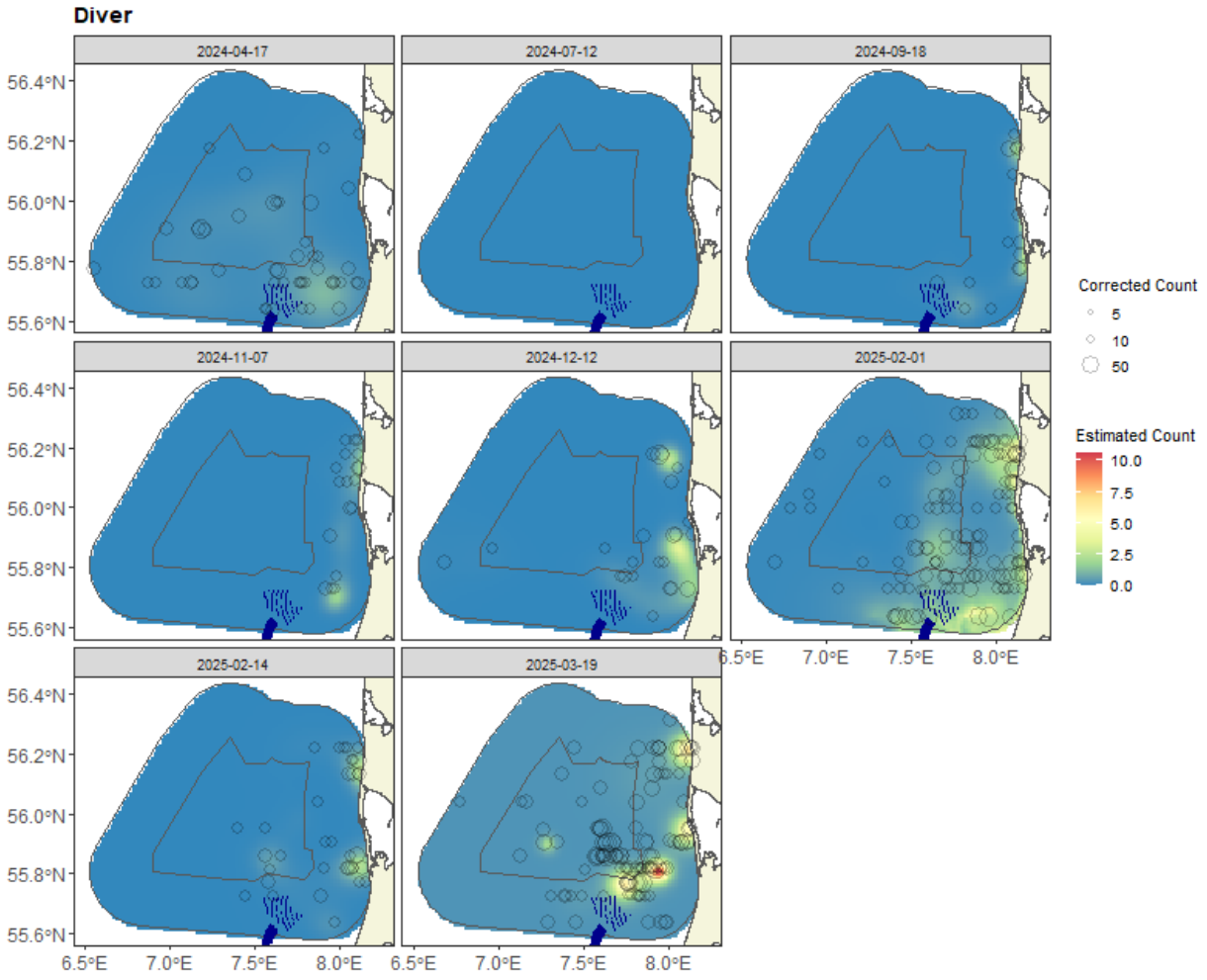

Figure 3-6. Figure showing the estimated diver abundance across the NSI survey area for each Y2 survey. The estimated numbers are based on a 1 km x 1 km grid cell. The open circles represent the distance-corrected counts.

3.1.1.5 Uncertainty in spatial predictions

Broadly, the highest coefficients of variation (CoV) scores were associated with the `almost zero' predictions, and it is known that the CoV metric is highly sensitive to any uncertainty for very small predictions. There was one larger value for the eastern side of the survey area for one of the surveys that was otherwise lacking in data. There was no material overlap between high values of the CoV metric and the transect lines/locations with non-zero counts, resulting in no concerns in this case (Figure 3-7).

In the case where the very small predicted values were excluded (Figure 3-8), a few areas of high CoV remained, which are reflected in the related confidence intervals for the abundances (Figure 3-5, Table 3-3).

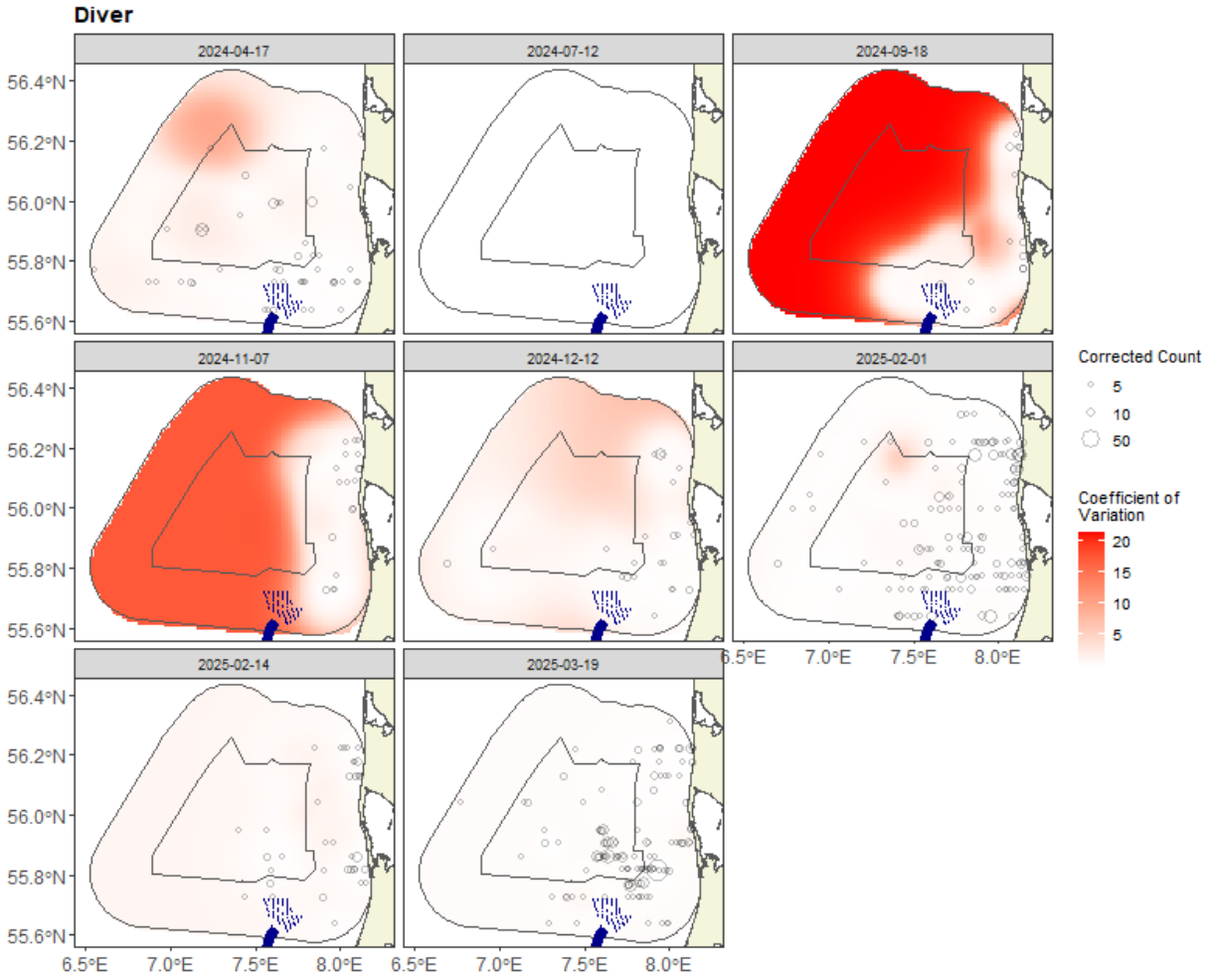

Figure 3-7. Figure showing the coefficient of variation (CoV) across the NSI survey area for each Y2 survey. The open circles represent the distance-corrected counts. The presence of dark red CoV scores in areas with virtually zero predictions is an artefact of the very small prediction rather than any notable concern.

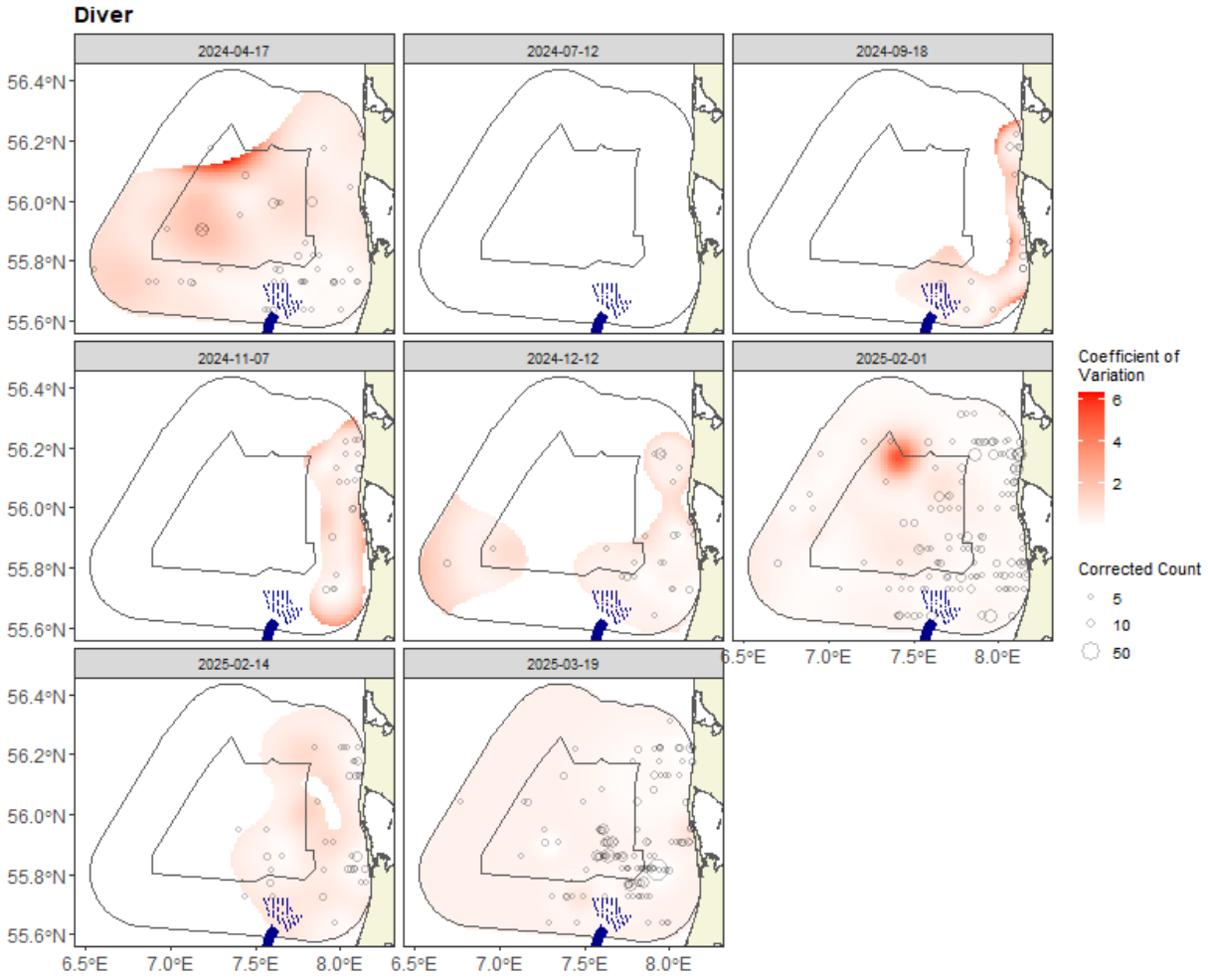

Figure 3-8. Figure showing the Y2 coefficient of variation (CoV) for all cells above a density of 0.001. The open circles represent the distance-corrected counts. The presence of dark red CoV scores in areas with virtually zero predictions is an artefact of the very small prediction rather than any notable concern.

3.1.1.6 Model diagnostics

A blocking structure was used to account for potential residual non-independence for each model, and a robust standard error approach was based on unique transects. In each case, a reassuring decay to zero was observed (indicated by the red and grey lines in Figure 3-9), implying that an appropriate blocking structure was employed.

The assumed mean-variance relationship was examined, and generally, good agreement was observed between the assumed (red) lines and the observed values. Figure 3-10 and Figure 3-11 show example relationships for a quasi-Poisson and Tweedie model. Figure 3-12 shows an example of a diagnostic QQ plot.

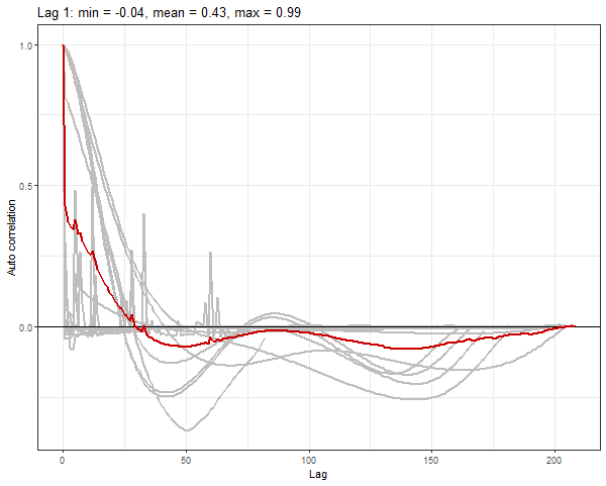

Figure 3-9. Example diagnostics for divers. The grey lines represent the residual correlation observed in each transect, and the red line is the average of these values across transects.

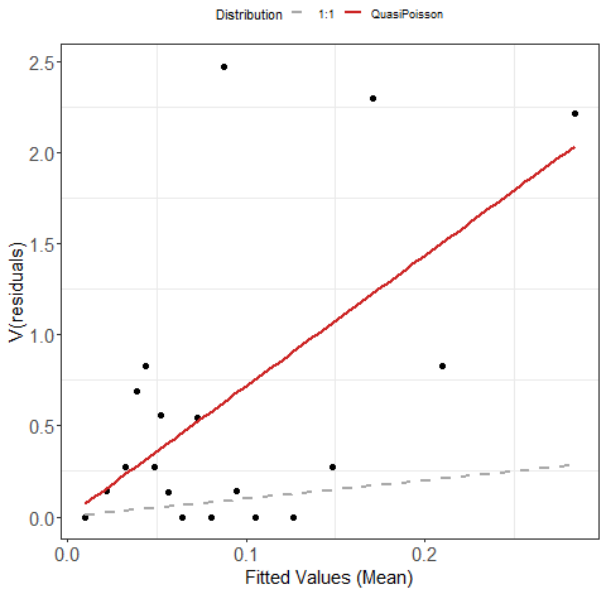

Figure 3-10. Example diagnostics for divers. The plot displays the estimated quasi-Poisson mean-variance relationship (red line) and the actual values (black dots). The black dots are based on 20 quantiles of the model residuals. For reference, the grey dashed line represents the 1:1 relationship.

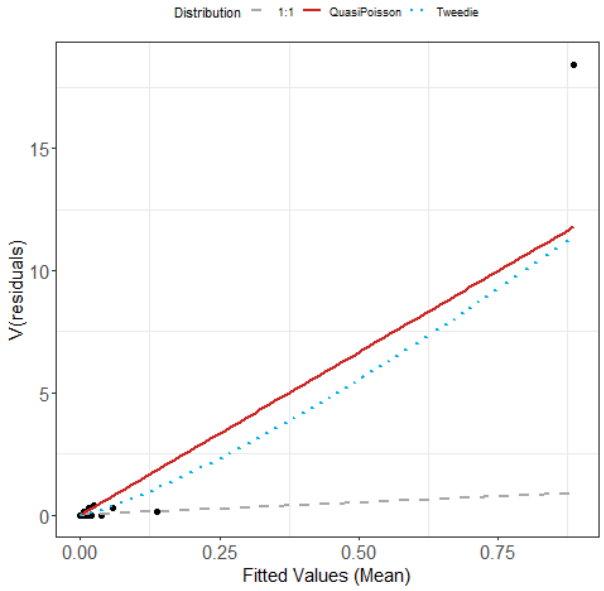

Figure 3-11. Example plot showing the estimated Tweedie mean-variance relationship (blue dashed line) for divers. The red line represents the V(μ) = ϕμ relationship, and the grey line illustrates the 1:1 relationship.

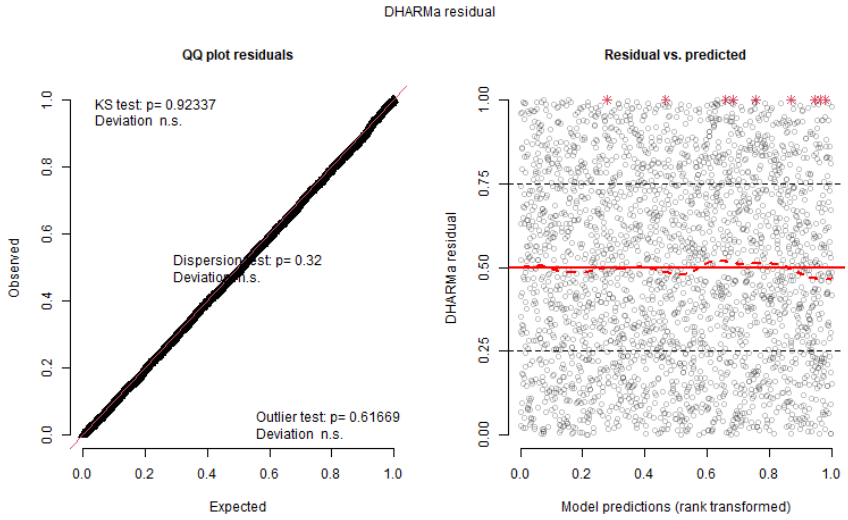

Figure 3-12. Example diagnostics for divers. QQ plot (left) and residuals against predicted values (right). The red stars are outliers, and the red line represents a smooth spline fit to the mean of the residuals.

3.1.1.7 Red-throated diver/black-throated diver (Y1 and Y2)

This section provides combined Y1 and Y2 outputs across all 16 surveys for diver species.

The estimated abundances, densities and associated 95% percentile confidence intervals for each survey are given in Table 3-4 and Figure 3-13. The diver abundances were very similar across the 16 Y1 and Y2 surveys, with the most abundant being in March 2024 and the early February and March surveys from 2025.

Table 3-4. Estimated abundance and density of diver species for each of the 16 Y1 and Y2 surveys conducted. The 95% CI is a percentile-based confidence interval.

Date	Area (Km^2)	Estimation Type	Estimated Count	95% CI Count	Estimated Density	95% CI Density
2023-04-30	7833	Spatial	1289	(653, 2722)	0.2	(0.1, 0.3)
2023-07-07	7833	H-T	31	(29, 34)	0.0	(0, 0)
2023-09-05	7833	H-T	89	(83, 97)	0.0	(0, 0)
2023-11-26	7833	Spatial	209	(90, 543)	0.0	(0, 0.1)
2023-12-14	7833	Spatial	936	(431, 3526)	0.1	(0.1, 0.5)
2024-02-08	7833	Spatial	1921	(798, 5407)	0.2	(0.1, 0.7)
2024-02-25	7833	Spatial	776	(367, 1895)	0.1	(0, 0.2)
2024-03-21	7833	Spatial	7548	(4797, 12752)	1.0	(0.6, 1.6)
2024-04-17	7833	Spatial	1106	(474, 4553)	0.1	(0.1, 0.6)
2024-07-12	7833	H-T	0	(0, 0)	0.0	(0, 0)
2024-09-18	7833	Spatial	349	(148, 972)	0.0	(0, 0.1)
2024-11-07	7833	Spatial	362	(155, 1104)	0.0	(0, 0.1)
2024-12-12	7833	Spatial	902	(479, 1923)	0.1	(0.1, 0.2)
2025-02-01	7833	Spatial	4223	(2587, 7442)	0.5	(0.3, 1)
2025-02-14	7833	Spatial	628	(338, 1370)	0.1	(0, 0.2)
2025-03-19	7833	Spatial	4401	(2477, 8648)	0.6	(0.3, 1.1)

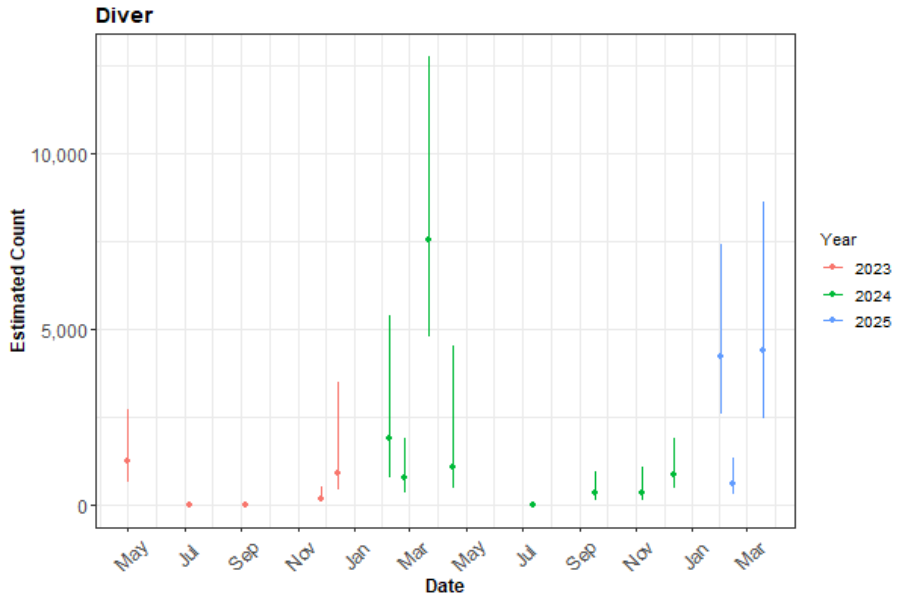

Figure 3-13. The estimated count of diver species for each of the 16 Y1 and Y2 surveys conducted. The 95% CI are percentile-based confidence intervals are from a parametric bootstrap with 500 replicates. As the survey area is the same for each survey, the abundances are comparable.

Figure 3-14 and Figure 3-15 show the estimated numbers of diver species in each 1 km^2 grid cell for each Y1 and Y2 survey. The first figure displays the surfaces on the same scale for all surveys, while the second (Figure 3-15) limits the estimated densities to 15 individuals per km^2 to provide more detail. Generally, the estimated abundances fitted well

with the raw data, and there were no notable misalignments. In areas where the estimated numbers were systematically higher, the abundances were also relatively high, and there were no areas with large, estimated abundances that were unsupported by the data.

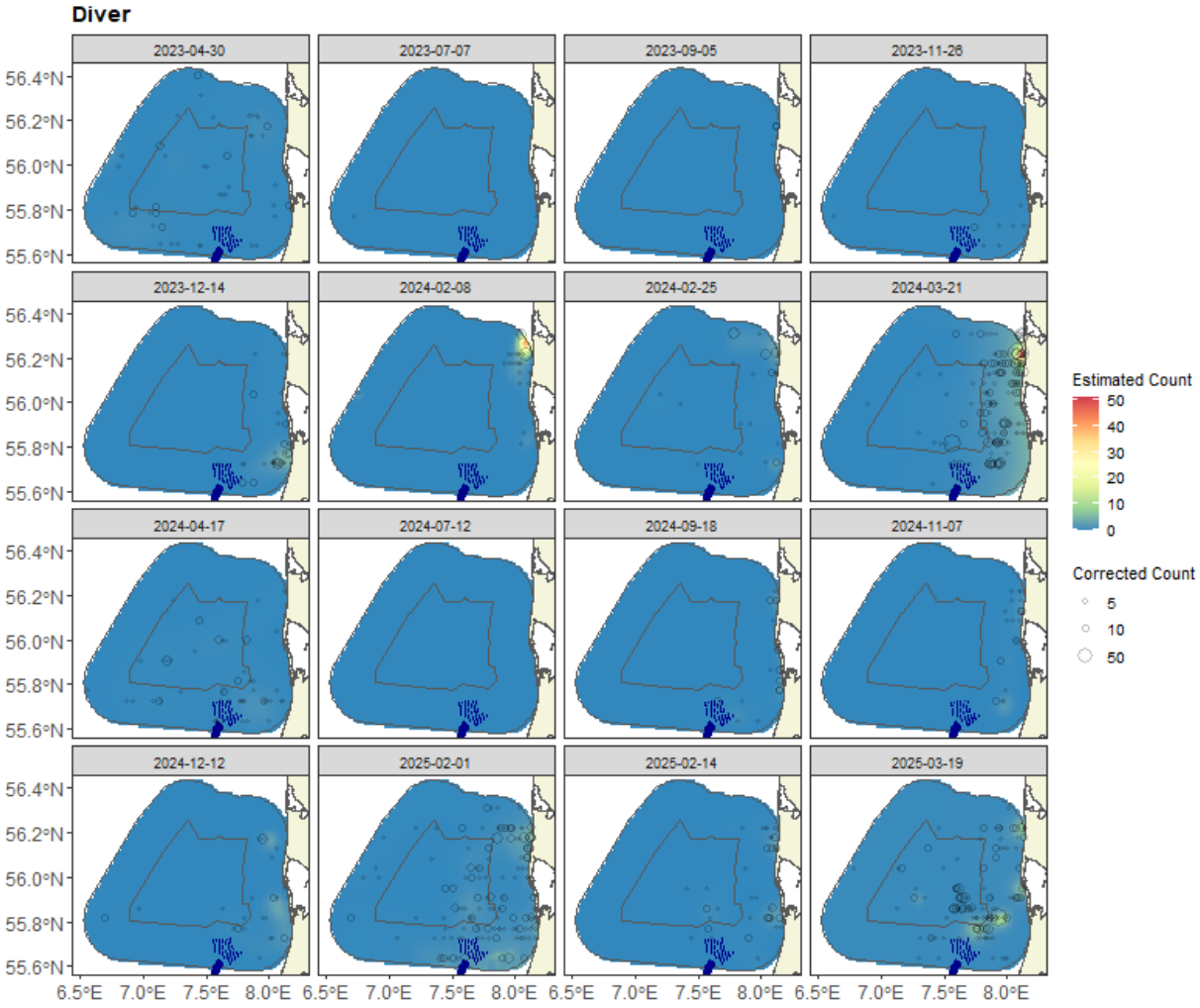

Figure 3-14. Figure showing the estimated diver species abundance across the NSI survey area for each of the 16 surveys conducted in Y1 and Y2. The estimated numbers are based on a 1 km x 1 km grid cell. The open circles represent the distance-corrected counts.

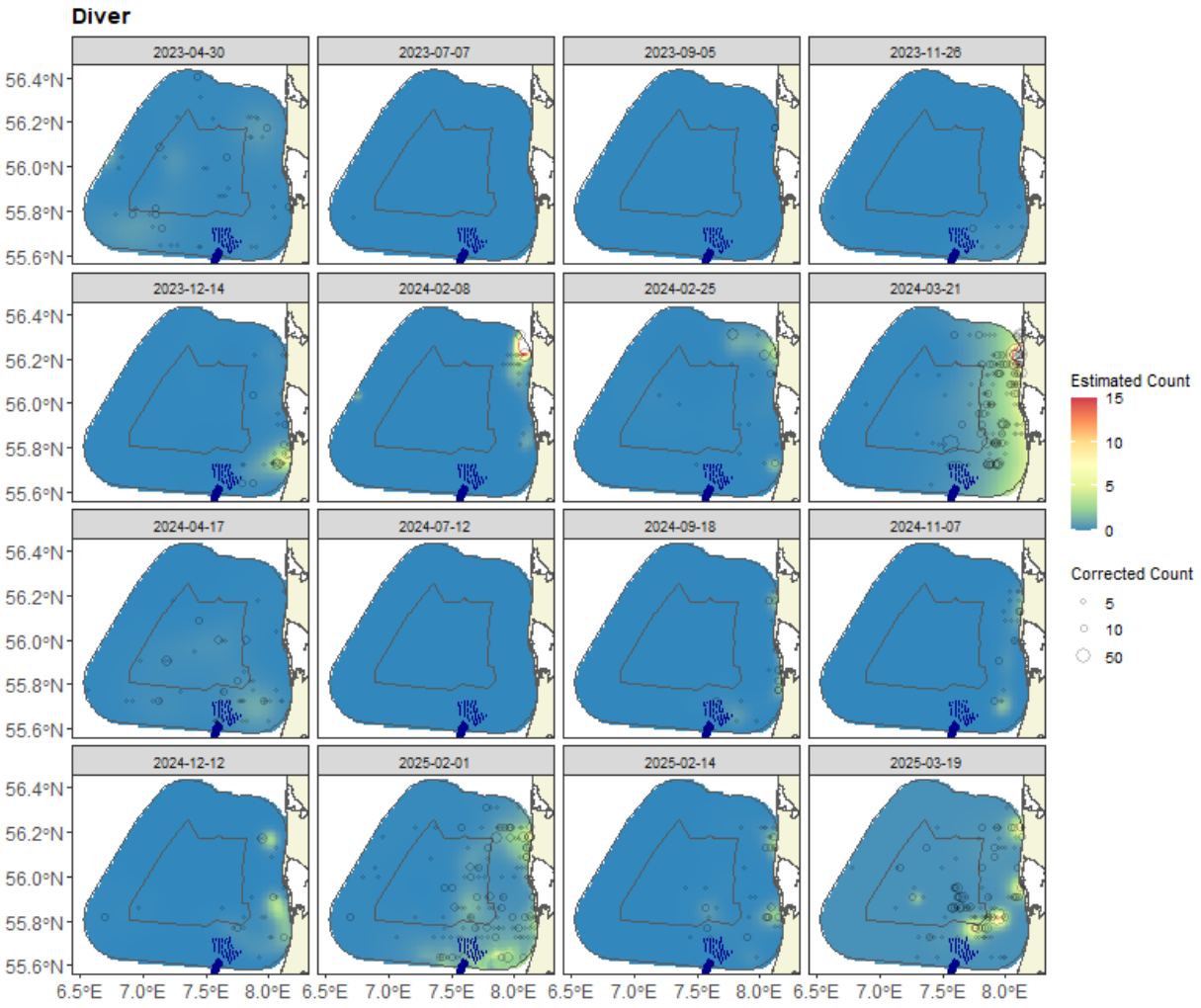

Figure 3-15. Figure showing the estimated diver species abundance across the NSI survey area for each of the 16 surveys conducted in Y1 and Y2. The estimated numbers are based on a 1 km x 1 km grid cell. The open circles represent the distance-corrected counts.

3.1.1.8 Areas of persistence

Figure 3-16 and Figure 3-17 show the persistence across the Y1 and Y2 surveys. In the Y1 surveys, moderate persistence was observed across the eastern survey area, particularly in the northeast and southeast (Figure 3-17). The highest persistence (~ 60%) occurs to the northeast along the coastline. The plot indicates that when diver species are present during these surveys, they are predominantly found in the eastern coastal parts of the survey area. The pattern for the Y2 surveys is very similar. The persistence is similarly distributed to the northeast and southeast but higher. The highest persistence occurs across Y2 surveys in the central and southern regions (~ 77%).

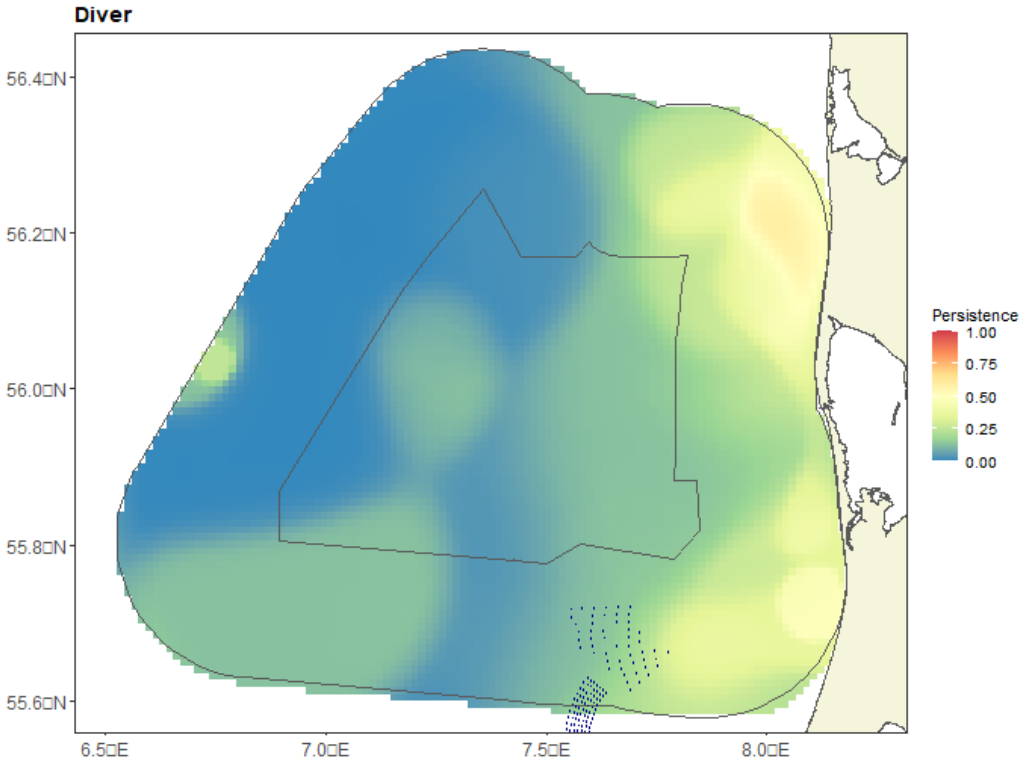

Figure 3-16. Persistence scores for diver species across the Y1 surveys from April 2023 to March 2024. The polygons representing the wind farm pre-investigation area and the NSI survey area are indicated by black lines.

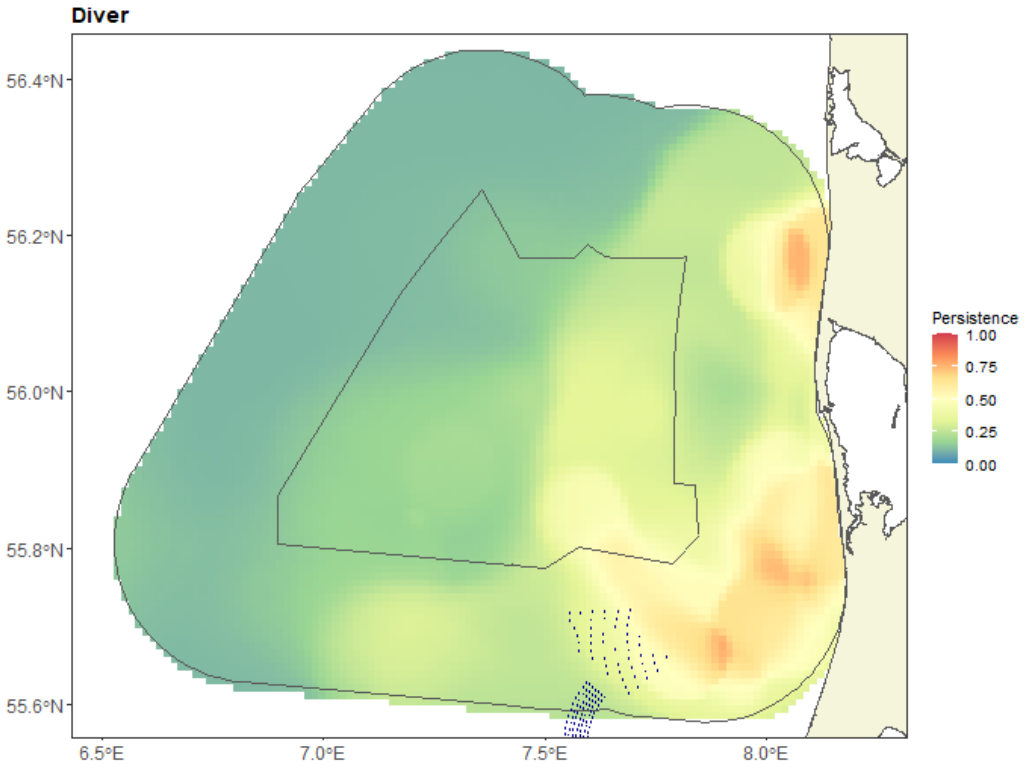

Figure 3-17. Persistence scores for diver species across the Y2 surveys from April 2024 to March 2025. The polygons represent the NSI pre-investigation area and the NSI survey area are indicated by black lines.

Figure 3-18 shows the persistence across all 16 Y1 and Y2 surveys. As expected, given the distributional similarities of the separate persistence maps, the overall persistence is highest in the eastern parts of the survey area, with medium persistence values for the central parts. The highest persistence is ~66%.

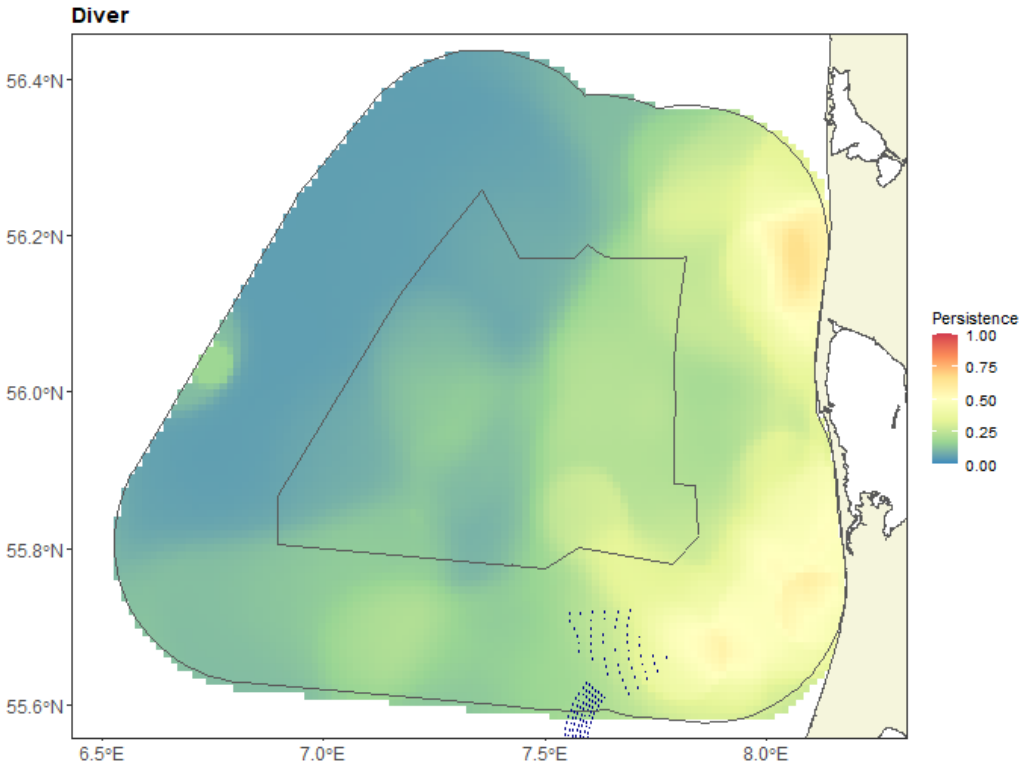

Figure 3-18. Persistence scores for diver species across all 16 Y1 and Y2 surveys conducted between April 2023 and March 2025. The polygons represent the NSI pre-investigation area and the NSI survey area are indicated by black lines.

3.1.2 Northern gannet (*Morus bassanus*)

Northern gannets were recorded during most Y2 surveys in the area. A total of 793 birds were encountered, most of which were seen in April 2024 (263 birds) and March 2025 (301 birds). During the November 2024 and mid-February 2025 surveys, only two, four and five northern gannets were recorded (Table 3-1).

Northern gannets were observed throughout the survey area, with notable differences in distribution between Y2 surveys. Concentrations were observed in the central, western and northern parts, while fewer birds were observed in the eastern, coastal and southern parts (Figure 3-19 and Figure 3-20). The average flock size was 1.24, with a maximum of 15 birds.

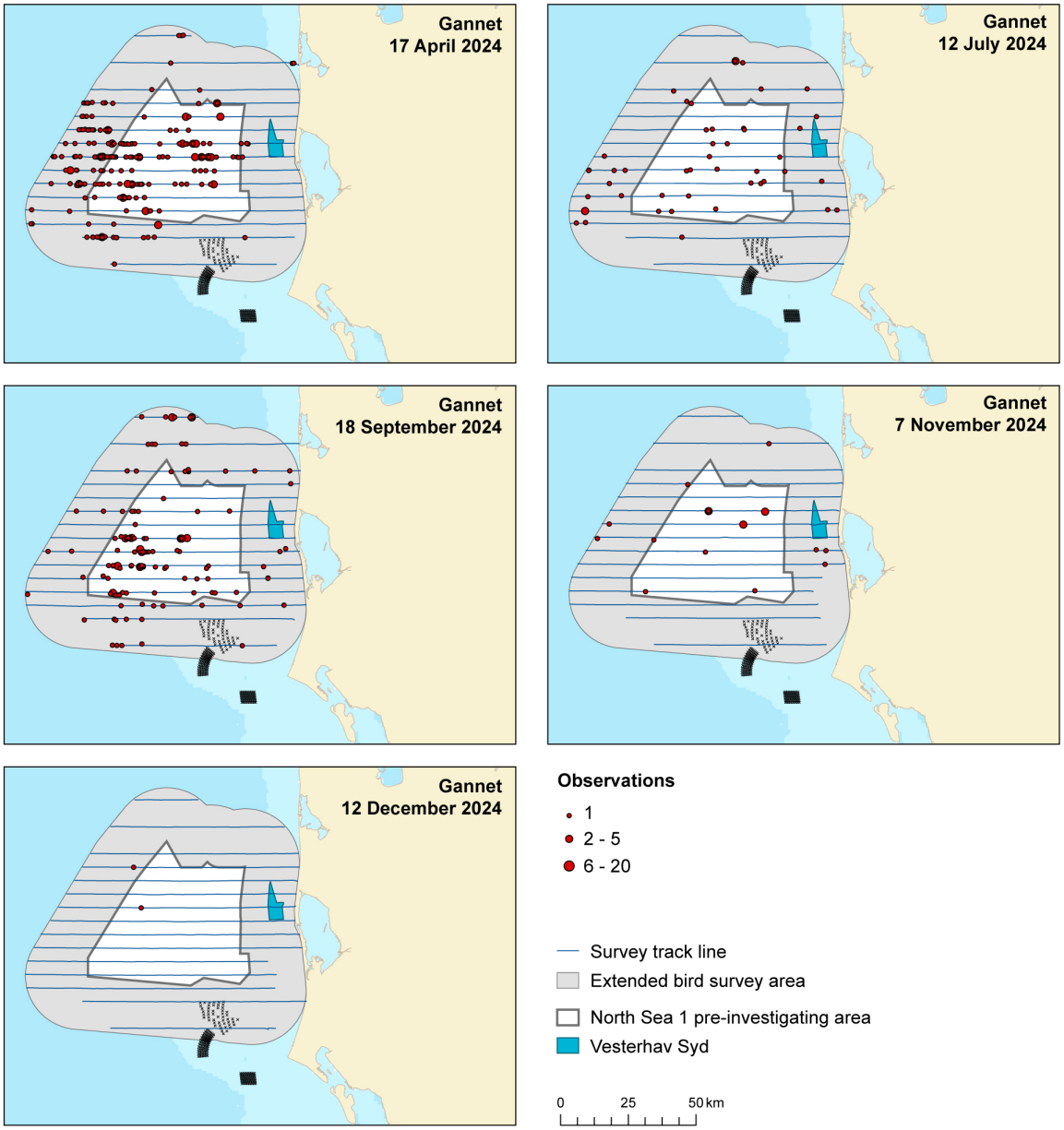

Figure 3-19. The numbers and distribution of northern gannets observed during five Y2 surveys in the NSI survey area.

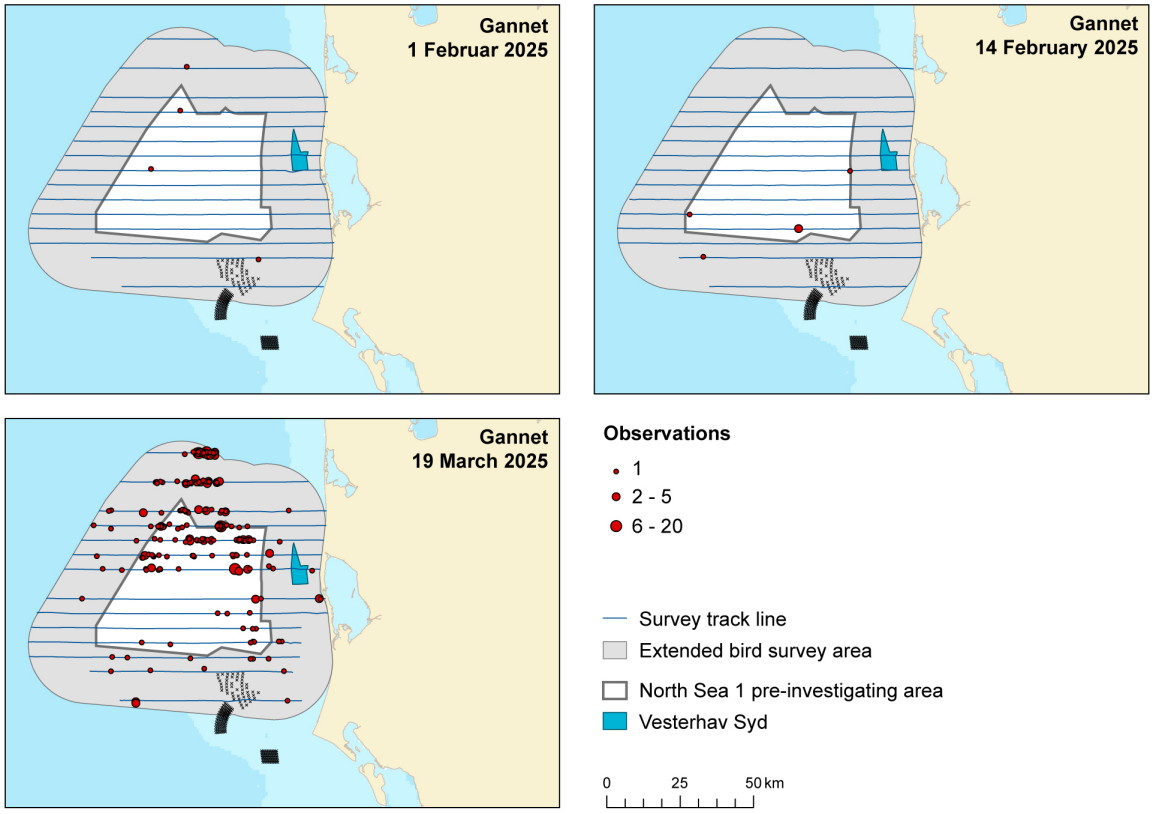

Figure 3-20. The numbers and distribution of northern gannets observed during five Y2 surveys in the NSI survey area.

3.1.2.1 Distance analysis

The average probability of sighting a northern gannet was estimated to be 0.31 (CoV = 0.04). This probability was estimated using a half-normal detection function with group size as a covariate (Figure 3-21). This detection function was estimated using the Y1 surveys, and this model was then used to estimate the number of birds in the Y2 surveys. The probability of detection for larger groups is slightly higher than for smaller groups in all distance bins (Figure 3-21).

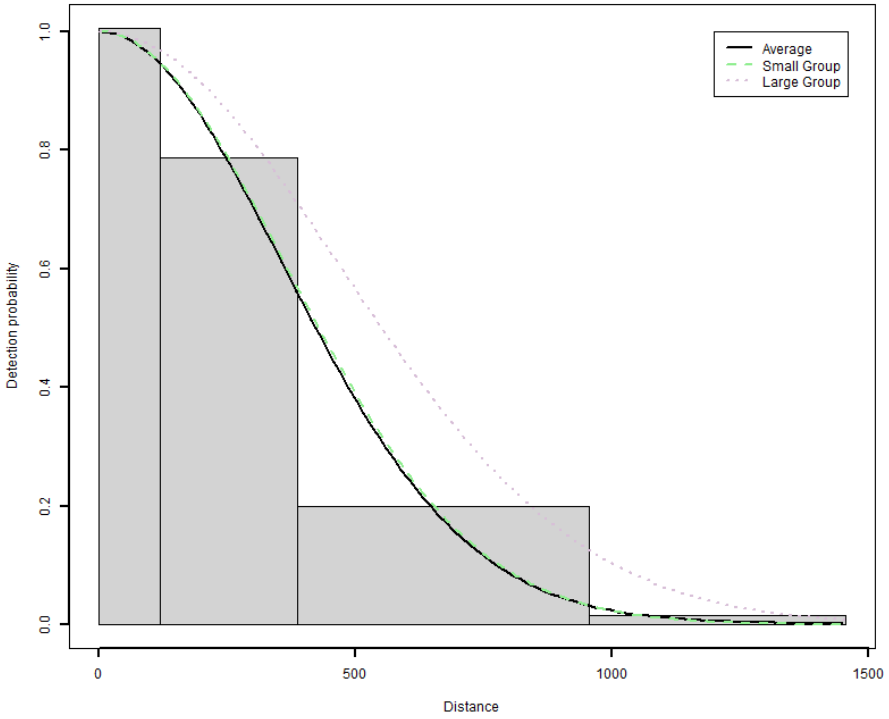

Figure 3-21. Figure showing the estimated detection function for a small and large group of northern gannets. The histogram represents the distances of the observed sightings.

3.1.2.2 Spatial analysis

Figure 3-22 shows the distribution of the distance-corrected counts for each of the eight Y2 surveys.

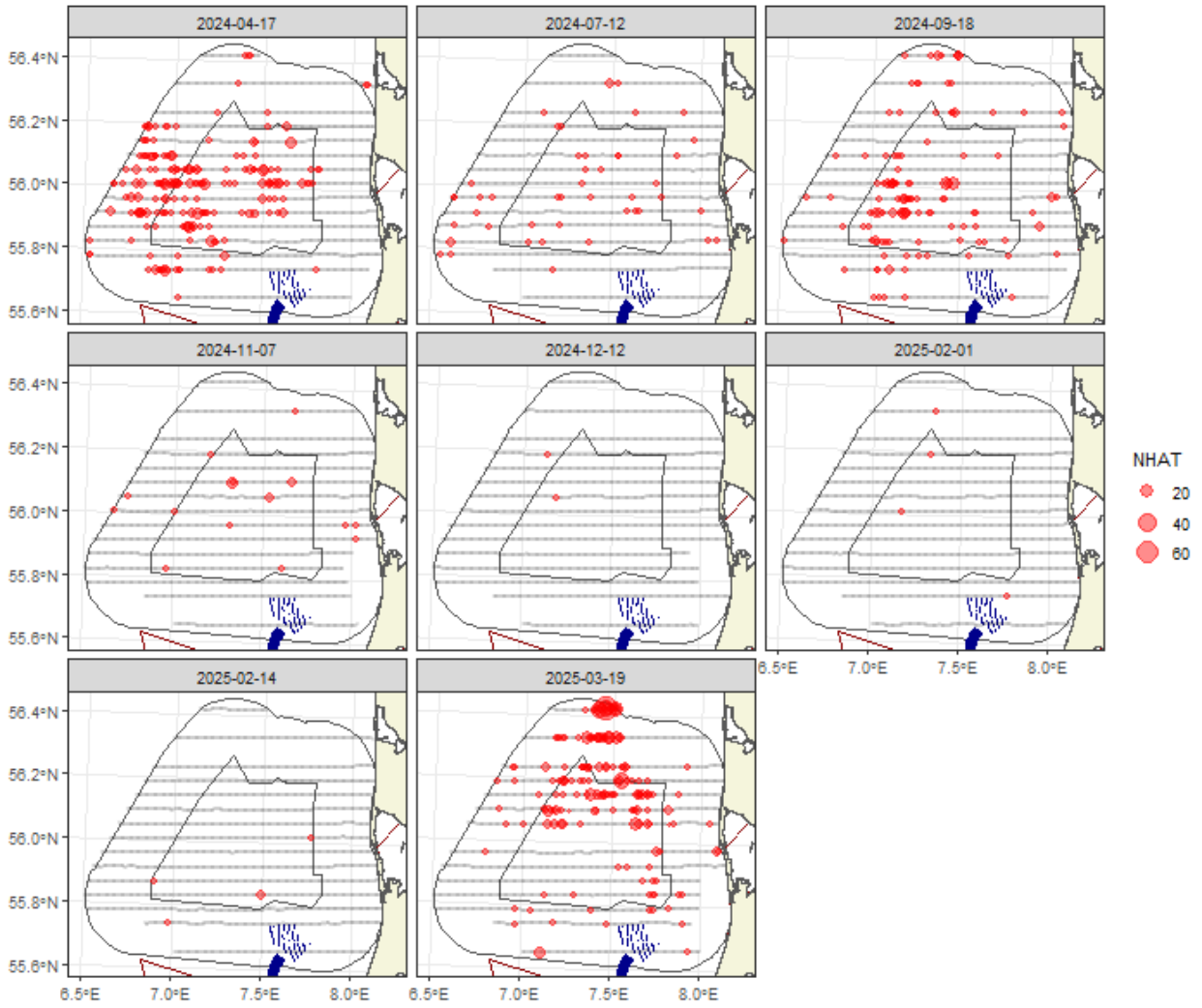

Figure 3-22. Distance-corrected counts for the northern gannet across the eight Y2 surveys. The red circles indicate the distance-corrected counts along the transect lines. The grey dots are segments with a count of zero.

3.1.2.3 Model selection

For three of the eight Y2 surveys, there was insufficient data to fit spatial models. For the other five surveys, the models included a spatial term (of varying complexity). A linear term for depth was selected for one survey, while the distance to the coast (either as a linear or smooth term) was not selected for any surveys. This indicates that there was compelling evidence for non-uniform spatial patterns in five of the Y2 surveys. However, despite these spatial patterns, there was no evidence of relationships between depth or distance to the coast. The spatial surfaces selected ranged from three to 12 parameters for the spatial term (Table 3-5).

Table 3-5. Model selection results for northern gannet for each Y2 survey. The model column represents the terms in the model.

Date	Model	Distribution	Variable 1D	Variable 2D	Number of parameters	Dispersion parameter	Tweedie parameter
2024-04-17	Best 1D2D	quasipoisson	depth, df=1	s(x,y, df=10)	12	4.6	NA
2024-07-12	2D Only	quasipoisson	NA	s(x,y, df=8)	9	2.8	NA

Date	Model	Distribution	Variable 1D	Variable 2D	Number of parameters	Dispersion parameter	Tweedie parameter
2024-09-18	2D Only	quasipoisson	NA	s(x,y, df=2)	3	4.9	NA
2024-11-07	2D Only	quasipoisson	NA	s(x,y, df=8)	9	6.0	NA
2024-12-12	No Model	NA	NA	NA	NA	NA	NA
2025-02-01	No Model	NA	NA	NA	NA	NA	NA
2025-02-14	No Model	NA	NA	NA	NA	NA	NA
2025-03-19	2D Only	quasipoisson	NA	s(x,y, df=11)	12	7.9	NA

The estimated abundances, densities, and associated 95% confidence intervals for each survey are presented in Table 3-6 and Figure 3-23. For the December 2024 and February 2025 surveys, there was not enough data to fit a spatial model, and therefore, the abundance estimates were calculated using the Horvitz-Thompson method (H-T). The greatest abundance was estimated for the March 2025 survey (4,145 birds, 95% IC: 2,415-7,253). However, this confidence interval overlapped with the April 2024 survey, indicating there may be no difference between the two (Table 3-6).

Table 3-6. Estimated abundance and density of northern gannet for each Y2 survey. The 95% CI is a percentile-based confidence interval.

Date	Area (Km^2)	Estimator type	Estimated count	95% CI count	Estimated density	95% CI density
2024-04-17	7,833	Spatial	2,237	(1,345, 3,536)	0.3	(0.2, 0.5)
2024-07-12	7,833	Spatial	323	(200, 465)	0.0	(0, 0.1)
2024-09-18	7,833	Spatial	979	(590, 1,499)	0.1	(0.1, 0.2)
2024-11-07	7,833	Spatial	145	(59, 430)	0.0	(0, 0.1)
2024-12-12	7,833	H-T	17	(16, 18)	0.0	(0, 0)
2025-02-01	7,833	H-T	33	(31, 35)	0.0	(0, 0)
2025-02-14	7,833	H-T	35	(33, 37)	0.0	(0, 0)
2025-03-19	7,833	Spatial	4,145	(2,415, 7,253)	0.5	(0.3, 0.9)

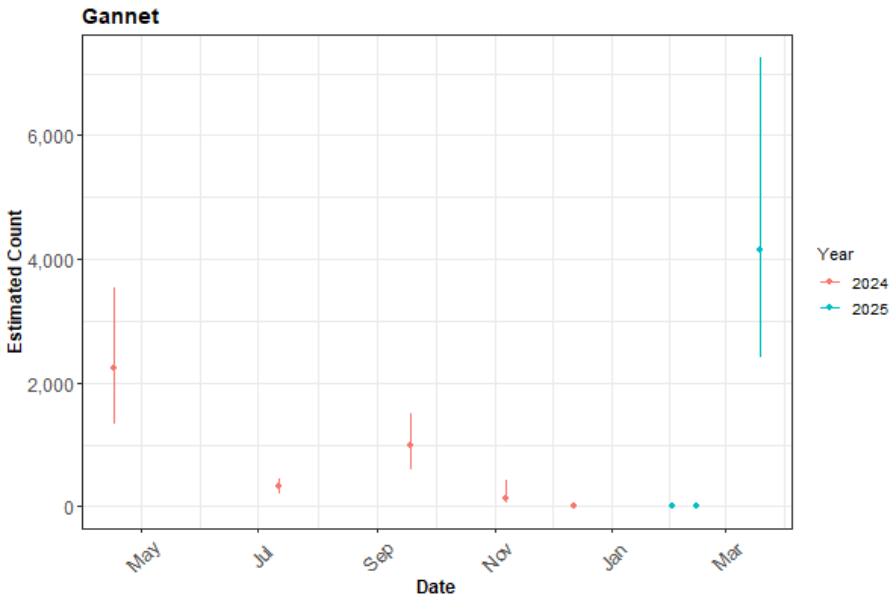

Figure 3-23. The estimated count of northern gannet for each Y2 survey. The 95% CI are percentile-based confidence intervals are from a parametric bootstrap with 500 replicates.

3.1.2.4 Spatial results

Figure 3-24 shows the estimated numbers of northern gannets in each 1 km^2 grid cell for each of the eight Y2 surveys. Generally, the estimated abundances fit well with the raw data, and there were no notable misalignments. In areas where the estimated numbers were systematically higher, the abundances were also relatively high, and there were no areas with large, estimated abundances unsupported by the data.

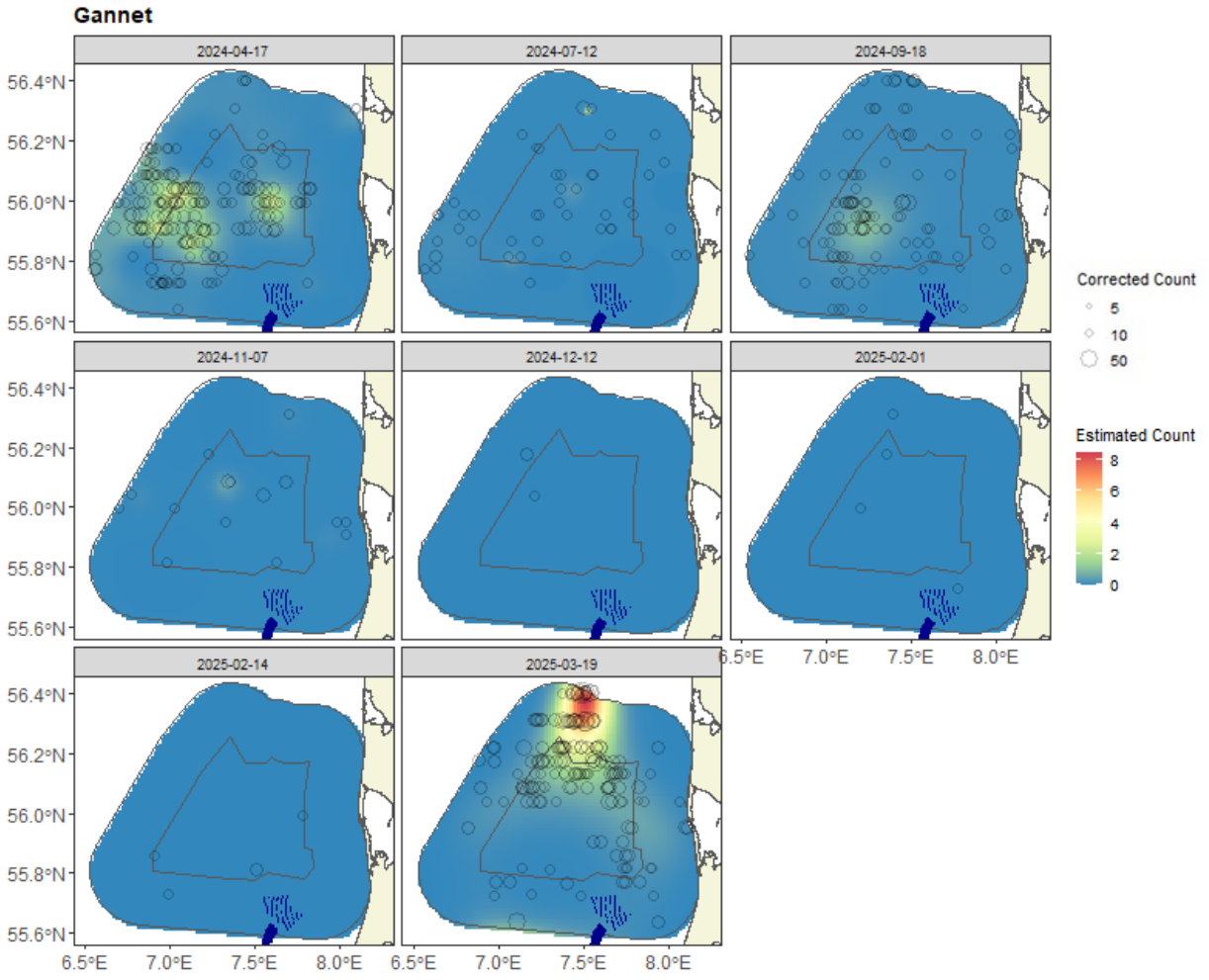

Figure 3-24. Figure showing the estimated northern gannet abundance across the NSI survey area for each Y2 survey. The estimated numbers are per 1 km x 1 km grid cell. The open circles represent the distance-corrected counts.

3.1.2.5 Uncertainty in spatial predictions

Broadly, the highest coefficient of variation (CoV) scores was associated with the `almost zero' predictions, and it is known that the CoV metric is highly sensitive to any uncertainty for very small predictions. There was no material overlap between high values of the CoV metric and the transect lines/locations with non-zero counts, resulting in no concerns in this case (Figure 3-25).

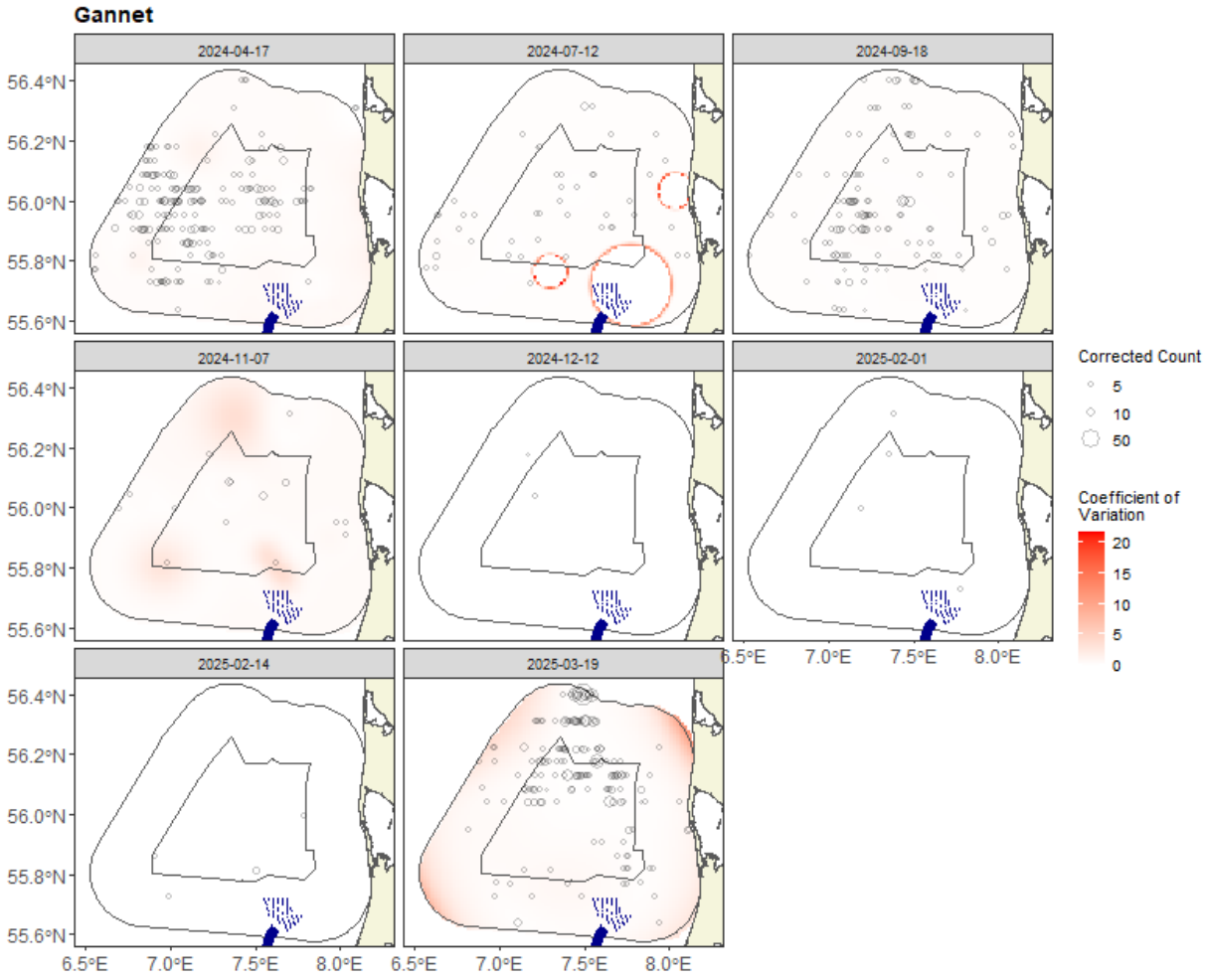

Figure 3-25. Figure showing the coefficient of variation across the NSI survey area for each Y2 survey. The open circles show the distance corrected counts, where applicable, and the polygons represent the NSI pre-investigation area (black line). The presence of dark red CoV scores in areas with virtually zero predictions is an artefact of the very small prediction rather than of any notable concern.

In the case where the very small, predicted values were excluded (Figure 3-26), the CoV for most surveys was <1, and so was of no material concern. For one survey, there remained some high uncertainty around very small values, which

play a role in the related confidence intervals for the abundances (Table 3-6 and Figure 3-23).

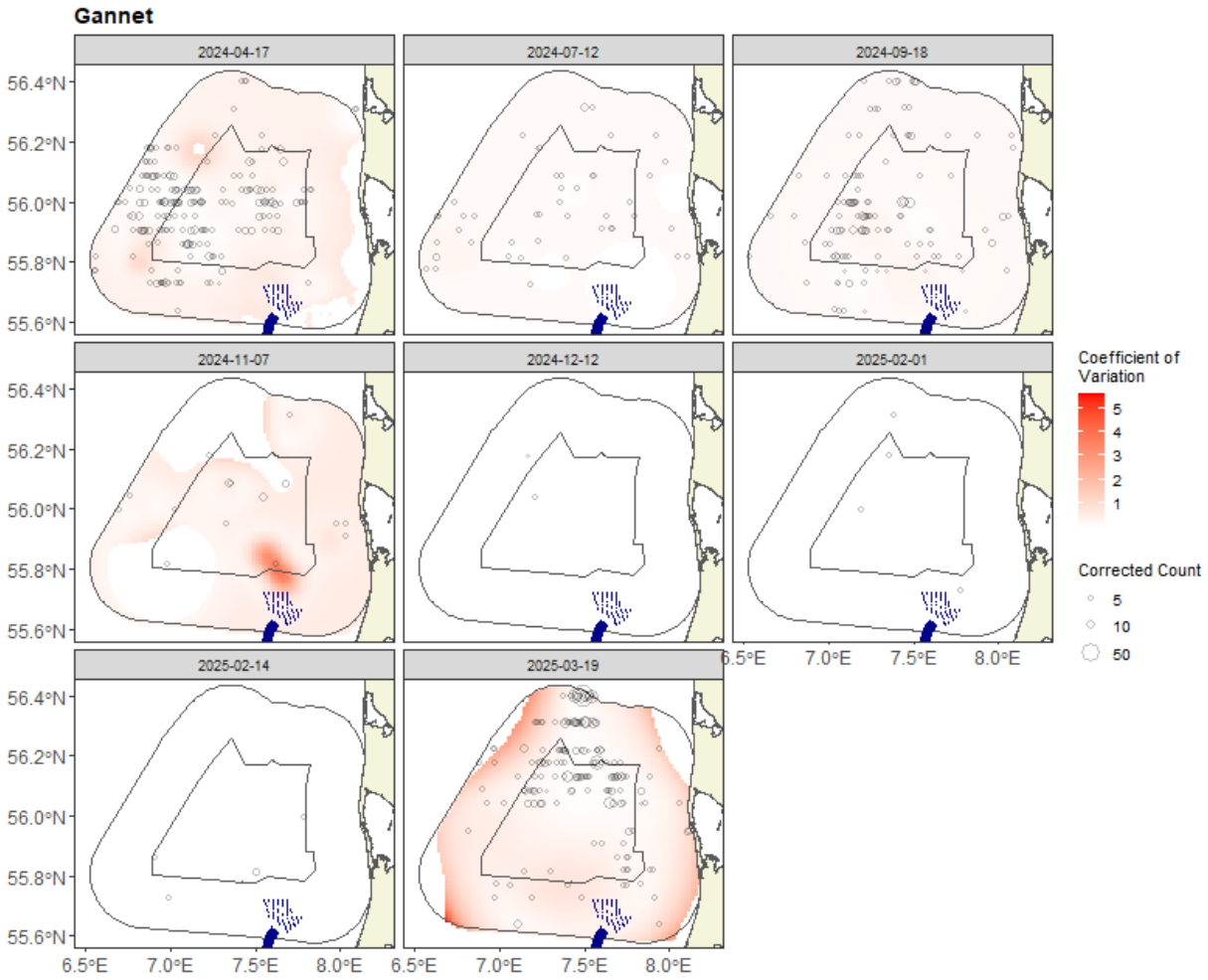

Figure 3-26. Figure showing the Y2 coefficient of variation for all cells above the 25% quantile of predicted values. The open circles show the distance corrected counts, where applicable, and the polygons represent the NSI pre-investigation area (black line). The presence of dark red CoV scores in areas with virtually zero predictions is an artefact of the very small prediction rather than any notable concern.

3.1.2.6 Model diagnostics

A blocking structure was used to account for potential residual non-independence for each Y2 model, and a robust standard error approach was based on unique transects. In each case, a reassuring decay to zero was seen (indicated by the red and grey lines in Figure 3-27), implying that an appropriate blocking structure was used.

The assumed mean-variance relationship was examined, and agreement was generally shown between the assumed (red) lines and the observed values. Figure 3-28 shows example relationships for a quasi-Poisson model. No models used a Tweedie mixing parameter greater than 1. Figure 3-29 shows an example of a diagnostics QQ plot, and no issues were identified.

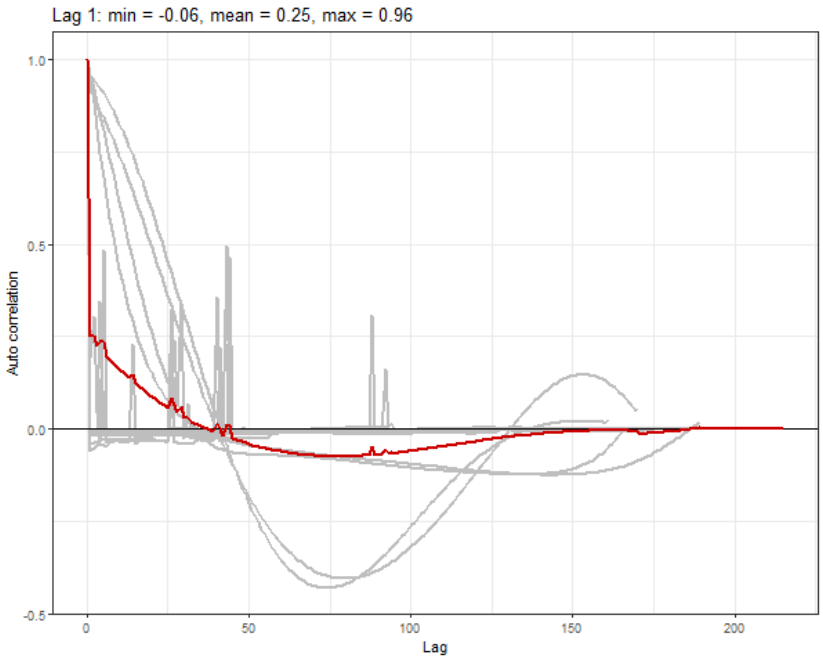

Figure 3-27. Example ACF plot for northern gannet. The grey lines represent the residual correlation observed in each transect, and the red line is the average of these values across transects.

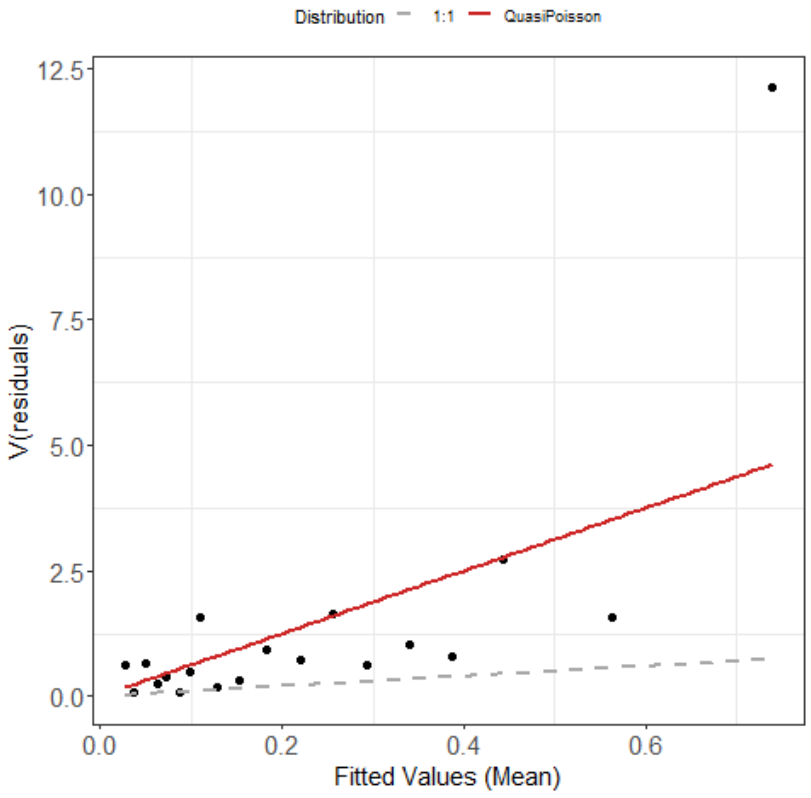

Figure 3-28. Example plot showing the estimated quasi-Poisson mean-variance relationship (red line) and actual (black dots) for northern gannet. The black dots are based on 20 quantiles of the model residuals, and for reference, the grey dashed line shows the 1:1 relationship.

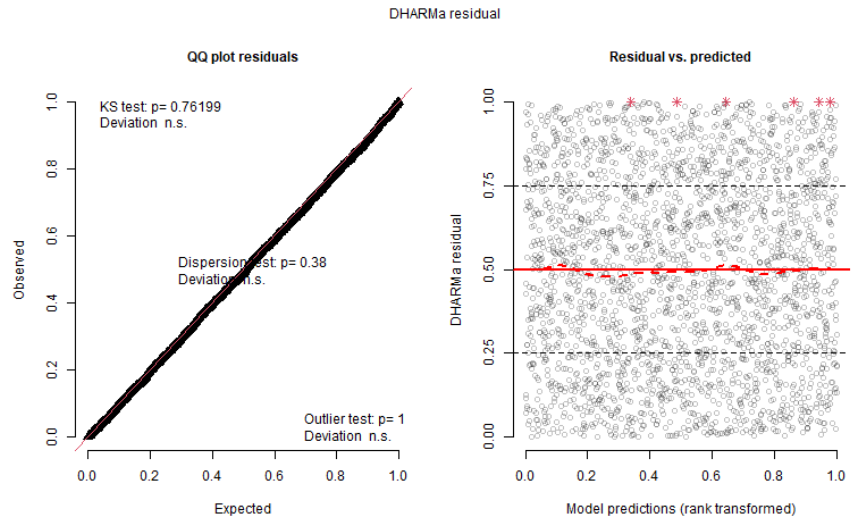

Figure 3-29. Example diagnostics for northern gannet. QQ plot (left) and residuals against predicted values (right). The red stars are outliers, and the red line is a smooth spline around the mean of the residuals.

3.1.2.7 Gannet (Y1 and Y2)

This section provides combined outputs across all 16 Y1 and Y2 surveys for northern gannets. The estimated abundances, densities and associated 95-percentile confidence intervals for each Y1 and Y2 survey are given in Table 3-7 and Figure 3-30. The highest estimated abundances were found in March and April 2024 and March 2025 in the region of 1,350-7,250 birds.

Table 3-7. Estimated abundance and density of northern gannets for each of the 16 Y1 and Y2 surveys conducted. The 95% CI are percentile-based confidence intervals

Date	Area (Km^2)	Estimation Type	Estimated Count	95% CI Count	Estimated Density	95% CI Density
2023-04-30	7,833	Spatial	332	(147, 890)	0.0	(0, 0.1)
2023-07-07	7,833	Spatial	221	(97, 556)	0.0	(0, 0.1)
2023-09-05	7,833	Spatial	1137	(601, 2,271)	0.1	(0.1, 0.3)
2023-11-26	7,833	H-T	0	(0, 0)	0.0	(0, 0)
2023-12-14	7,833	H-T	15	(14, 16)	0.0	(0, 0)
2024-02-08	7,833	H-T	0	(0, 0)	0.0	(0, 0)
2024-02-25	7,833	Spatial	124	(47, 329)	0.0	(0, 0)
2024-03-21	7,833	Spatial	2642	(1,713, 4,439)	0.3	(0.2, 0.6)
2024-04-17	7,833	Spatial	2237	(1,345, 3,536)	0.3	(0.2, 0.5)
2024-07-12	7,833	Spatial	323	(200, 465)	0.0	(0, 0.1)
2024-09-18	7,833	Spatial	979	(590, 1499)	0.1	(0.1, 0.2)
2024-11-07	7,833	Spatial	145	(59, 430)	0.0	(0, 0.1)
2024-12-12	7,833	H-T	17	(16, 18)	0.0	(0, 0)
2025-02-01	7,833	H-T	33	(31, 35)	0.0	(0, 0)
2025-02-14	7,833	H-T	35	(33, 37)	0.0	(0, 0)
2025-03-19	7,833	Spatial	4,145	(2,415, 7,253)	0.5	(0.3, 0.9)

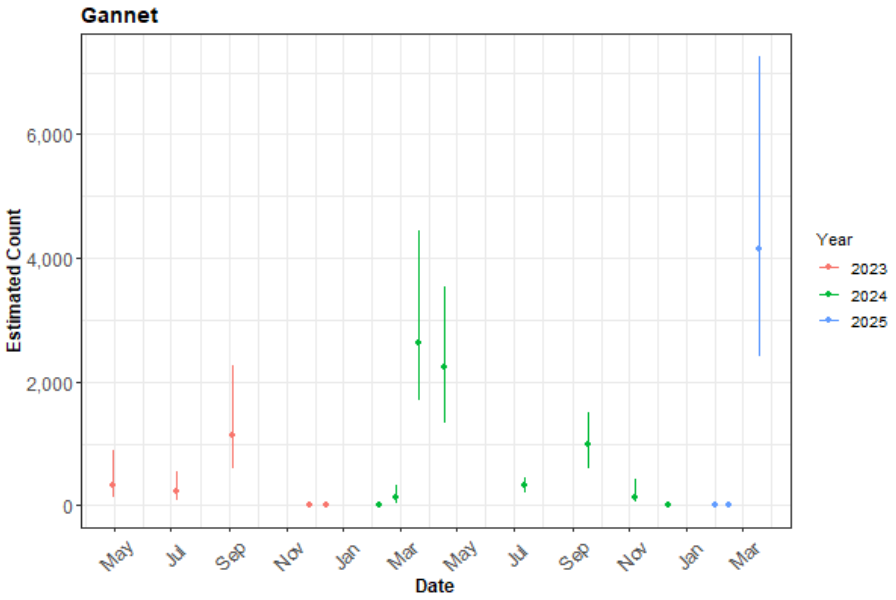

Figure 3-30. The estimated count of northern gannets for each of the 16 Y1 and Y2 surveys conducted. The 95% CI are percentile-based confidence intervals are from a parametric bootstrap with 500 replicates. As the survey area is the same for each survey, the abundances are comparable.

Figure 3-31 and Figure 3-32 show the estimated numbers of northern gannet in each 1 km^2 grid cell for each Y1 and Y2 survey. The first figure shows the surfaces on the same scale for all surveys, and the second Figure 3-32 limits the estimated density of birds pr. km^2 to four birds to provide a little more detail. Generally, the estimated abundances fitted well with the raw data, and there were no notable misalignments. In areas where the estimated numbers were systematically higher, the abundances were also relatively high, and there were no areas with large, estimated abundances unsupported by the data.

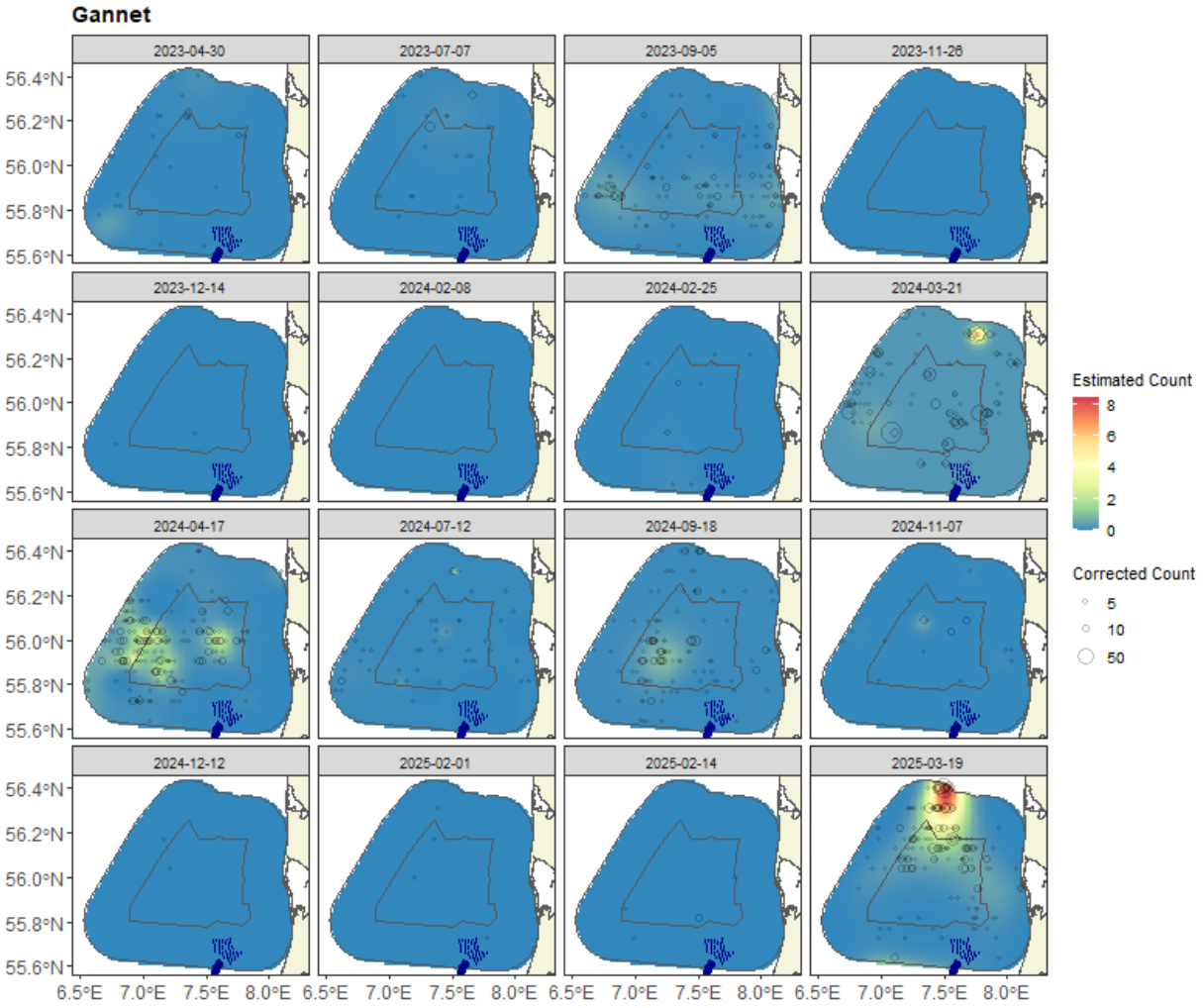

Figure 3-31. Figure showing the estimated gannet abundance across the NSI survey area for each of the 16 Y1 and Y2 surveys. The estimated counts are per 1 km x 1 km grid cell.The open circles represent the distance-corrected counts.

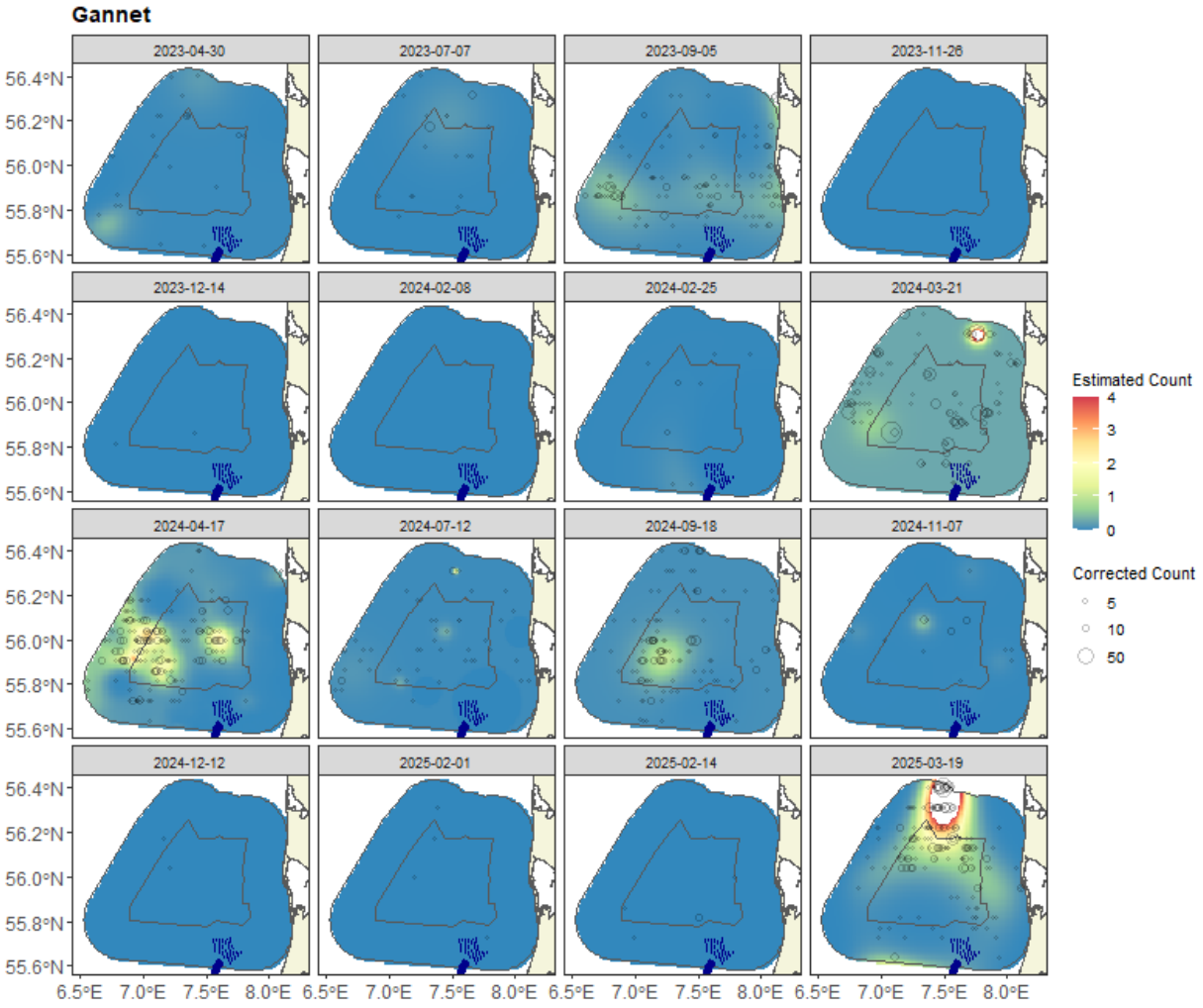

Figure 3-32. Figure showing the estimated northern gannet abundance across the NSI survey area for each of the 16 Y1 and Y2 surveys conducted. The estimated numbers are per 1 km x 1 km grid cell. The open circles represent the distance-corrected counts. White areas indicate data intentionally omitted from one or more surveys with exceptionally high abundances to allow finer detail to be seen in lower-density distributions.

3.1.2.8 Areas of Persistence

Figure 3-33 and Figure 3-34 show the persistence across the Y1 and Y2 surveys. In the Y1 surveys, there was moderate to low persistence (~ 43%) across the whole survey area (Figure 3-34). This shows that northern gannets do not consistently use specific regions of the survey area but use the whole area more generally. In the Y2 surveys, the persistence is more concentrated in the central area and higher at ~ 58%.

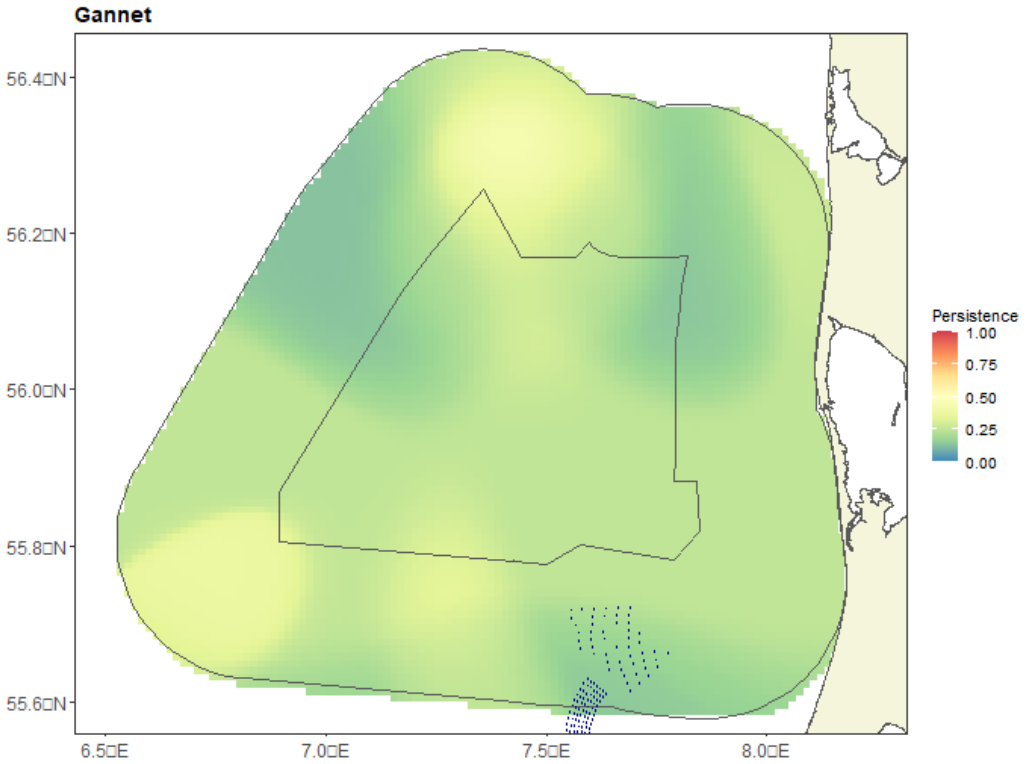

Figure 3-33. Persistence scores for northern gannet across the Y1 surveys, conducted between April 2023 and March 2024. The polygons represent the NSI pre-investigation area and the NSI survey area (black lines).

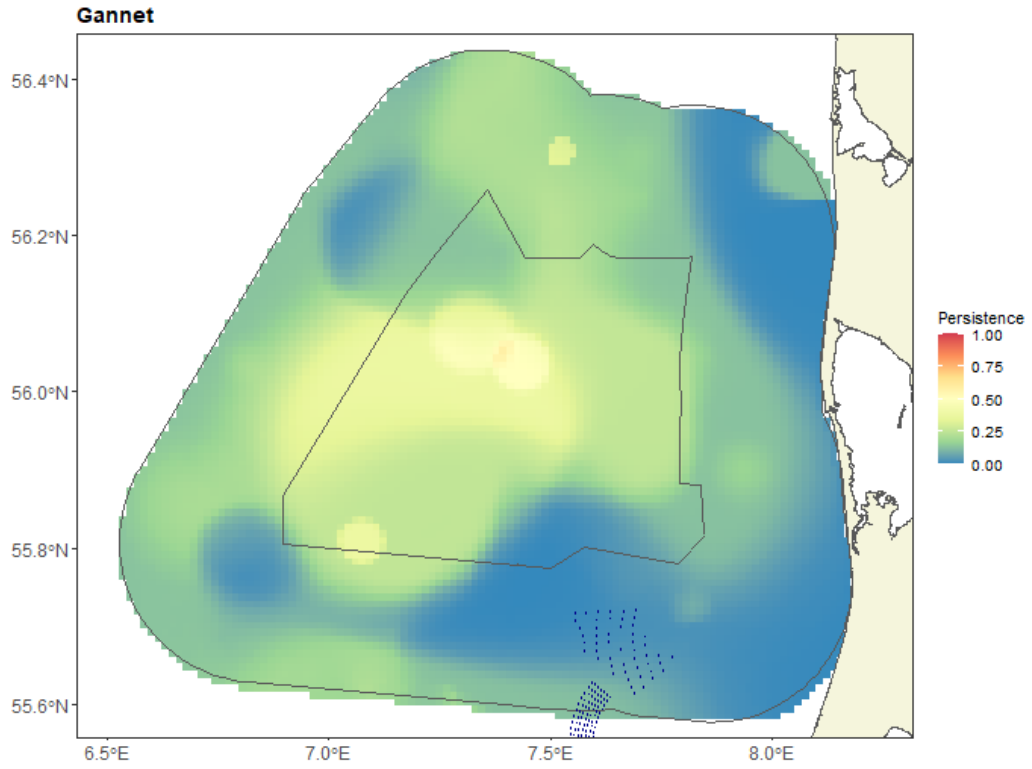

Figure 3-34. Persistence scores for northern gannet across the Y2 surveys, conducted between April 2024 and March 2025. The polygons represent the NSI pre-investigation area and the NSI survey area (black lines).

Figure 3-35 shows the persistence across all 16 Y1 and Y2 surveys. When combined, the result shows that the highest persistence is low (~ 41%) and that northern gannets use the whole survey area fairly consistently.

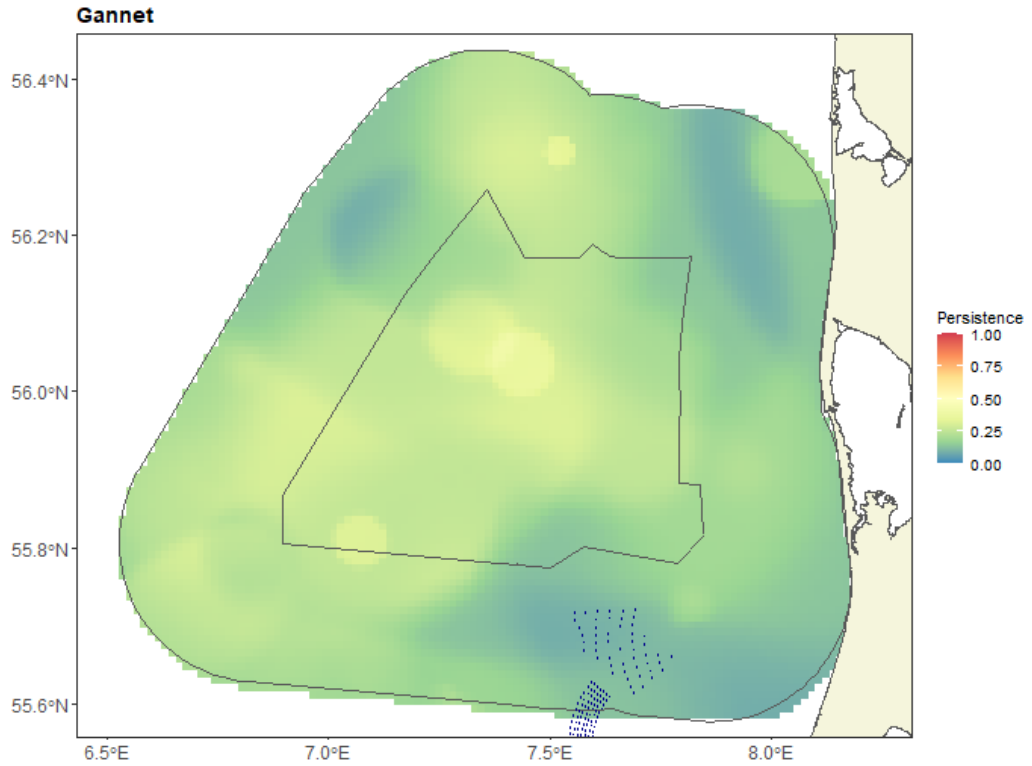

Figure 3-35. Persistence scores for northern gannet across all 16 Y1 and Y2 surveys. The polygons represent the NSI pre-investigation area and the NSI survey area (black lines).

3.1.3 Common scoter (*Melanitta nigra*)

In total, 2,841 common scoters were recorded during Y2, with 88% of those recorded from November through February. The mean flock size of the 187 recordings was 15.2, and the maximum flock size was 500 birds. The species was recorded during all eight Y2 surveys.

Common scoters were almost entirely recorded in the eastern coastal areas and in the Horns Rev area in the southern parts of the area (Figure 3-36 and Figure 3-37).

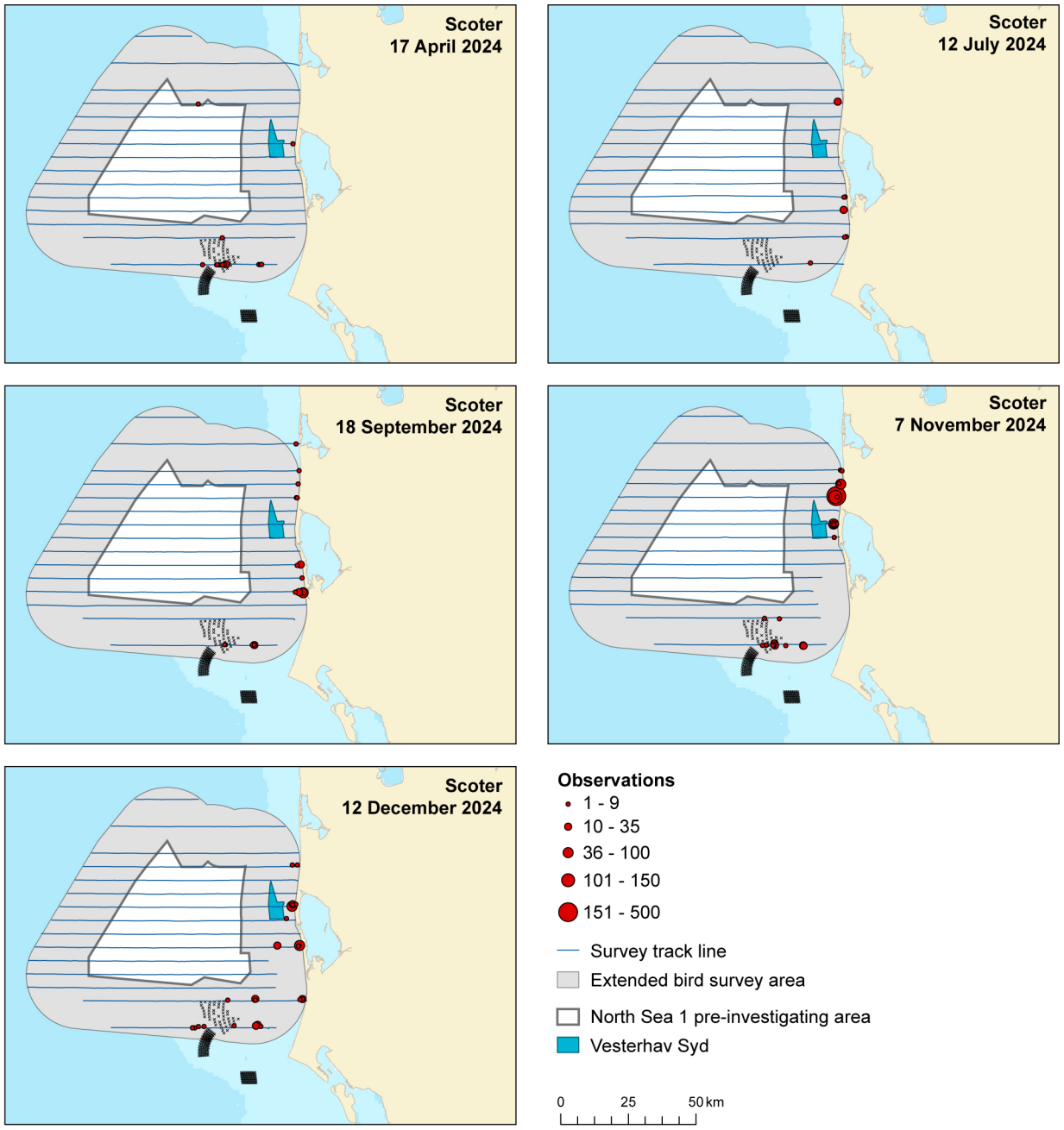

Figure 3-36. The numbers and distribution of common scoters observed during five Y2 surveys in the NSI survey area.

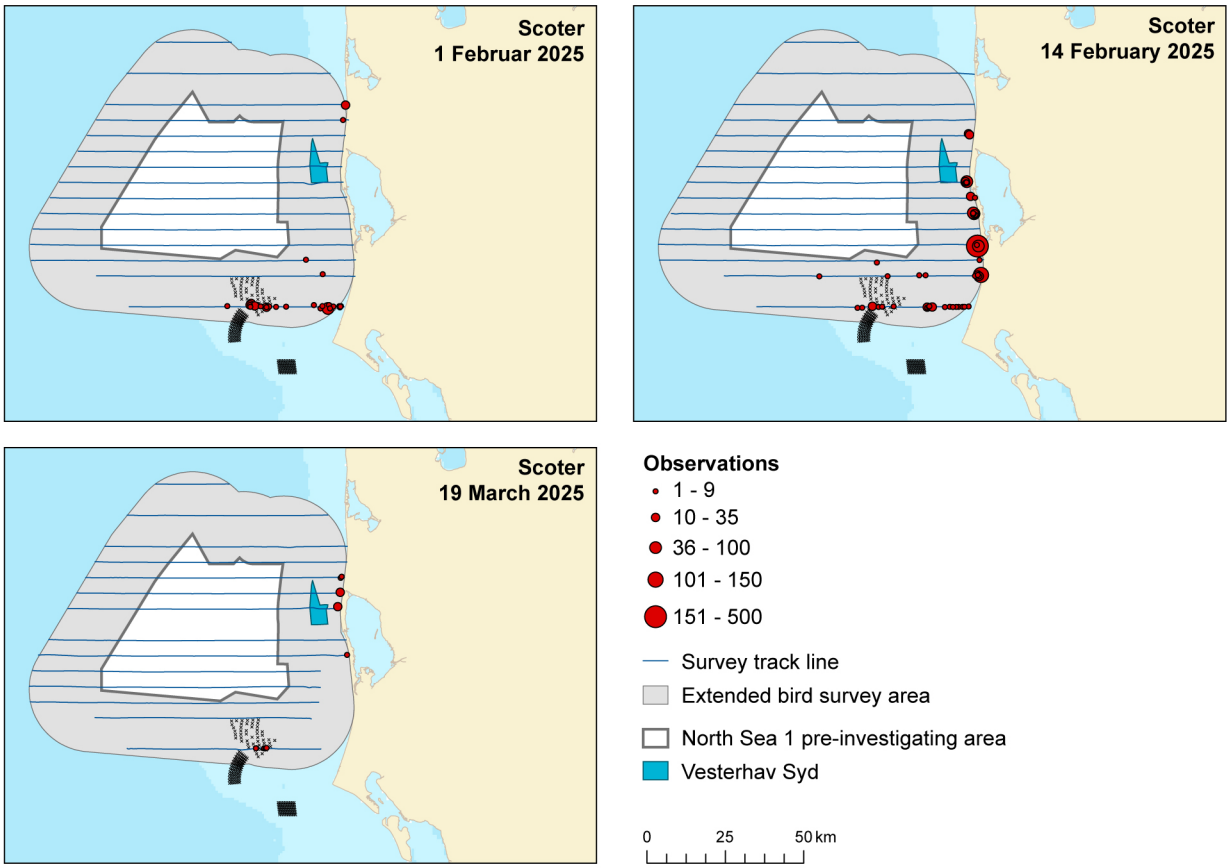

Figure 3-37. The numbers and distribution of common scoters observed during five Y2 surveys in the NSI survey area.

3.1.4 Little gull (*Hydrocoloeus minutus*)

Little gulls were recorded in significantly higher numbers in the NSI survey area During Y2 than Y1. 409 individuals were recorded during Y2, with the highest numbers recorded in November 2024 (280 birds). No little gulls were recorded during the April and July 2024 surveys, five birds during the September 2024 survey and 89 birds during the December 2024 survey (Table 3-1).

Most of the little gulls recorded during Y2 were seen in the southern and eastern parts of the survey area (Figure 3-38 and Figure 3-39). The observations of little gulls contain 266 records, with a mean flock size of 1.54 birds and a maximum flock size of 12 birds.

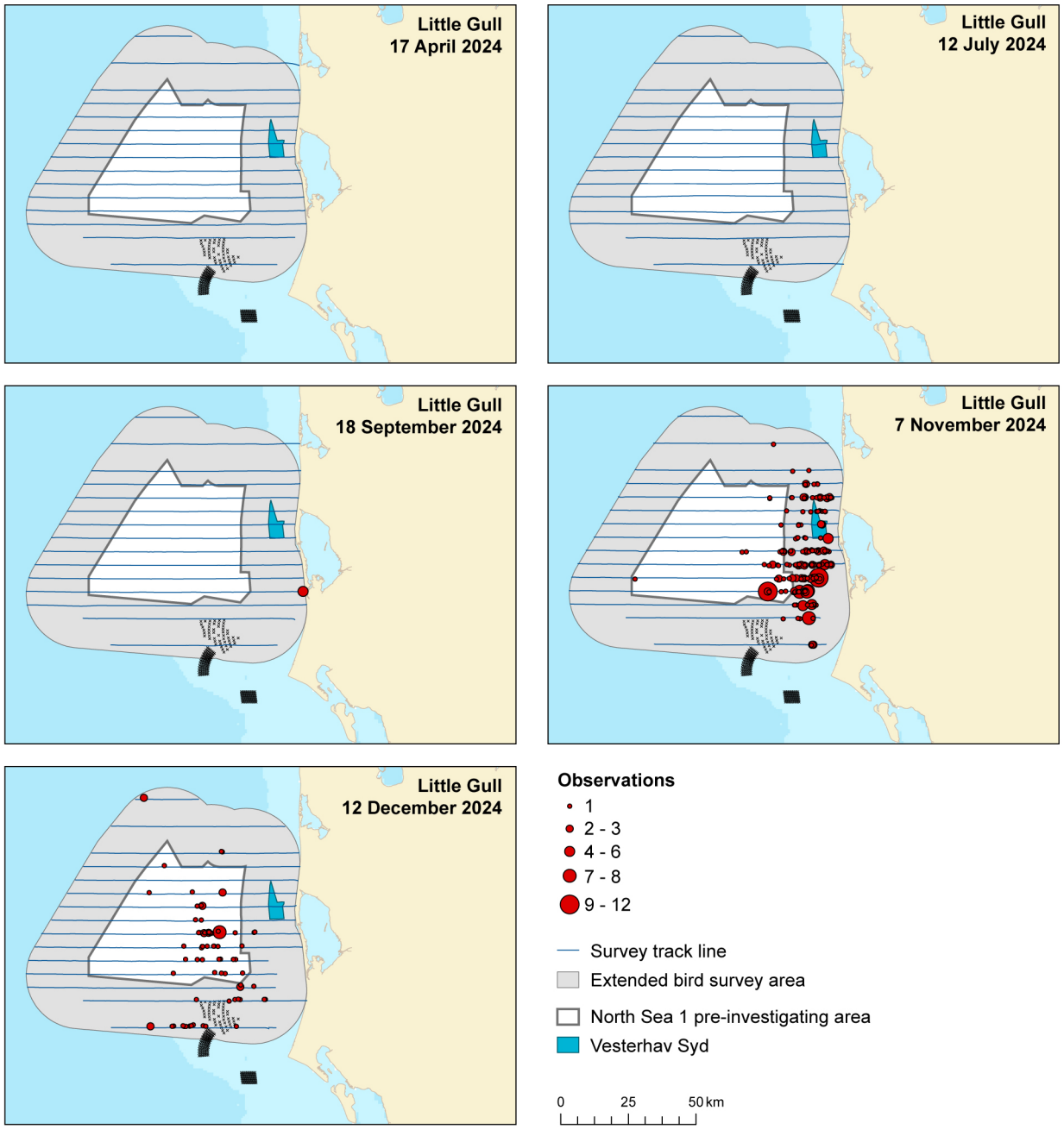

Figure 3-38. The numbers and distribution of little gulls observed during five Y2 surveys in the NSI survey area.

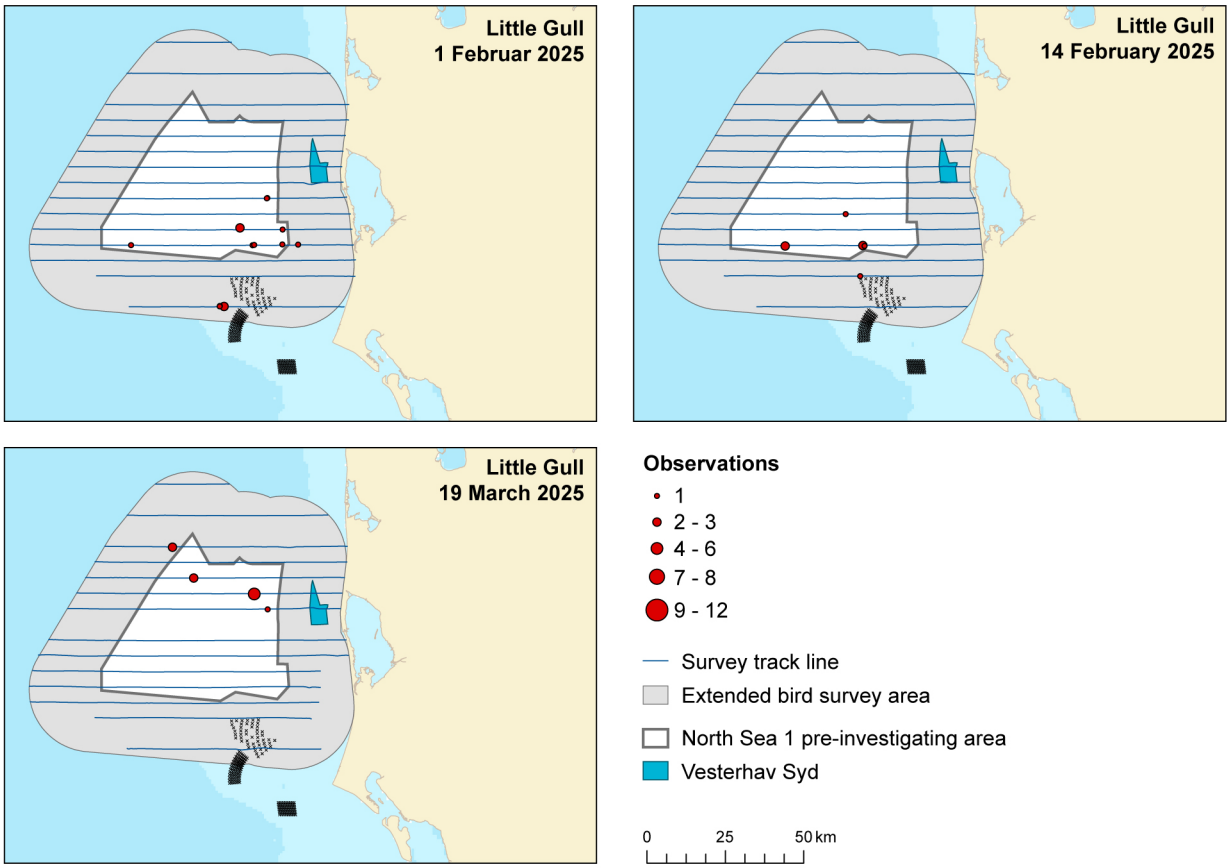

Figure 3-39. The numbers and distribution of little gulls observed during three Y2 surveys in the NSI survey area.

3.1.4.1 Distance analysis

The average probability of sighting little gulls was estimated to be 0.2 (CoV=0.05). This probability was estimated using a half-normal detection function with no covariates selected (Figure 3-40). Since this species was not analysed in the original report, this is a new detection function fitted to the eight surveys conducted in Y2.

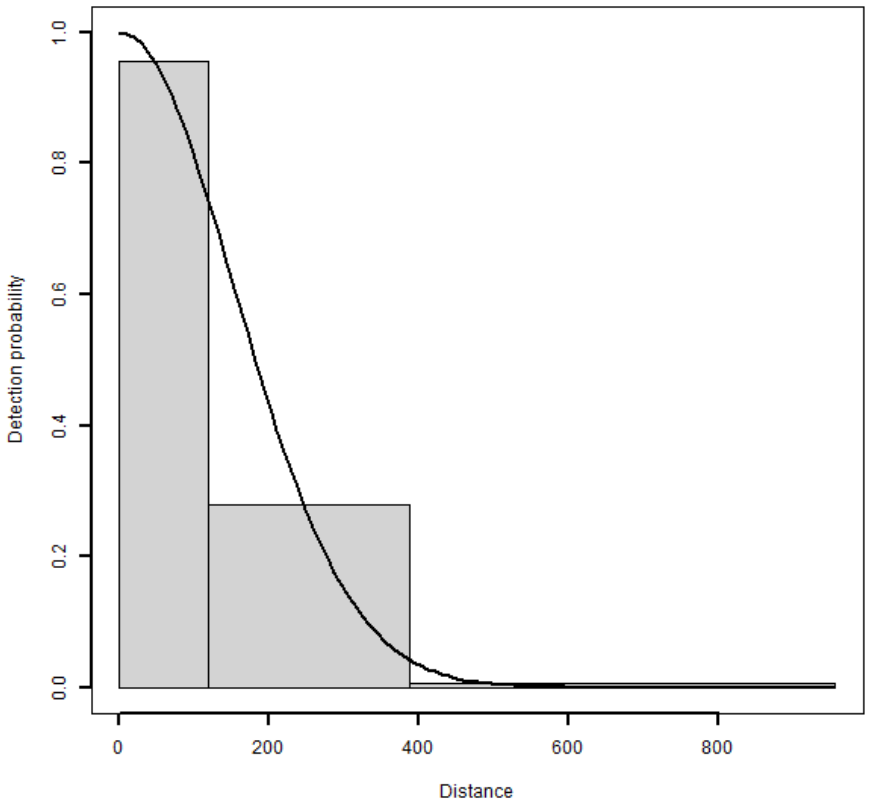

Figure 3-40. Figure showing the estimated detection function for observations of little gulls. The histogram represents the distances of the observed sightings.

3.1.4.2 Spatial analysis

Figure 3-41 shows the distribution of the distance corrected counts for each of the Y2 surveys.

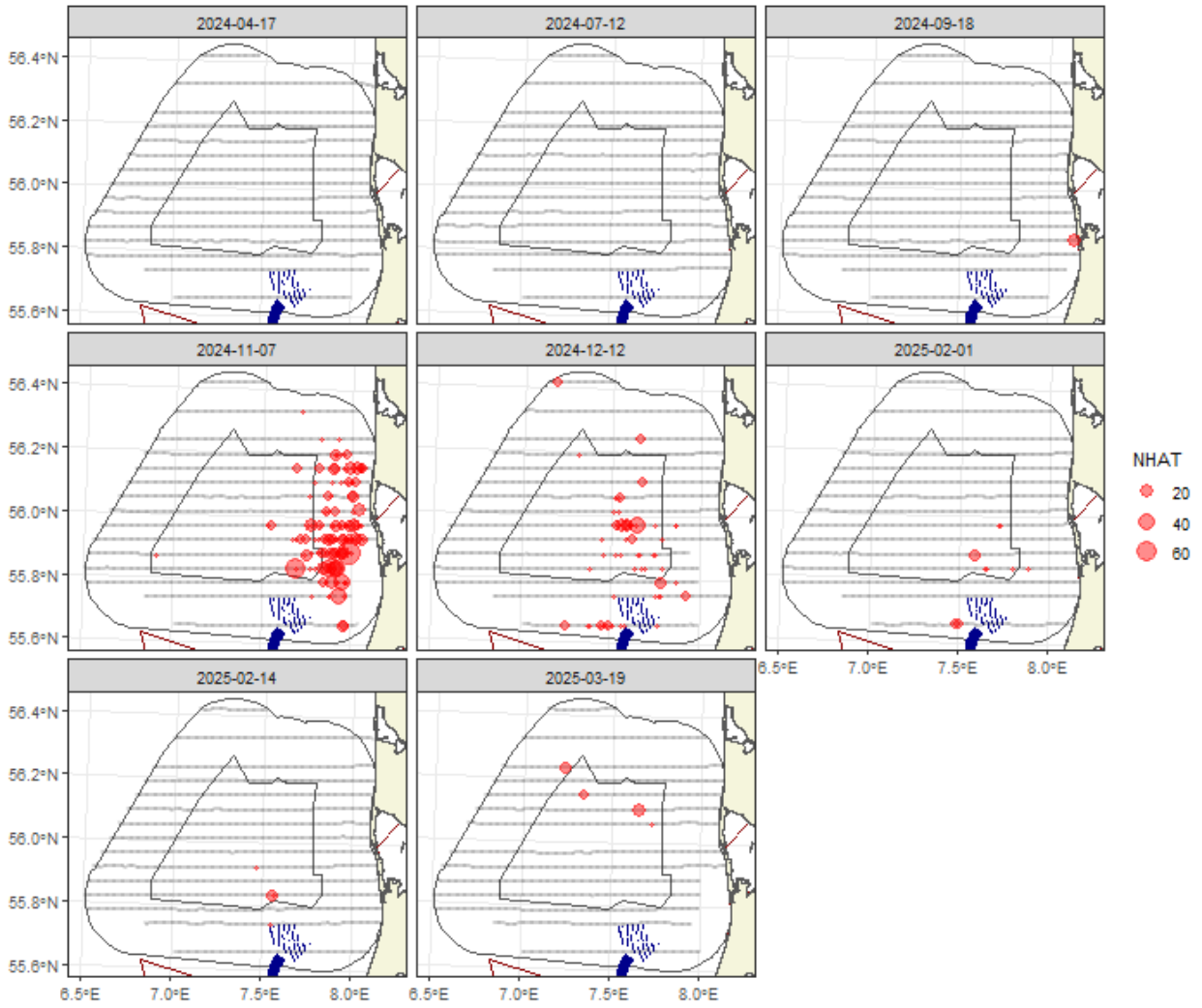

Figure 3-41. Distance-corrected counts for little gulls across the eight Y2 surveys. The red circles indicate the distance-corrected counts along the transect lines. The grey dots are segments with a count of zero.

3.1.4.3 Model Selection

Reliable models could only be fitted to three of the eight Y2 surveys due to insufficient data for the five remaining surveys. For two of the three models, a spatial term was selected, and the remaining model was intercept-only. A smooth term for depth was selected for one of the three models, while the distance to the coast was not selected for any surveys. The two spatial surfaces used eight and nine parameters for the spatial term (Table 3-8).

Table 3-8. Model selection results for little gull for each Y2 survey. The model column represents the terms in the model.

Date	Model	Distribution	Variable 1D	Variable 2D	Number of Parameters	Dispersion parameter	Tweedie parameter
2024-04-17	No Model	NA	NA	NA	NA	NA	NA
2024-07-12	No Model	NA	NA	NA	NA	NA	NA
2024-09-18	No Model	NA	NA	NA	NA	NA	NA
2024-11-07	2D Only	quasipoisson	NA	s(x,y, df=8)	9	7.4	NA
2024-12-12	Best 1D2D	quasipoisson	s(depth, df=2)	s(x,y, df=9)	12	4.2	NA

2025-02-01	Intercept only	quasipoisson	NA	NA	1	13.0	NA
2025-02-14	No Model	NA	NA	NA	NA	NA	NA
2025-03-19	No Model	NA	NA	NA	NA	NA	NA

The estimated abundances, densities and associated 95 percentile confidence intervals for each Y2 survey are given in Table 3-9 and Figure 3-42. For five of the eight surveys, there was insufficient data to fit a spatial model, and therefore, the abundance estimates were calculated using the Horvitz-Thompson method (H-T). The greatest abundance was estimated from the November 2024 survey (4,869 birds, 95% CI: 3,058 – 8,547), with no overlap with other surveys.

Table 3-9. Estimated abundance and density of little gulls for each Y2 survey. The 95% CI percentile-based confidence intervals.

Date	Area (Km^2)	Estimator Type	Estimated Count	95% CI Count	Estimated Density	95% CI Density
2024-04-17	7,833	H-T	0	(0, 0)	0.0	(0, 0)
2024-07-12	7,833	H-T	0	(0, 0)	0.0	(0, 0)
2024-09-18	7,833	H-T	82	(75, 89)	0.0	(0, 0)
2024-11-07	7,833	Spatial	4,869	(3,058, 8,547)	0.6	(0.4, 1.1)
2024-12-12	7,833	Spatial	1,451	(828, 2,828)	0.2	(0.1, 0.4)
2025-02-01	7,833	Spatial	246	(93, 616)	0.0	(0, 0.1)
2025-02-14	7,833	H-T	98	(89, 106)	0.0	(0, 0)
2025-03-19	7,833	H-T	308	(280, 331)	0.0	(0, 0)

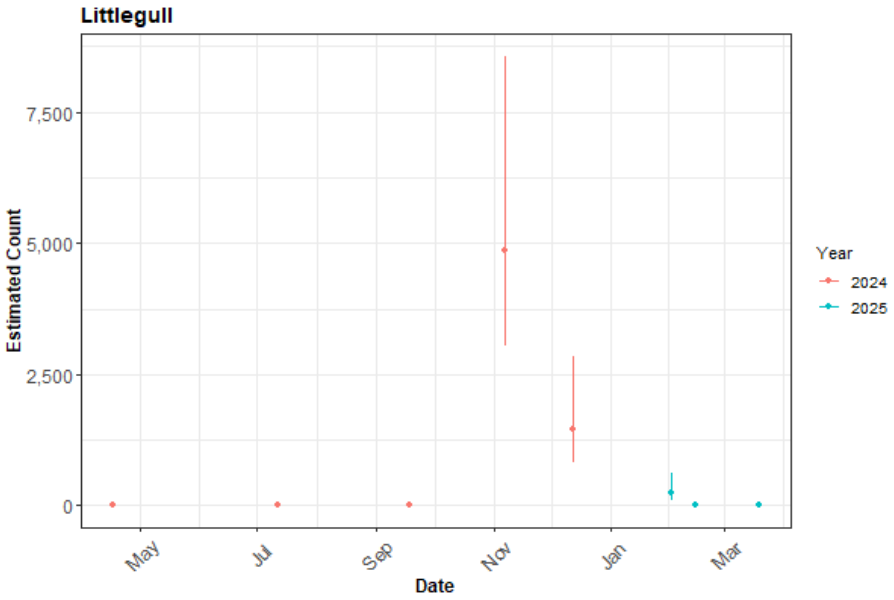

Figure 3-42. The estimated count of little gulls for each Y2 survey. The 95% CI is a percentile-based confidence interval from a parametric bootstrap with 500 replicates.

3.1.4.4 Spatial Results

Figure 3-43 shows the estimated numbers of little gulls in each 1 km² grid cell for each Y2 survey. Generally, the estimated abundances fitted well with the raw data, and there were no notable misalignments. In areas where the estimated numbers were systematically higher, the abundances were also relatively high, and there were no areas with large, estimated abundances unsupported by the data.

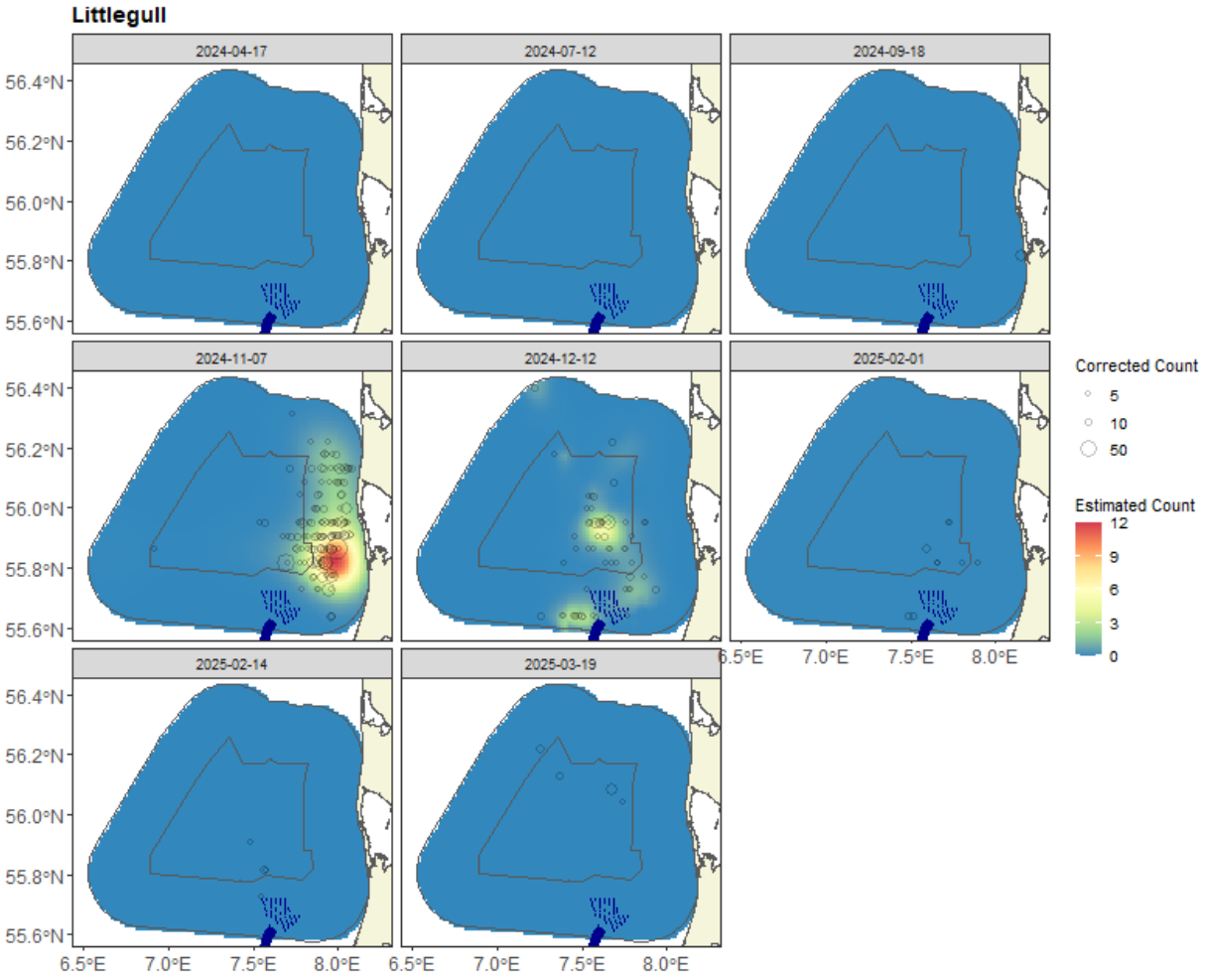

Figure 3-43. Figure showing the estimated little gull abundance across the NSI survey area for each of the eight Y2 surveys. The estimated numbers are per 1 km x 1 km grid cell. The open circles represent the distance-corrected counts.

3.1.4.5 Uncertainty in spatial predictions

Broadly, the highest Y2 coefficient of variation (CoV) scores was associated with the `almost zero' predictions, and it is known that the CoV metric is highly sensitive to any uncertainty for very small predictions. There was no material overlap between high values of the CoV metric and the transect lines/locations with non-zero counts, and therefore results in no concerns in this case (Figure 3-44).

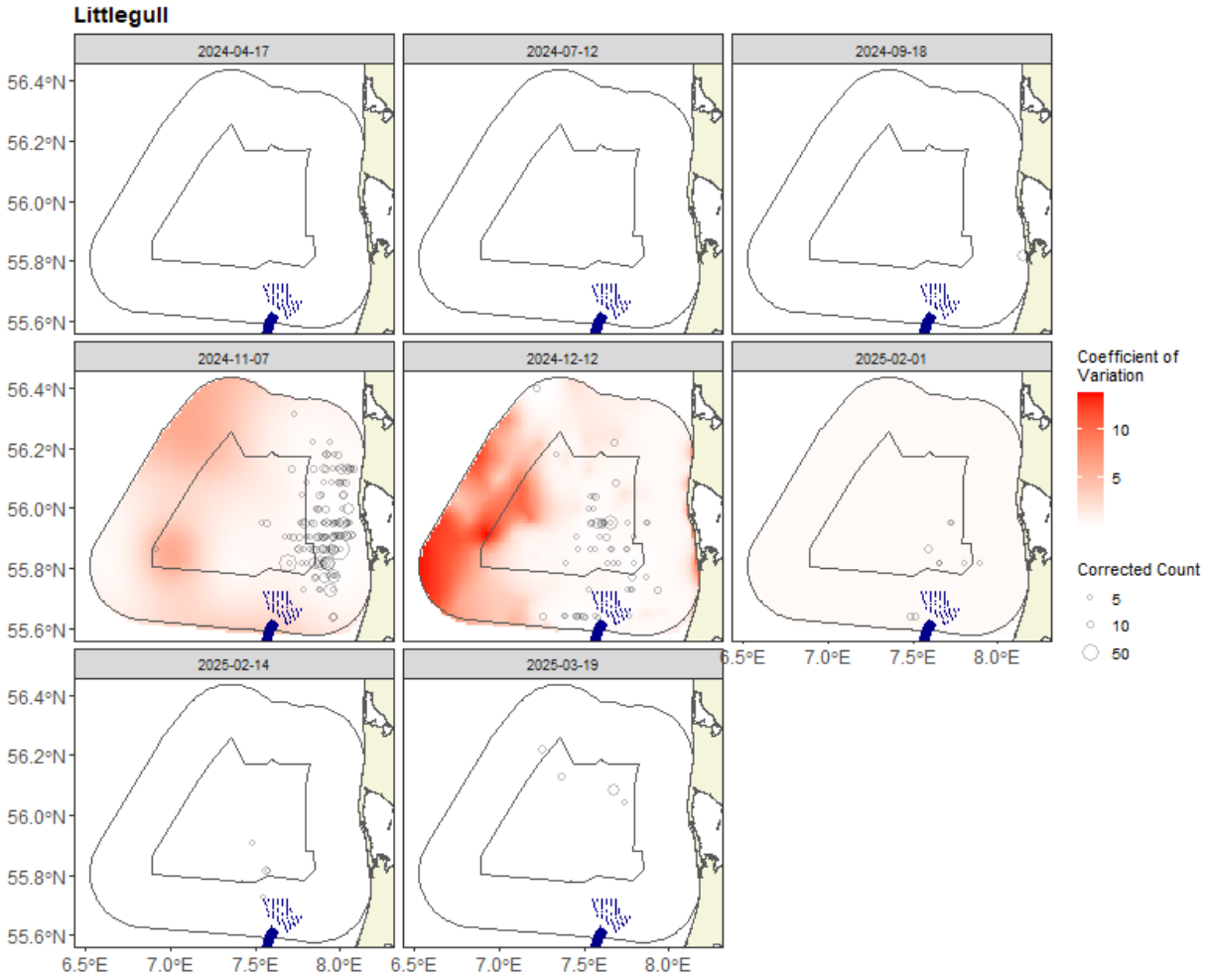

Figure 3-44 Figure showing the coefficient of variation across the NSI survey area for each of the Y2 surveys. The open circles show the distance corrected counts, where applicable, and the polygons represent the NSI pre-investigation area and the NSI survey area (black lines). The presence of dark red CV scores in areas with virtually zero predictions is an artefact of the very small prediction rather than of any notable concern.

In the case where the very small predicted values were excluded (Figure 3-45) the CoV was <1 for most Y2 surveys and therefore of no material concern. For one survey, there remains some high uncertainty around very small values, which will play a role in the related confidence intervals for the abundances (Table 3-9 and Figure 3-42).

Figure 3-45. Figure showing the Y2 coefficient of variation for all cells with density > 0.01 birds pr. km^2. The open circles show the distance corrected counts, where applicable, and the polygons represent the NSI pre-investigation area and the NSI survey area (black lines). The presence of dark red CV scores in areas with virtually zero predictions is an artefact of the very small prediction rather than of any notable concern.

3.1.4.6 Little gull (Y1 and Y2)

This section provides combined outputs across all 16 Y1 and Y2 surveys for little gulls. The estimated abundances, densities and associated 95 percentile confidence intervals for each Y1 and Y2 survey are given in Table 3-10 and Figure 3-46. In the Y1 surveys, only one survey had sufficient data for a spatial model, and therefore, the majority of abundance estimates come from the Horvitz-Thomson method. There was a marked increase in little gulls in the November and December surveys from 2023 to 2024, whereas there were fewer sighted in the February and March 2025 surveys compared with the same months in 2024.

Table 3-10. Estimated abundance and density of little gulls for each of the 16 Y1 and Y2 surveys conducted. The 95% CI are percentile-based confidence intervals

Date	Area (km²)	Estimation Type	Estimated Count	95% CI Count	Estimated Density	95% CI Density
2023-04-30	7,833	H-T	627	(131, 1,322)	0.1	(0, 0.2)
2023-07-07	7,833	H-T	0	(0, 0)	0.0	(0, 0)
2023-09-05	7,833	H-T	45	(9, 95)	0.0	(0, 0)
2023-11-26	7,833	H-T	128	(27, 270)	0.0	(0, 0)
2023-12-14	7,833	H-T	44	(9, 94)	0.0	(0, 0)
2024-02-08	7,833	H-T	86	(18, 182)	0.0	(0, 0)
2024-02-25	7,833	Spatial	789	(71, 4,293)	0.1	(0, 0.5)
2024-03-21	7,833	H-T	643	(135, 1,356)	0.1	(0, 0.2)
2024-04-17	7,833	H-T	0	(0, 0)	0.0	(0, 0)
2024-07-12	7,833	H-T	0	(0, 0)	0.0	(0, 0)
2024-09-18	7,833	H-T	82	(75, 89)	0.0	(0, 0)
2024-11-07	7,833	Spatial	4,869	(3,058, 8,547)	0.6	(0.4, 1.1)
2024-12-12	7,833	Spatial	1,451	(828, 2,828)	0.2	(0.1, 0.4)
2025-02-01	7,833	Spatial	246	(93, 616)	0.0	(0, 0.1)
2025-02-14	7,833	H-T	98	(89, 106)	0.0	(0, 0)
2025-03-19	7,833	H-T	308	(280, 331)	0.0	(0, 0)

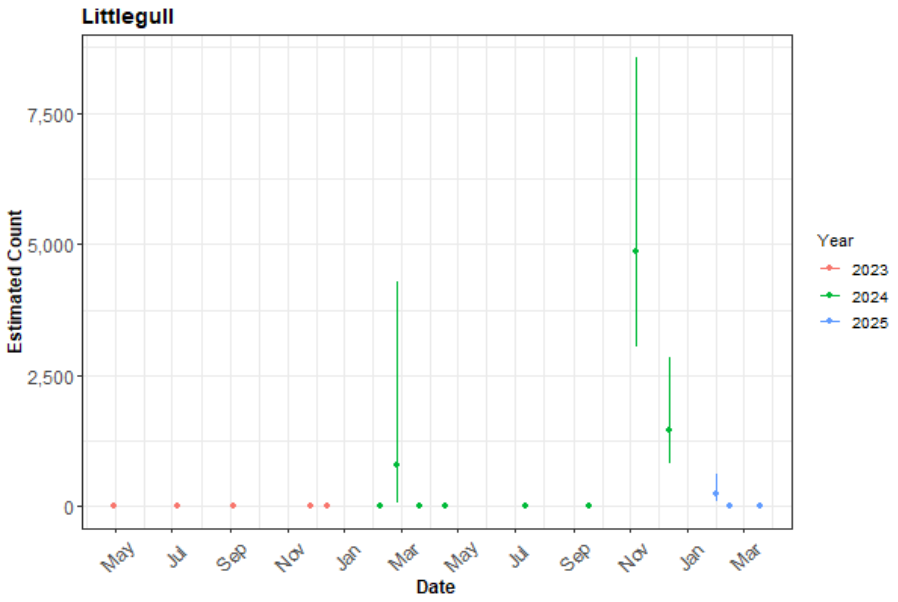

Figure 3-46. The estimated count of little gulls for each of the 16 Y1 and Y2 surveys conducted. The 95% CI are percentile-based confidence intervals are from a parametric bootstrap with 500 replicates. As the survey area is the same for each survey, the abundances are comparable.

Figure 3-47 and Figure 3-48 show the estimated numbers of little gulls in each 1 km² grid cell for each Y1 and Y2 survey. The first figure shows the surfaces on the same scale, and the second Figure 3-48, limits the estimated density to

five birds pr. km^2 to provide a little more detail. Generally, the estimated abundances fitted well with the raw data, and there were no notable misalignments. In areas where the estimated numbers were systematically higher, the abundances were also relatively high, and there were no areas with large, estimated abundances unsupported by the data.

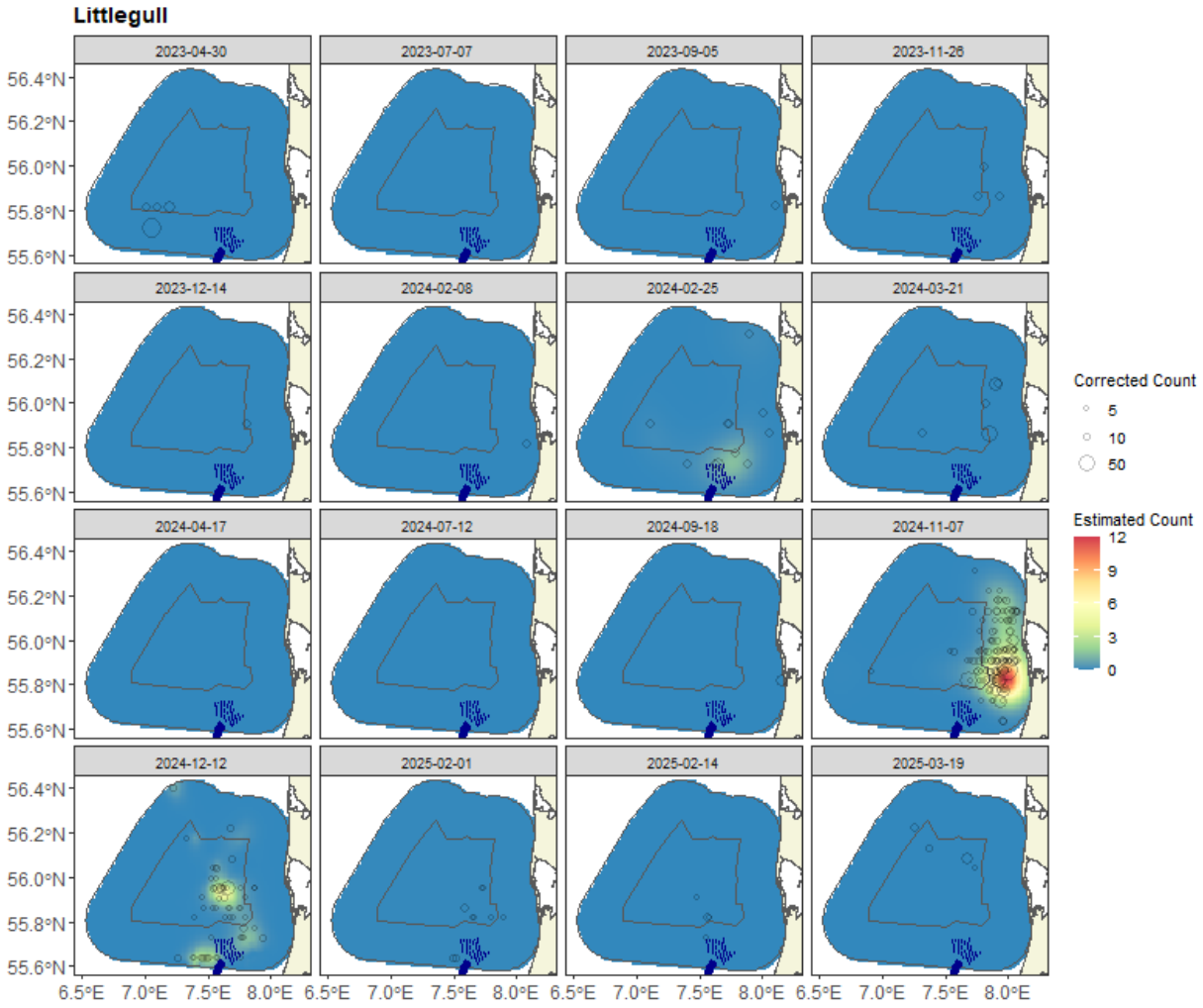

Figure 3-47. Figure showing the estimated little gull abundance across the NSI survey area for each of the 16 Y1 and Y2 surveys conducted. The estimated numbers are per 1 km x 1 km grid cell. The open circles represent the distance-corrected counts.

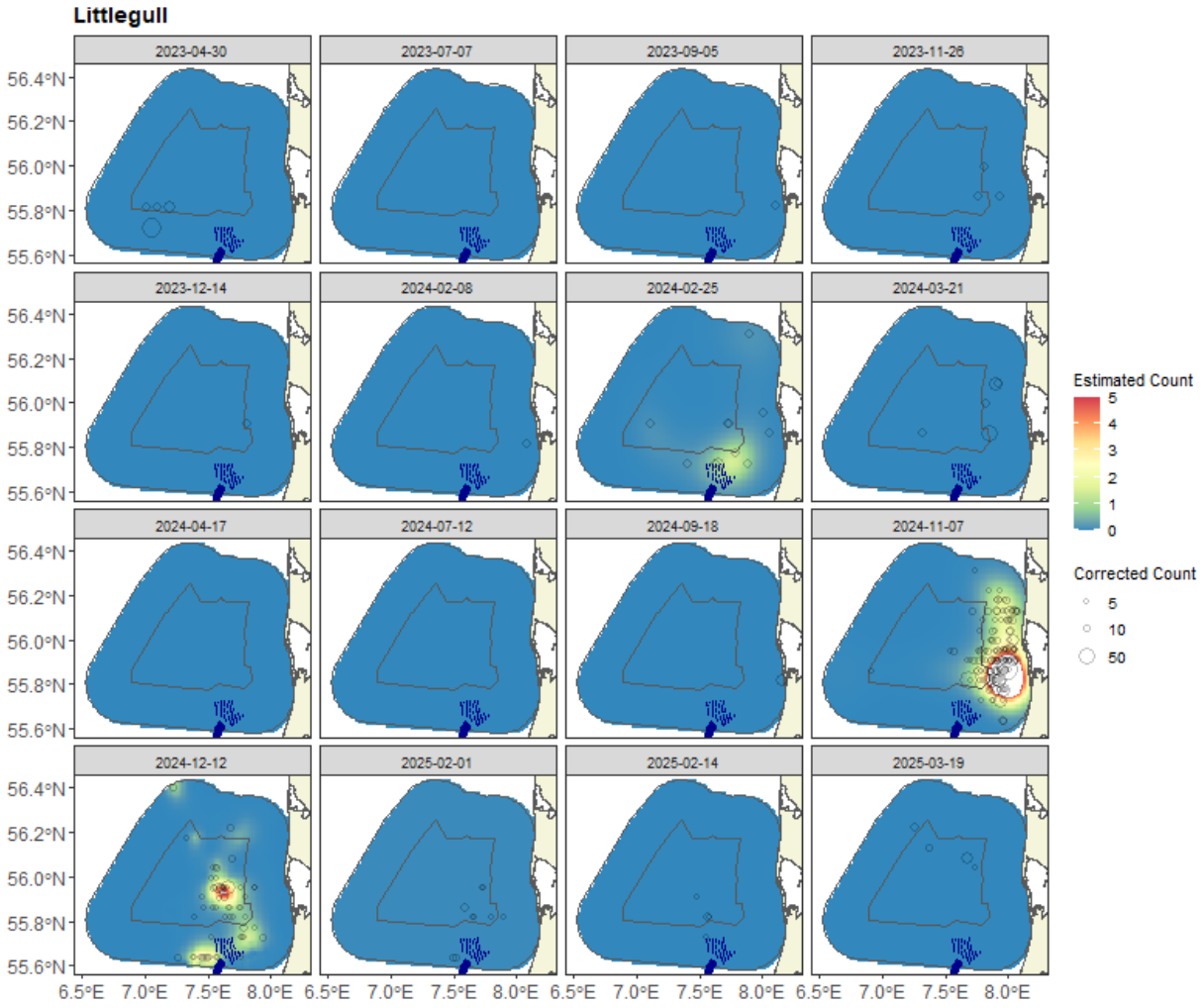

Figure 3-48. Figure showing the estimated little gull abundance across the NSI survey area for each of the 16 Y1 and Y2 surveys conducted. The estimated numbers are per 1 km x 1 km grid cell. The open circles represent the distance-corrected counts. The coloured graphics represent the predicted numbers in each location and are limited to five birds/km^2 to provide more detail. White areas indicate data intentionally omitted from one or more surveys with exceptionally high abundances to allow finer detail to be seen in lower-density distributions.

3.1.4.7 Areas of Persistence

In the Y1 surveys, there was only one survey which could be modelled spatially, so it was not sensible to estimate a persistence score. In Y2, three surveys could be modelled spatially, and the persistence of these three surveys is presented in Figure 3-49. The highest persistence was in the southeastern parts of the survey area but with very low persistence scores of ~25%.

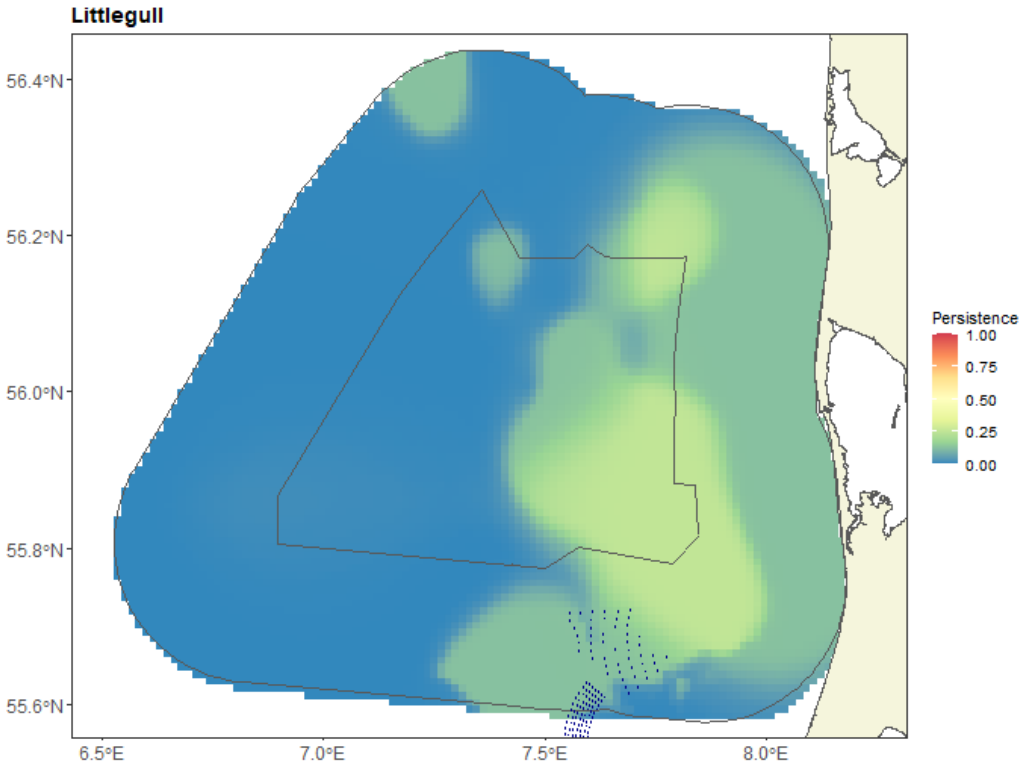

Figure 3-49. Persistence scores for little gulls across the Y2 surveys. The polygons represent the NSI pre-investigation area and the NSI survey area (black lines).

Figure 3-50 shows the persistence across all 16 Y1 and Y2 surveys. When combined, the result shows that the highest persistence is very low (~ 19%) and that little gulls are not common, but when present, use the eastern parts of the survey area.

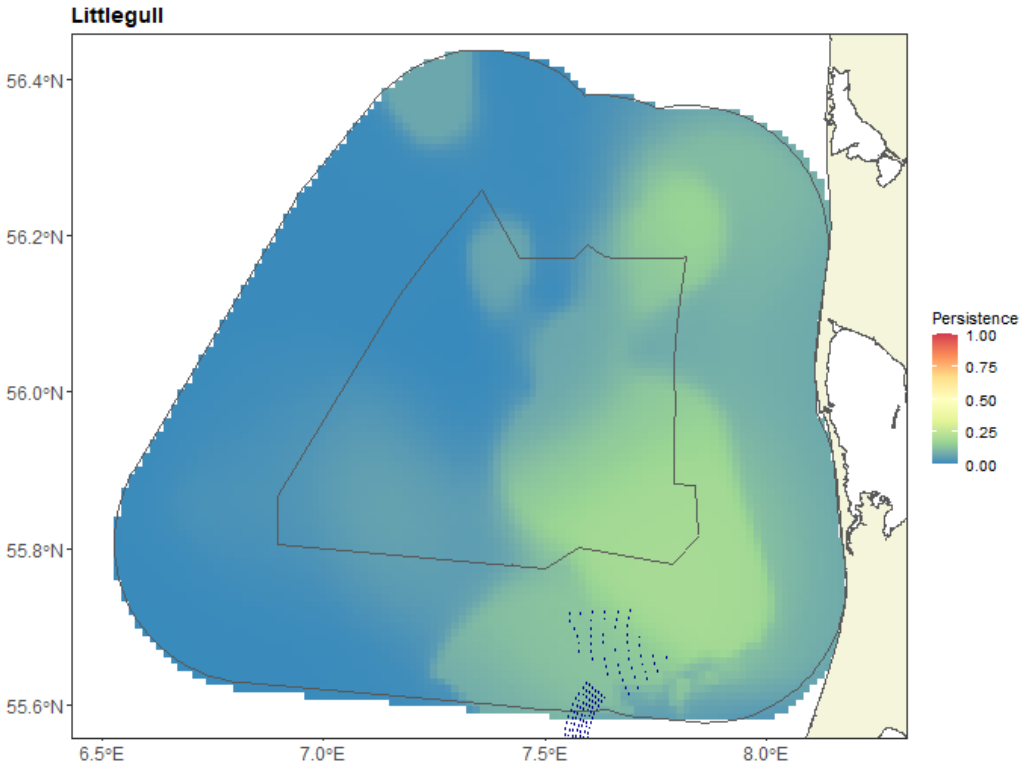

Figure 3-50. Persistence scores for little gulls across all 16 Y1 and Y2 surveys. The polygons represent the NSI pre-investigation area and the NSI survey area (black lines).

3.1.5 Black-legged kittiwake (*Rissa tridactyla*)

Black-legged kittiwake was observed during all eight Y2 surveys, with 1,786 individuals recorded across all surveys and a maximum of 745 birds observed birds on a single survey in December 2024. Most black-legged kittiwakes were recorded over the winter and spring periods, while few birds were recorded in July and September (Table 3-1).

Black-legged kittiwake was recorded across the entire survey area, although less frequently in the very eastern coastal parts (Figure 3-51 and Figure 3-52). There were 1,157 records of black-legged kittiwakes, with a mean flock size of 1.54 birds. The recorded number per flock ranged from one to 70 individuals.

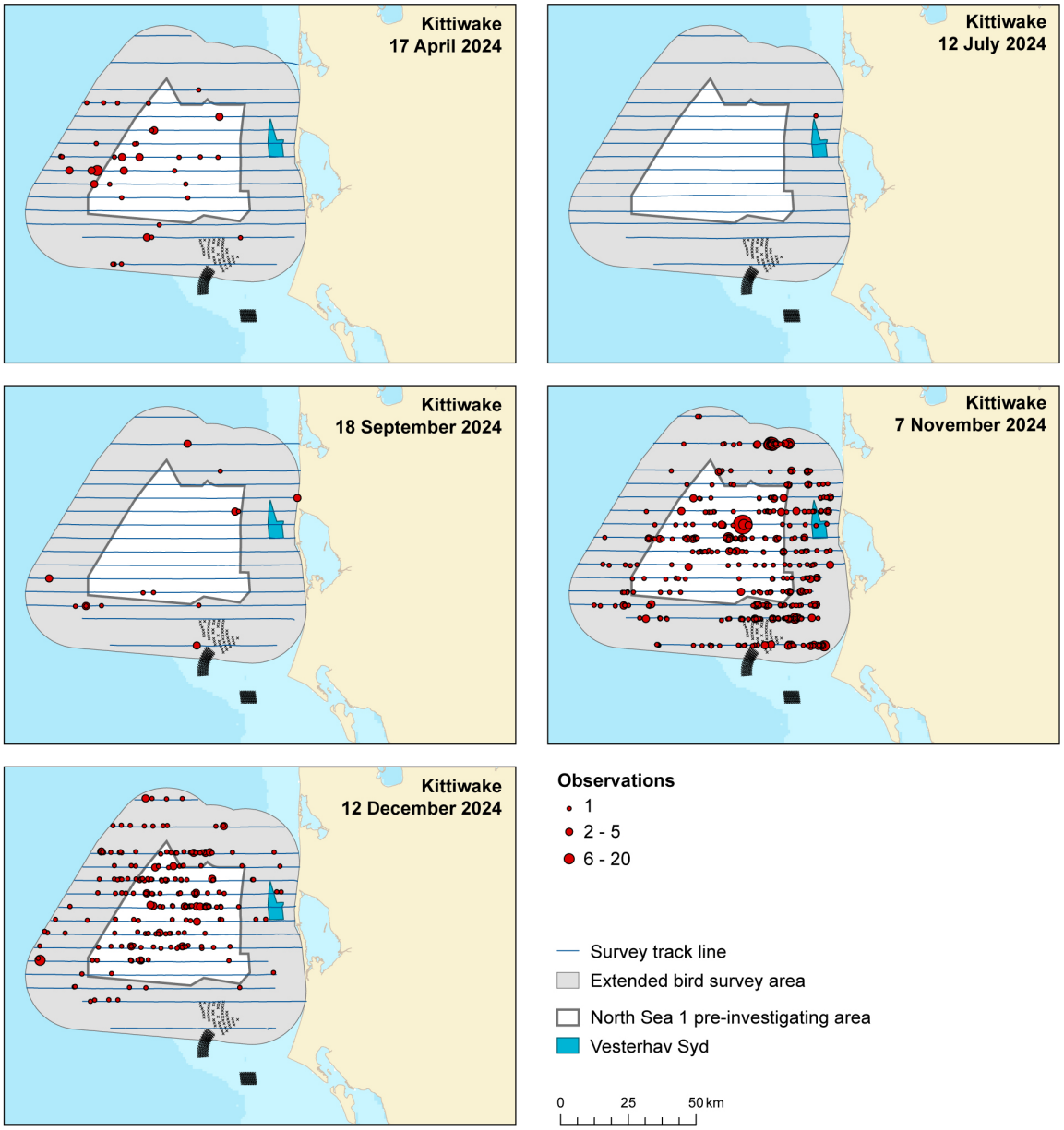

Figure 3-51. The numbers and distribution of black-legged kittiwakes observed during five Y2 surveys in the NSI survey area.

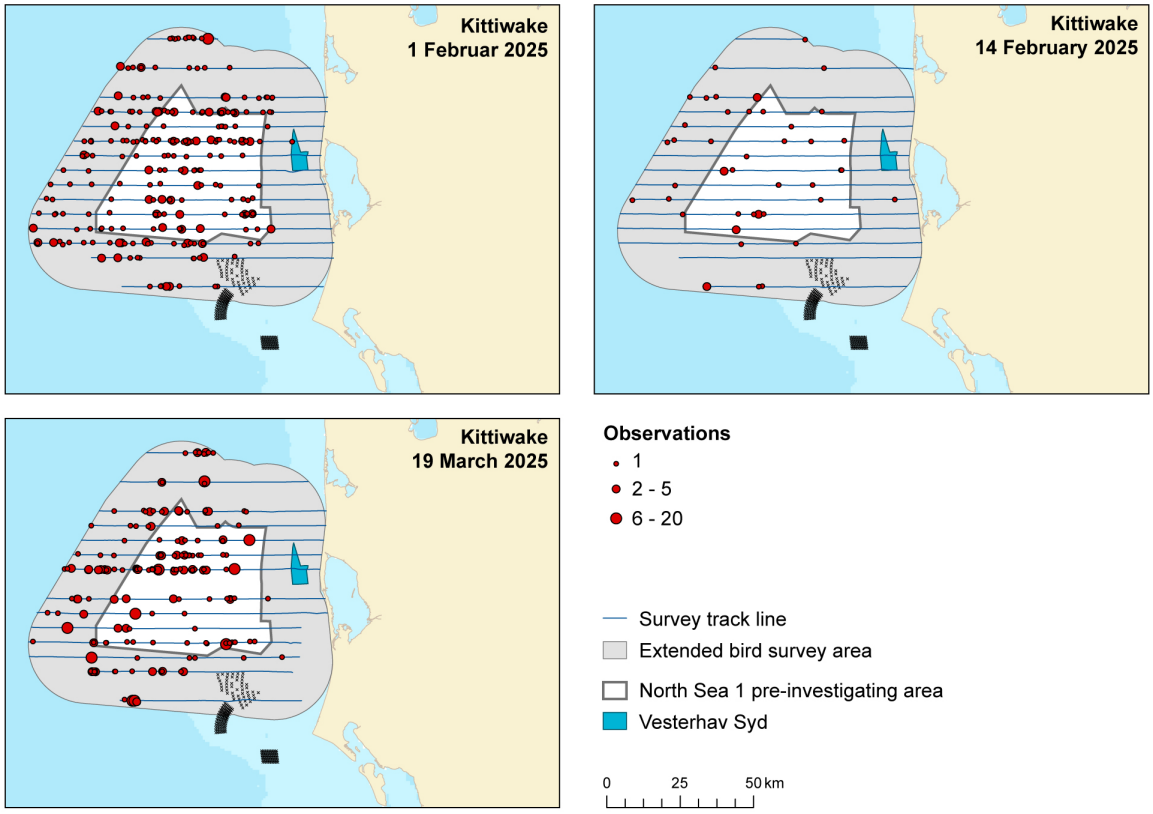

Figure 3-52. The numbers and distribution of black-legged kittiwakes observed during three Y2 surveys in the NSI survey area.

3.1.5.1 Distance analysis

The average probability of sighting a black-legged kittiwake was estimated to be 0.22 (CoV = 0.04). This probability was estimated using a hazard rate detection function, and no covariates were selected (Figure 3-53). This detection function was estimated using the Y1 surveys, and this model was used to estimate the number of birds in the Y2 surveys.

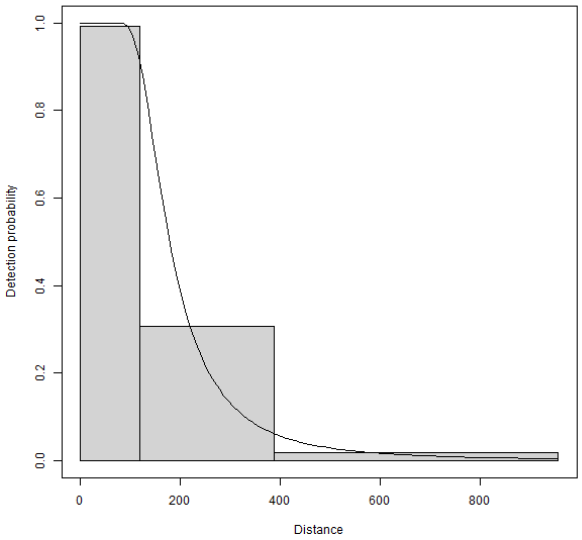

Figure 3-53. Figure showing the estimated detection function for black-legged kittiwake. The histogram represents the distances of the observed sightings.

3.1.5.2 Spatial analysis

Figure 3-54 shows the distribution of the distance corrected counts for each of the eight Y2 surveys.

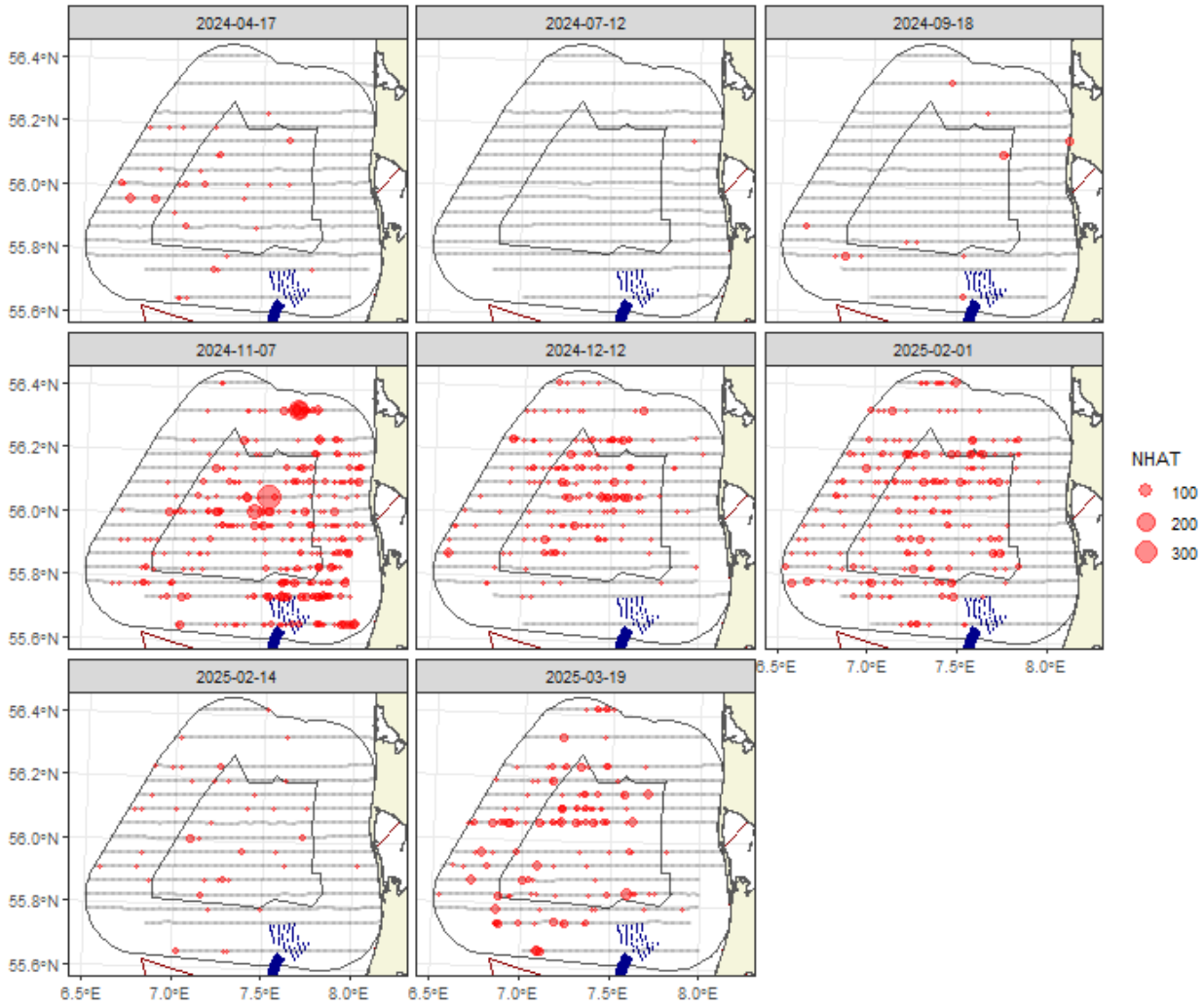

Figure 3-54. Distance-corrected counts for the black-legged kittiwake across the eight Y2 surveys. The red circles indicate the distance-corrected counts along the transect lines. The grey dots are segments with a count of zero.

3.1.5.3 Model selection

For one of the eight Y2 surveys, there was insufficient data to produce a credible spatial model. For the remaining seven surveys, six of the models selected included a spatial term (of varying complexity), while the remaining model was intercept-only. The depth covariate was selected as a smooth term for one survey, while the distance from the coast covariate was not selected in any. This shows there was compelling evidence for non-uniform spatial patterns in six of the surveys, but given these spatial patterns, there was little to no evidence for depth or distance-to-coast relationships. The spatial surfaces selected ranged from six to 10 parameters for the spatial term (Table 3-11).

Table 3-11. Model selection results for black-legged kittiwake for each survey. The model column represents the terms in the model.

Date	Model	Distribution	Variable 1D	Variable 2D	Number of Parameters	Dispersion parameter	Tweedie parameter
2024-04-17	Best 1D2D	quasipoisson	s(depth, df=2)	s(x,y, df=10)	13	5.2	NA

2024-07-12	No Model	NA	NA	NA	NA	NA	NA
2024-09-18	2D Only	Tweedie	NA	s(x,y, df=10)	11	10.2	1.26
2024-11-07	2D Only	Tweedie	NA	s(x,y, df=9)	10	22.7	1.40
2024-12-12	2D Only	quasipoisson	NA	s(x,y, df=6)	7	7.4	NA
2025-02-01	Intercept only	quasipoisson	NA	NA	1	9.4	NA
2025-02-14	2D Only	quasipoisson	NA	s(x,y, df=7)	8	6.2	NA
2025-03-19	2D Only	Tweedie	NA	s(x,y, df=9)	10	18.3	1.30

The estimated abundances, densities and associated 95 percentile confidence intervals for each Y2 survey are given in Table 3-12 and Figure 3-55. For the July surveys in 2024, there was insufficient data to produce a credible spatial model, and therefore, the abundance estimate was calculated using the Horvitz-Thompson method (H-T). The greatest abundance was estimated on the November 2024 survey (11,659 birds; 95% CI: 8324-17,440). However, its confidence interval overlaps with the March 2025 survey and the highly uncertain April 2024 survey.

Table 3-12. Estimated abundance and density of black-legged kittiwake for each Y2 survey. The 95% CI are percentile-based confidence intervals.

Date	Area (Km^2)	Estimator Type	Estimated Count	95% CI Count	Estimated Density	95% CI Density
2024-04-17	7,833	Spatial	770	(291, 11,193)	0.1	(0, 1.4)
2024-07-12	7,833	H-T	15	(14, 16)	0.0	(0, 0)
2024-09-18	7,833	Spatial	372	(89, 2,641)	0.0	(0, 0.3)
2024-11-07	7,833	Spatial	11,659	(8,234, 17,140)	1.5	(1.1, 2.2)
2024-12-12	7,833	Spatial	3,867	(2,535, 6,017)	0.5	(0.3, 0.8)
2025-02-01	7,833	Spatial	5,474	(3,720, 8,072)	0.7	(0.5, 1)
2025-02-14	7,833	Spatial	722	(346, 1,739)	0.1	(0, 0.2)
2025-03-19	7,833	Spatial	7,304	(4,140, 13,681)	0.9	(0.5, 1.7)

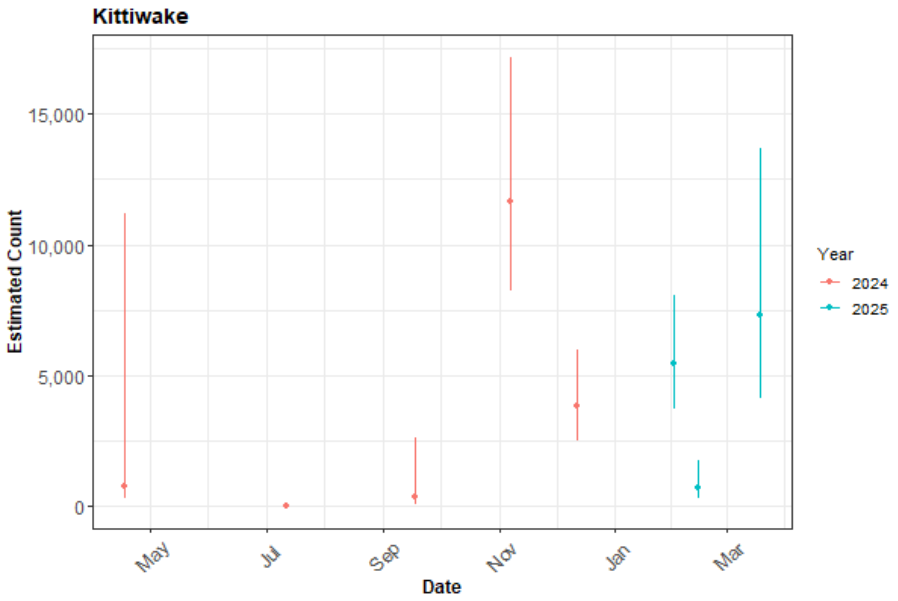

Figure 3-55. The estimated count of black-legged kittiwakes for each Y2 survey. The 95% CI are percentile-based confidence interval from a parametric bootstrap with 500 replicates.

3.1.5.4 Spatial results

Figure 3-56 shows the estimated numbers of black-legged kittiwakes in each 1 km^2 grid cell for each Y2 survey. Generally, the estimated abundances fitted well with the raw data, and there were no notable misalignments. In areas where the estimated numbers were systematically higher, the abundances were also relatively high, and there were no areas with large, estimated abundances unsupported by the data.

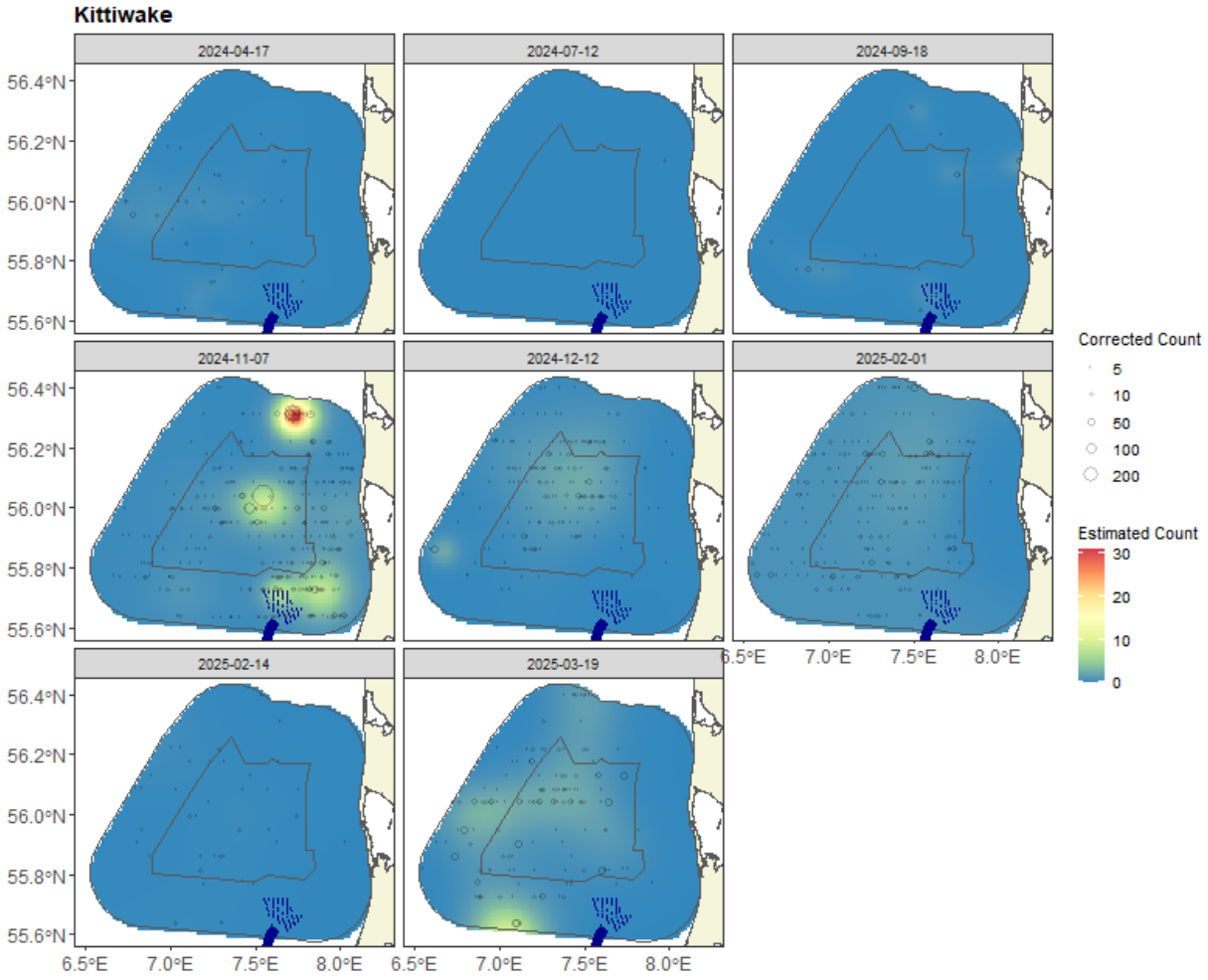

Figure 3-56. Figure showing the estimated black-legged kittiwake abundance across the NSI survey area for each Y2 survey. The estimated numbers are per 1 km x 1 km grid cell. The open circles represent the distance-corrected counts.

3.1.5.5 Uncertainty in spatial predictions

Broadly, the highest Y2 coefficient of variation (CoV) scores was associated with the `almost zero' predictions, and it is known that the CoV metric is highly sensitive to any uncertainty for very small predictions. There was one larger value in the western edge of the survey area, but that was otherwise absent of data. There was no material overlap between the high values of the CoV metric and the transect lines/locations with non-zero counts. Therefore, there were no concerns in this case (Figure 3-57).

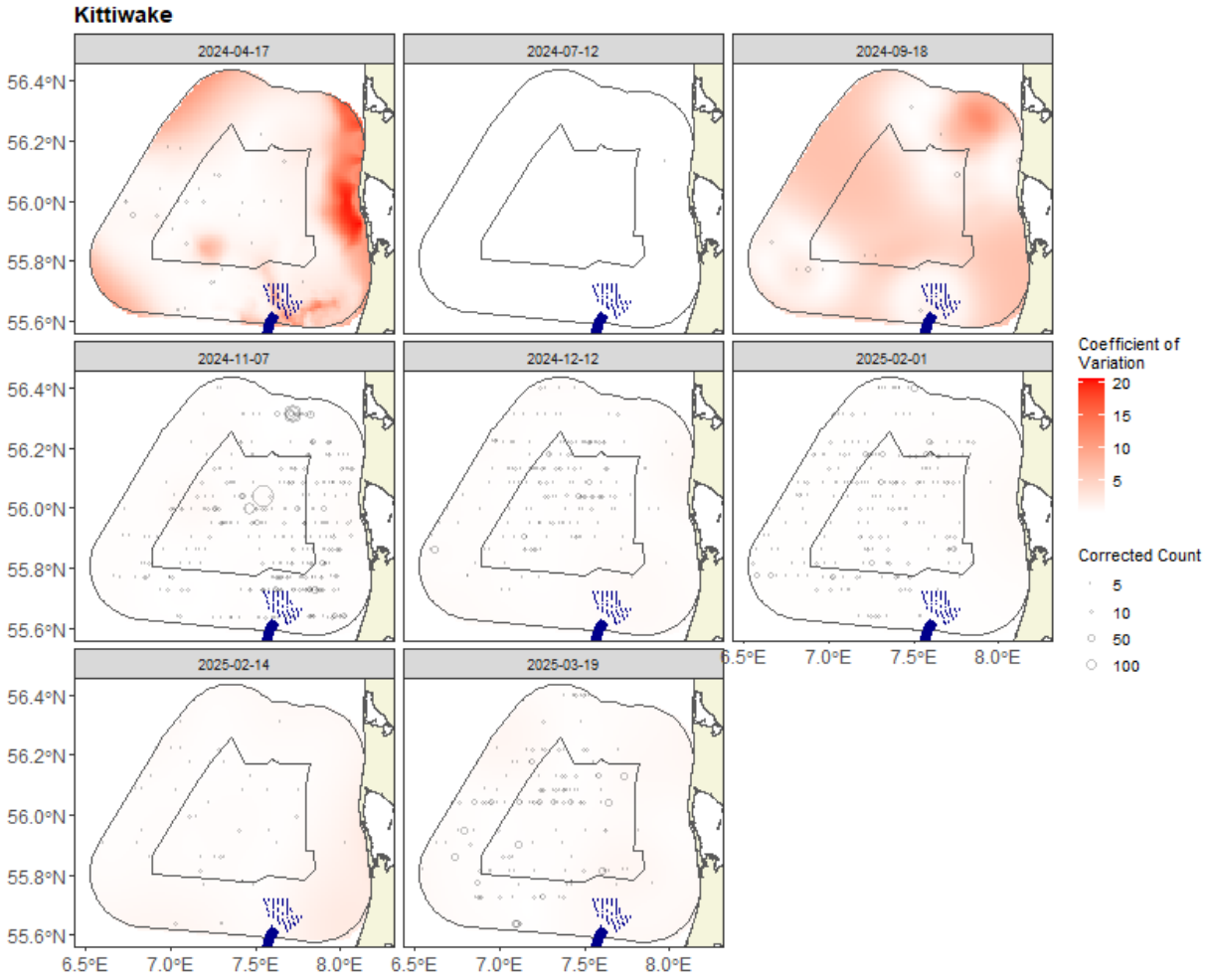

Figure 3-57. Figure showing the coefficient of variation (CoV) across the NSI survey area for each Y2 survey. The open circles show the distance corrected counts. The presence of dark red CoV scores in areas with virtually zero predictions is an artefact of the very small prediction rather than of any notable concern.

In the case where the very small, predicted values were excluded (Figure 3-58), the CoV for all Y2 surveys was <1 for most surveys and so of no material concern. There remains some high uncertainty for some surveys, reflected in the large confidence interval for the abundance (Table 3-12 and Figure 3-55).

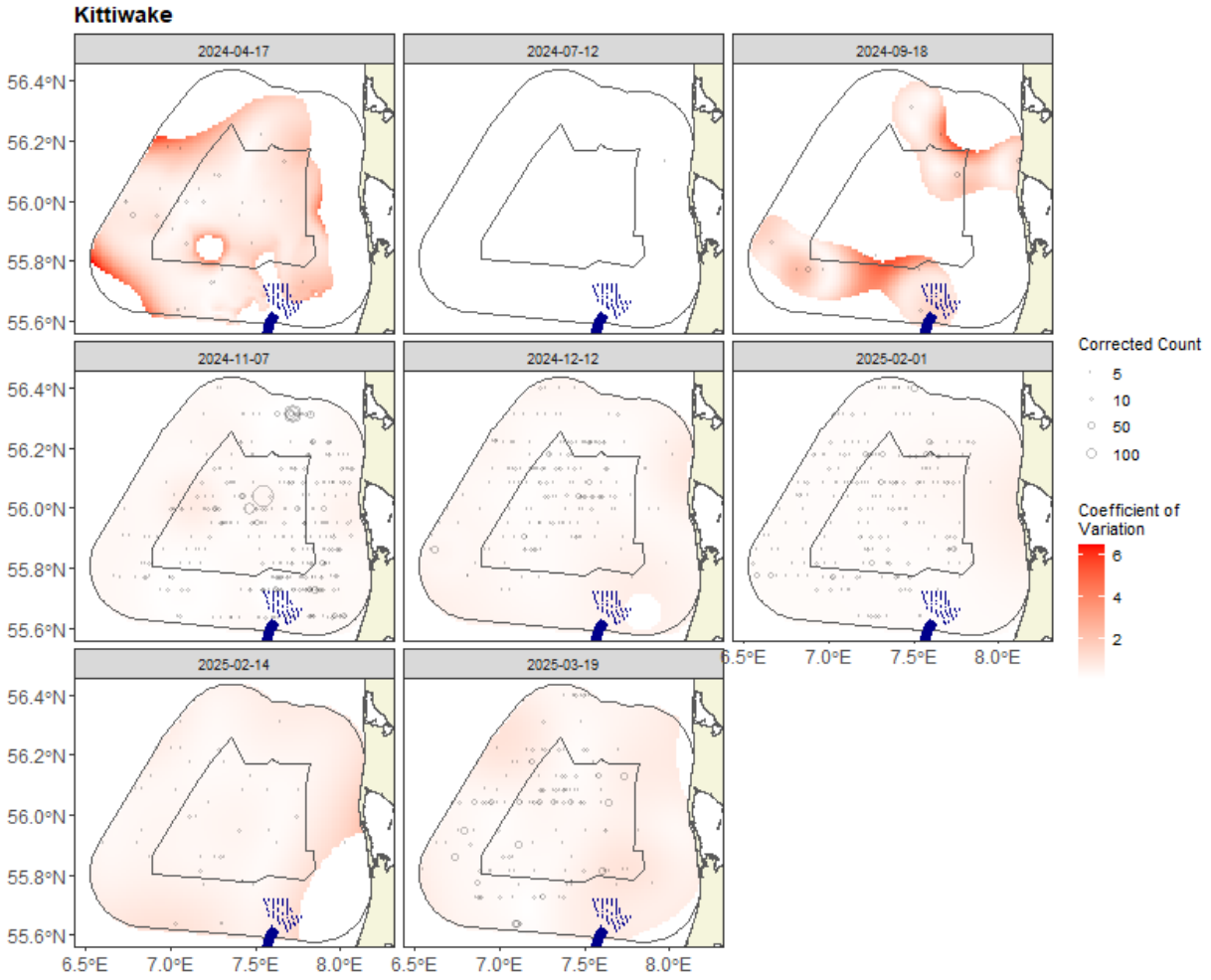

Figure 3-58. Figure showing the Y2 coefficient of variation for all cells with density > 0.001 birds/km^2. The open circles show the distance corrected counts. The presence of dark red CoV scores in areas with virtually zero predictions is an artefact of the very small prediction rather than of any notable concern.

3.1.5.6 Model diagnostics

A blocking structure accounted for potential residual non-independence for each Y2 model, and a robust standard error approach was based on unique transects. In each case, a reassuring decay to zero was seen (indicated by the red and grey lines in Figure 3-59), implying that an appropriate blocking structure was used.

The assumed mean-variance relationship was examined and generally showed agreement between the assumed (red) lines and the observed values. Figure 3-60 and Figure 3-61 show example relationships for a quasi-Poisson and Tweedie model. Figure 3-62 shows an example of a diagnostics QQ plot and no issues were identified.

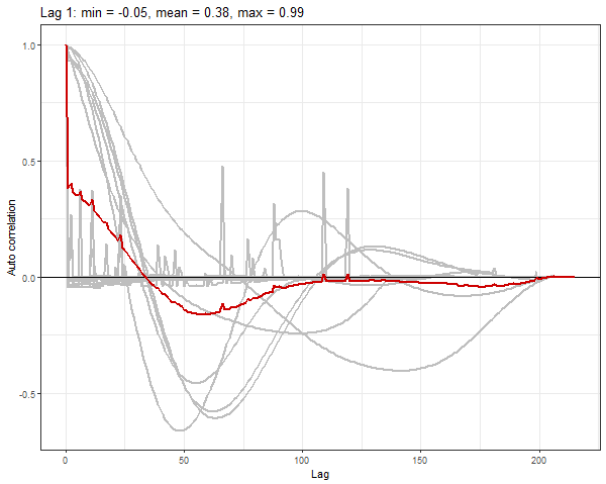

Figure 3-59. Example ACF plot for black-legged kittiwake. The grey lines represent the residual correlation observed in each transect, and the red line is the average of these values across transects.

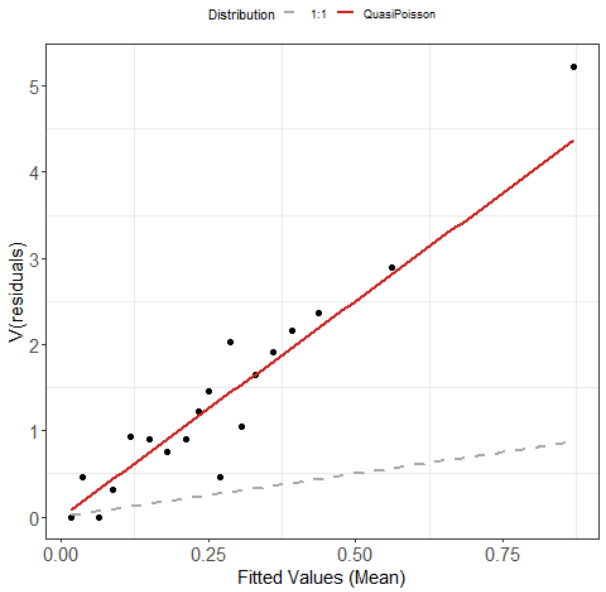

Figure 3-60. Example plot showing the estimated quasi-Poisson mean-variance relationship (red line) and actual (black dots) for black-legged kittiwake. The black dots are based on 20 quantiles of the model residuals, and for reference, the grey dashed line shows the 1:1 relationship.

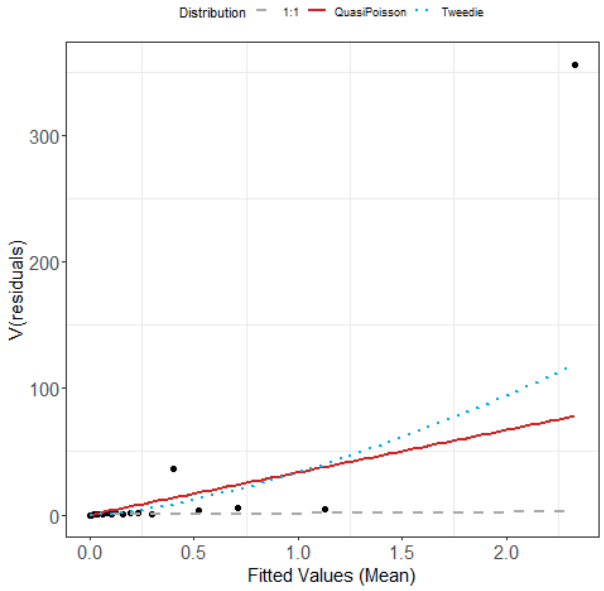

Figure 3-61. Example plot showing the estimated Tweedie mean-variance relationship (blue dashed line) for black-legged kittiwake. The red line shows the V(μ)=ϕμ relationship, and the grey line shows the 1:1 relationship.

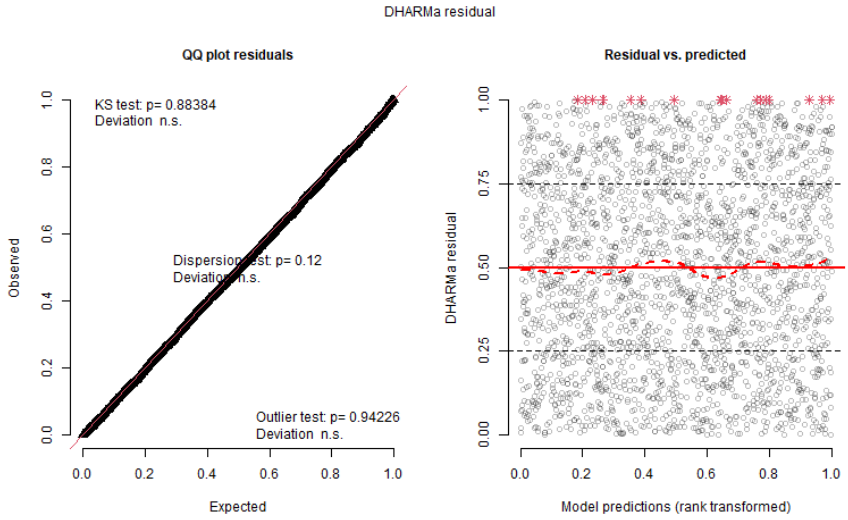

Figure 3-62. Example diagnostics for black-legged kittiwake. QQ plot and residuals against predicted values. The red stars are outliers, and the red line is a smooth spline around the mean of the residuals.

3.1.5.7 Black-legged kittiwake (Y1 and Y2)

This section provides combined outputs across all 16 Y1 and Y2 surveys for black-legged kittiwakes. The estimated abundances, densities and associated 95 percentile confidence intervals for each Y1 and Y2 survey are given in Table 3-13 and Figure 3-63. These results show that there were generally higher densities of black-legged kittiwakes estimated in the November to March surveys of Y2, and the most abundant survey was November 2024 (11,659, 95% cI: 8,234 - 17,140). However, the confidence intervals overlap with several other surveys.

Table 3-13. Estimated abundance and density of black-legged kittiwakes for each of the 16 Y1 and Y2 surveys conducted. The 95% CI are percentile-based confidence intervals

Date	Area (km^2)	Estimation Type	Estimated Count	95% CI Count	Estimated Density	95% CI Density
2023-04-30	7,833	Spatial	1,382	(620, 3,582)	0.2	(0.1, 0.5)
2023-07-07	7,833	H-T	66	(61, 71)	0.0	(0, 0)
2023-09-05	7,833	H-T	32	(29, 34)	0.0	(0, 0)
2023-11-26	7,833	Spatial	2,339	(1,475, 3,977)	0.3	(0.2, 0.5)
2023-12-14	7,833	Spatial	3,669	(1,917, 7,664)	0.5	(0.2, 1)
2024-02-08	7,833	Spatial	785	(367, 1,879)	0.1	(0, 0.2)
2024-02-25	7,833	Spatial	1,929	(1,091, 3,549)	0.2	(0.1, 0.5)
2024-03-21	7,833	Spatial	3,349	(1,480, 8,419)	0.4	(0.2, 1.1)
2024-04-17	7,833	Spatial	770	(291, 11,193)	0.1	(0, 1.4)
2024-07-12	7,833	H-T	15	(14, 16)	0.0	(0, 0)
2024-09-18	7,833	Spatial	372	(89, 2,641)	0.0	(0, 0.3)
2024-11-07	7,833	Spatial	11,659	(8,234, 17,140)	1.5	(1.1, 2.2)
2024-12-12	7,833	Spatial	3,867	(2,535, 6,017)	0.5	(0.3, 0.8)
2025-02-01	7,833	Spatial	5,474	(3,720, 8,072)	0.7	(0.5, 1)
2025-02-14	7,833	Spatial	722	(346, 1,739)	0.1	(0, 0.2)
2025-03-19	7,833	Spatial	7,304	(4,140, 13,681)	0.9	(0.5, 1.7)

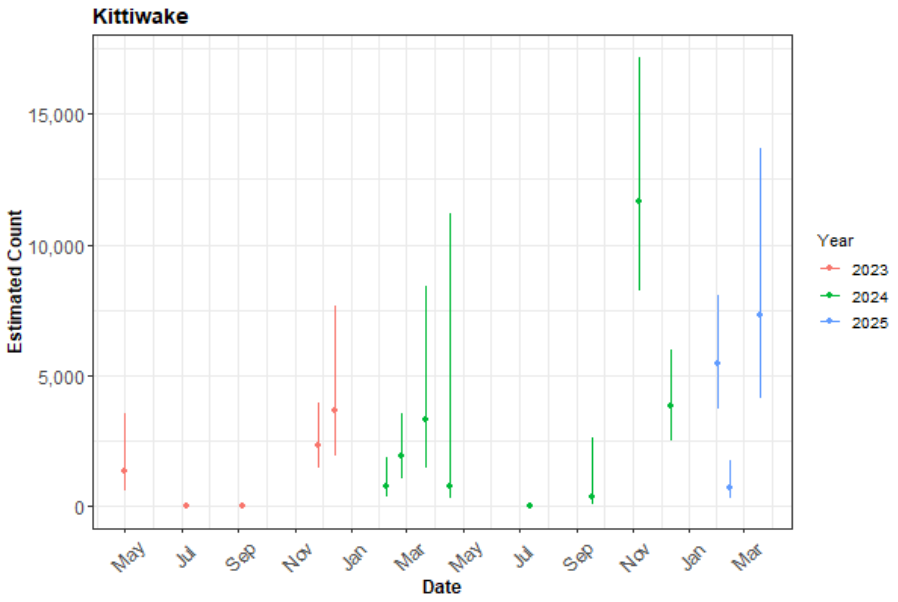

Figure 3-63. The estimated count of black-legged kittiwakes for each of the 16 Y1 and Y2 surveys conducted. The 95% CI are percentile-based confidence intervals from a parametric bootstrap with 500 replicates. As the survey area is the same for each survey, the abundances are comparable.

Figure 3-64 and Figure 3-65 show the estimated numbers of black-legged kittiwake in each 1 km² grid cell for each Y1 and Y2 survey. The first figure shows the surfaces on the same scale, and the second figure (Figure 3-65) limits the estimated density to 20 birds/km^2 to provide more detail. Generally, the estimated abundances fitted well with the raw data, and there were no notable misalignments. In areas where the estimated numbers were systematically higher, the abundances were also relatively high, and there were no areas with large, estimated abundances unsupported by the data.

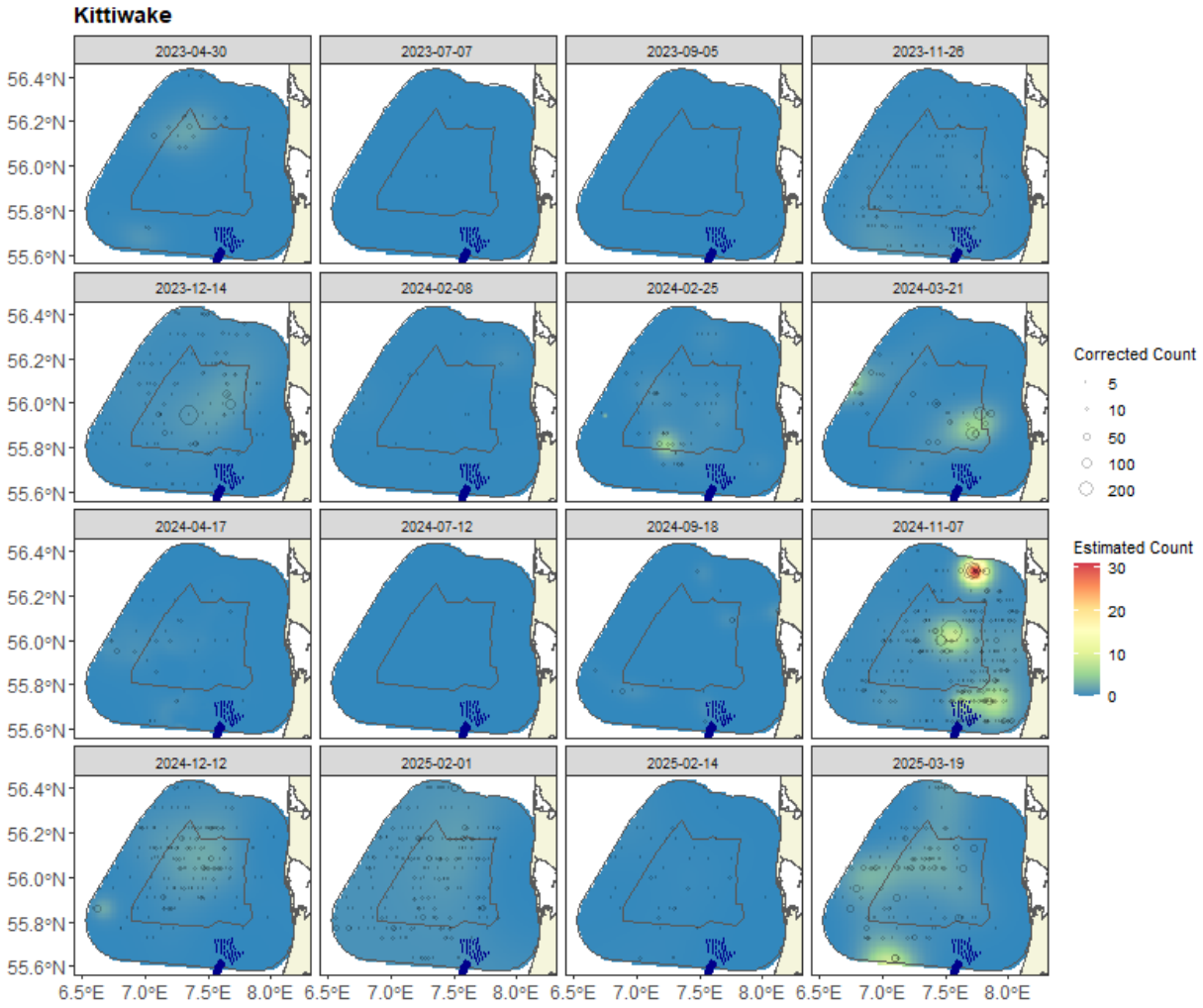

Figure 3-64. Figure showing the estimated black-legged kittiwake abundance across the NSI survey area for each of the 16 Y1 and Y2 surveys. The estimated numbers are per 1 km x 1 km grid cell. The open circles represent the distance-corrected counts.

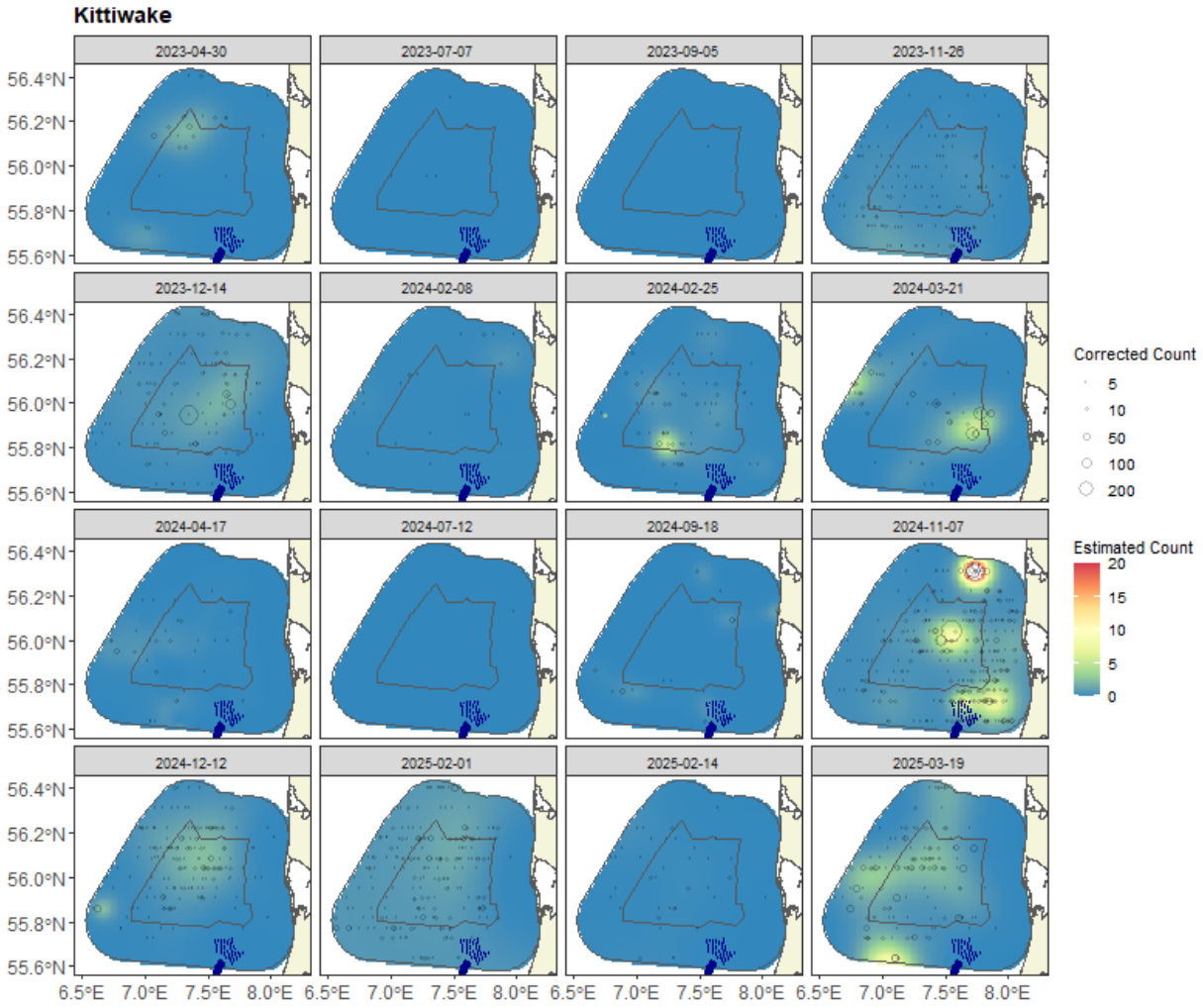

Figure 3-65. Figure showing the estimated black-legged kittiwake abundance across the NSI survey area for each of the 16 Y1 and Y2 surveys. The estimated numbers are per 1 km x 1 km grid cell. The open circles represent the distance-corrected counts. The colour scale is here limited to 20 birds/km^2 to provide more detail. White areas indicate data intentionally omitted from one or more surveys with exceptionally high abundances to allow finer detail to be seen in lower-density distributions.

3.1.5.8 Areas of persistence

Figure 3-66 and Figure 3-67 show the black-legged kittiwake persistence across the Y1 and Y2 surveys. In the Y1 surveys, there was moderate persistence (~ 62%), which was focused on the centre west of the survey area (Figure 3-66). There was little persistence towards the coast and, in particular, in the southeast of the survey area, indicating that the birds utilize those areas less. In the Y2 surveys, the persistence is similarly distributed, but the lowest persistence was in the northeast coastal region. The highest persistence in the Y2 surveys was (~ 60%).

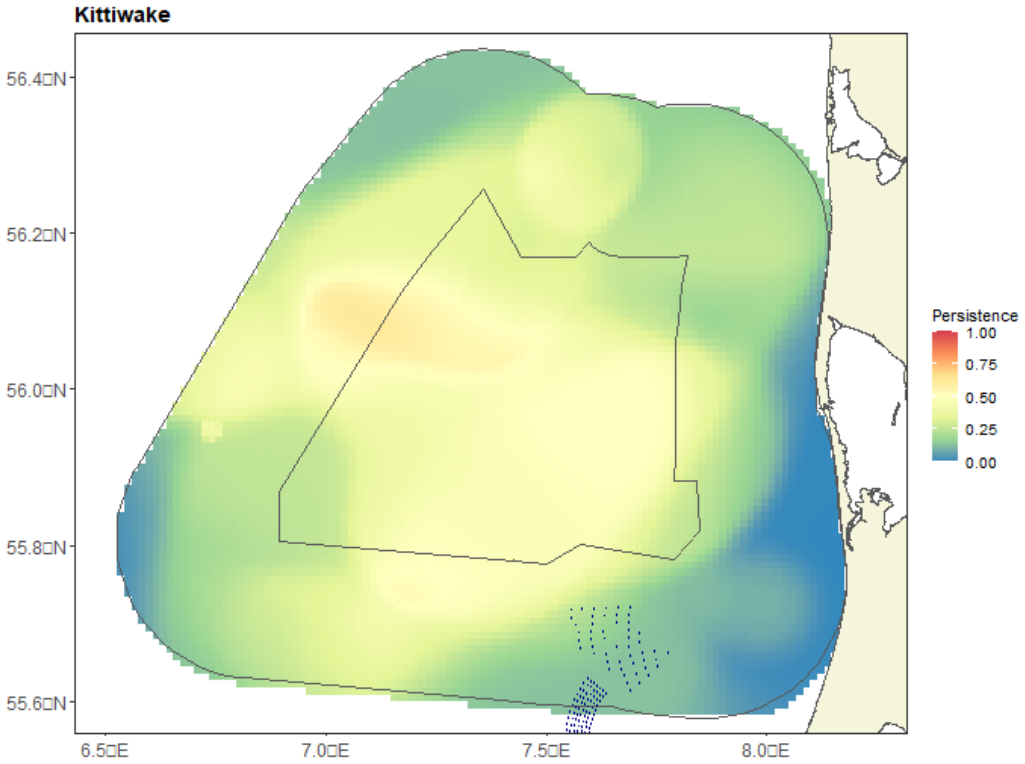

Figure 3-66. Persistence scores for black-legged kittiwake across the Y1 surveys. The polygons represent the NSI pre-investigation area and the NSI survey area (black lines).

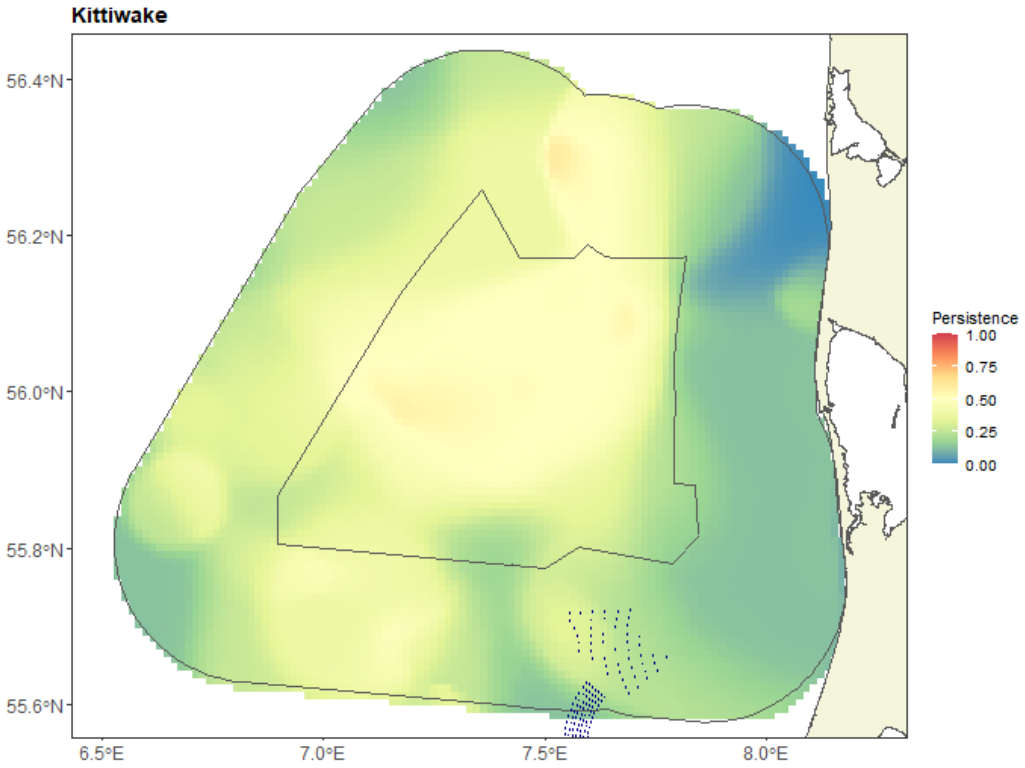

Figure 3-67. Persistence scores for black-legged kittiwake across the Y2 surveys. The polygons represent the NSI pre-investigation area and the NSI survey area (black lines).

Figure 3-68 shows the persistence across all 16 Y1 and Y2 surveys. As expected, given the distributional similarities of the separate persistence maps, the overall persistence is highest in the central region, the wind farm pre-investigation area. The highest persistence is ~49%.

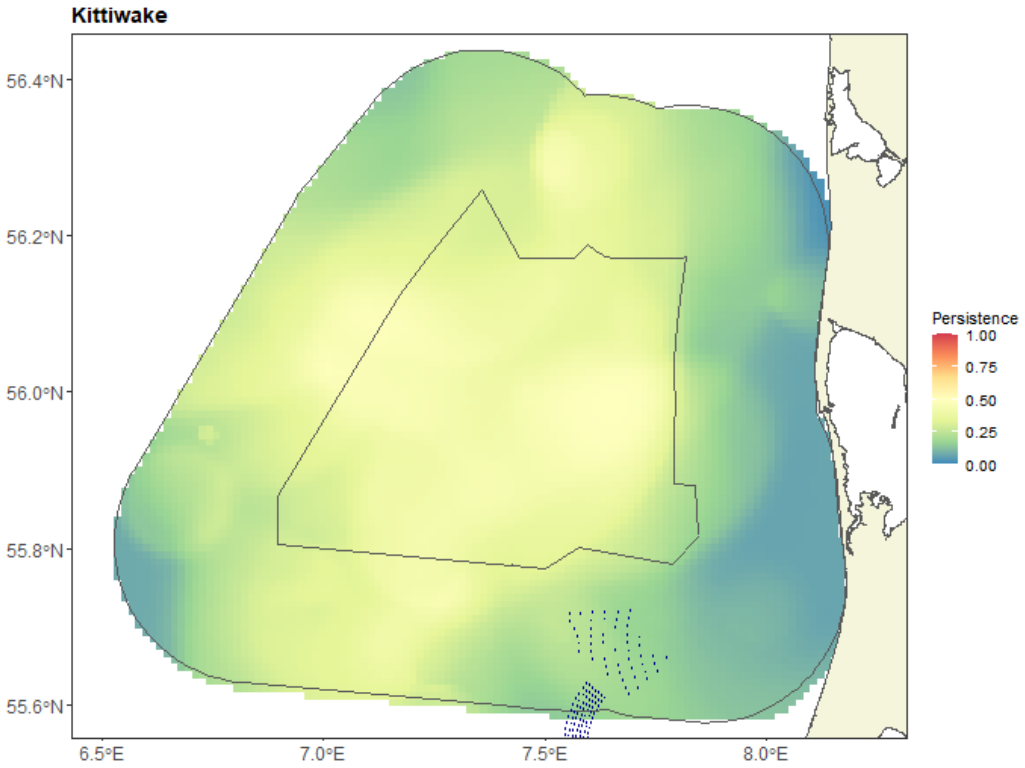

Figure 3-68. Persistence scores for black-legged kittiwake across all 16 Y1 and Y2 surveys. The polygons represent the NSI pre-investigation area and the NSI survey area (black lines).

3.1.6 Gulls (Larus sp.)

In addition to the above-mentioned gull species, black-legged kittiwake and little gull, five more species and two species groups of gulls were recorded during Y2. These were the following species: black-headed gull, common gull, lesser black-backed gull, herring gull, great black-backed gull and the following species groups: herring gull/common gull and gull sp.

Within this group, a total of 3,793 birds were recorded during Y2. Most of those (935) were recorded on 17 April 2024. Herring gull and common gull were recorded in the highest numbers (1,711 and 769 birds, respectively).

In spring, summer and autumn, most gulls were recorded in the eastern and southern parts of the survey area. In winter, gulls were recorded more widely throughout the survey area. Black-headed gull was not recorded from December to late February, and lesser black-backed gulls were not recorded from November to late February.

Of the 1,474 recordings, the mean group size was 2.3 birds, and the maximum group size was 250 birds.

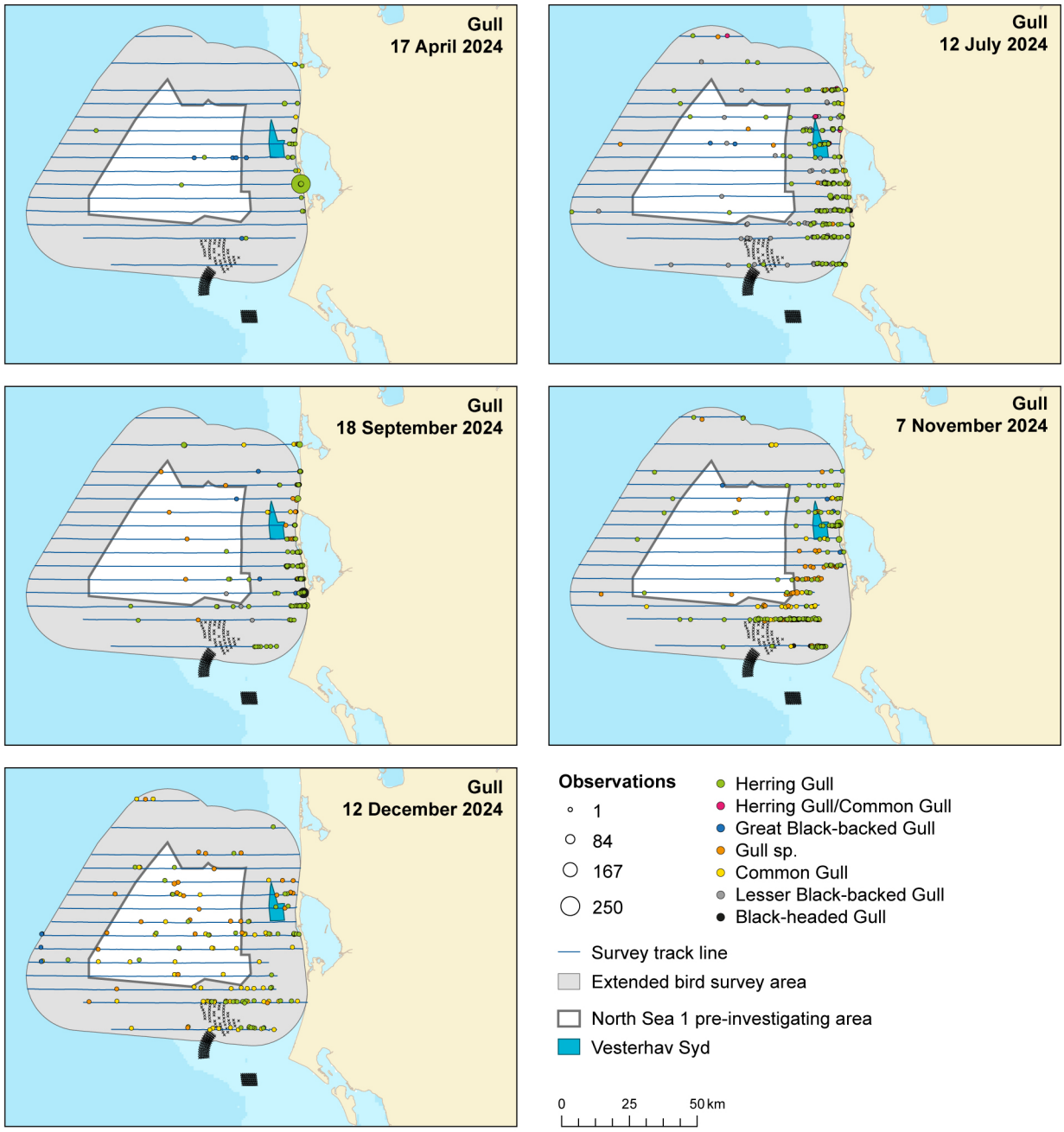

Figure 3-69. The numbers and distribution of common gull, herring gull, herring/common gull, great black-backed gull, lesser black-backed gull, gull sp., and black-headed gull observed during five Y2 surveys in the NSI survey area.

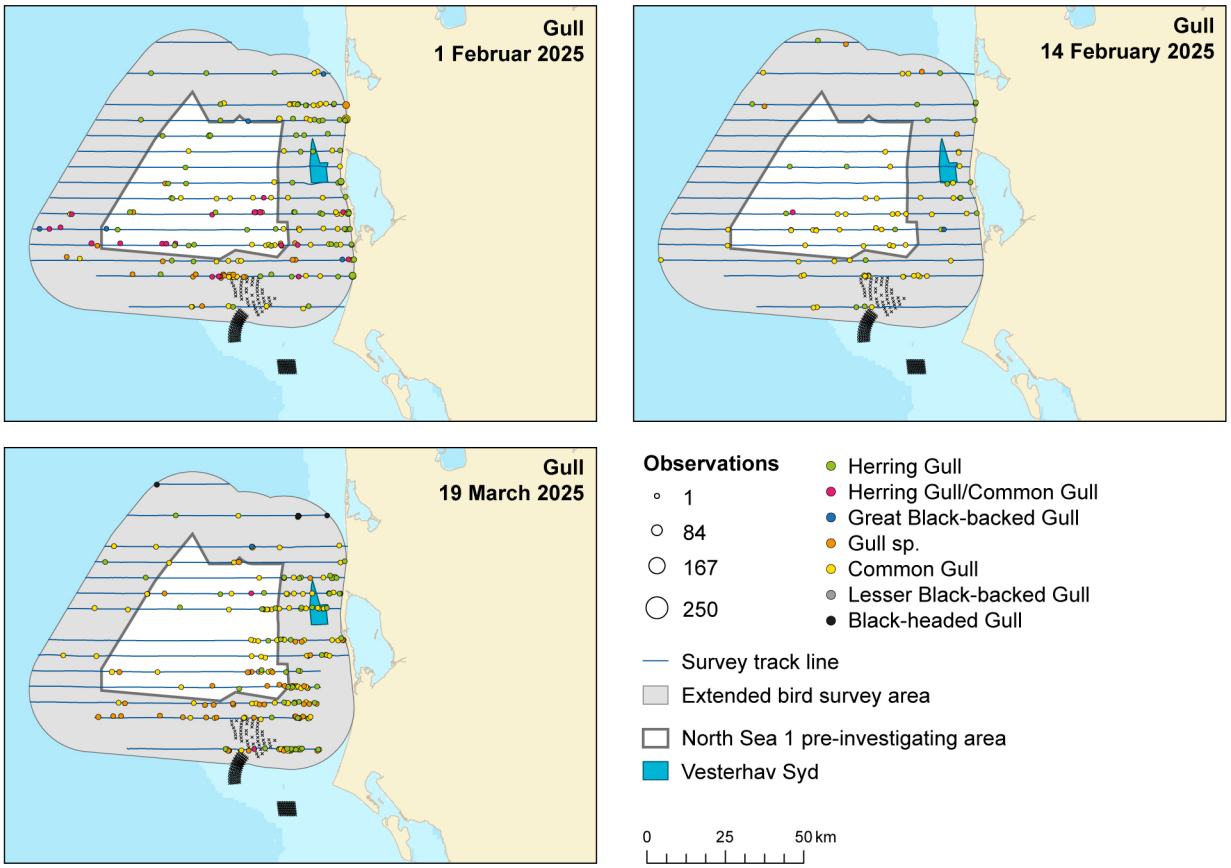

Figure 3-70. The numbers and distribution of common gull, herring gull, herring/common gull, great black-backed gull, lesser black-backed gull, gull sp., and black-headed gull observed during three Y2 surveys in the NSI survey area.

3.1.7 Terns (Sterna sp.)

Two species of terns were recorded during the eight Y2 surveys, sandwich terns and common terns. In addition, two tern species groups were recorded, common tern/arctic tern and tern sp. Terns are difficult to distinguish from species from aerial surveys, and thus, 93% of the birds were assigned to a species group. Arctic tern/common tern was the most frequently recorded species group.

Terns were solely recorded in the area between April and September, while during the rest of the period, no terns were recorded. Most terns were recorded on 17 April 2024, when groups of mainly arctic/common terns were seen migrating northwards in the central part of the survey area. During the surveys in July and September, terns were seen more frequently in the eastern parts of the area (Table 3-1, Figure 3-71 and Figure 3-72).

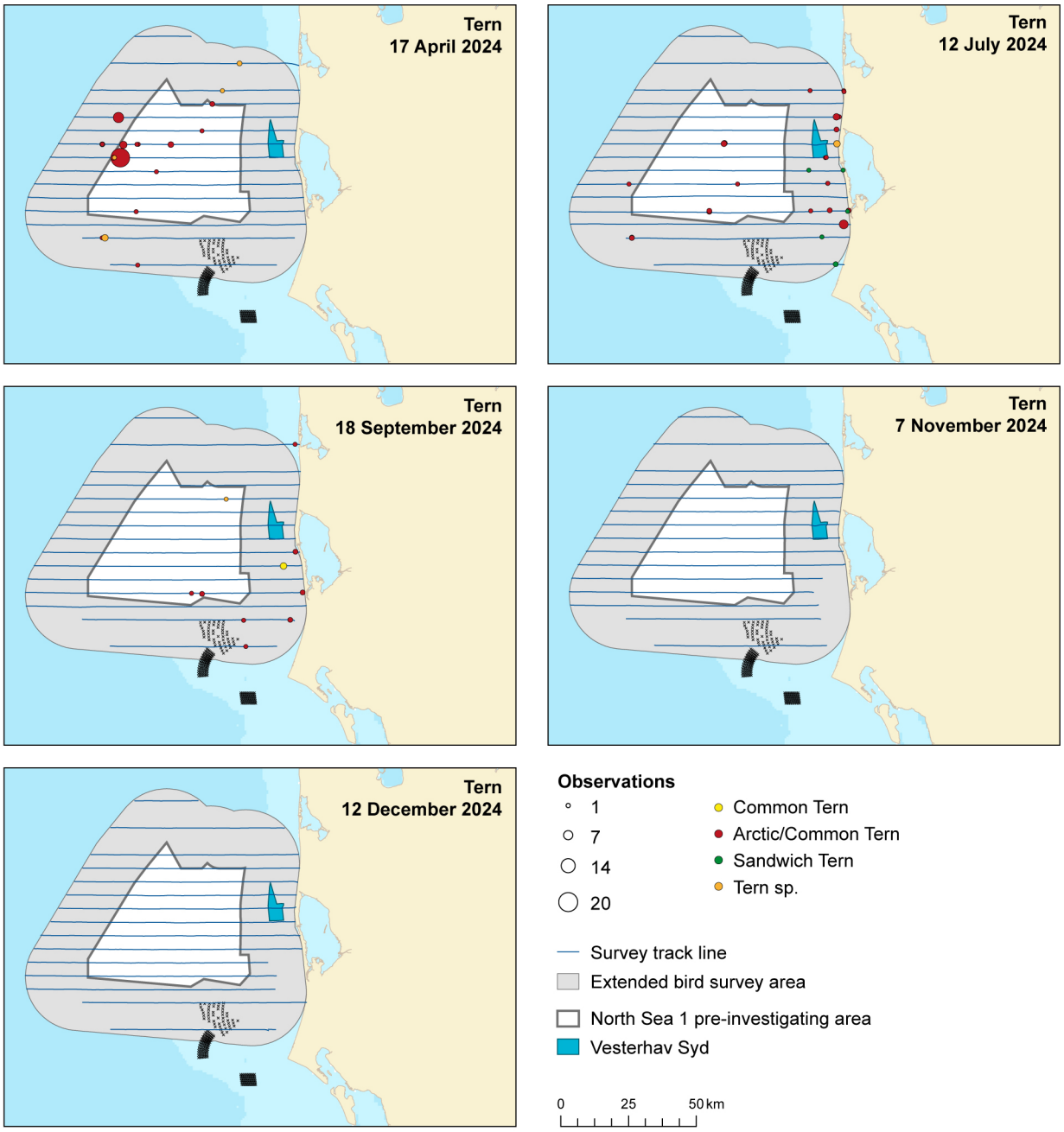

Figure 3-71. The numbers and distribution of common terns, common/arctic terns, sandwich terns and tern sp. observed during five Y2 surveys in the NSI survey area.

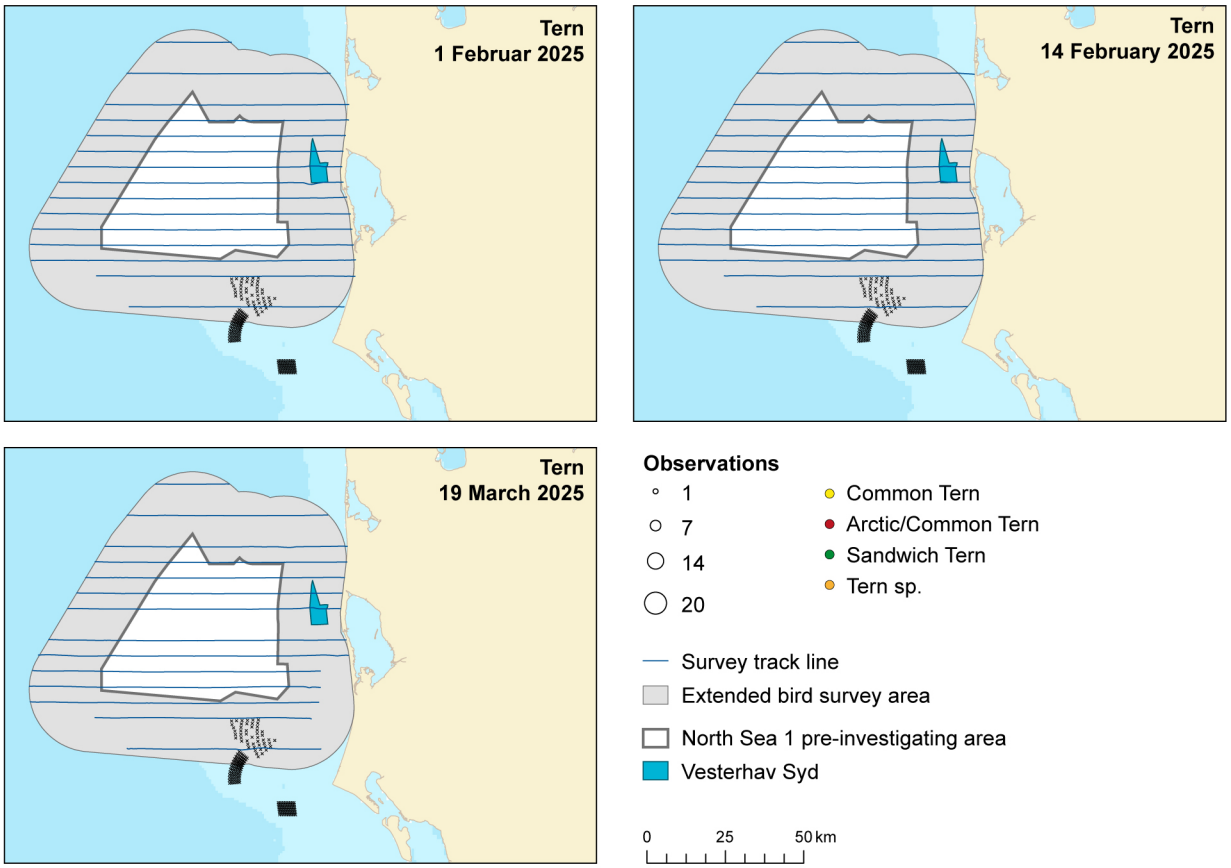

Figure 3-72. The numbers and distribution of common terns, common/arctic terns, sandwich terns and tern sp. observed during three Y2 surveys in the NSI survey area.

3.1.8 Razorbill/common guillemot (*Alca torda/Urea aalge*)

Razorbills/common guillemots were recorded during all eight Y2 surveys. A total of 4,031 birds were observed, respectively: 2,983 unidentified razorbills/common guillemots, 251 razorbills and 789 common guillemots summed for all eight surveys (Table 3-1). Thus, more than 74% of those were recorded as unidentified razorbills/common guillemots. 6% of the total numbers from this group were identified as razorbills, while 20% were identified as common guillemots. There were 1,629 records made within this group of species. The mean flock size was 1.9, and the maximum flock size recorded was 55 individuals.

The razorbills/common guillemots were recorded in the highest numbers from November 2024 until March 2025. In March 2025, the highest number of razorbills/common guillemots were observed, consisting of 27% of the total number of observed razorbills/common guillemots across the eight Y2 surveys. Razorbills/common guillemots were recorded in most parts of the survey area, varying between surveys. The eastern coastal areas had fewer birds, while the central parts of the survey area had the most (Figure 3-73 and Figure 3-74).

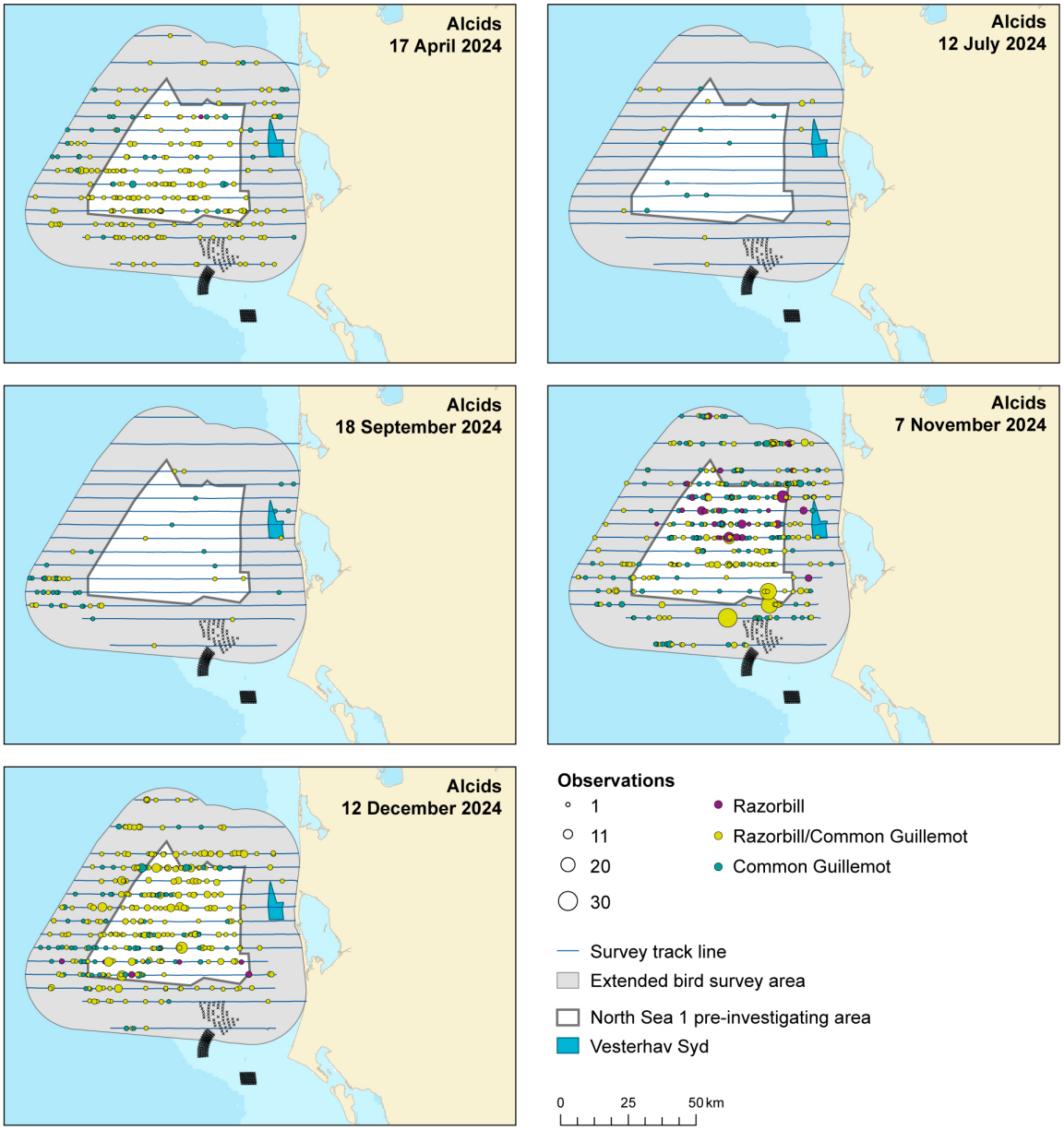

Figure 3-73. The numbers and distribution of razorbills, common guillemots and unidentified razorbills/common guillemots observed during five Y2 surveys in the NSI survey area.

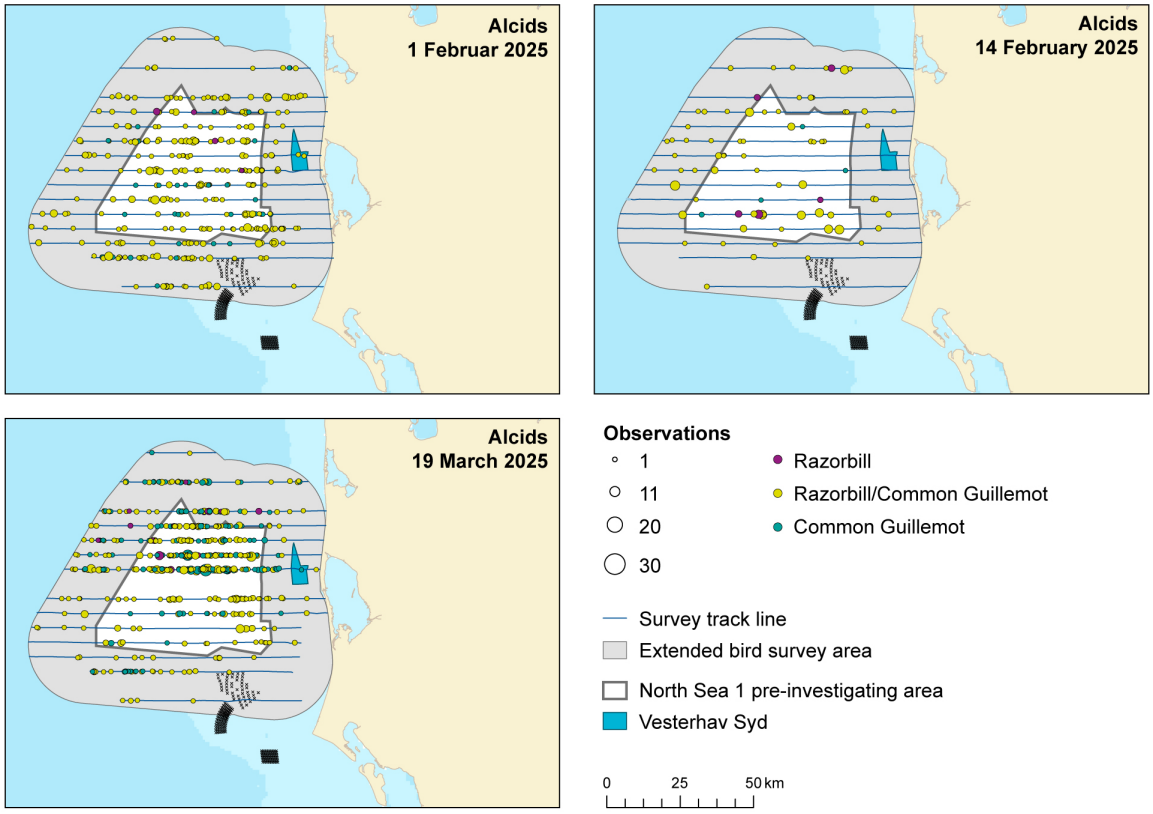

Figure 3-74. The numbers and distribution of razorbills, common guillemots and unidentified razorbills/common guillemots observed during three Y2 surveys in the NSI survey area.

3.1.8.1 Distance analysis

The average probability of sighting razorbills/common guillemots was estimated to be 0.19 (CoV = 0.02). This probability was estimated using a hazard rate detection function and observer as a covariate (Figure 3-75). Using observer as a covariate required fitting of a detection function based on the Y2 data set since new observers were introduced between the Y1 and Y2 surveys.

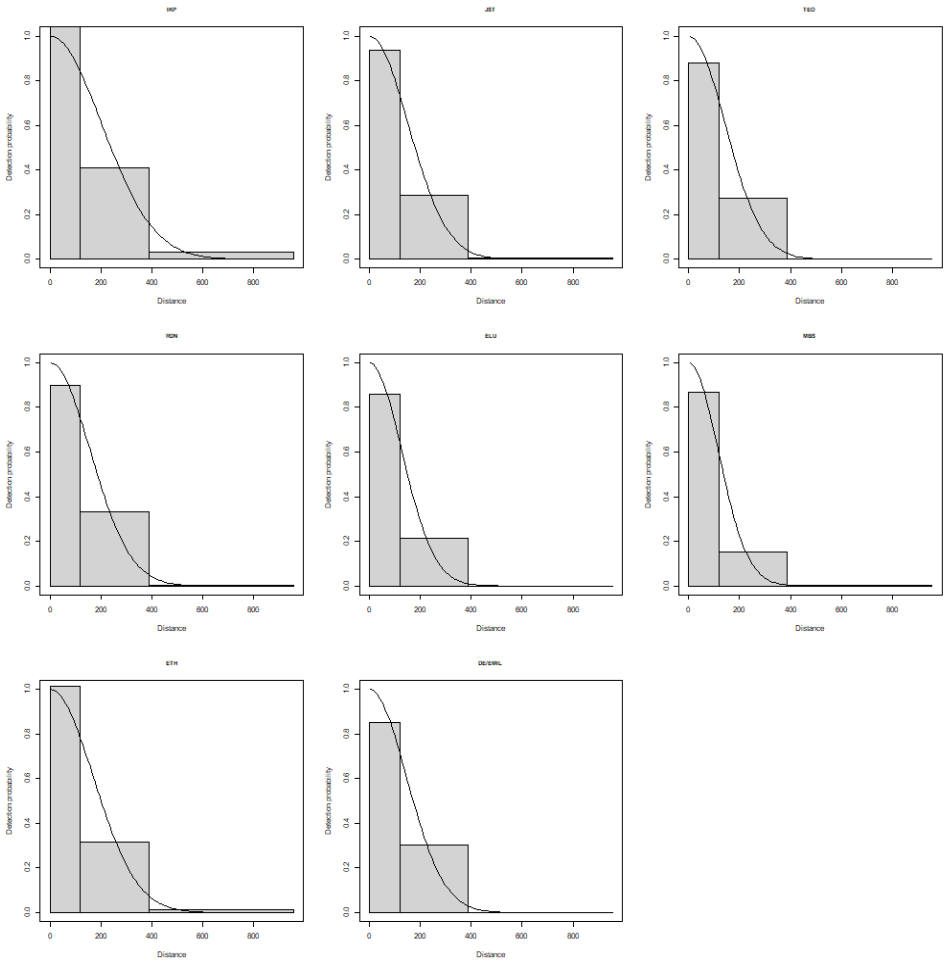

Figure 3-75. Figure showing the estimated detection function for razorbill/common guillemot. The histograms represent the distances of the observed sightings for each of the eight observers.

3.1.8.2 Spatial analysis

Figure 3-76 shows the distribution of the distance corrected counts for each of the eight Y2 surveys.

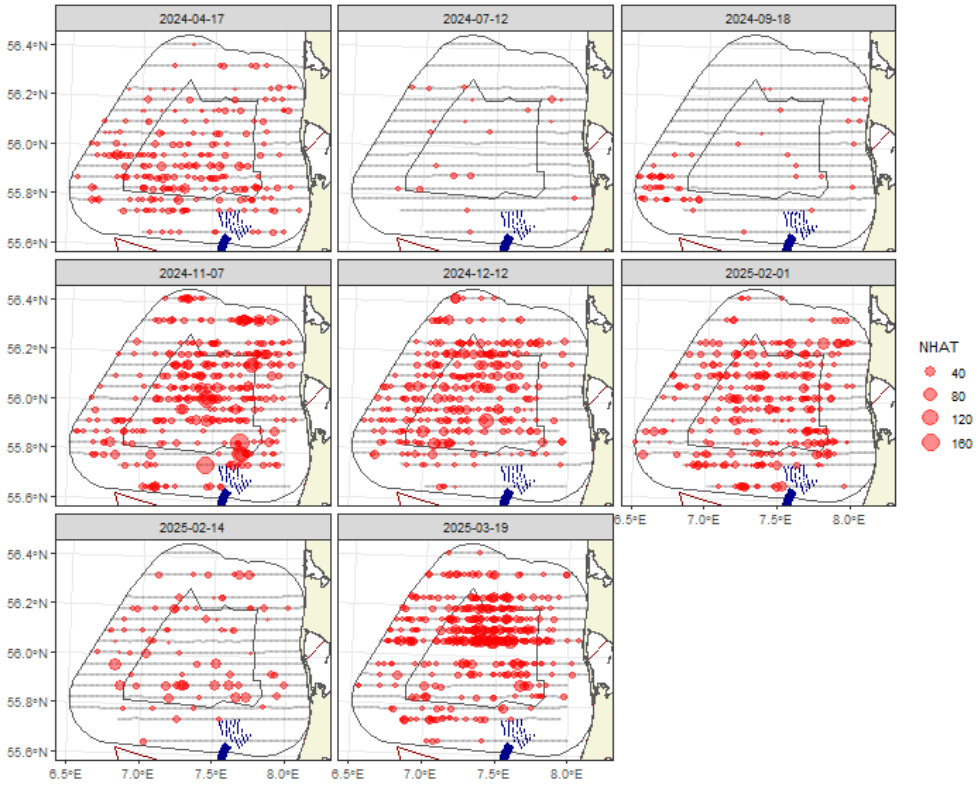

Figure 3-76. Distance-corrected counts for the razorbill/common guillemot species group across the eight Y2 surveys. The red circles indicate the distance-corrected counts along the transect lines. The grey dots are segments with a count of zero.

3.1.8.3 Model selection

For all Y2 surveys, the models selected included a spatial term (of varying complexity), while the depth covariate (either as a linear or smooth term) was selected for two surveys. The distance-to-coast covariate was selected as a smooth term for one model. This shows there was compelling evidence for non-uniform spatial patterns in all Y2 surveys. The spatial surfaces selected ranged from six to nine parameters for the spatial term (Table 3-14).

Table 3-14. Model selection results for razorbill/common guillemot for each Y2 survey. The model column represents the terms in the model.

Date	Model	Distribution	Variable 1D	Variable 2D	Number of Parameters	Dispersion parameter	Tweedie parameter
2024-04-17	2D Only	Tweedie	NA	s(x,y, df=8)	9	11.0	1.15
2024-07-12	2D Only	Tweedie	NA	s(x,y, df=9)	10	8.4	1.15
2024-09-18	2D Only	quasipoisson	NA	s(x,y, df=8)	9	6.8	NA
2024-11-07	Best 1D2D	Tweedie	s(depth, df=2)	s(x,y, df=8)	11	18.6	1.38
2024-12-12	Best 1D2D	Tweedie	s(depth, df=2)	s(x,y, df=7)	10	18.6	1.32
2025-02-01	Best 1D2D	Tweedie	s(distcoast, df=3)	s(x,y, df=9)	13	15.4	1.28
2025-02-14	2D Only	Tweedie	NA	s(x,y, df=9)	10	24.3	1.36
2025-03-19	2D Only	Tweedie	NA	s(x,y, df=6)	7	15.4	1.28

The estimated abundances and associated 95 percentile confidence intervals for each Y2 survey are given in Table 3-15 and Figure 3-77. The greatest abundance, 26,953 birds (95% CI: 17,641-41,803), was estimated for the survey on 19th March 2025, although the confidence interval for this overlapped with the surveys in November, December and the first February survey.

Table 3-15. Estimated abundance and density of razorbill/common guillemot for each Y2 survey. The 95% CI is a percentile-based confidence interval.

Date	Area (Km^2)	Estimation Type	Estimated Count	95% CI Count	Estimated Density	95% CI Density
2024-04-17	7,833	Spatial	6,998	(5,142, 10,241)	0.9	(0.7, 1.3)
2024-07-12	7,833	Spatial	280	(170, 487)	0.0	(0, 0.1)
2024-09-18	7,833	Spatial	976	(476, 3,507)	0.1	(0.1, 0.4)
2024-11-07	7,833	Spatial	16,039	(10,402, 25,432)	2.0	(1.3, 3.2)
2024-12-12	7,833	Spatial	13,751	(8,657, 22,189)	1.8	(1.1, 2.8)
2025-02-01	7,833	Spatial	14,043	(8,501, 24,488)	1.8	(1.1, 3.1)
2025-02-14	7,833	Spatial	3,314	(1,855, 6,313)	0.4	(0.2, 0.8)
2025-03-19	7,833	Spatial	26,953	(17,641, 41,803)	3.4	(2.3, 5.3)

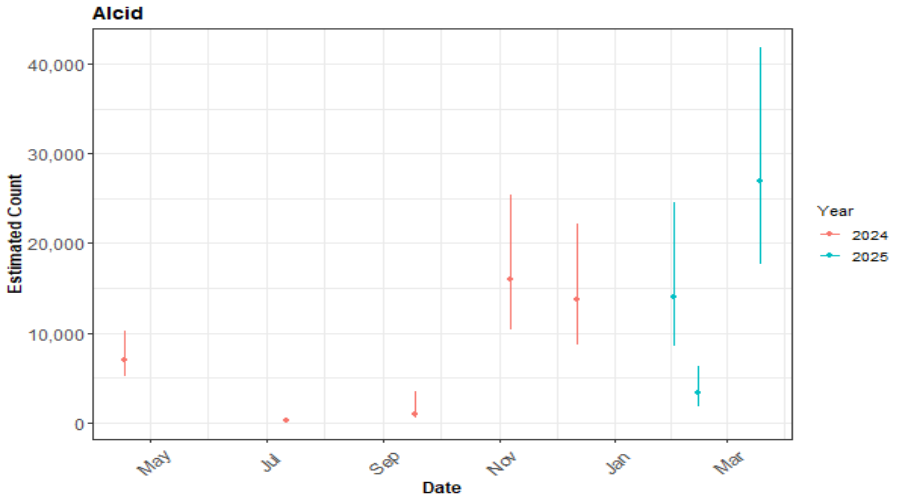

Figure 3-77. The estimated count of razorbills/common guillemots for each Y2 survey. The 95% CI are percentile-based confidence intervals are from a parametric bootstrap with 500 replicates. As the survey area is the same for each survey, the abundances are comparable.

3.1.8.4 Spatial results

Figure 3-78 and Figure 3-79 show the estimated numbers of razorbills/common guillemots in each 1 km^2 grid cell for each Y2 survey. Generally, the estimated abundances fitted well with the raw data, and there were no notable misalignments. In areas where the estimated numbers were systematically higher, the abundances were also relatively high, and there were no areas with large, estimated abundances unsupported by the data. In general, the birds are well distributed throughout the area.

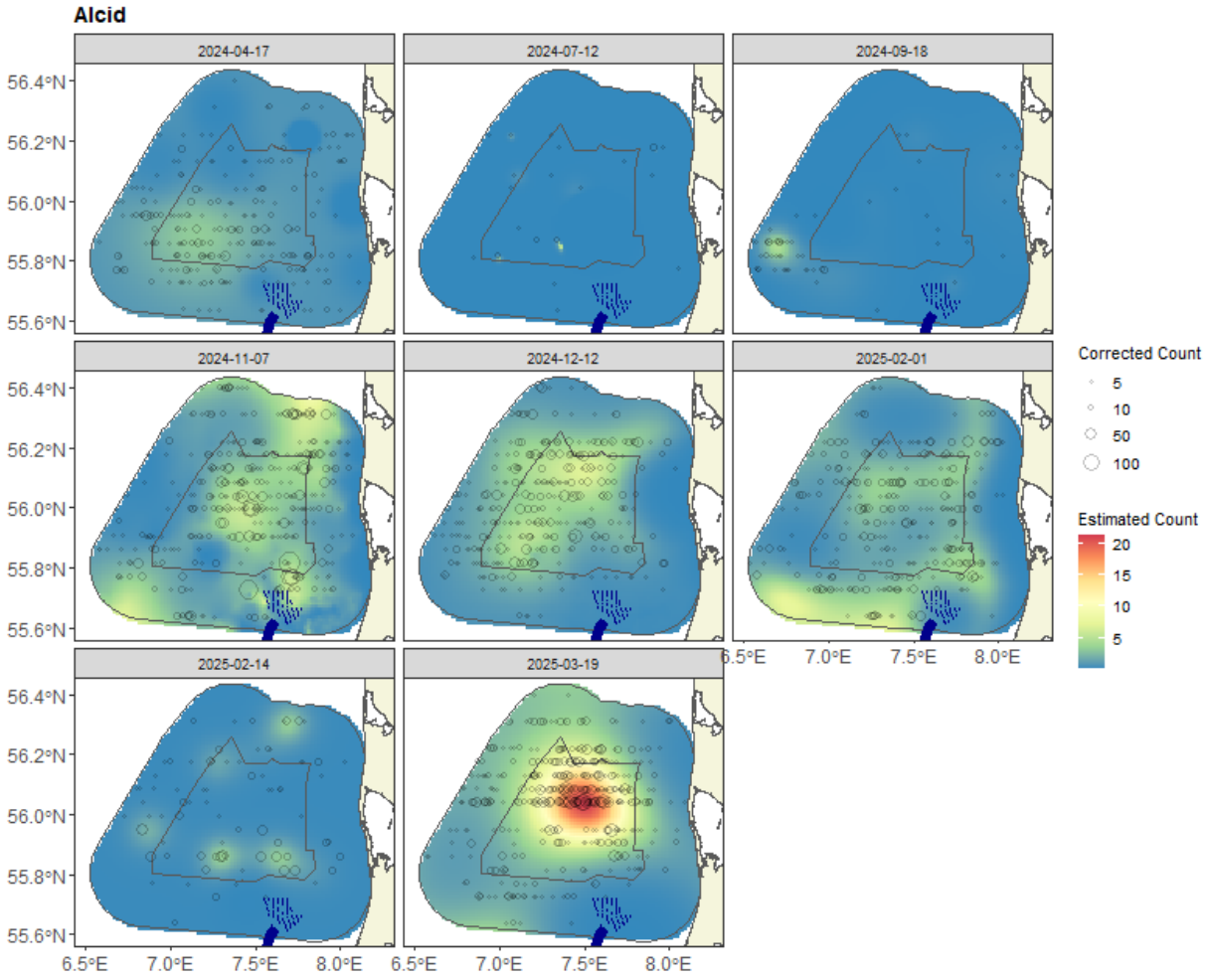

Figure 3-78. Figure showing the estimated razorbill/common guillemot abundance across the NSI survey area for each Y2 survey. The estimated numbers are per 1 km x 1 km grid cell. The open circles represent the distance-corrected counts.

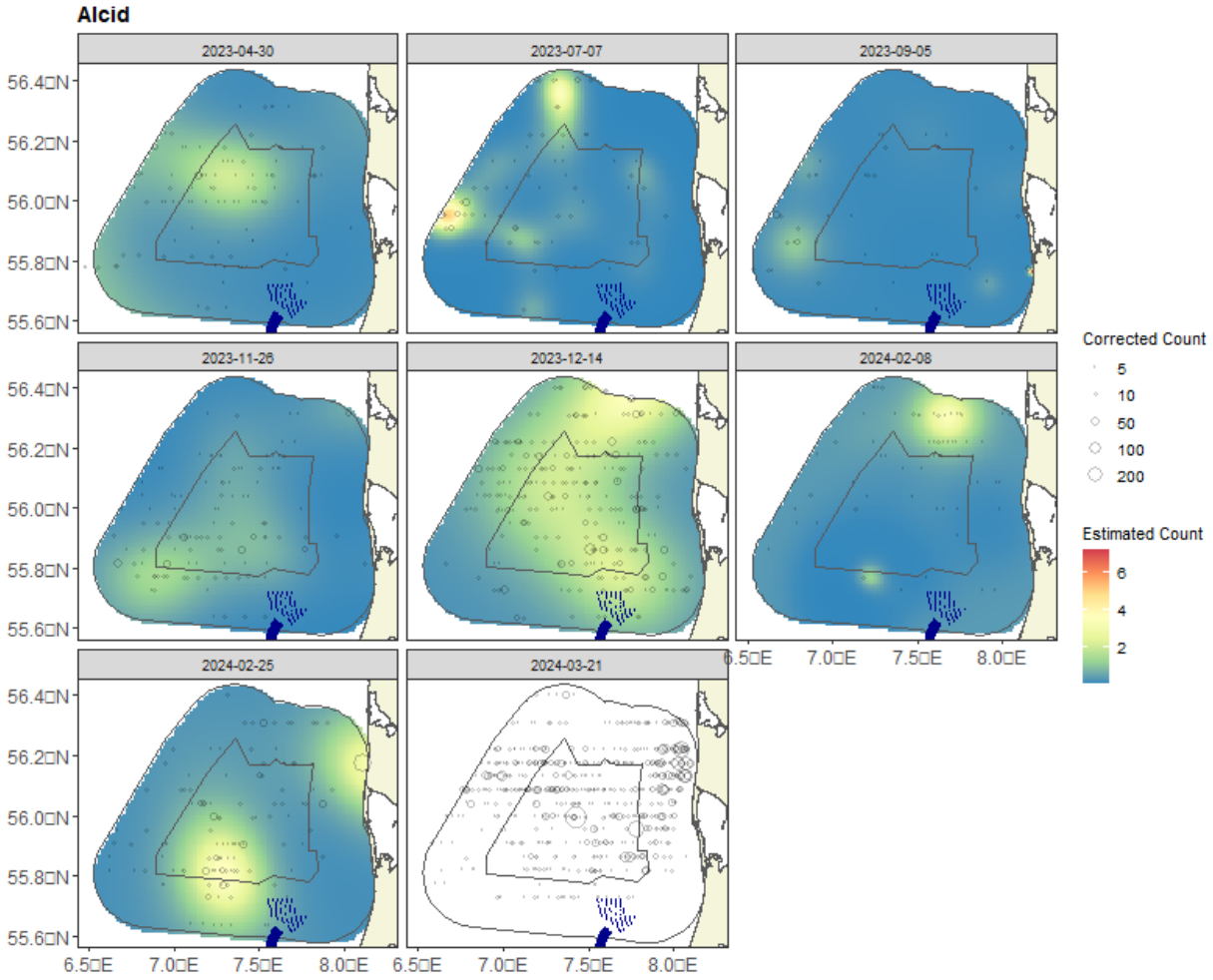

Figure 3-79. Figure showing the estimated razorbill/common guillemot abundance across the NSI survey area for each Y2 survey except the high abundance last one. The estimated numbers are per 1 km x 1 km grid cell. The open circles represent the distance-corrected counts. White areas indicate data intentionally omitted from one or more surveys with exceptionally high abundances to allow finer detail to be seen in lower-density distributions.

3.1.8.5 Uncertainty in spatial predictions

Broadly, the highest Y2 coefficient of variation (CoV) scores was associated with the `almost zero' predictions, and it is known that the CoV metric is highly sensitive to any uncertainty for very small predictions. There was no material overlap between the high values of the CoV metric and the transect lines/locations with non-zero counts. Therefore, there were no concerns in this case (Figure 3-80).

In the case where the very small predicted values were excluded (Figure 3-80), a few areas of high CoV remained, which will play a role in the related confidence intervals for the abundances (Table 3-15 and Figure 3-77).

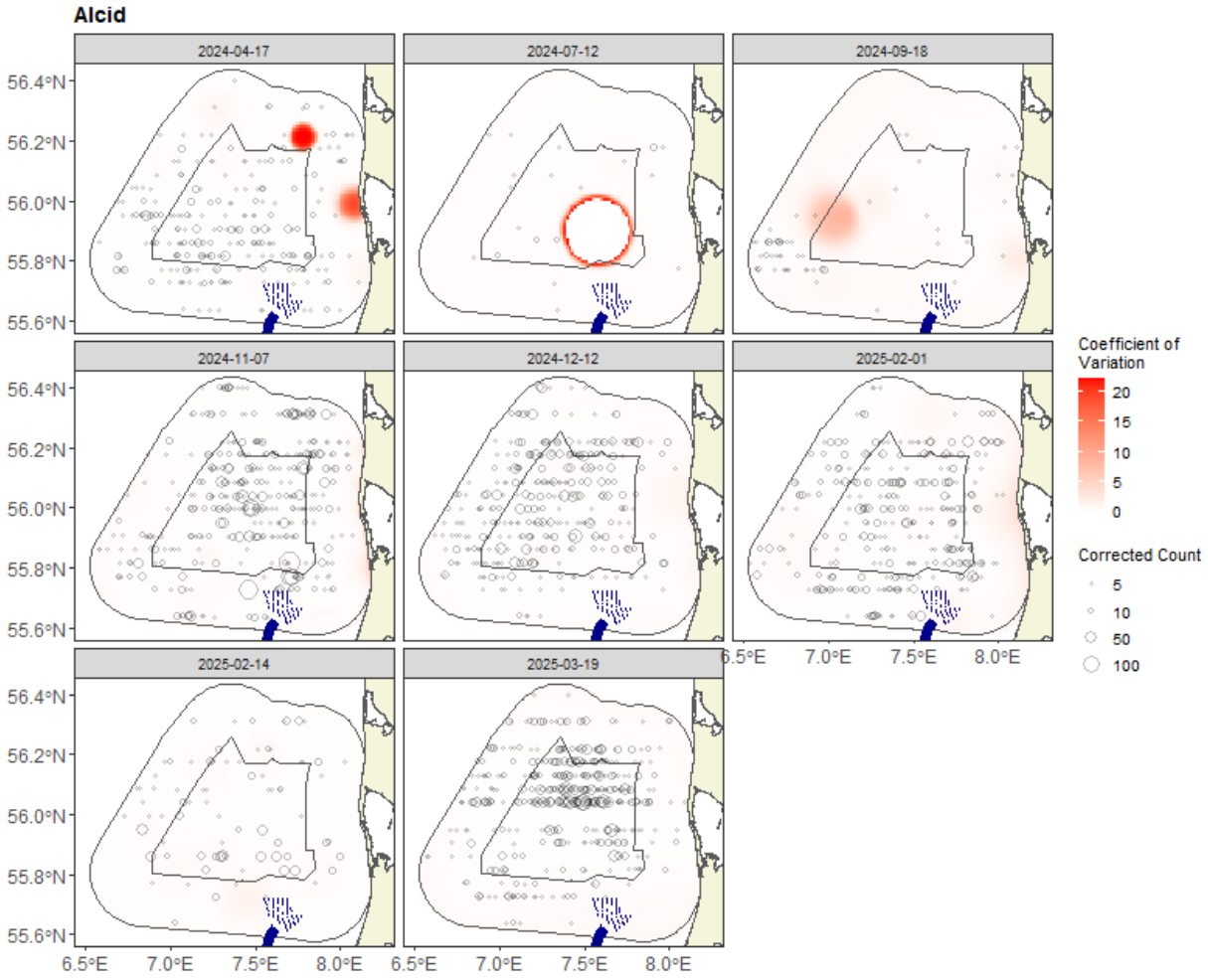

Figure 3-80. Figure showing the coefficient of variation (CoV) across the NSI survey area for each Y2 survey. The open circles show the distance corrected counts. The presence of dark red CoV scores in areas with virtually zero predictions is an artefact of the very small prediction rather than of any notable concern.

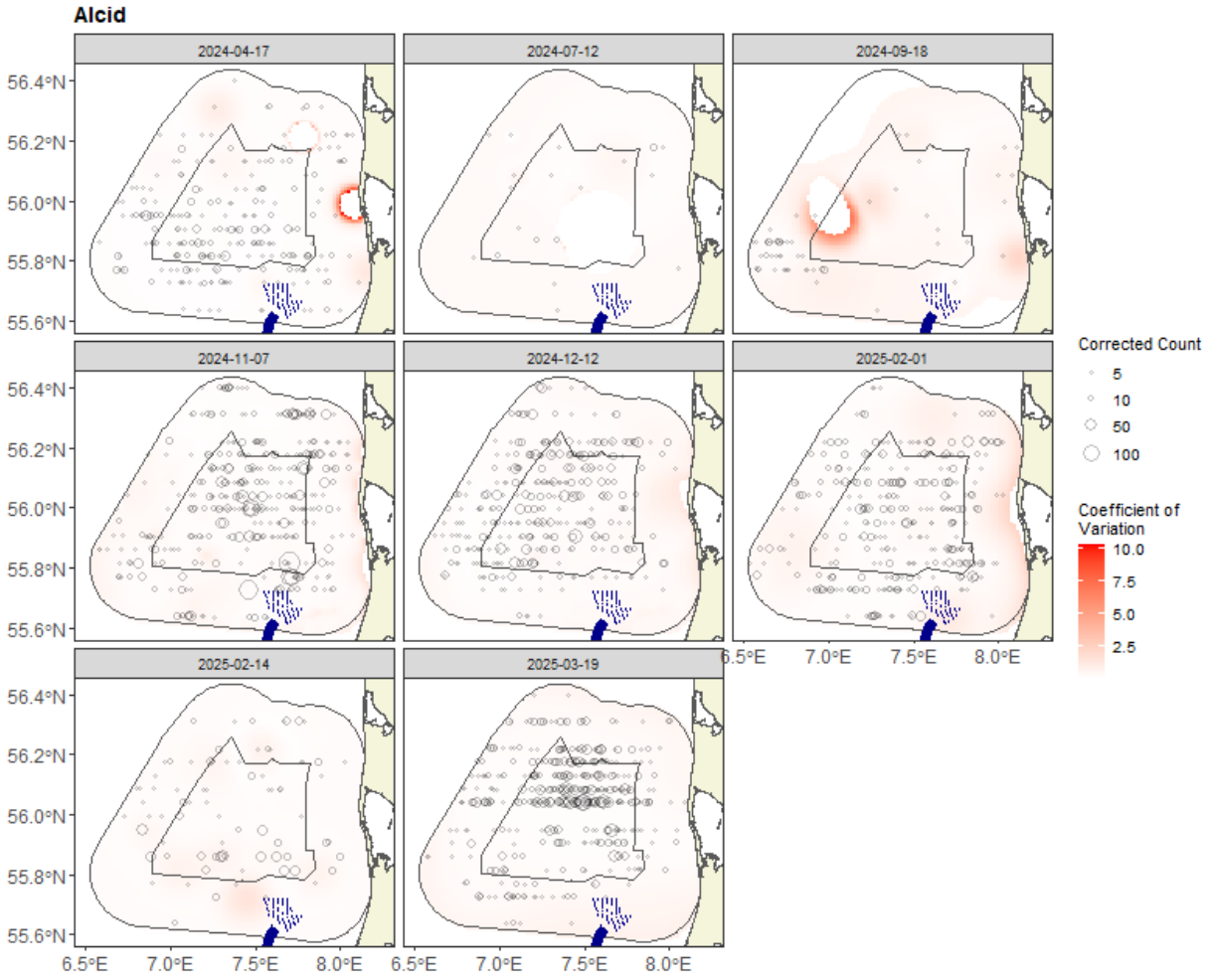

Figure 3-81. Figure showing the Y2 coefficient of variation for all cells above a density of 0.001. The open circles show the distance corrected counts. The presence of dark red CV scores in areas with virtually zero predictions is an artefact of the very small prediction rather than of any notable concern.

3.1.8.6 Model diagnostics

A blocking structure was used to account for potential residual non-independence for each Y2 model, and a robust standard error approach was based on unique transects. In each case, a reassuring decay to zero was seen (indicated by the red and grey lines in Figure 3-82), implying that an appropriate blocking structure was used. All the plots in Figure 3-83 and Figure 3-84 are examples from the eight Y2 razorbill/common guillemot models.

The assumed mean-variance relationship was examined, and agreement was generally shown between the assumed (red) lines and the observed values. Figure 3-83 and Figure 3-84 show example relationships for a quasi-Poisson and Tweedie model. The example DHARMa diagnostic plots (Figure 3-85) show that the distributional assumption for the model is appropriate and that the model is correctly specified.

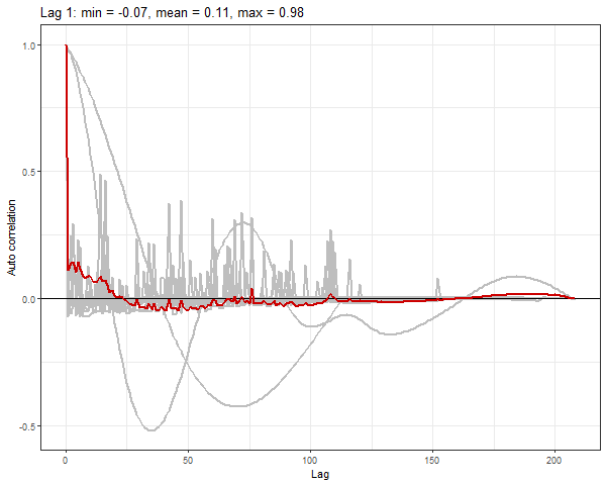

Figure 3-82. Example ACF plot for razorbill/common guillemot. The grey lines represent the residual correlation observed in each transect, and the red line is the average of these values across transects.

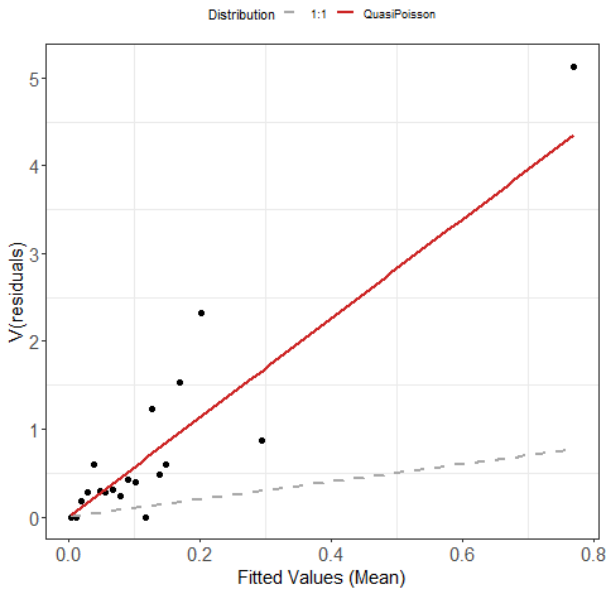

Figure 3-83. Example plot showing the estimated quasi-Poisson mean-variance relationship (red line) and actual (black dots) for razorbill/common guillemot. The black dots are based on 20 quantiles of the model residuals, and for reference, the grey dashed line shows the 1:1 relationship.

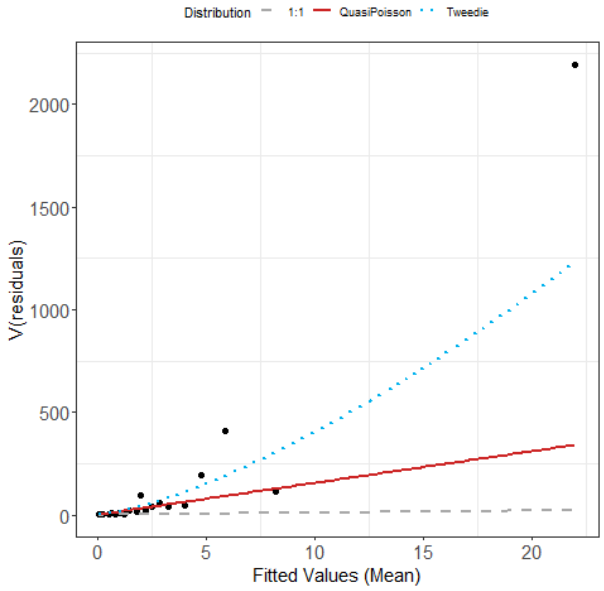

Figure 3-84. Example plot showing the estimated Tweedie mean-variance relationship (blue dashed line) for razorbill/common guillemot. The red line shows the V(μ)=ϕμ relationship, and the grey line shows the 1:1 relationship.

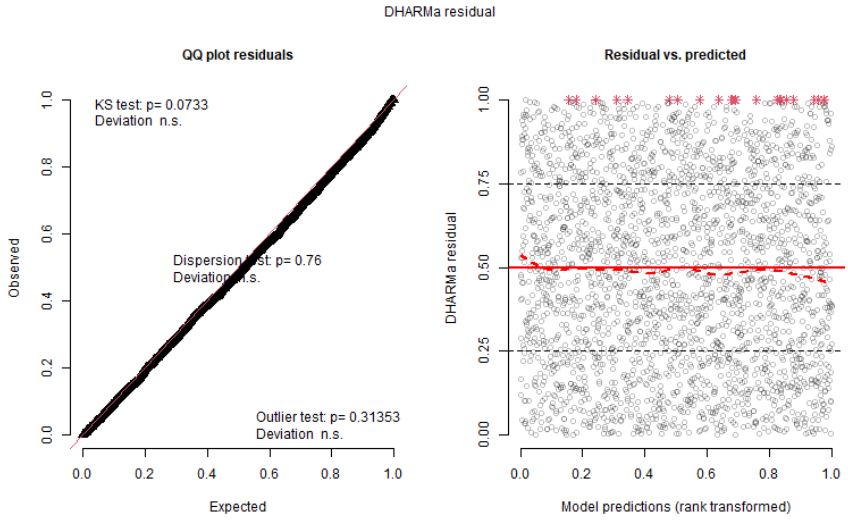

Figure 3-85. Example diagnostics. QQ plot and residuals against predicted values for razorbill/common guillemot. The red stars are outliers, and the red line is a smooth spline around the mean of the residuals.

3.1.8.7 Razorbill/common guillemot (Y1 and Y2)

This section provides combined outputs across all 16 Y1 and Y2 surveys for Alcids. The estimated abundances, densities and associated 95-percentile confidence intervals for each Y1 and Y2 survey are given in Table 3-16 and Figure 3-86. It is clear from these results that there were generally higher densities of razorbills/common guillemots seen in the Y2 November to March surveys. However, the most abundant single survey was the Y1 March survey from 2024. However, its confidence intervals strongly overlap that of March 2025, indicating a speculative difference between the two.

Table 3-16. Estimated abundance and density of razorbills/common guillemots for each of the 16 Y1 and Y2 surveys conducted. The 95% CI are percentile-based confidence intervals

Date	Area (Km^2)	Estimation Type	Estimated Count	95% CI Count	Estimated Density	95% CI Density
2023-04-30	7,833	Spatial	3,365	(1,794, 6,785)	0.4	(0.2, 0.9)
2023-07-07	7,833	Spatial	2,064	(1,192, 3,929)	0.3	(0.2, 0.5)
2023-09-05	7,833	Spatial	971	(417, 2,634)	0.1	(0.1, 0.3)
2023-11-26	7,833	Spatial	2,974	(1,551, 7,037)	0.4	(0.2, 0.9)
2023-12-14	7,833	Spatial	9,474	(6,584, 13,888)	1.2	(0.8, 1.8)
2024-02-08	7,833	Spatial	2,617	(1,511, 5,105)	0.3	(0.2, 0.7)
2024-02-25	7,833	Spatial	5,839	(3,050, 12,141)	0.7	(0.4, 1.5)
2024-03-21	7,833	Spatial	35,069	(23,704, 53,636)	4.5	(3, 6.8)
2024-04-17	7,833	Spatial	6,998	(5,142, 10,241)	0.9	(0.7, 1.3)
2024-07-12	7,833	Spatial	280	(170, 487)	0.0	(0, 0.1)
2024-09-18	7,833	Spatial	976	(476, 3507)	0.1	(0.1, 0.4)
2024-11-07	7,833	Spatial	16,039	(10,402, 25,432)	2.0	(1.3, 3.2)
2024-12-12	7,833	Spatial	13,751	(8,657, 22,189)	1.8	(1.1, 2.8)
2025-02-01	7,833	Spatial	14,043	(8,501, 24,488)	1.8	(1.1, 3.1)
2025-02-14	7,833	Spatial	3,314	(1,855, 6,313)	0.4	(0.2, 0.8)
2025-03-19	7,833	Spatial	26,953	(17,641, 41,803)	3.4	(2.3, 5.3)

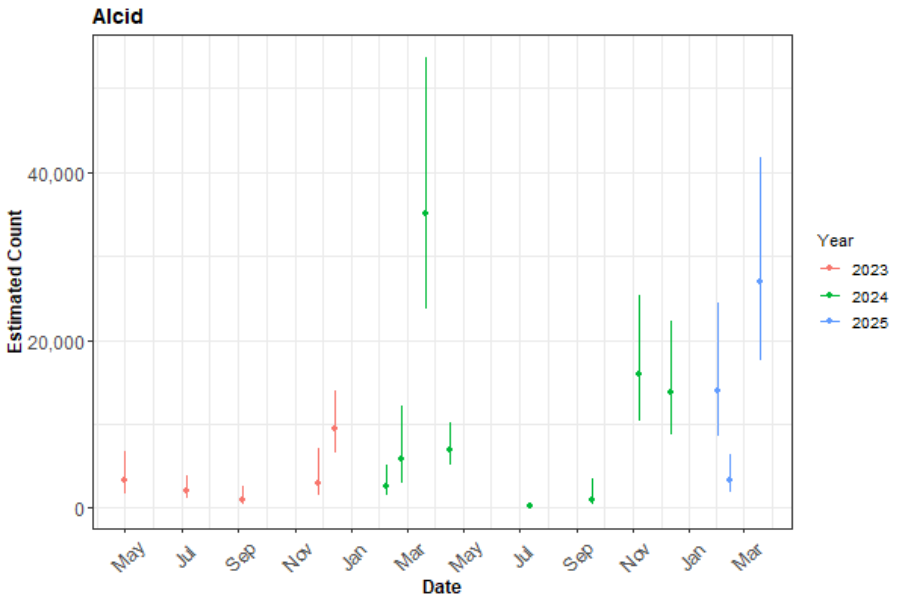

Figure 3-86. The estimated count of razorbills/common guillemots for each of the 16 Y1 and Y2 surveys conducted. The 95% CI are percentile-based confidence intervals from a parametric bootstrap with 500 replicates. As the survey area is the same for each survey, the abundances are comparable.

Figure 3-87 and Figure 3-88 show the estimated numbers of razorbills/common guillemots in each 1 km² grid cell for each Y1 and Y2 survey. The first figure shows the surfaces on the same scale, which masks the patterns in all but one survey due to the large number of birds seen in the March 2024 survey. Figure 3-88 shows the estimated numbers without that survey included. Generally, the estimated abundances fitted well with the raw data, and there were no notable misalignments. In areas where the estimated numbers were systematically higher, the abundances were also relatively high, and there were no areas with large, estimated abundances unsupported by the data.

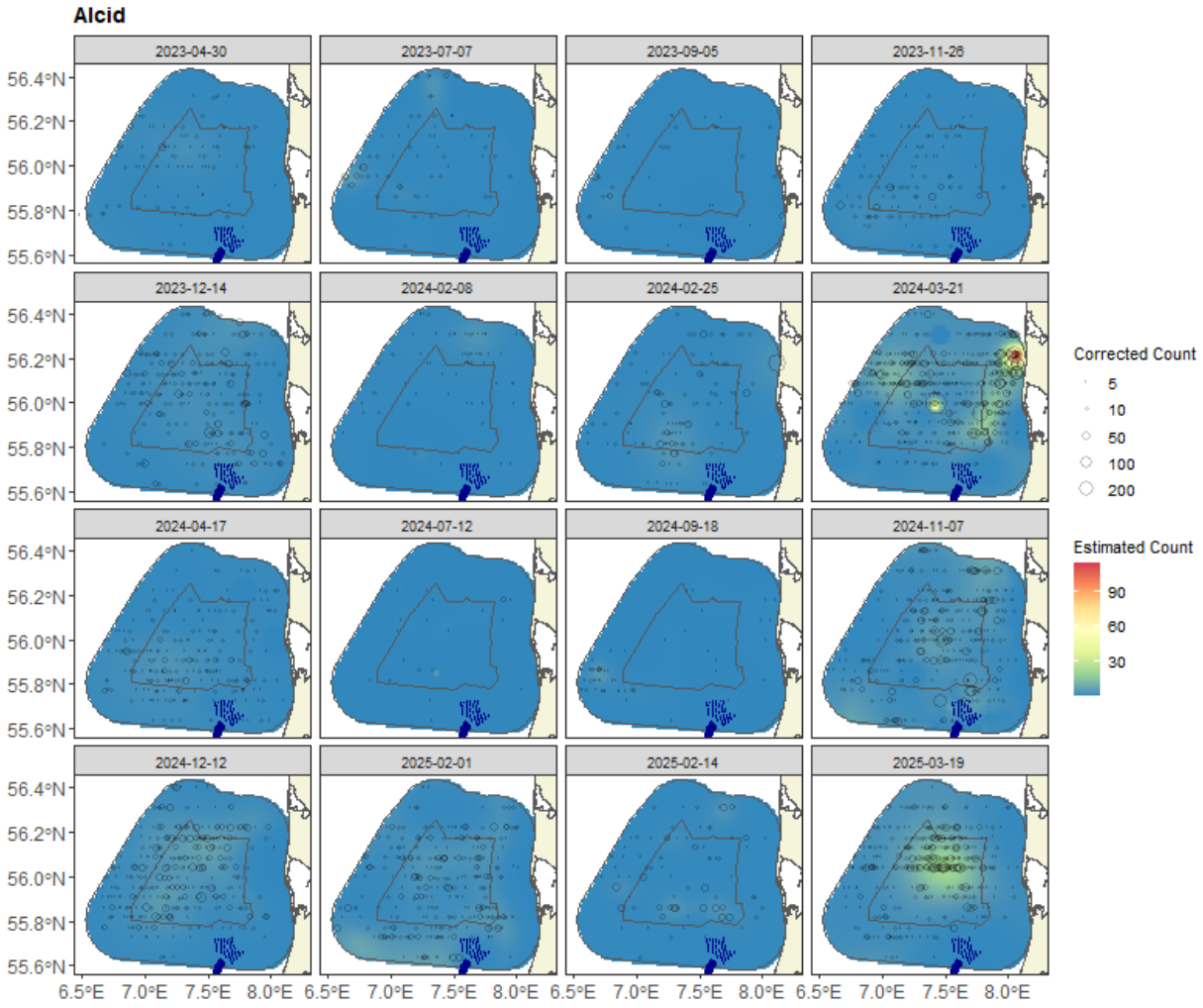

Figure 3-87. Figure showing the estimated razorbills/common guillemots' abundance across the NSI survey area for each of the 16 Y1 and Y2 surveys conducted. The estimated numbers are per 1 km x 1 km grid cell. The open circles represent the distance-corrected counts.

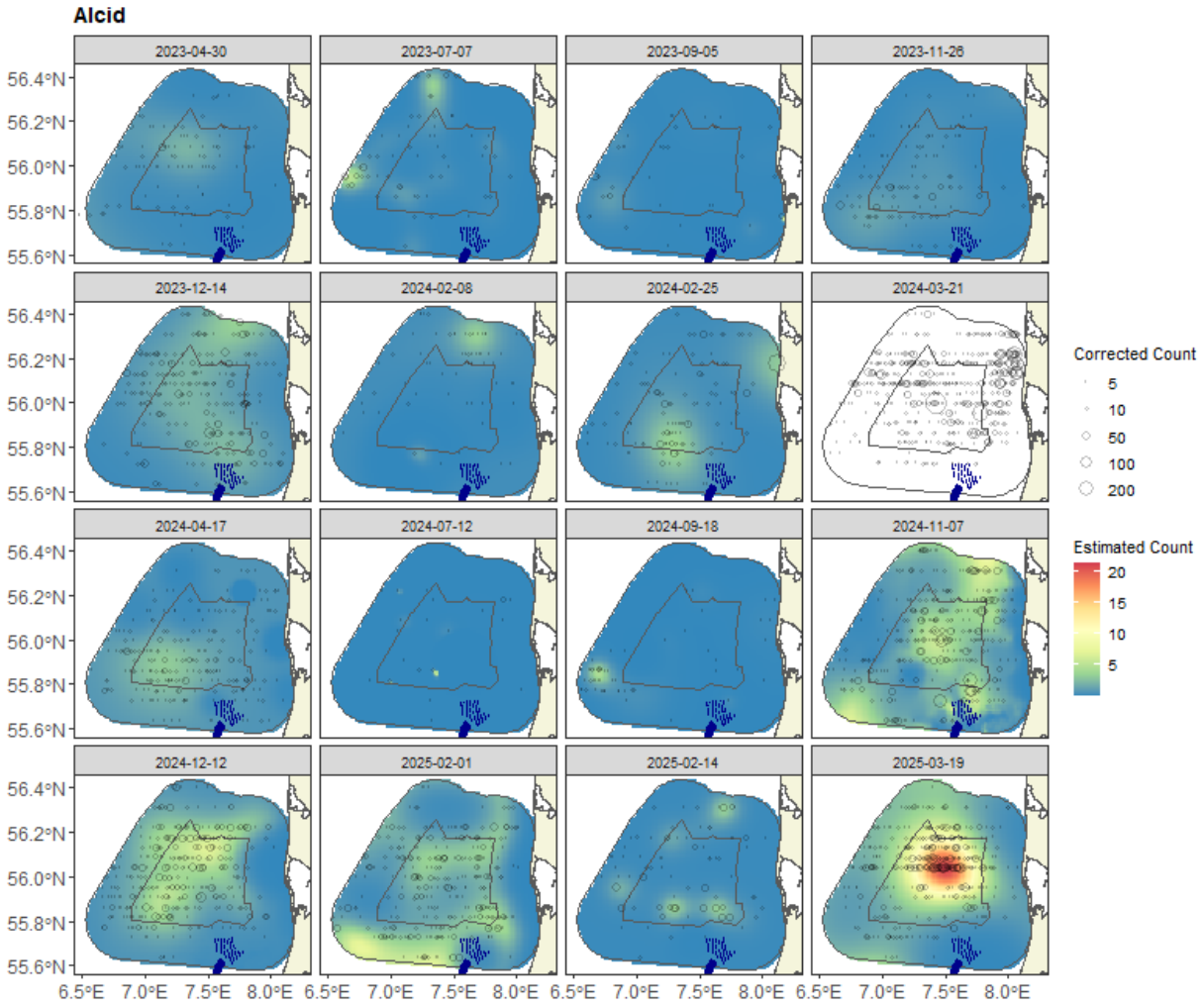

Figure 3-88. Figure showing the estimated razorbills/common guillemots' abundance across the NSI survey area for each of the 16 Y1 and Y2 surveys conducted. The estimated numbers are per 1 km x 1 km grid cell. The open circles represent the distance-corrected counts. The March 2024 survey is omitted from this figure to allow for more detail in the other surveys. White areas indicate data intentionally omitted from one or more surveys with exceptionally high abundances to allow finer detail to be seen in lower-density distributions.

3.1.8.8 Areas of persistence

Figure 3-89 and Figure 3-90 show the persistence across the Y1 and Y2 surveys. The distribution of razorbills/common guillemots can vary considerably between surveys. This is shown by the moderate to low persistence across the survey area seen in the Y1 surveys. In Y2, the persistence is similarly distributed but higher, particularly in the proposed wind farm area. This indicates greater consistency in the distribution of birds during the Y2 surveys. The highest persistence occurs in the map for the Y2 surveys in the central and southern regions (~ 80%).

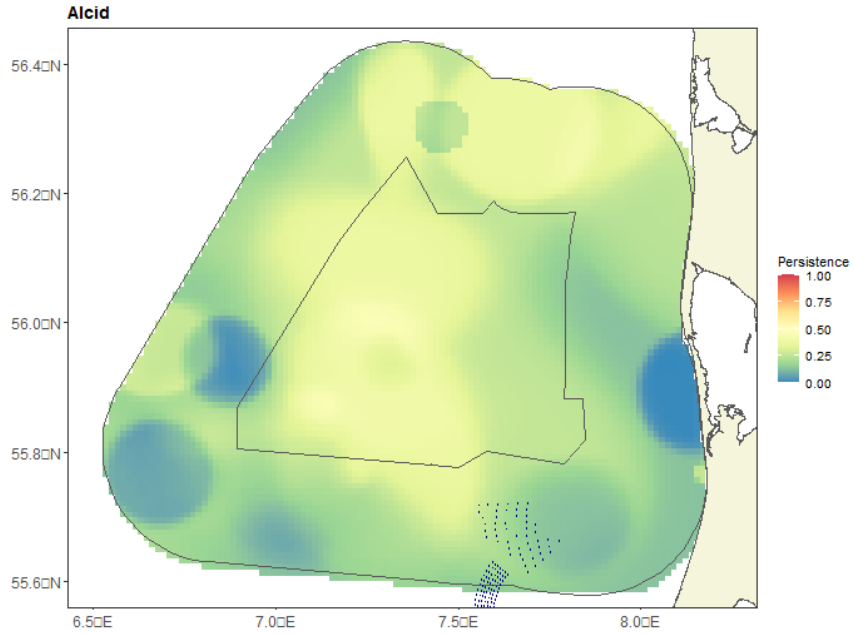

Figure 3-89. Persistence scores for razorbill/common guillemot across the eight Y1 surveys. The polygons represent the NSI pre-investigation area and the NSI survey area (black lines).

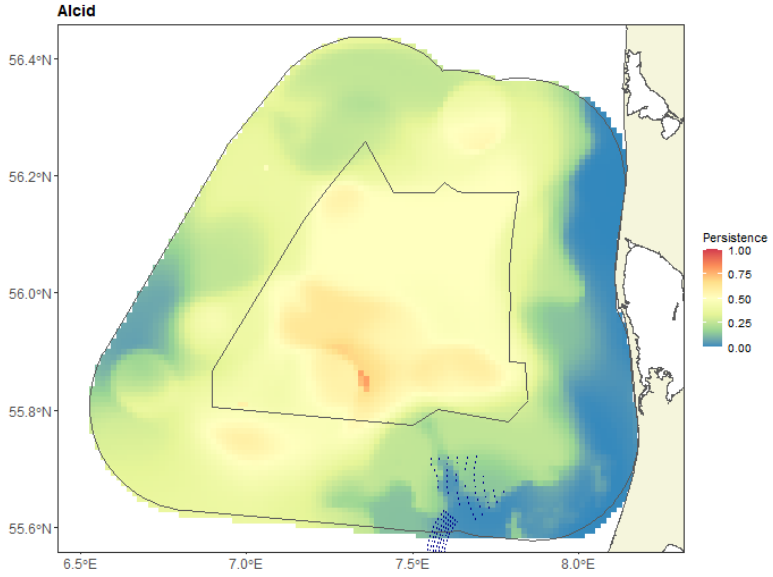

Figure 3-90. Persistence scores for razorbill/common guillemot across the eight Y2 surveys. The polygons represent the NSI pre-investigation area and the NSI survey area (black lines).

Figure 3-91 shows the persistence across all 16 Y1 and Y2 surveys. As expected, given the distributional differences of the separate persistence maps, the overall persistence is highest in the central region and in the south (but inside) of the proposed wind farm area. The highest persistence is ~61%.

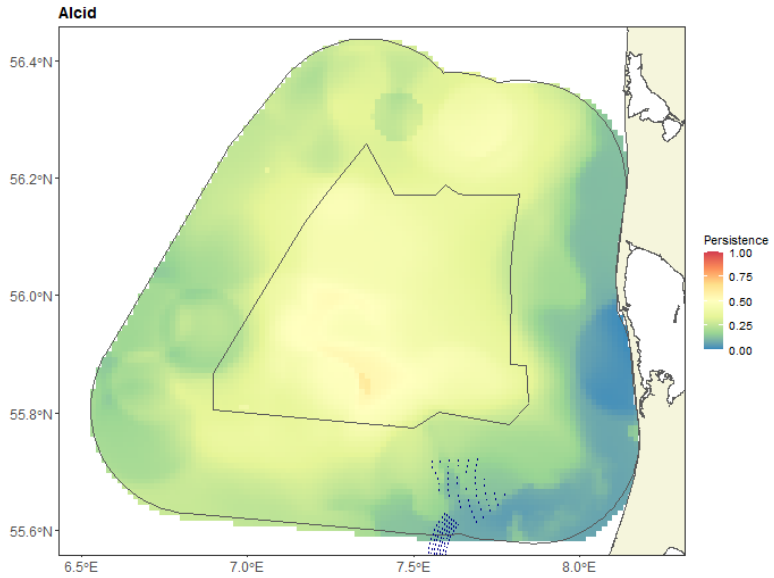

Figure 3-91. Persistence scores for razorbills/common guillemots across all 16 Y1 and Y2 surveys. The polygons represent the NSI pre-investigation area and the survey area (black lines).

3.2 Ship-based surveys

The 16 ship-based surveys conducted within the NSI pre-investigation area during Y1 and Y2 yielded a total of 8,159 observations, comprising 21,304 individual birds from 131 species or species groups (Table 3-17). On average, each survey resulted in 510 (±199 SD) observations of 1,332 (±944 SD) individuals and 34 (±14 SD) species or species groups, highlighting the consistency of data collection across surveys. A comprehensive list of all species and species groups observed during the Y1 and Y2 surveys is provided in 3B4BAppendix 5.

Table 3-17. Results of the 16 ship-based surveys conducted in the NSI pre-investigation area during Y1 (April 2023 to March 2024) and Y2 (April 2024 to March 2025). The table shows the number of observations (N = 8,159) made, as well as the number of individuals (N = 21,304) and species or species groups (N = 131) observed. An overview of the results at each observation position can be found in Table 0-4, Table 0-5 and Table 0-6 in 3B4BAppendix 4.

Survey ID	Survey month	Observations	Individuals	Species
S01	April 2023	638	1,418	39
S02	May 2023	394	751	47
S03	June 2023	465	790	20
S04	August 2023	493	1,489	30
S05	September 2023	578	1,193	50
S06	October 2023	292	433	38
S07	December 2023	418	1,763	16
S08	February 2024	168	250	15
S09	April 2024	715	1,288	38
S10	Mau 2024	378	685	40
S11	June 2024	350	629	17
S12	August 2024	698	3,393	49
S13	September 2024	859	3,145	59

Survey ID	Survey month	Observations	Individuals	Species
S14	October 2024	861	2,531	48
S15	December 2024	392	791	19
S16	February/March 2025	460	755	21
Total	-	8,159	21,304	131

Overall, Y2 (S09-S16) contributed a greater volume of data, with a higher total number of observations (37%), individuals (63%), and species (23%). This increase reflects both improved survey conditions and the modest expansion in total observation hours.

Furthermore, survey success was distributed equally across the three observation positions, with each position contributing a comparable number of observations (Table 0-4, 3B4BAppendix 4), individuals (Table 0-5, 3B4BAppendix 4) and species (Table 0-6, 3B4BAppendix 4). The relative uniformity in spatial sampling ensured that the resulting dataset was well suited for spatial comparisons of abundance, flight behaviour and composition. These are detailed in the following sections.

3.2.1 Migration magnitude

Across the 16 ship-based surveys, observers recorded 12,251 individual birds from 107 species migrating through transects at the North, Southwest, and Southeast observation points. Of these, 4,078 were observed in Y1 and 8,173 in Y2. Migration intensity and its temporal and directional distribution varied significantly by observation position and survey year, highlighting both spatial and temporal dynamics in diurnal bird migration.

3.2.1.1 Migration intensity

Migration intensity, expressed as the number of individuals observed per hour of observation effort, varied considerably between survey years, observation positions, and individual surveys. Across all 16 surveys, the overall mean migration intensity was 14 (±7.3 SD) individuals/hour, with values ranging from 4.5 to 26 individuals/hour.

During Y1 (S01-S08), migration intensity remained relatively low across all observation positions (Figure 3-92). At the North position, values ranged from approximately 3.8 to 11 individuals/hour, with a gradual increase over the survey period, peaking in September (S05) and again in February (S08). However, the North position was not surveyed during the April survey (S01). The Southeast position followed a similar pattern, starting with a moderate peak in migration intensity during April (S01) and reaching its highest intensity of 18 individuals/hour in December (S07). In contrast, the highest survey-specific migration intensity of 20 individuals/hour was observed at the Southwest position in April (S01), followed by a fluctuating but generally moderate intensity across the remaining surveys. However, the Southwest position was not surveyed during the October survey (S06).

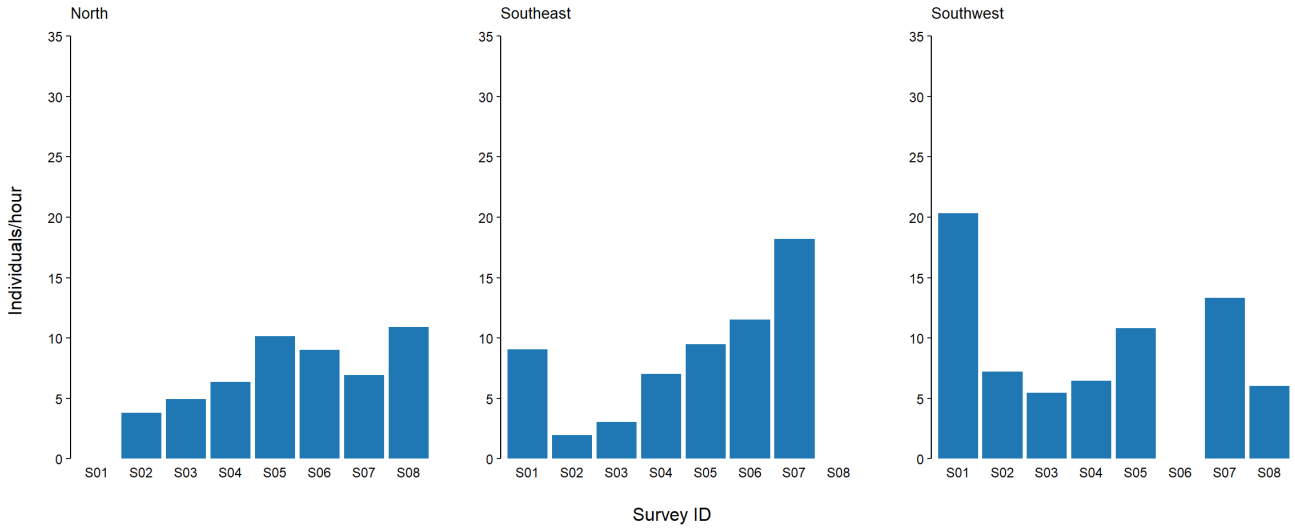

Figure 3-92. Migration intensity recorded during each of the eight ship-based surveys conducted in the NSI pre-investigation area during Y1 (April 2023-March 2024). The figure shows the number of individuals observed per hour of survey effort at each observation position (N = 4,078). Note that the North and Southwest positions were not surveyed during the S01 and S06 surveys, respectively.

In Y2 (S09-S16), migration intensity increased markedly at all three observation positions (Figure 3-93). The North position had its highest activity in September (S13) at 31 individuals/hour, while the Southeast position had the highest activity in October (S14) at 30 individuals/hour. The Southwest position showed the most concentrated migration activity during September (S13) and October (S14), reaching 30 and 25 individuals/hour, respectively.

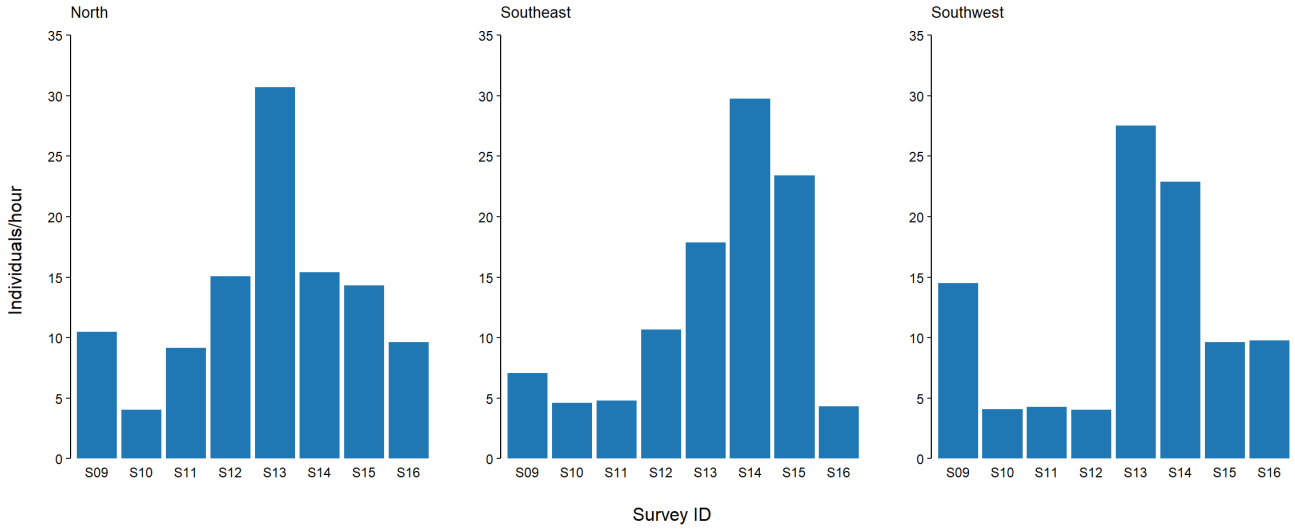

Figure 3-93. Migration intensity recorded during each of the eight ship-based surveys conducted in the NSI pre-investigation area during Y2 (April 2024-March 2025). The figure shows the number of individuals observed per hour of survey effort at each observation position (N = 8,173).

Overall, most high-intensity migration events occurred between September and October, indicating a broad seasonal peak in migratory activity during early autumn. This pattern was consistent across all three observation positions and

both survey years, suggesting that this period represents the core passage window for the dominant migrating species in the NSI pre-investigation area.

3.2.1.2 Temporal distribution

Migration occurred across all daylight hours, but some differences in activity levels were observed across day length and between survey years (Figure 3-94).

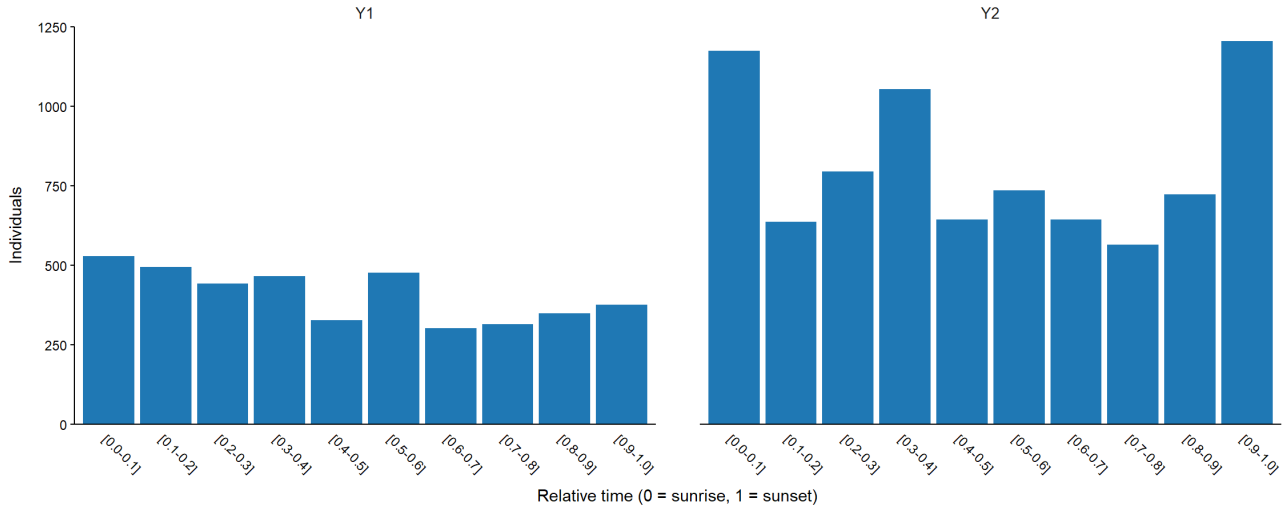

Figure 3-94. Migration intensity recorded during the ship-based surveys conducted in the NSI pre-investigation area during Y1 (N = 4,078) and Y2 (N = 8,173). The figure shows the number of individuals observed normalised relative to the day length (i.e., the period between sunrise and sunset).

During Y1, migration activity was evenly distributed throughout the day, with only moderate variation between time intervals (Figure 3-94). A slight increase was observed right after sunrise and again at midday. However, activity remained low. In contrast, the temporal distribution of migratory activity followed a clear diurnal pattern during Y2 (Figure 3-94). Migration intensity increased in the early morning, peaking in the hours after sunrise. This was followed by a gradual decline in activity through the afternoon. A second, pronounced peak was recorded right before sunset, primarily caused by a single observation of 800 lesser black-backed gulls.

3.2.1.3 Directional distribution

Flight direction data, grouped into 45-degree compass bins, revealed clear inter-annual, seasonal, and spatial patterns in bird migration orientation. Overall, migration occurred across a wide range of directions but followed consistent seasonal and spatial patterns across observation positions. Spring migration was generally dominated by movements toward the NE, especially at the Southwest and Southeast observation positions. Autumn migration showed a broader spread of directions, with pronounced peaks toward the southeast (SE), south (S), and southwest (SW) at all observation positions, suggesting more variable southbound departure routes. Summer and winter migration activity was more limited overall and showed less consistent movement. While these general seasonal patterns were consistent, there was notable inter-annual variation in the concentration and distribution of flight directions.

During Y1, migration patterns were generally less concentrated, with birds observed flying in a wide range of directions (Figure 3-95). At the North observation position, flight directions were broadly distributed. During autumn migration, increased activity was observed toward the SE, S, and SW, while a smaller peak toward the NW was evident during spring. In winter, a modest increase in flight direction toward the NE suggested possible coastal movement along the North Sea. At the Southeast observation position, a clear peak in flight activity occurred toward the NE

during spring migration, with a smaller increase toward the NW. In autumn, additional but less pronounced activity was observed toward the SE and SW, indicating a broader spread of southbound movements. At the Southwest observation position, flight directions were more strongly concentrated. A dominant peak toward the NE during spring migration accounted for most individuals observed at this position. During the autumn migration, a broader peak extending from SE to SW indicated the use of a wider corridor during return migration.

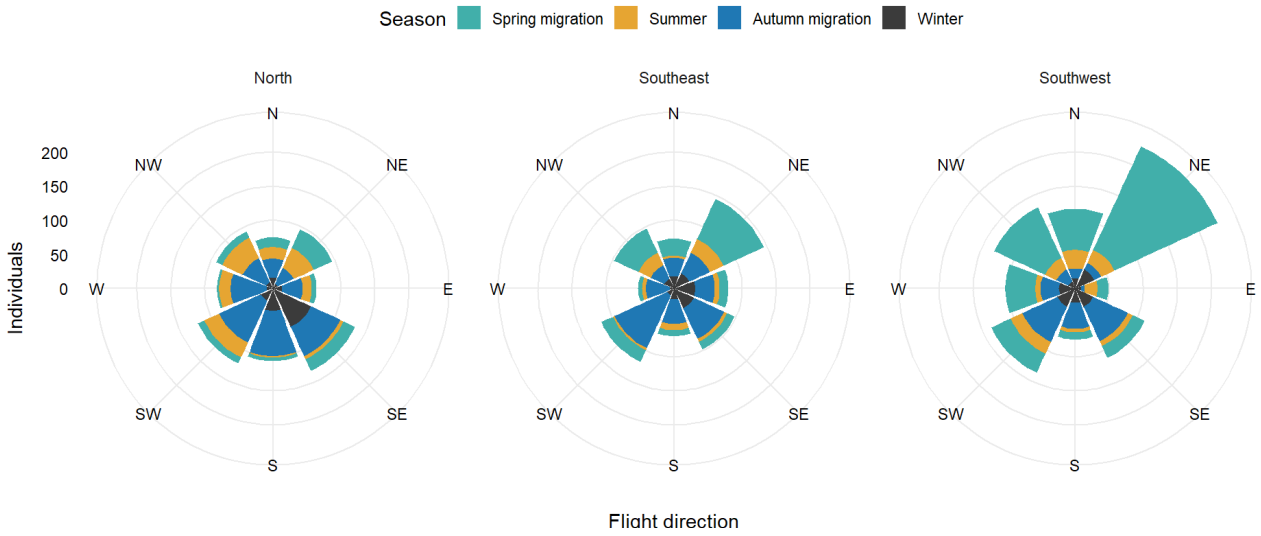

Figure 3-95. Flight direction of migrating birds recorded at each observation position during the eight ship-based surveys conducted in the NSI pre-investigation area during Y1 (April 2023-March 2024). The figure shows the total number of individuals observed in each 45° compass bin (N = 2,456).

In contrast, Y2 exhibited more structured and multidirectional migration patterns, with clearer seasonal patterns (Figure 3-96). At the North observation position, flight directions were more seasonally defined than in the previous survey year. During spring migration, most birds flew toward the NE. During the autumn migration, strong directionality toward both the SE and SW were observed, indicating the use of multiple southbound routes. During winter, fewer individuals were recorded, but flight directions showed concentrations toward the NW and SW. At the Southeast observation position, most birds migrated toward the NE and E during the spring migration, like the first survey year. In autumn, distinct peaks in migration were recorded toward the SE, S, and SW, indicating a stronger directional preference for southern and southwestern routes. During winter, flight activity was less concentrated, though most individuals moved toward the NW and N. At the Southwest observation position, migration remained strong and directionally varied. During spring migration, birds again showed a peak toward the NE, though this was less pronounced than in the first year. During autumn migration, the most prominent peak was directed toward the SE, with additional activity observed toward the SW and W, suggesting broader use of southern and western pathways. During winter, flight directions remained dispersed, with continued movement toward SW and W.

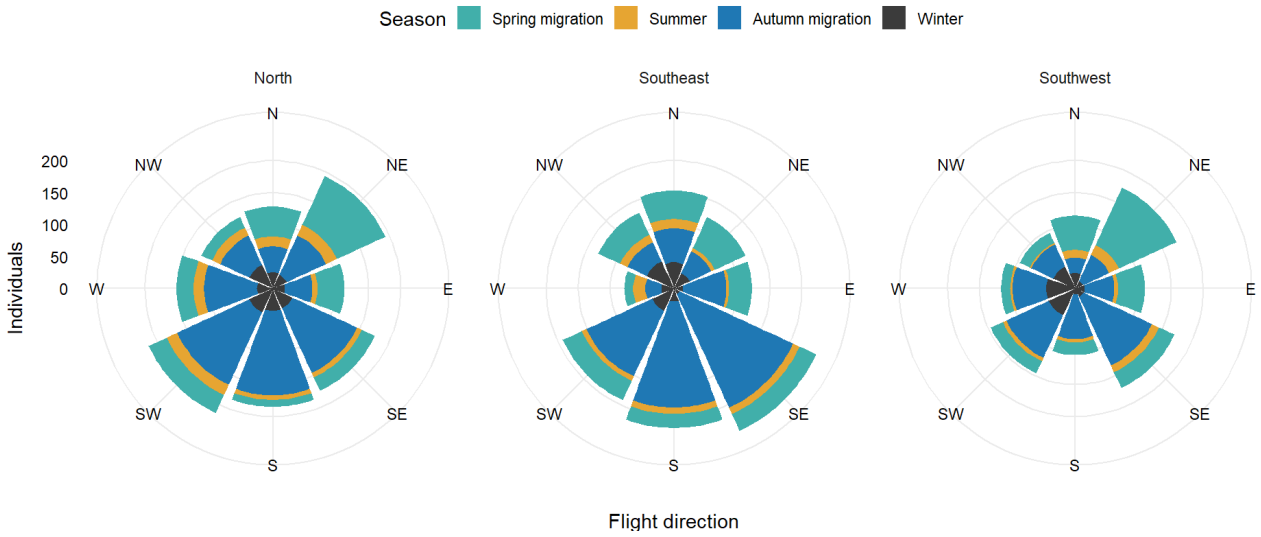

Figure 3-96. Flight direction of migrating birds recorded at each observation position during the eight ship-based surveys conducted in the NSI pre-investigation area during Y2 (April 2024-March 2025). The figure shows the total number of individuals observed in each 45° compass bin (N = 3,575).

3.2.2 Flight altitude

During the 16 ship-based surveys conducted in Y1 and Y2, a total of 7,627 flight altitudes were recorded, covering 15,338 individual birds from 124 species and an altitude range of 0 to 250 meters (Table 0-7). Of these altitude records, 399 (5.2%) were obtained through rangefinder measurement, while the remaining 7,228 (94.8%) were observer estimates.

Table 3-18. Flight altitude distribution of species groups recorded during the 16 ship-based surveys conducted in the NSI pre-investigation area during Y1 and Y2. The table shows the number of observations within each 25 m altitude interval for species groups with ten or more flight altitude records (N = 7,613).

Species group	Altitude interval (m)									
	0-25	26-50	51-75	76-100	101-125	126-150	151-175	176-200	201-225	226-250
Divers	136	16	1	0	0	0	0	0	0	0
Petrels	419	0	0	0	0	0	0	0	0	0
Gannets	934	176	19	3	0	0	0	0	0	0
Herons	8	3	0	0	0	0	0	0	0	0
Dabbling ducks	37	11	1	2	0	0	0	0	0	0
Sea ducks	84	3	0	0	0	0	0	0	0	0
Birds of prey	33	1	1	0	0	0	0	0	0	0
Plovers	51	3	2	1	0	0	0	0	0	0
Sandpipers	86	8	1	0	1	2	1	0	0	0
Skuas	50	3	0	2	0	0	0	0	0	1
Gulls	1,850	658	137	73	13	12	3	3	1	1
Kittiwakes	797	85	7	3	2	0	0	0	0	0
Terns	471	11	3	0	0	0	0	0	0	0

Species group	Altitude interval (m)									
	0-25	26-50	51-75	76-100	101-125	126-150	151-175	176-200	201-225	226-250
Auks	602	1	0	0	0	0	0	0	0	0
Swifts	55	7	0	0	0	0	0	0	0	0
Passerines	599	103	10	5	0	0	0	1	0	0
Total	6,212	1,089	182	89	16	14	4	4	1	2

Most individuals were recorded flying at lower altitudes, with 83% observed within the 0-25 m altitude interval, indicating a strong preference for near-surface flight (Table 3-18, Figure 3-97). For example, certain species groups, such as auks and petrels, were almost exclusively observed within this altitude interval. Although other groups, including gulls, exhibited a broader distribution across altitude intervals, observations of birds flying above 100 meters over the sea surface were rare (fewer than 1% were above 100 meters).

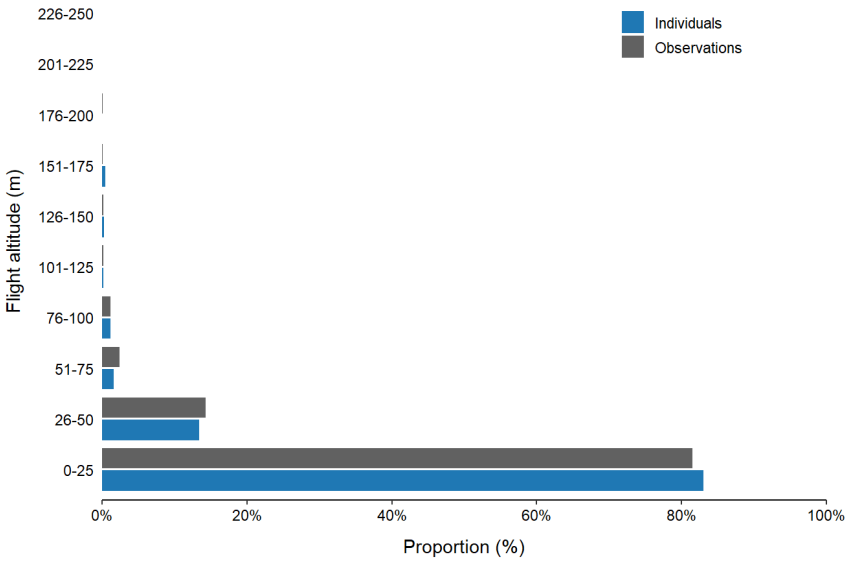

Figure 3-97. Flight altitude distribution of all birds observed during the 16 ship-based surveys conducted in the NSI pre-investigation area during Y1 and Y2. The figure shows the proportion (%) of individuals and observations recorded within each 25 m altitude interval.

The subsequent subchapters provide a detailed analysis of the flight altitude distribution of the species and species groups that were frequently observed during both Y1 and Y2.

3.2.2.1 Divers (Gaviidae)

This group comprised red-throated divers (*Gavia stellata*), black-throated divers (*Gavia arctica*), great northern divers (*Gavia immer*), and unidentified diver individuals (diver sp.), with red-throated diver being the most frequently recorded species (3B4BAppendix 5). A total of 82 diver flight altitudes were recorded, encompassing 118 individual birds. Most records were made of divers flying alone (74.5%) or in pairs (16.3%), with the largest flock observed containing five birds. All recorded flights occurred at altitudes below 75 meters, with most individuals (86.4%) flying at altitudes

below 25 meters (Figure 3-98), indicating a preference for near-surface flight. The highest recorded flight reached 70 meters and was made by a red-throated diver.

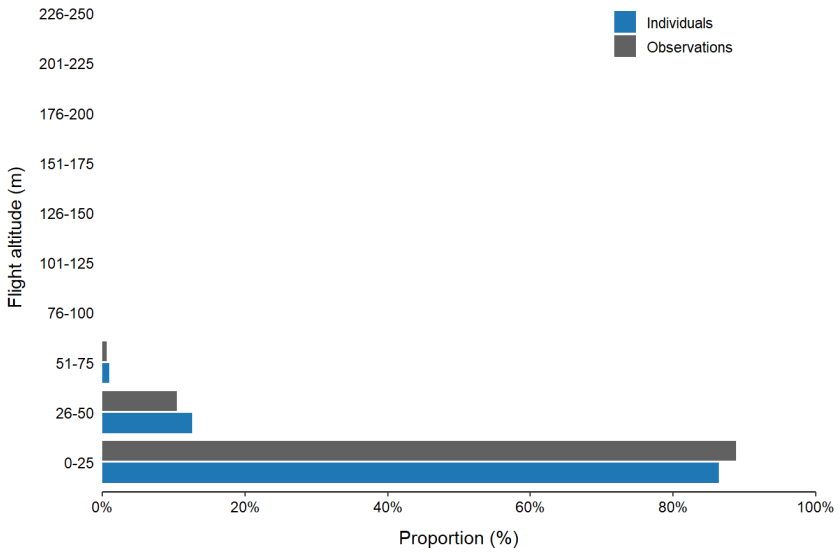

Figure 3-98. Flight altitude distribution of divers observed during the 16 ship-based surveys conducted in the NSI pre-investigation area during Y1 and Y2. The figure shows the proportion (%) of individuals (N = 118) and observations (N = 82) recorded within each 25 m altitude interval.

3.2.2.2 Fulmar (Fulmarus glacialis)

Flight altitude was recorded for 368 fulmar observations, comprising 422 individuals. Fulmars were almost exclusively observed flying alone (90.8%), with the largest flock recorded consisting of eight birds. Individuals predominantly flew close to the sea surface and were only recorded flying at altitudes below 25 meters, with the highest recorded flight altitude being 20 meters (Figure 3-99).

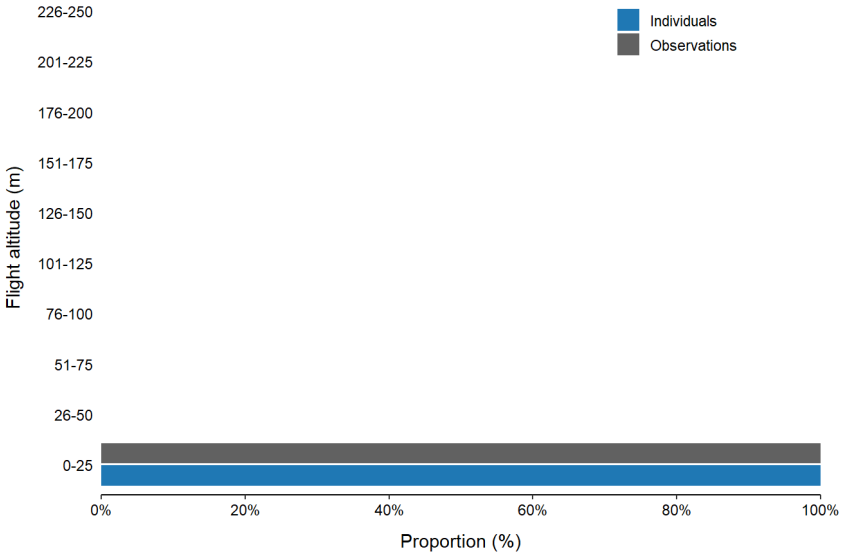

Figure 3-99. Flight altitude distribution of fulmars observed during the 16 ship-based surveys conducted in the NSI pre-investigation area during Y1 and Y2. The figure shows the proportion (%) of individuals (N = 422) and observations (N = 368) recorded within each 25 m altitude interval.

3.2.2.3 *Petrels (Procellariidae)*

This group excluded fulmar and comprised great shearwaters (*Ardenna gravis*), sooty shearwaters (*Ardenna grisea*), Manx shearwaters (*Puffinus puffinus*), storm petrels (*Hydrobates pelagicus*), and unidentified petrel individuals (petrel sp.), with sooty shearwater being the most frequently recorded species (3B4BAppendix 5). Flight altitude data for petrels included 51 records of 53 individual birds. Nearly all were recorded flying alone (96.1%), with only a small fraction (3.9%) recorded while flying in pairs. All individuals remained consistently close to the sea surface, with every flight recorded below 25 meters (Figure 3-100). The highest altitude recorded was 15 meters, reached by a sooty shearwater, which is consistent with that of fulmar.

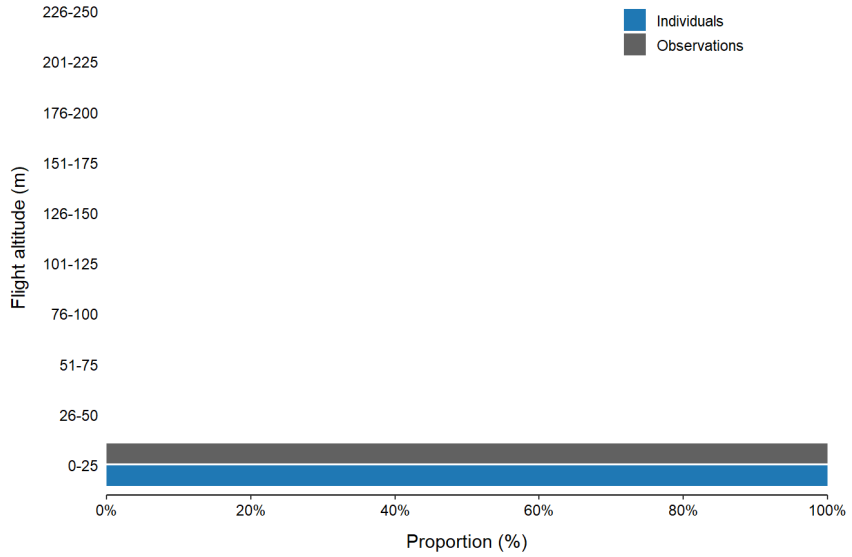

Figure 3-100. Flight altitude distribution of petrels observed during the 16 ship-based surveys conducted in the NSI pre-investigation area during Y1 and Y2. The figure shows the proportion (%) of individuals (N = 53) and observations (N = 51) recorded within each 25 m altitude interval.

3.2.2.4 *Gannet (Morus bassanus)*

Observers recorded 1,124 gannet flight events involving 1,255 individual birds. Of these, most were seen flying alone (82.7%) or in pairs (15.5%), with the largest flock recorded consisting of ten birds. All flights were recorded below 100 meters, and a substantial majority (82.7%) occurred under 25 meters (Figure 3-101), indicating a strong preference for near-surface flight. This low-altitude tendency was broadly consistent with the patterns seen in other large-bodied seabirds, such as divers, though gannets reached slightly higher maximum altitudes, with the highest recorded flight altitude being 80 meters.

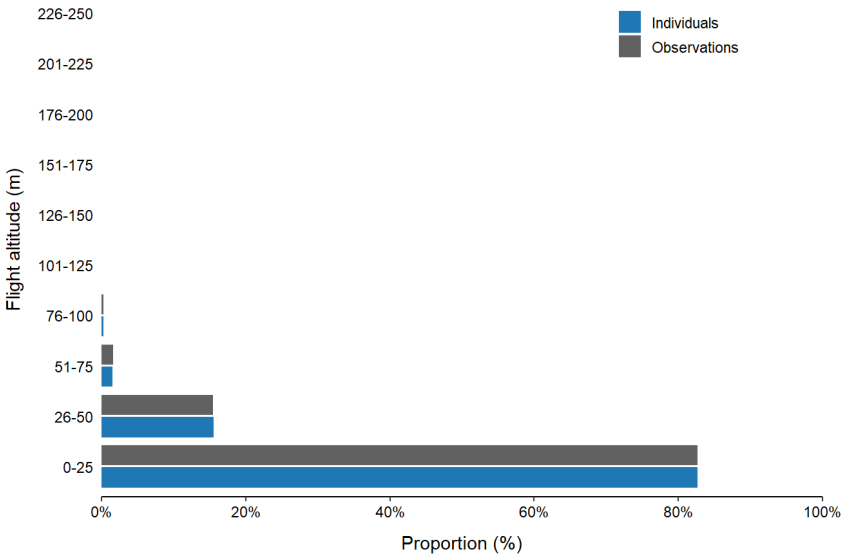

Figure 3-101. Flight altitude distribution of gannets observed during the 16 ship-based surveys conducted in the NSI pre-investigation area during Y1 and Y2. The figure shows the proportion (%) of individuals (N = 1,255) and observations (N = 1,124) recorded within each 25 m altitude interval.

3.2.2.5 Dabbling ducks (Anatinae)

This group comprised wigeons (*Mareca penelope*), teals (*Anas crecca*), mallards (*Anas platyrhynchos*), pintails (*Anas acuta*), shovelers (*Spatula clypeata*), and unidentified dabbling duck individuals (dabbling duck sp.), with teal being the most frequently recorded species (3B4BAppendix 5). Flight altitude data were collected from 51 observations covering 323 individual dabbling ducks. These birds were typically seen flying alone (31.4%) or in small flocks, with an average flock size of 6.3 individuals. The largest flock observed included 45 unidentified ducks. Most flight activity occurred below 25 meters (61.9%), though a notable portion of individuals flew between 26 and 100 meters (Figure 3-102). The highest altitude recorded was 100 meters, reached by an unidentified individual.

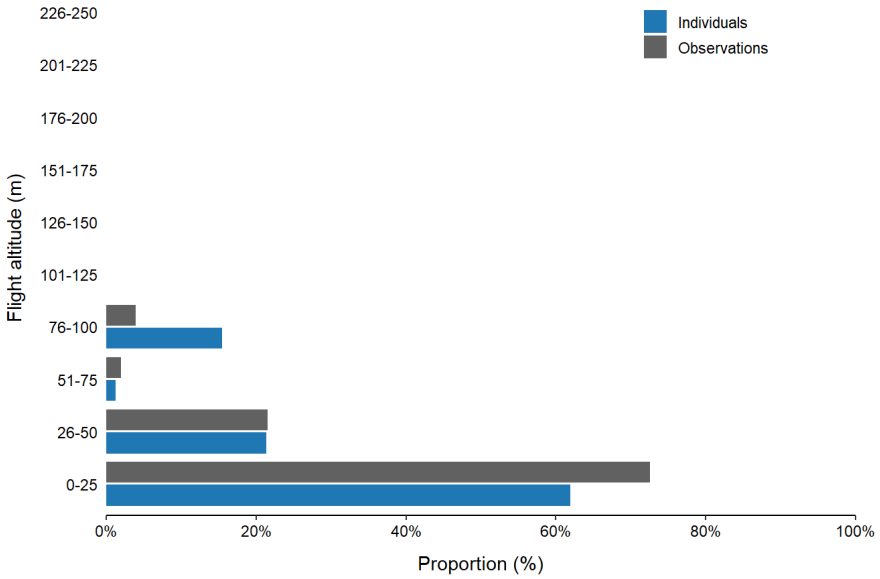

Figure 3-102. Flight altitude distribution of dabbling ducks observed during the 16 ship-based surveys conducted in the NSI pre-investigation area during Y1 and Y2. The figure shows the proportion (%) of individuals (N = 323) and observations (N = 51) recorded within each 25 m altitude interval.

3.2.2.6 *Common scoter (Melanitta nigra)*

Flight altitude was recorded during 81 observations involving 346 common scoters. These were generally seen in small flocks, averaging 4.3 individuals, with the largest flock recorded consisting of 39 birds. Nearly all common scoters (96.2%) were observed flying below 25 meters, and no individuals exceeded 50 meters in altitude (Figure 3-103). The highest flight recorded reached 35 meters, indicating a tendency toward low-altitude flight.

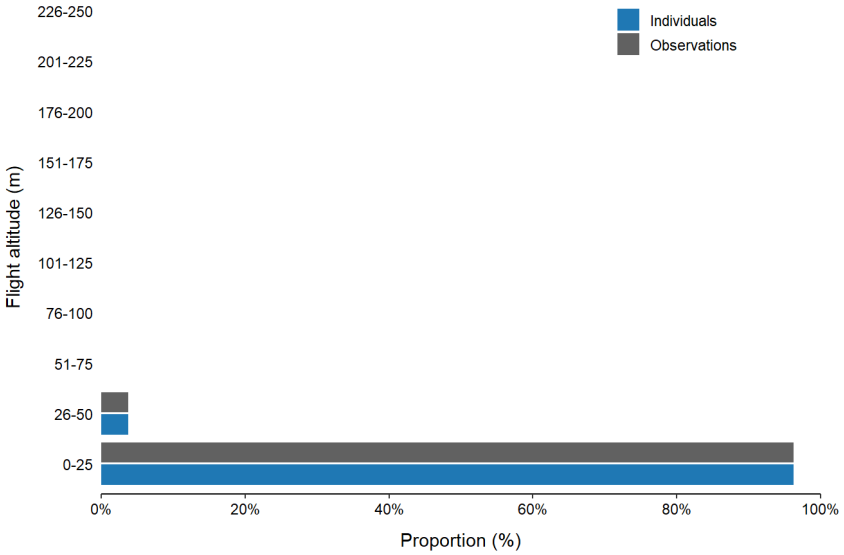

Figure 3-103. Flight altitude distribution of common scoters observed during the 16 ship-based surveys conducted in the NSI pre-investigation area during Y1 and Y2. The figure shows the proportion (%) of individuals (N = 346) and observations (N = 81) recorded within each 25 m altitude interval.

3.2.2.7 *Birds of prey*

This group comprised marsh harriers (*Circus aeruginosus*), sparrowhawks (*Accipiter nisus*), ospreys (*Pandion haliaetus*), kestrels (*Falco tinnunculus*), merlin (*Falco columbarius*), and unidentified falcon individuals (falcon sp.), with kestrel being the most frequently recorded species (3B4BAppendix 5). Flight altitude was recorded during 35 observations involving 37 individual birds of prey. Nearly all were observed flying alone (94.3%), though two records were made of sparrowhawks flying in pairs. The vast majority (94.6%) of birds of prey were seen below 25 meters, and no individuals exceeded 75 meters in altitude (Figure 3-104). The highest recorded flight was 55 meters, made by a kestrel.

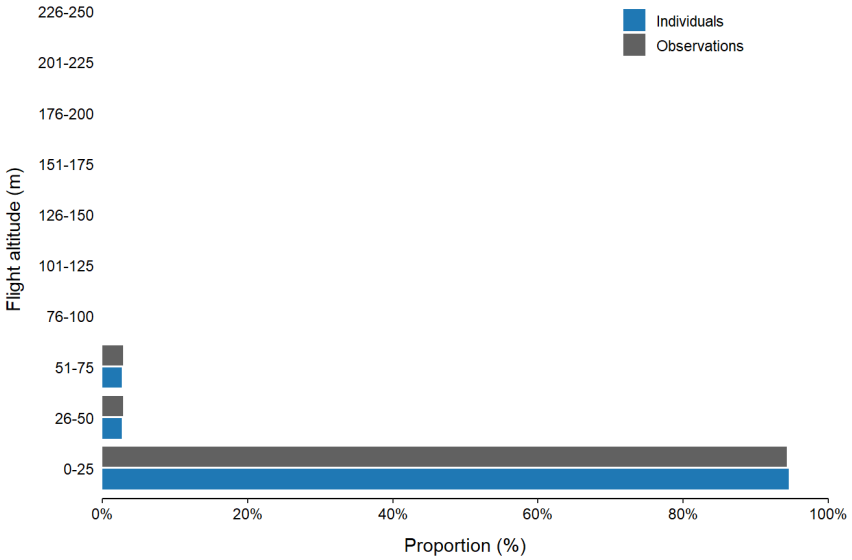

Figure 3-104. Flight altitude distribution of birds of prey observed during the 16 ship-based surveys conducted in the NSI pre-investigation area during Y1 and Y2. The figure shows the proportion (%) of individuals (N = 37) and observations (N = 35) recorded within each 25 m altitude interval.

3.2.2.8 Plovers (Charadriidae)

This group comprised ringed plovers (*Charadrius hiaticula*), golden plovers (*Pluvialis apricaria*) and grey plovers (*Pluvialis squatarola*), with golden plover being the most frequently recorded species (3B4BAppendix 5). Flight altitude data were gathered from 57 observations involving 248 individual plovers. Most were seen flying alone (24.6%) or in small flocks, averaging 4.4 individuals. The largest flock observed included 20 golden plovers. Most flights recorded (77%) occurred below 25 meters, with an additional 16.9% recorded between 26 and 50 meters (Figure 3-105). The highest altitude was 80 meters, recorded for a golden plover.

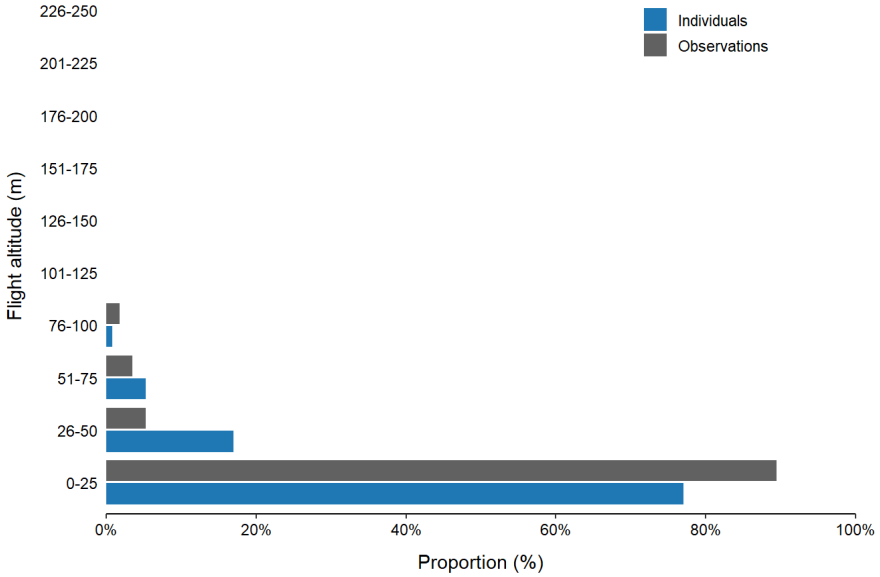

Figure 3-105. Flight altitude distribution of plovers observed during the 16 ship-based surveys conducted in the NSI pre-investigation area during Y1 and Y2. The figure shows the proportion (%) of individuals (N = 248) and observations (N = 57) recorded within each 25 m altitude interval.

3.2.2.9 *Sandpipers (Scolopacidae)*

This group comprised knots (*Calidris canutus*), sanderlings (*Calidris alba*), dunlins (*Calidris alpina*), common snipes (*Gallinago gallinago*), bar-tailed godwits (*Limosa lapponica*), whimbrels (*Numenius phaeopus*), curlews (*Numenius arquata*), redshanks (*Tringa totanus*), greenshanks (*Tringa nebularia*), wood sandpipers (*Tringa glareola*), common sandpipers (*Actitis hypoleucos*), turnstones (*Arenaria interpres*), and unidentified wader individuals (wader sp.). Of these, dunlin was the most frequently recorded species (3B4BAppendix 5). Flight altitude was recorded during 99 observations involving 370 individual sandpipers. Just over half (51.5%) were recorded while flying alone, with 12.1% in pairs and the remainder in flocks of up to 25 individuals. The average flock size was 4.4, like that observed in plovers. Furthermore, like plovers, sandpipers predominantly flew at low altitudes, with 81.1% recorded flying at altitudes below 25 meters. However, unlike plovers, whose maximum recorded altitude was 80 meters, sandpipers included individuals flying at much higher altitudes. The highest altitude recorded was 175 meters, reached by a curlew (Figure 3-106), suggesting more variable flight behaviour within this group.

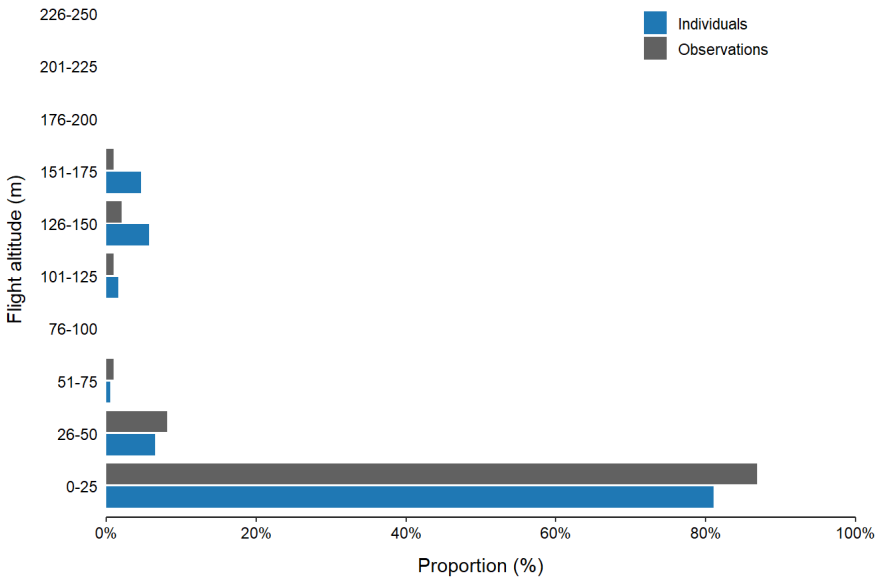

Figure 3-106. Flight altitude distribution of sandpipers observed during the 16 ship-based surveys conducted in the NSI pre-investigation area during Y1 and Y2. The figure shows the proportion (%) of individuals (N = 370) and observations (N = 99) recorded within each 25 m altitude interval.

3.2.2.10 *Skuas (Stercorariidae)*

This group comprised arctic skuas (*Stercorarius parasiticus*), great skuas (*Stercorarius skua*), and unidentified skua species (skua sp.), with arctic skua being the most frequently recorded species (3B4BAppendix 5). Flight altitude was recorded during 56 observations involving 58 individual skuas. These birds were almost always seen flying alone, with only a few instances of recorded paired flight. The majority (89.7%) were recorded flying at altitudes below 25 meters (Figure 3-107), reflecting a strong tendency toward low-altitude flight like many other pelagic seabirds. However, skuas also demonstrated the greatest vertical range in the dataset, with an unidentified individual recorded flying at 250 meters - the highest altitude recorded across all species in the analysis.

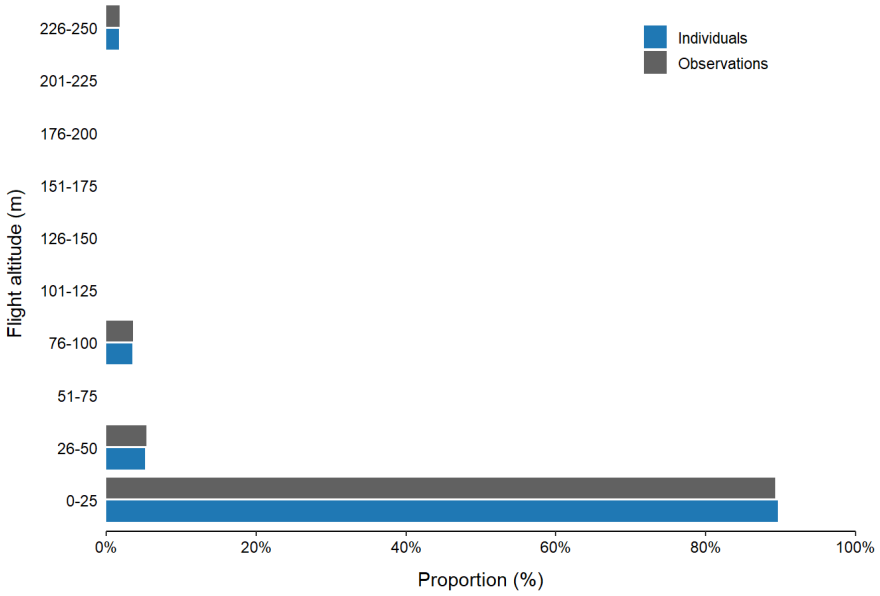

Figure 3-107. Flight altitude distribution of skuas observed during the 16 ship-based surveys conducted in the NSI pre-investigation area during Y1 and Y2. The figure shows the proportion (%) of individuals (N = 58) and observations (N = 56) recorded within each 25 m altitude interval.

3.2.2.11 Little gull (Hydrocoloeus minutus)

In total, flight altitude was recorded during 200 observations of 340 individuals. Little gulls were most often recorded while flying alone (66.5%) or in pairs (17.5%), with a smaller fraction being recorded while flying in flocks of up to eight birds. Nearly all flights (97.9%) occurred below 50 meters, with the highest flight altitude recorded being 70 meters (Figure 3-108).

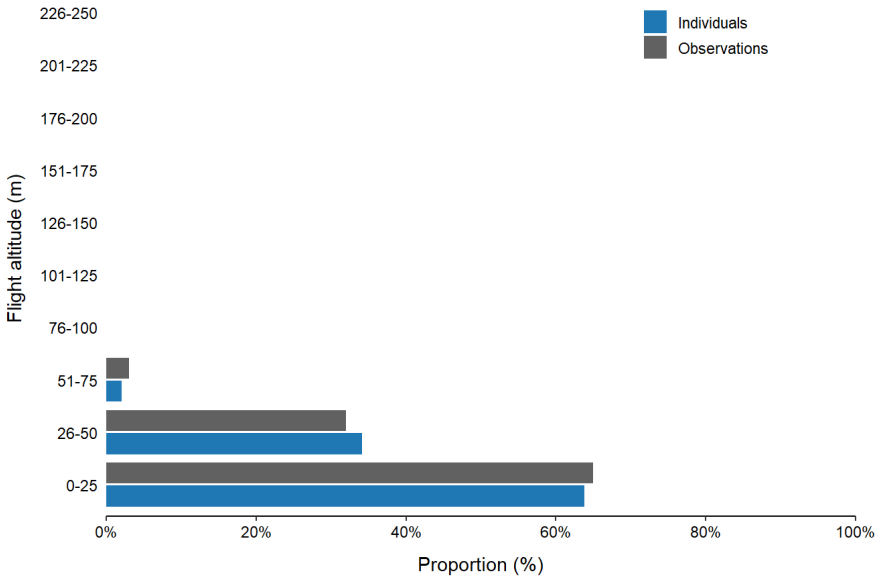

Figure 3-108. Flight altitude distribution of little gulls observed during the 16 ship-based surveys conducted in the NSI pre-investigation area during Y1 and Y2. The figure shows the proportion (%) of individuals (N = 340) and observations (N = 200) recorded within each 25 m altitude interval.

3.2.2.12 *Common gull (Larus canus)*

Flight altitude data were collected from 523 observations of common gulls, covering 852 individuals. These birds were most often observed flying alone (78%) or in pairs (14%), with an average flock size of 1.6. The largest flock recorded included 46 individuals. Like little gulls, common gulls showed a strong tendency for low-altitude flight, with 94.1% observed below 50 meters and 80% flying under 25 meters (Figure 3-109). However, common gulls exhibited a broader vertical range, with the highest recorded flight reaching 150 meters, more than twice that of the little gull.

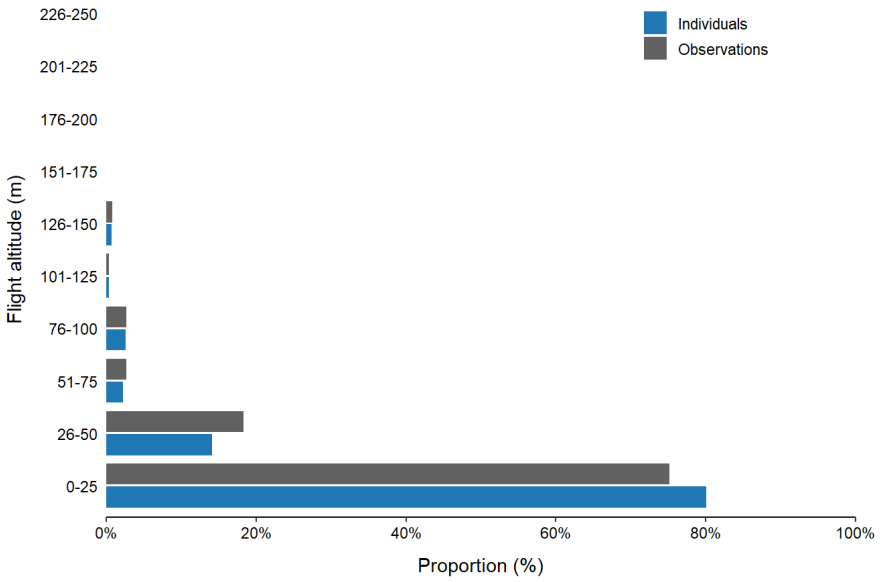

Figure 3-109. Flight altitude distribution of common gulls observed during the 16 ship-based surveys conducted in the NSI pre-investigation area during Y1 and Y2. The figure shows the proportion (%) of individuals (N = 852) and observations (N = 523) recorded within each 25 m altitude interval.

3.2.2.13 *Lesser black-backed gull (Larus fuscus)*

Flight altitude was recorded during 1,190 observations involving 2,587 lesser black-backed gulls, making it one of the most frequently recorded species in the dataset. Most individuals were observed flying alone (84.6%) or in pairs (8.7%), though some flocks were substantially larger, with the largest comprising up to 800 birds. The species showed a strong preference for low-altitude flight, with 95.1% of individuals recorded below 50 meters (Figure 3-110). A few were observed flying between 51 and 150 meters, and the highest altitude reached was 200 meters. Compared to other gull species, lesser black-backed gulls demonstrated both a wider range of flock sizes and a greater vertical flight range.

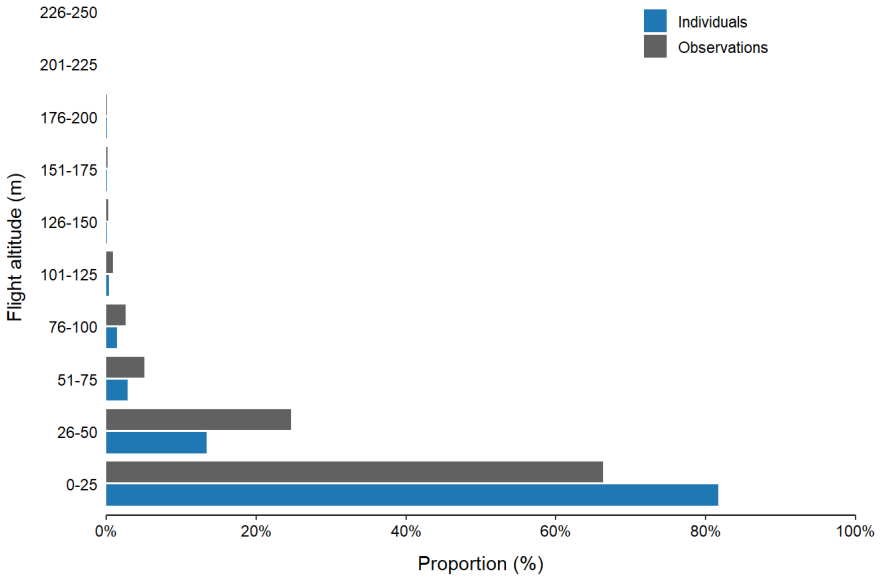

Figure 3-110. Flight altitude distribution of greater black-backed gulls observed during the 16 ship-based surveys conducted in the NSI pre-investigation area during Y1 and Y2. The figure shows the proportion (%) of individuals (N = 2,587) and observations (N = 1,190) recorded within each 25 m altitude interval.

3.2.2.14 Herring gull (Larus argentatus)

Flight altitude was recorded during 447 observations involving 539 herring gulls. The vast majority were seen flying alone (89.5%), and the largest flock recorded included 15 individuals. Most herring gulls (91.8%) were observed flying below 50 meters, with only a small number exceeding this altitude and none exceeding 150 meters. (Figure 3-111).

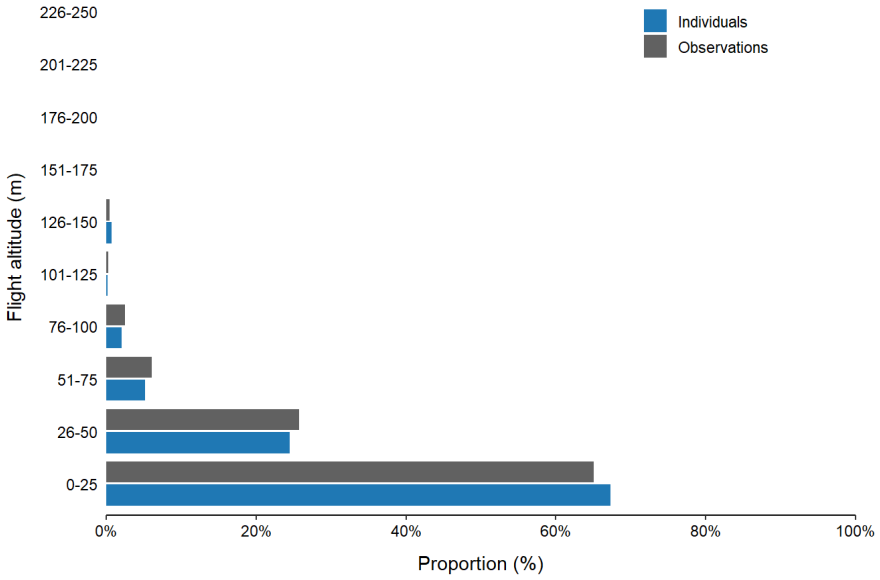

Figure 3-111. Flight altitude distribution of herring gulls observed during the 16 ship-based surveys conducted in the NSI pre-investigation area during Y1 and Y2. The figure shows the proportion (%) of individuals (N = 539) and observations (N = 447) recorded within each 25 m altitude interval.

3.2.2.15 *Great black-backed gull (Larus marinus)*

In total, flight altitude was recorded during 233 observations of 275 great black-backed gulls. The majority were observed flying alone (89.3%) or in pairs (7.3%), with the largest flock comprising just five individuals. Most flights (91.7%) occurred below 50 meters, though a few individuals were recorded between 51 and 100 (Figure 3-112). Like other large gulls, great black-backed gulls showed a preference for low-altitude flight, with the highest recorded flight altitude being 200 meters.

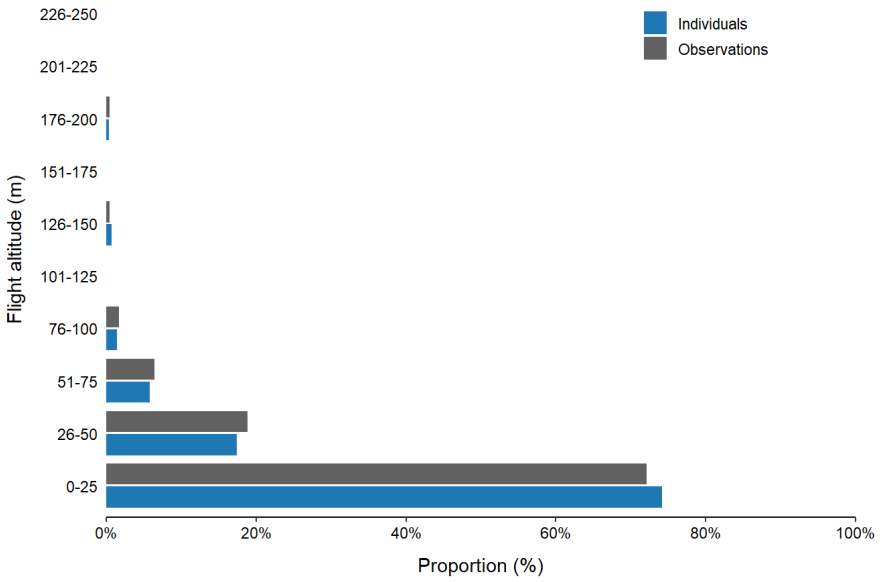

Figure 3-112. Flight altitude distribution of lesser black-backed gulls observed during the 16 ship-based surveys conducted in the NSI pre-investigation area during Y1 and Y2. The figure shows the proportion (%) of individuals (N = 275) and observations (N = 233) recorded within each 25 m altitude interval.

3.2.2.16 *Kittiwake (Rissa tridactyla)*

In total, flight altitude was recorded during 894 observations of kittiwakes, encompassing 1,228 individuals. Kittiwakes were predominantly observed flying alone (80.8%) or in pairs (12.1%), with only a small number of altitude records being made of individuals flying in flocks. The largest kittiwake flock recorded consisted of 30 individuals. Kittiwakes exhibited a strong preference for low-altitude flight, with 91.6% of individuals flying below 25 meters and no flight exceeding 120 meters (Figure 3-113).

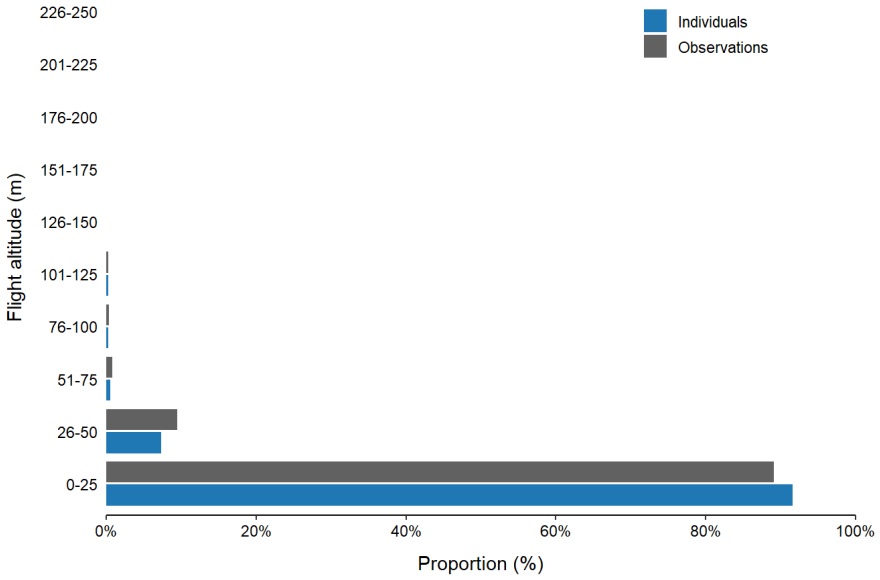

Figure 3-113. Flight altitude distribution of kittiwakes observed during the 16 ship-based surveys conducted in the NSI pre-investigation area during Y1 and Y2. The figure shows the proportion (%) of individuals (N = 1,228) and observations (N = 894) recorded within each 25 m altitude interval.

3.2.2.17 Gulls (Larus sp.)

This group excluded the gull species that were analysed individually and comprised Mediterranean gulls (*Ichthyaetus melanocephalus*), black-headed gulls (*Chroicocephalus ridibundus*), yellow-legged gulls (*Larus michahellis*), Caspian gulls (*Larus cachinnans*), and unidentified gull individuals (gull sp.) (3B4BAppendix 5). Flight altitude was recorded during 158 observations involving 242 individuals. Most were seen flying alone (84.2%), with the largest flock recorded consisting of 30 unidentified gulls. Most flights (83.9%) occurred below 50 meters (Figure 3-114), consistent with patterns observed in the other gull species. However, this group exhibited a broader vertical range overall, with some individuals flying as high as 250 meters - the highest recorded altitude across all gulls and in the entire dataset. This suggests that while low-altitude flight remains typical, occasional high-altitude movement is more pronounced in this mixed-species group.

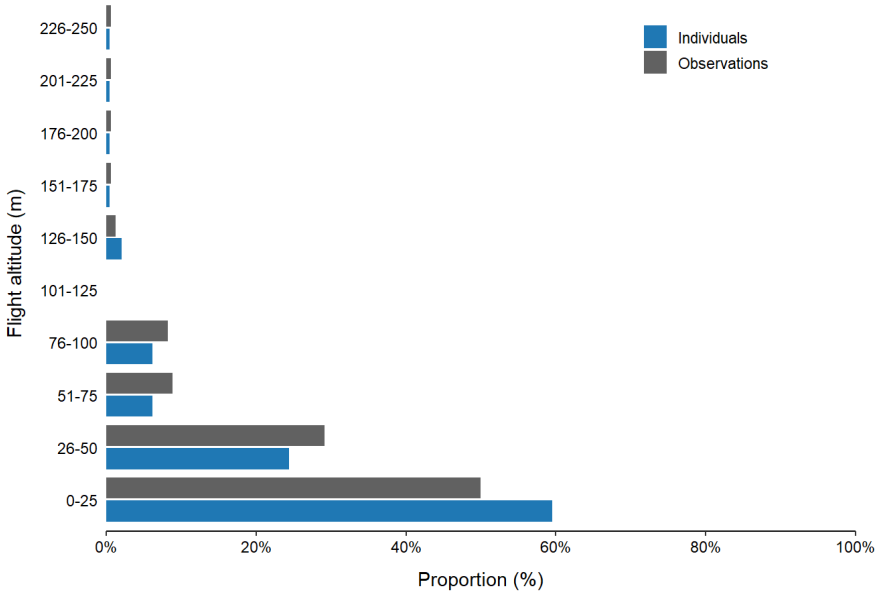

Figure 3-114. Flight altitude distribution of gulls observed during the 16 ship-based surveys conducted in the NSI pre-investigation area during Y1 and Y2. The figure shows the proportion (%) of individuals (N = 242) and observations (N = 158) recorded within each 25 m altitude interval.

3.2.2.18 Terns (Sterna sp.)

This group comprised sandwich terns (*Thalasseus sandvicensis*), common terns (*Sterna hirundo*), arctic terns (*Sterna paradisaea*), black terns (*Chlidonias niger*), and unidentified tern individuals (tern sp.), with common tern being the most frequently recorded species (3B4BAppendix 5). Tern flight altitudes were recorded during 485 observations involving 1,419 individuals. Nearly half were observed flying alone (49.1%), while the remainder formed small flocks with an average size of 2.9 individuals. The largest flock recorded included 32 common terns. Terns exhibited a strong preference for low-altitude flight, with 97.5% flying below 25 meters (Figure 3-115). The highest recorded flight reached 72 meters, made by a common tern. Compared to gulls, terns flew at consistently lower altitudes, with fewer individuals exceeding 50 meters.

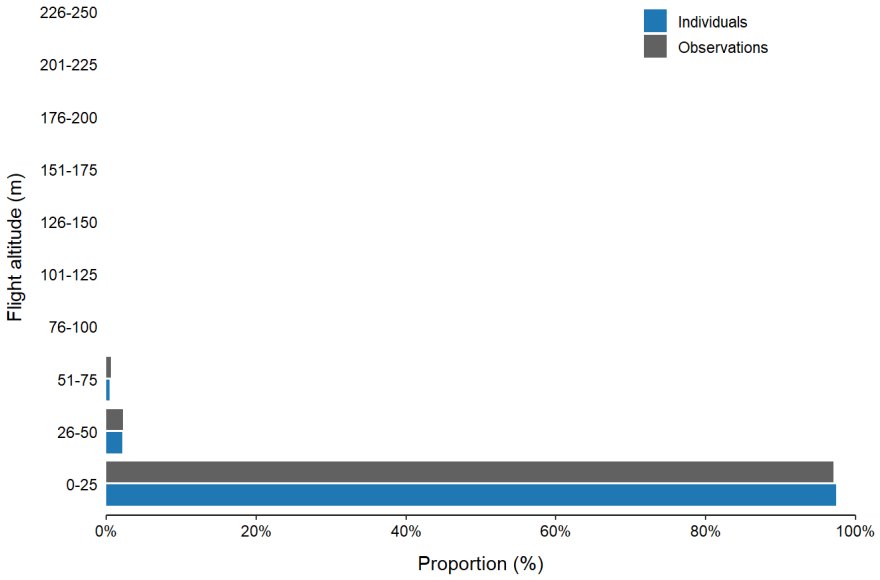

Figure 3-115. Flight altitude distribution of terns observed during the 16 ship-based surveys conducted in the NSI pre-investigation area during Y1 and Y2. The figure shows the proportion (%) of individuals (N = 1,419) and observations (N = 485) recorded within each 25 m altitude interval.

3.2.2.19 Auks (Alcidae)

This group comprised common guillemots (*Uria aalge*), razorbills (*Alca torda*), black guillemots (*Cepphus grylle*), little auks (*Alle alle*), and puffins (*Fratercula arctica*), with common guillemot being the most frequently recorded species (3B4BAppendix 5). Flight altitude was recorded during 603 observations involving 853 individual auks. Most were seen flying alone (79.3%) or in pairs (11.9%), with altitude records of flocks being relatively uncommon. The largest group recorded consisted of 20 common guillemots. Auks showed a strong preference for low-altitude flight, with 99.9% of individuals recorded below 25 meters (Figure 3-115). The highest flight observed was just 30 meters, made by a common guillemot, distinguishing auks from most other seabird groups in the dataset.

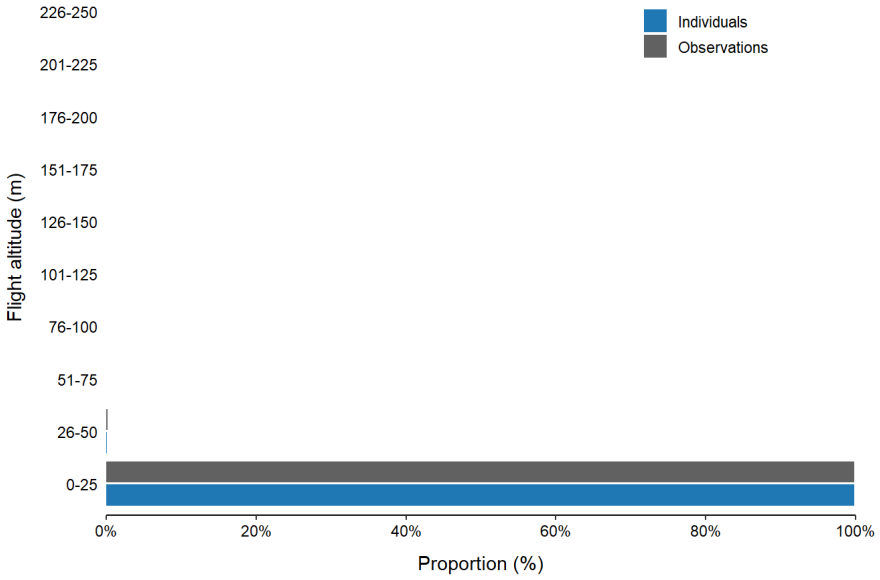

Figure 3-116. Flight altitude distribution of auks observed during the 16 ship-based surveys conducted in the NSI pre-investigation area during Y1 and Y2. The figure shows the proportion (%) of individuals (N = 853) and observations (N = 603) recorded within each 25 m altitude interval.

3.2.2.20 Swift (Apus apus)

In total, flight altitude was recorded during 62 observations of 112 individual birds. Swifts were predominantly observed flying alone (58.1%) or in pairs (24.2%). Only a small number of altitude records were made of individuals flying in flocks, and the largest flock consisted of seven individuals. Despite being a highly aerial species capable of sustained flight, swifts were predominantly recorded flying at low altitudes, with 92.9% of individuals below 25 meters and the highest recorded flight altitude being 41 meters (Figure 3-117).

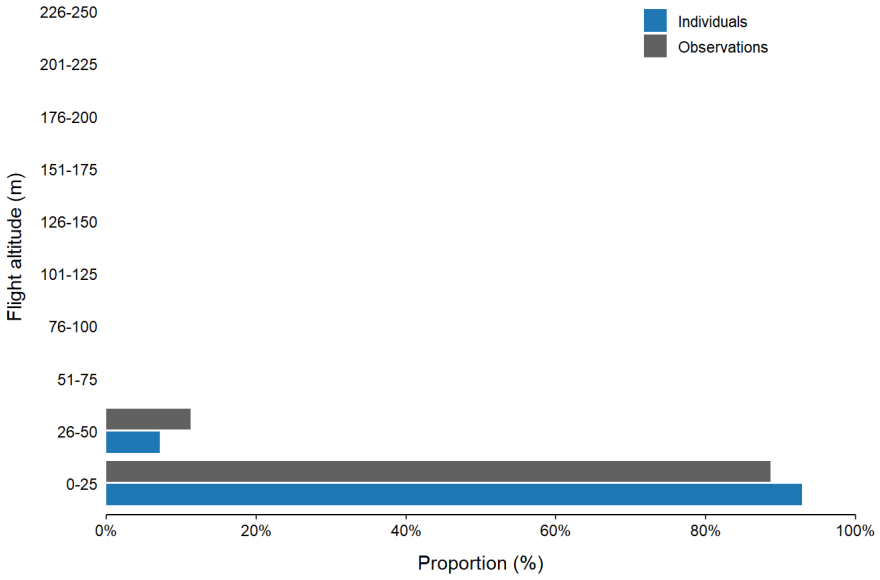

Figure 3-117. Flight altitude distribution of swifts observed during the 16 ship-based surveys conducted in the NSI pre-investigation area during Y1 and Y2. The figure shows the proportion (%) of individuals (N = 112) and observations (N = 62) recorded within each 25 m altitude interval.

3.2.2.21 *Passerines (Passeriformes)*

Passerines represented the largest and most taxonomically diverse species group included in the flight altitude analysis. This group encompassed a wide range of species, including wagtails, flycatchers, thrushes, and warblers. A comprehensive list of all species included in this group is provided in 3B4BAppendix 5. In total, flight altitude was recorded during 718 observations involving 3,427 individuals. Most passerines were observed flying alone (43.3%) or in small flocks, with an average flock size of 4.8 individuals. The largest passerine flock recorded consisted of 190 starlings. Passerines flew predominantly below 50 meters (99.3%), suggesting a preference for low-altitude flight across the group. The highest recorded altitude was 200 meters, reached by an unidentified individual (Figure 3-118).

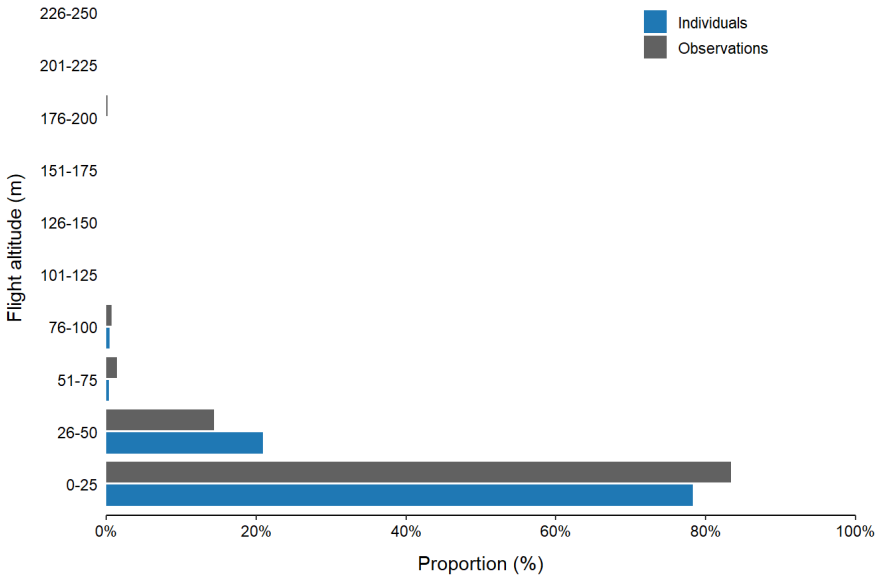

Figure 3-118. Flight altitude distribution of passerines observed during the 16 ship-based surveys conducted in the NSI pre-investigation area during Y1 and Y2. The figure shows the proportion (%) of individuals (N = 3,427) and observations (N = 718) recorded within each 25 m altitude interval.

3.2.3 Species composition

Species composition within divers (Gaviidae), gulls (Larinae excluding kittiwakes), terns (*Sterna* sp.), and auks (Alcidae) was analysed separately for each survey year and observation position to assess spatial and inter-annual variation. These groups were selected due to common identification challenges during aerial surveys, and composition ratios derived from ship-based observations provided valuable insight into likely species composition.

3.2.3.1 *Divers (Gaviidae)*

Diver observations were dominated by red-throated divers, which accounted for most individuals observed across all surveys (Table 3-19). In both years, this species consistently comprised 99% of all divers observed.

Table 3-19. Species composition of divers observed during the 16 ship-based surveys conducted in the NSI pre-investigation area during Y1 and Y2. The table shows the number and proportion of individuals for each species (N = 204).

Species	Individuals	Proportion (%)
Red-throated diver	202	99
Black-throated diver	1	0.5
Great northern diver	1	0.5

In Y1, red-throated divers made up the entire diver composition at both the North and Southwest observation positions throughout all surveys. At the Southeast position, a minor proportion of black-throated divers was observed during the early season, comprising one individual observed in the May survey (S02, Figure 3-119).

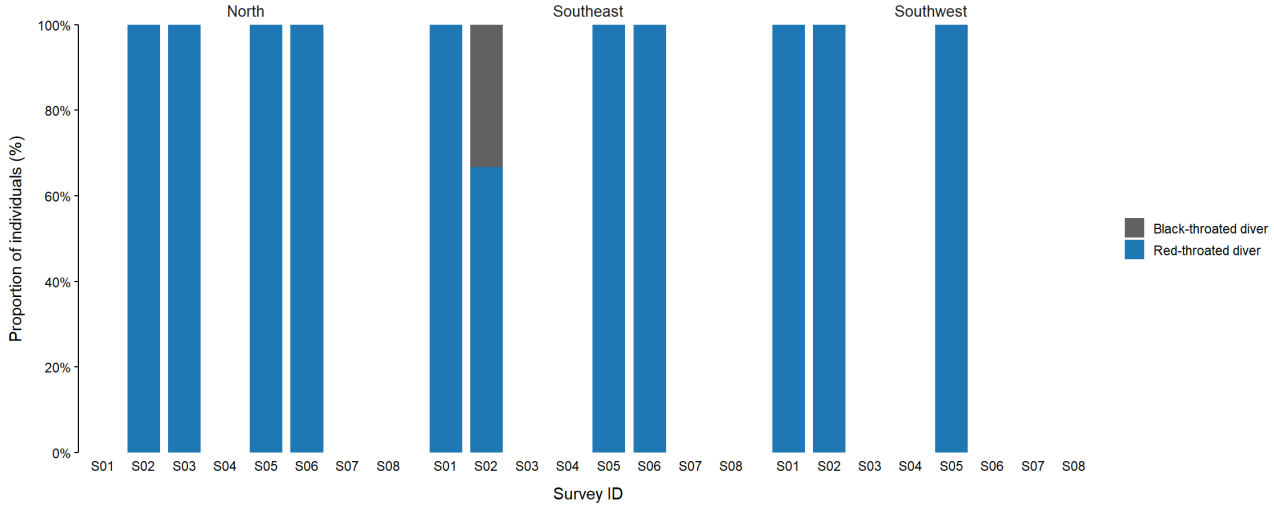

Figure 3-119. Species composition of diver species observed during the eight ship-based surveys conducted in the NSI pre-investigation area during the first survey year (April 2023-March 2024). The figure shows the proportion of individuals for each species (N = 89).

In Y2, red-throated divers continued to dominate at all observation positions. However, one great northern diver was observed in the Southeast during the October survey (S14, Figure 3-120).

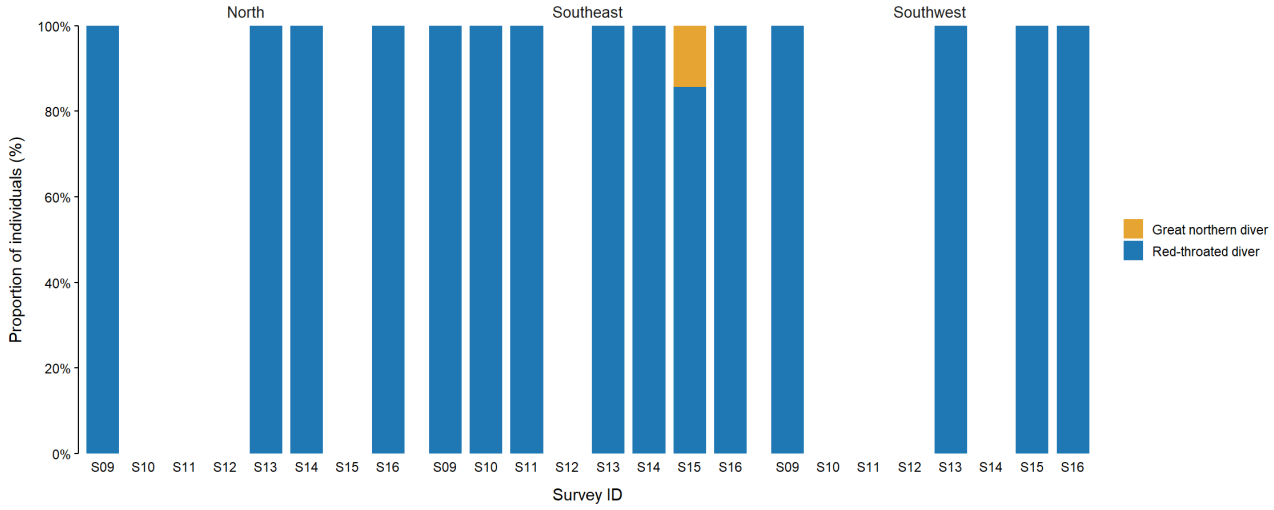

Figure 3-120. Species composition of diver species observed during the eight ship-based surveys conducted in the NSI pre-investigation area during the second survey year (April 2024-March 2025). The figure shows the proportion of individuals for each species (N = 115).

Notably, the highest numbers of divers overall were recorded during the early spring surveys (S01 and S09). These peaks occurred consistently across all observation positions, indicating that diver passage is most intense during the spring migration. Despite these temporal fluctuations in abundance, species composition remained highly stable, with

red-throated diver comprising nearly all individuals observed. These findings suggest that red-throated diver is the overwhelmingly dominant species among divers migrating through or staying in the NSI pre-investigation area, with other diver species appearing only occasionally and locally.

3.2.3.2 Gulls (Larinae)

Gulls were the most abundant species group observed during the surveys, with consistently high numbers of individuals across all observation positions and survey years. A total of seven gull species were regularly observed, with lesser black-backed gull being the most common overall (Table 3-20).

Table 3-20. Species composition of gulls observed during the 16 ship-based surveys conducted in the NSI pre-investigation area during Y1 and Y2. The table shows the number and proportion of individuals for each species (N = 9,422).

Species	Individuals	Proportion (%)
Lesser black-backed gull	5,336	56.6
Common gull	2,336	24.8
Herring gull	781	8.3
Great black-backed gull	529	5.6
Little gull	340	3.6
Black-headed gull	68	0.7
Caspian gull	29	0.3
Mediterranean gull	2	0
Yellow-legged gull	1	0

Species composition within the gull group showed substantial spatial and temporal variation. In Y1, the lesser black-backed gull was the dominant species from April to September, particularly at the North and Southwest observation positions (Figure 3-121). Toward the later surveys, the common gull became increasingly prominent, especially at the North position, where it constituted over 80% of gulls observed. Black-headed gulls were observed regularly but typically in low to moderate proportions. The Southeast position exhibited the greatest species diversity, including observations of little gulls during the September survey (S05) and Caspian gulls during the October survey (S06).

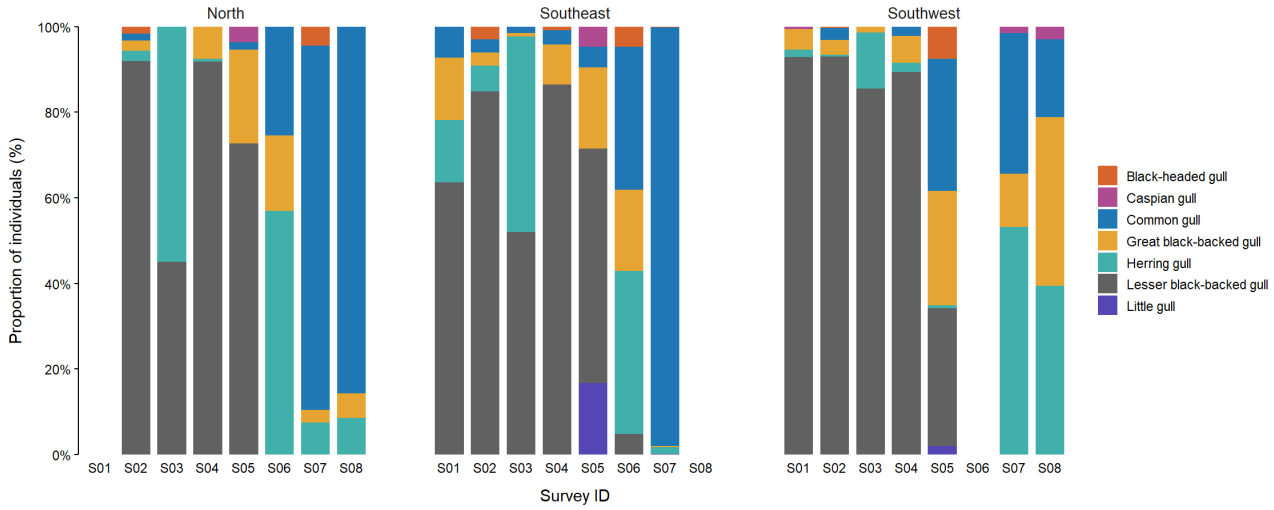

Figure 3-121. Species composition of gulls observed during the eight ship-based surveys conducted in the NSI pre-investigation area during Y1 (April 2023-March 2025). The figure shows the proportion of individuals for each of the seven most observed species (N = 4,072).

In Y2, lesser black-backed gulls remained abundant until September, particularly at the North and Southwest observation positions (Figure 3-122). This was followed by a proportional increase of little gulls, which became the most frequently recorded species during October (S14) at both the North and Southeast positions. Common gulls increased in proportion during winter, especially at the Southeast and Southwest positions. Black-headed gulls showed a similar seasonal presence compared to Y1. Caspian gull and great black-backed gull were observed intermittently and in low numbers, with a modest increase during September (S13) and October (S14), respectively.

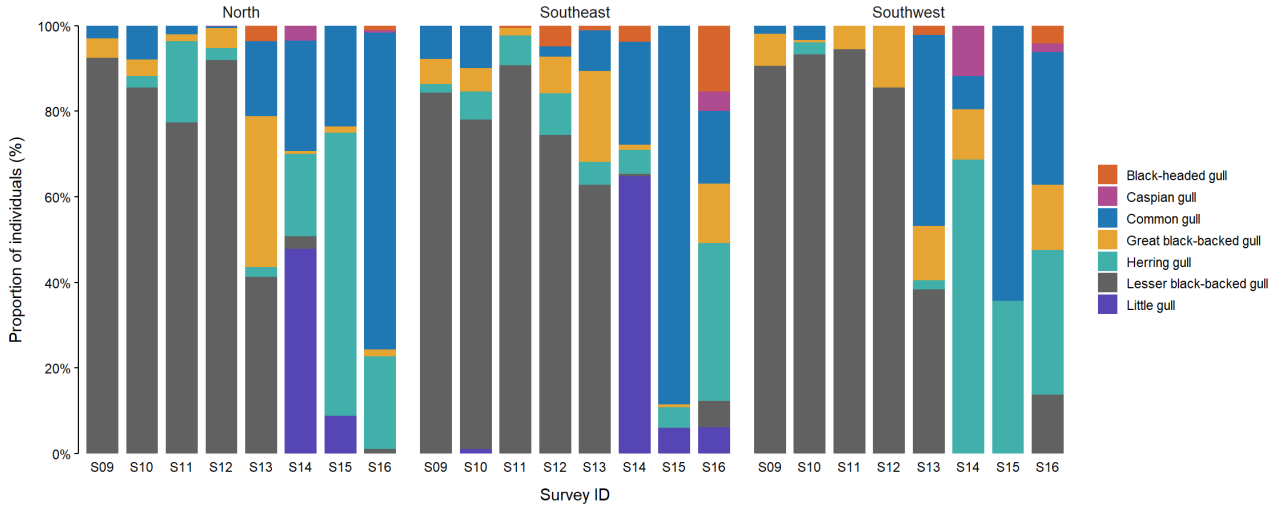

Figure 3-122. Species composition of gulls observed during the eight ship-based surveys conducted in the NSI pre-investigation area during Y2 (April 2014-March 2025). The figure shows the proportion of individuals for each of the seven most observed species (N = 5,350).

3.2.3.3 Terns (Sterna sp.)

Terns were consistently observed during spring and early summer surveys, with species composition showing both seasonal and spatial variation. Over the two survey years, four tern species were observed, with common and arctic

terns being the most abundant. Together, these two species accounted for 91% of all individuals observed (Table 3-21).

Table 3-21. Species composition of terns observed during the 16 ship-based surveys conducted in the NSI pre-investigation area during Y1 and Y2. The table shows the number and proportion of individuals for each species (N = 772).

Species	Individuals	Proportion (%)
Common tern	368	47.7
Arctic tern	342	43.3
Sandwich tern	59	7.6
Black tern	3	0.4

In Y1 (Figure 3-123), terns were recorded from April (S01) through September (S05), after which no terns were observed during the remaining autumn and winter surveys (S06–S08). Arctic tern was dominant at the North and Southwest observation positions, particularly in April and May (S01-S02), while common tern was most frequent at the Southeast position, where it persisted through to September (S05). Sandwich tern occurred mainly in early-season surveys (April-May), especially at the Southeast and Southwest positions. A notable peak of black tern was observed in May (S02) at the Southeast position, where it comprised over half of the recorded terns.

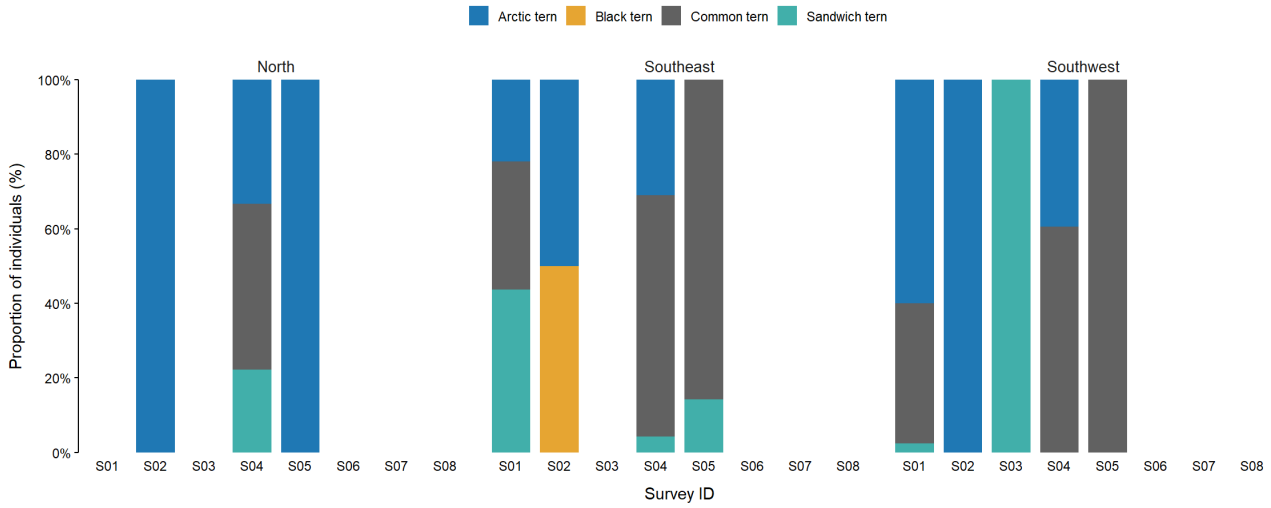

Figure 3-123. Species composition of terns observed during the eight ship-based surveys conducted in the NSI pre-investigation area during Y1 (April 2023-March 2024). The figure shows the proportion of individuals for each of the species (N = 580).

Terns followed a similar seasonal pattern during Y2 (Figure 3-124). Observations were limited to April through September (S09-S13). Common tern was the most frequently observed species, especially from May to August (S10-S12), with broad spatial distribution across all three observation positions. Arctic tern occurred more intermittently but was dominant at the North position in April (S09), at the Southeast position in May (S10) and at the Southwest in September (S13). Sandwich tern appeared in early spring surveys (S09-S10), particularly at the Southeast position. Black tern

was recorded only once in September (S12) at the Southwest position and in low numbers.

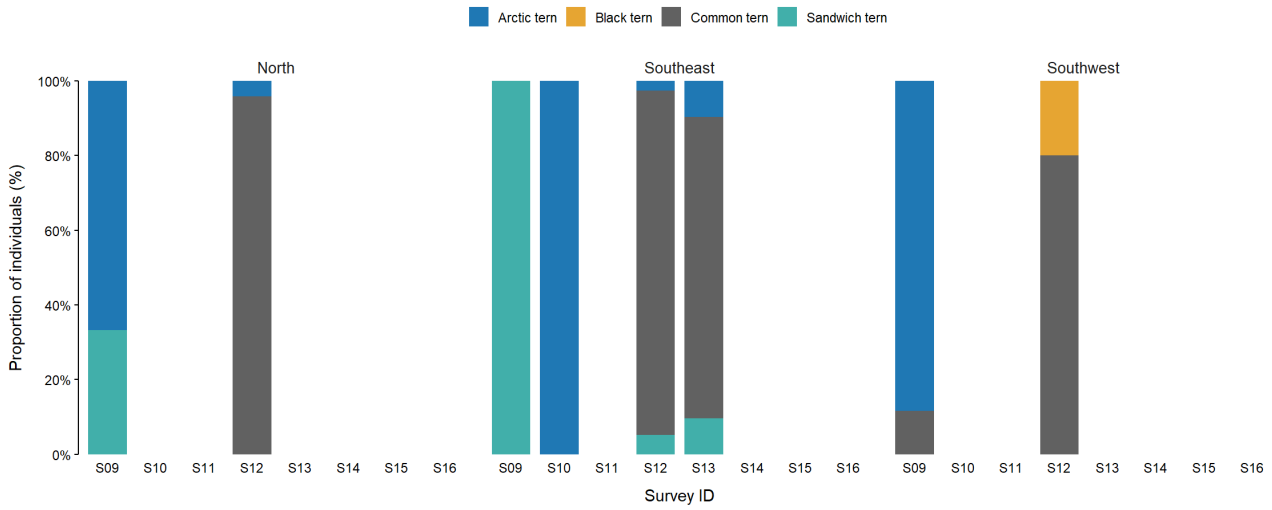

Figure 3-124. Species composition of terns observed during the eight ship-based surveys conducted in the NSI pre-investigation area during Y2 (April 2024-March 2025). The figure shows the proportion of individuals for each of the species (N = 192)

Overall, tern observations were strictly seasonal, confined to April-September in both survey years. Spatially, the Southeast and Southwest observation positions consistently supported a more variable tern composition, while the North position was generally dominated by arctic and common terns.

3.2.3.4 Auks (Alcidae)

Auks were regularly observed throughout the 16 ship-based surveys conducted in Y1 and Y2, and were primarily composed of common guillemot and razorbill, which accounted for over 99% of individuals observed (Table 3-22).

Table 3-22. Species composition of auks observed during the 16 ship-based surveys conducted in the NSI pre-investigation area during Y1 and Y2. The table shows the number and proportion of individuals for each species (N = 455).

Species	Individuals	Proportion (%)
Common guillemot	309	67.9
Razorbill	142	31.2
Black guillemot	2	0.4
Little auk	1	0.2
Puffin	1	0.2

During Y1, the common guillemot was the most abundant species at all three observation positions (Figure 3-125). Razorbill occurred frequently, particularly at the North and Southeast observation positions, during the fall and winter (S05-S08). At the Southwest observation position, razorbills were less common and only observed in notable proportions during the December (S7) and February (S8) surveys. Puffin was only observed once in May (S02) at the Southwest, and black guillemot was only observed at the North observation position in February (S08).

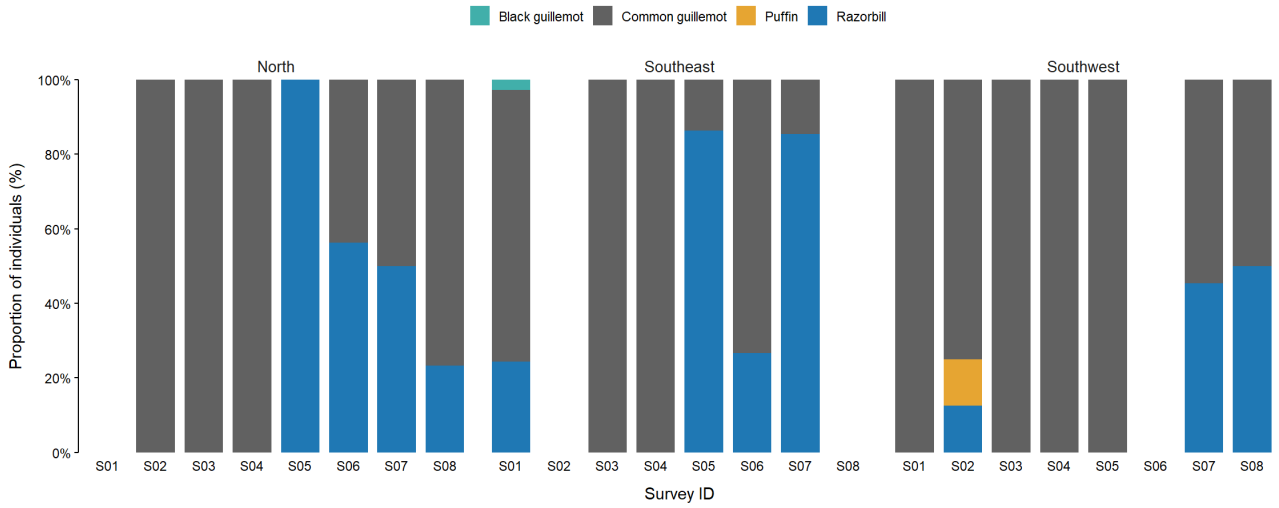

Figure 3-125. Species composition of auks observed during the eight ship-based surveys conducted in the NSI pre-investigation area during Y1 (April 2023-March 2024). The figure shows the proportion of individuals for each of the species (N = 249).

Similarly, common guillemot was overwhelmingly dominant, comprising almost 90% of auks observed in most surveys in Y2 (Figure 3-126). Interestingly, Razorbill occurrence dropped markedly compared to Y1, constituting only 10-25% of auks observed from October to February (S14-S16). Little auk was observed only once at the North observation position during the December survey (S15). Black guillemot was only observed once at the Southwest position in October (S14), while Puffin was not observed during Y2.

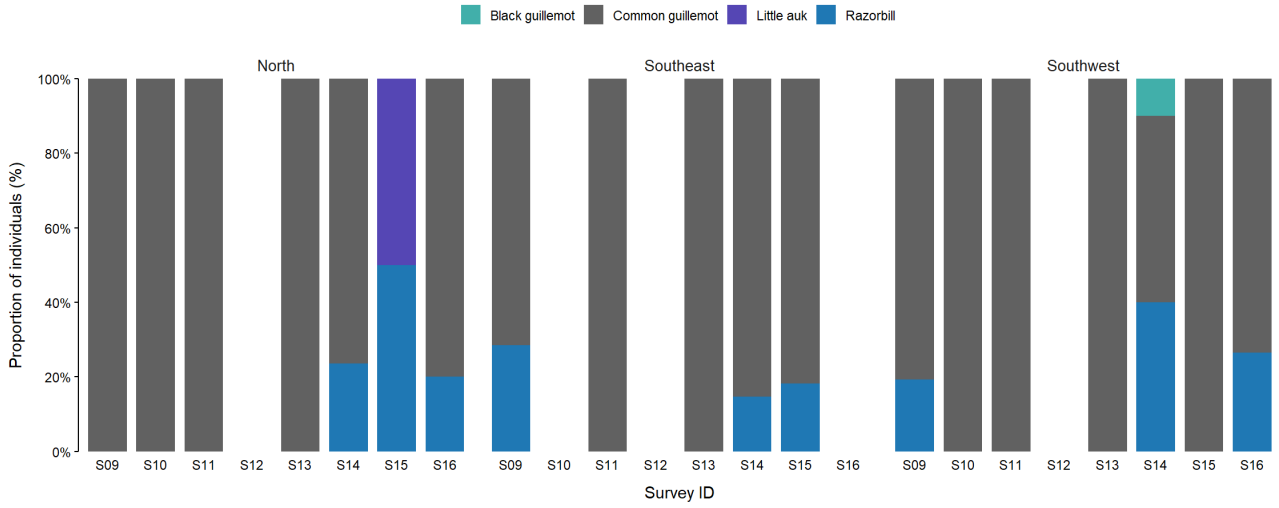

Figure 3-126. Species composition of auks observed during the eight ship-based surveys conducted in the NSI pre-investigation area during Y2 (April 2024-March 2025). The figure shows the proportion of individuals for each of the species (N = 206).

3.2.4 Vertical radar counts

Annotations resulted in a generated total of 7,450 birds across the eight observation periods in Y2, with the highest median putative bird count in October, 277 birds per observation day (Table 3-23).

The predictions of the computer vision algorithm (CVA) (see 2.2.1.3.3) only reached an acceptable range of agreement and correlation (≥ 0.8) with the annotated data in December. For August, September, and October, agreement and

correlation were low but above 0.3, whereas in April, May, June 2024 and February 2025, agreement and correlation were close to zero. The algorithm largely overestimated bird counts, irrespective of settings. The most common source of error was weather conditions, which were not strong enough to be detected as bad weather and could be misidentified as objects. These conditions were most commonly present in May and June (see Figure 3-127) and resulted in false peaks of putative bird counts.

Putative bird counts per hour showed no clear trend for peak hour activity concerning sun hours in Y2, irrespective of the observation period (Figure 3-128).

Table 3-23. The putative bird counts from vertical radar screen dumps for each of eight Y2 ship-based surveys from April 2024 to February 2025.

Period	Total putative bird count (annotated)	Median putative bird count per day (annotated)	Median putative bird count per day (predicted)	CCC agreement	Pearson correlation to March
April 24	556	61	394	0.03	0.06
May 24	211	21	426	0.00	-0.09
June 24	42	10	6352	0.00	-0.14
August 24	451	44	2571	0.37	0.37
September 24	1,279	153	218	0.41	0.44
October 24	3,950	277	5,603	0.69	0.79
December 24	635	55	336	0.8	0.86
February 25	326	47	745	0.03	0.09

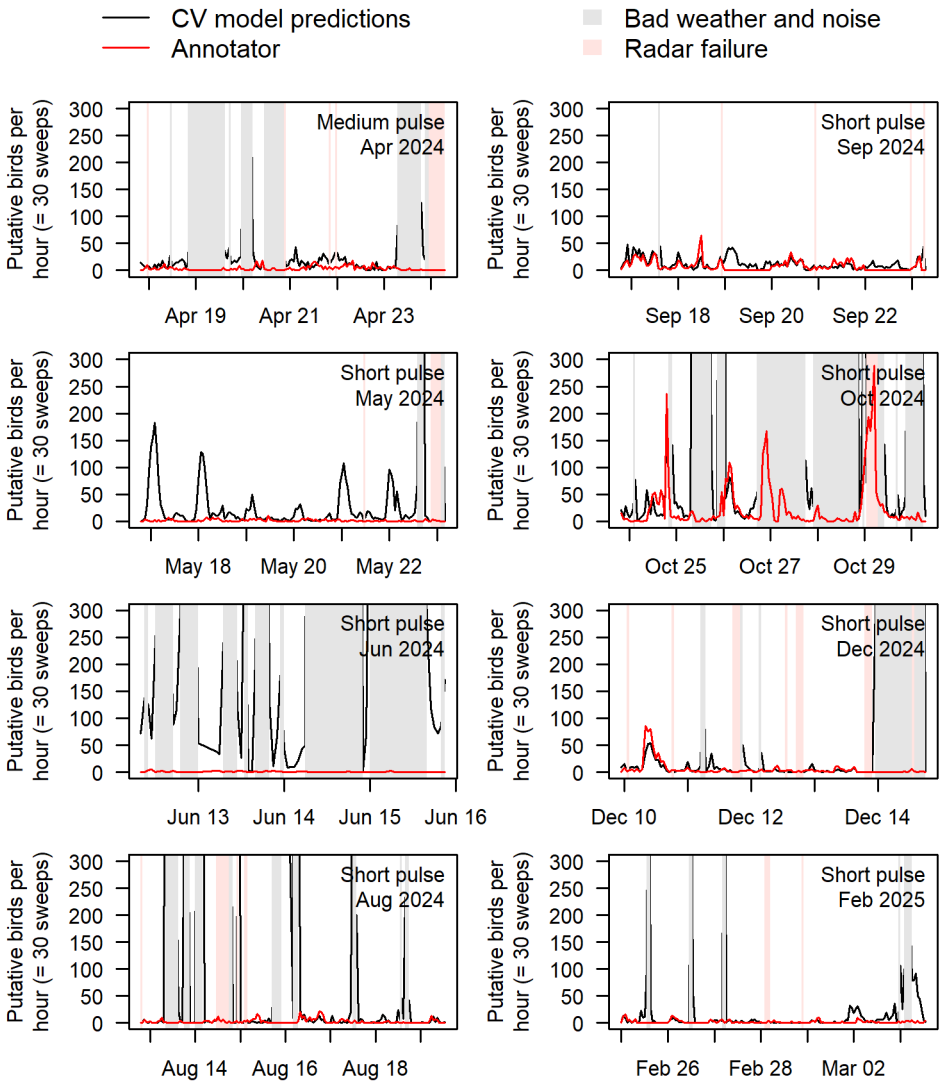

Figure 3-127. Putative bird counts across days during eight Y2 survey sessions, expressed as the number of bird detections per hour (i.e. summed across 30 sweeps). Solid black lines represent the predicted counts from a computer vision algorithm (CVA) model, and red lines represent counts from the annotator. Grey areas represent periods where there was too much noise or bad weather to get reliable predictions from the CVA model. The light red areas represent periods where the model could not detect a radar area or horizon.

Putative bird counts per hour showed increased activity during daylight hours in Y2 September as well as December. In contrast, in October, activity peaked around midnight and in the early morning hours after sunset (Figure 3-128).

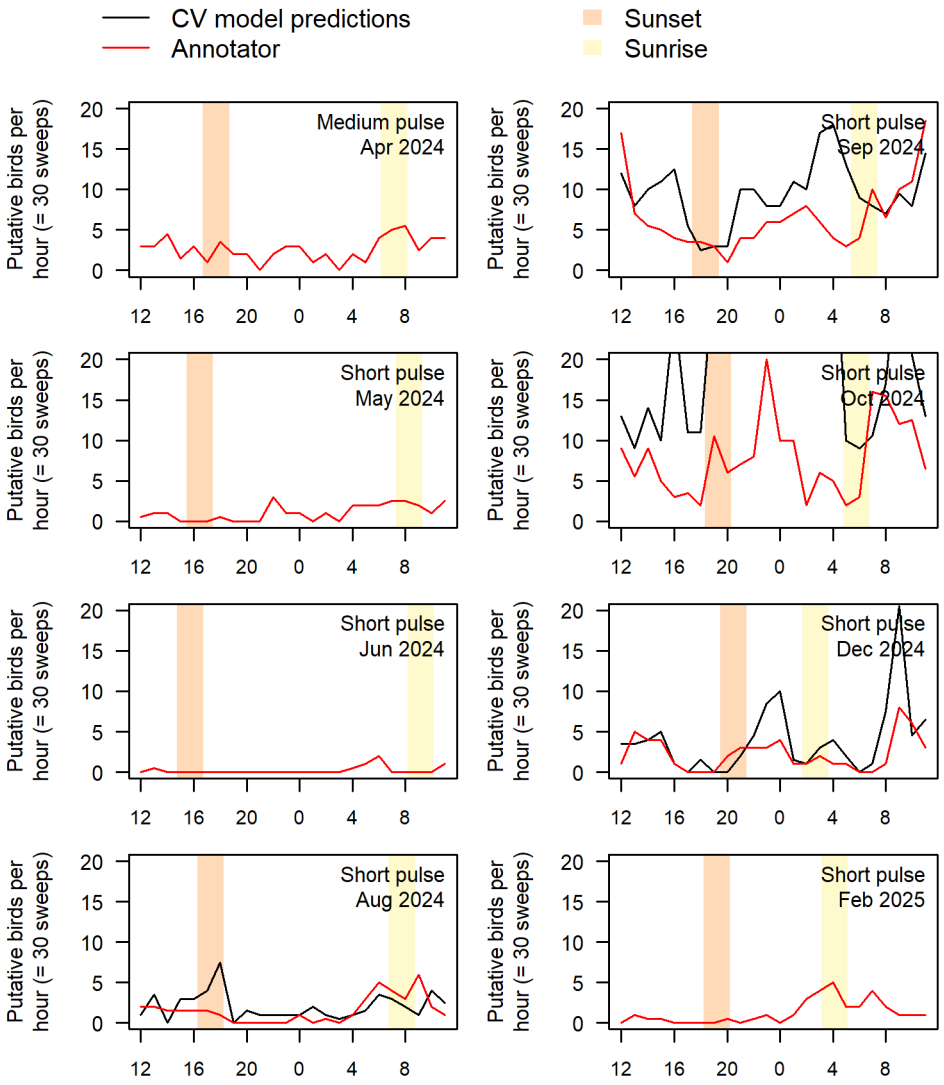

Figure 3-128. Putative bird counts across hours during eight Y2 survey sessions, expressed as the number of bird detections per hour (i.e. summed across 30 sweeps). Solid black lines represent the predicted counts from a computer vision algorithm (CVA), and red lines represent counts from the annotator. CVA was only plotted for months with CCC > 0.35. The orange areas represent dusk periods, while light yellow areas represent dawn periods, with midnight indicated with 0 in the centre of the x-axis.

3.2.5 Spatial results

The bird density during Y2 was significantly affected by an interaction of the x-and y-position within the radar screen and the distance ($F > 40$, $p < 0.001$), with effective degrees of freedom (EDF) indicating substantial non-linear structure (EDF = 15.6 for x, y, and EDF = 8.8 for distance). The model explained 89.5% of the deviance (adjusted R^2 = 0.783), indicating an excellent fit to the data. With increasing distance from the radar, the putative bird density decreased (see Figure 3-129). When controlling for distance, birds were most prominently found at low altitudes (< 250), while density was lowest at altitudes of approximately 500m (Figure 3-130).

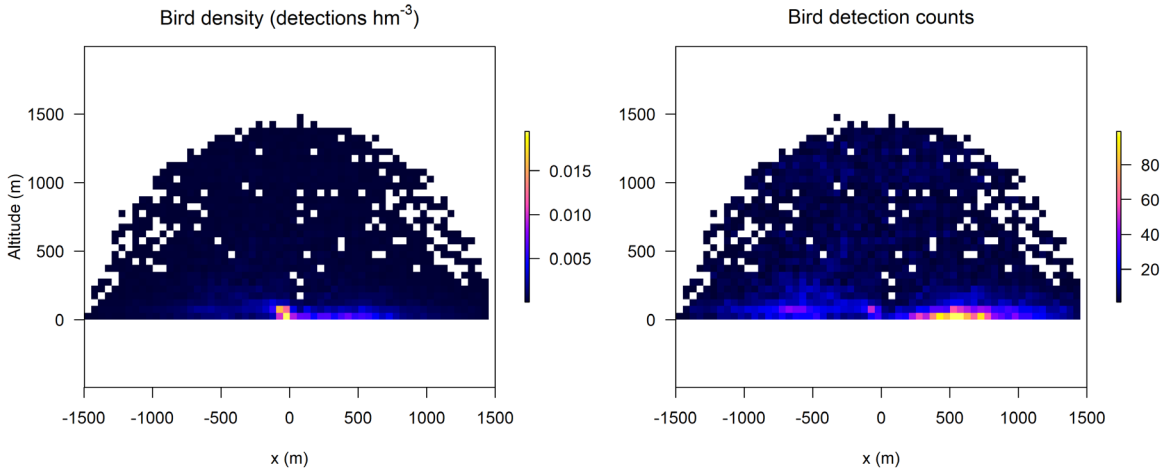

Figure 3-129. Spatial bird distribution. The left plot depicts putative bird densities (hm^{-3}) across 50×50m grid cells of the radar scan area across all observation periods during Y2. The density values reflect the sum of standardized densities per scan, aggregated over all detections, accounted for increasing volume with increasing distance from the radar. The right plot depicts raw detection counts across observation periods. Both plots are derived from manually annotated data.

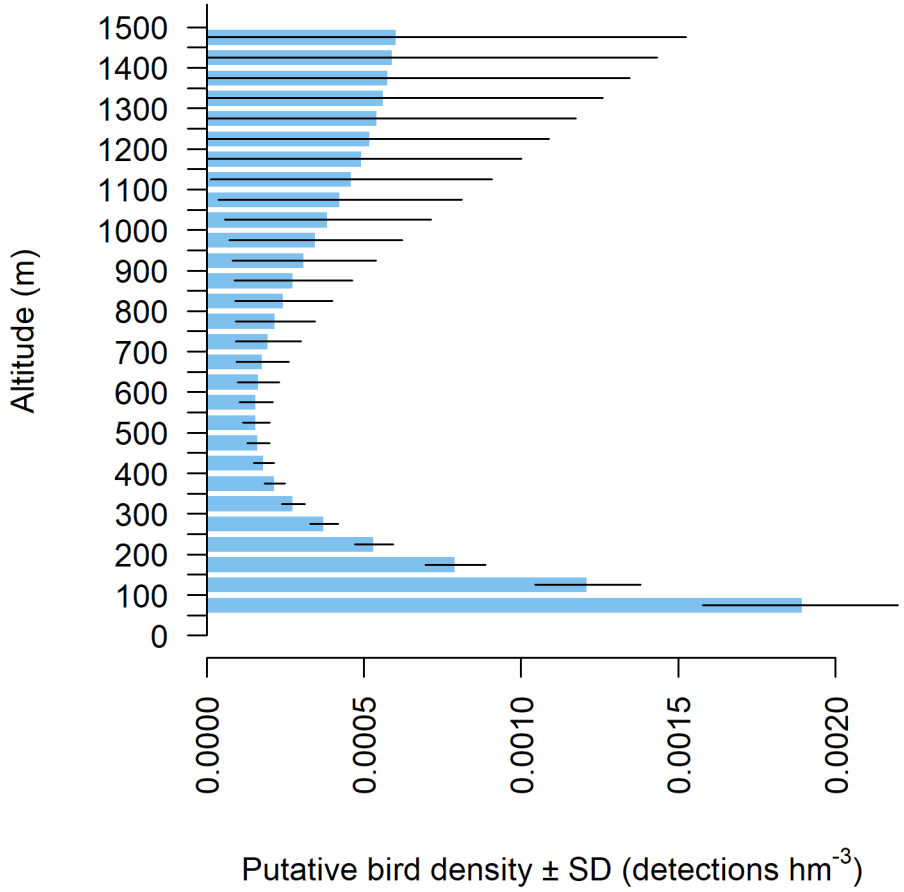

Figure 3-130. Predicted putative bird density at 50 m intervals from 50-1500 m above sea level during Y2. Predictions were made using a generalized additive model, capturing the effect of altitude on putative bird density while accounting for a nonlinear effect of distance from sensor. Putative bird densities were, in turn, derived from manual annotations. Confidence intervals represent the prediction ± 2× standard error of the prediction.

4. Data and knowledge gaps

The data collected in Y2 from the eight aerial surveys, which assessed bird abundances and distributions across the survey area, and eight ship-based surveys, which provided information on flight intensity, altitude, and species composition, are deemed to be of sufficient quality to meet the objectives outlined in the NSI bird program.

4.1 Bird abundance and distribution

Surveys of resting and staging birds in the survey area were conducted by human observers from aircraft. Initially, under the North Sea Energy Island project, the plan was to use digital orthophotos instead of human observers, but to ensure data compatibility between the NSI and the North Sea Energy Island aerial survey data, it was decided to use human-based observers for the NSI aerial surveys. Although the data from human observer-based surveys have been adequate for both tasks, the data quality could be improved using a digital monitoring method. Using a digital method would allow for bird density estimates without introducing the distance sampling detection function, which is expected to reduce the confidence intervals about the density estimates. While this improvement is not essential for the current project, it could enable more precise statistical comparisons of bird densities before and after future wind energy developments.

4.2 Bird flight data

Bird flight volume, altitude, and species composition data were collected from eight ship-based surveys across the annual cycle. Initially, it was planned that a 3D radar placed at HR3 OWF would provide continuous and very precise data for that purpose. This idea was abandoned due to time constraints and logistical challenges with installing the radar on an appropriate offshore installation. However, the available data on bird flight magnitude and altitude was considered sufficient with the data collection protocol used in this project.

Continuous data collection on flight altitudes concerning land-based wind farm projects is well established. However, logistical challenges limit data collection in the open sea. With the presence of the HR3 OWF, the Vesterhav Syd OWF, and, within a short time, the Thor OWF, options for overcoming these logistical challenges are present. Therefore, using a 3D radar could be reconsidered for future investigations concerning wind energy development in the area.

Information on birds' reactions to wind turbines is important when estimating the collision risk for birds in the marine environment. While some bird species may avoid the structures, others may be attracted to them. Information on this issue could be gained by introducing a 3D radar at the HR3 or the upcoming Thor OWF.

5. Discussion and conclusion

5.1 Aerial surveys

The abundances and spatial distributions of bird species in the survey area were described by conducting eight aerial surveys across an annual cycle from April 2024 to March 2025 during Y2. These surveys represent an extension of the Y1 ornithological survey previously undertaken in the same NSI area between April 2023 and March 2024 using the same method (Petersen I. K., et al., 2024). The results in this report confirm the Y1 surveys that the general abundance of staging birds in the survey area is higher in winter and spring than in summer and autumn. This was true for the diver species, common scoters, little gulls, black-legged kittiwakes and razorbills/common guillemots. The present annual spread of surveys is, therefore, seen as giving an optimal dataset for the objectives of this project.

Results from Y2 surveys generally confirmed the patterns of distribution and abundance observed in Y1 surveys using the same methods. For the five species of staging birds for which spatial models could be performed, black-legged kittiwakes and razorbills/common guillemots showed very similar distributions between the two survey years. The distribution of diver species (red-throated and black-throated divers combined) was found to be less confined to the coastal areas in Y2 compared to Y1. Diver species showed higher numbers over the winter and spring, from December through to late April, with comparable abundance estimates between years. Northern gannet numbers were highest in the survey area during autumn and spring, with a moderate peak in September of both years and a higher peak in March and April. The overall distribution of northern gannets was patchier during Y2, with lower numbers in the coastal eastern parts and on Horns Rev in the south of the survey area. Little gulls were especially common in the eastern half of the survey area, appearing in higher numbers and over a longer period during Y2 compared to Y1, enabling the application of spatial modelling to this species. Black-legged kittiwakes were most abundant from November to late April, with a tendency for greater numbers in Y2, but their distribution patterns were similar between years. Razorbills/common guillemots were similarly abundant in both survey years, being least abundant in spring and summer and occurring in higher numbers in autumn and winter.

Within the survey area in both survey years, several anthropogenic activities may have influenced the distribution of birds. The HR3 OWF is situated in the southern part of the survey area. The Vesterhav Syd OWF was operational from the spring and summer of 2024, and geophysical and geotechnical surveys in the Thor OWF area was ongoing in the northern part of the survey area during the survey period related to the present project. These activities may have influenced the abundance and distribution of some bird species. The potential impact of those activities on bird abundance and distribution, however, could not be quantified.

Marine birds respond to human activities at sea (Fox & Petersen, 2019). When considering the impact on the distribution of birds, shipping activity has been shown to have species-specific effects on birds (Garthe, S.; Hüppop, O., 2004; Fliessbach, et al., 2019). Diver species and common scoter are classified as species experiencing a high impact from such activities, whereas, for instance, gull species are less sensitive. Comparisons of before and after construction distribution of common scoters and long-tailed ducks in Danish waters showed marked displacement effects (Petersen, MacKenzie, Rexsted, Wisz, & Fox, 2011; Petersen, Nielsen, & Mackenzie, 2014; Petersen, Mackenzie, & Scott-Hayward, 2018; Scott-Hayward, et al., 2024). Data from these analyses also indicated a distribution effect on red-throated divers, though this was not at the time described to be an effect of the presence of the wind farms. Analyses of the distribution of red-throated divers in the German Bight concluded a marked displacement of this species from the wind farms (Mendel, et al., 2019). Common guillemots were shown to be displaced up to considerable distances from offshore wind farms in the German Bight (Peschko, et al., 2024). A project conducted in the Horns Rev area in the winter of 2024/2025 confirmed that the distribution of diver species in the area was still impacted by the presence of the wind farms (Scott-Hayward, et al., 2024).

The avifauna of the bird survey area was predominantly composed of marine species. True marine species such as northern fulmars, northern gannets, black-legged kittiwakes, and razorbills/common guillemots contributed most to the total number of birds in the survey area. However, species and species groups like common scoter, diver species, gulls, and terns were also present in significant numbers. The results from Y2 showed higher numbers of little gulls compared to Y1.

The razorbill/common guillemot group was estimated to be the most numerous of all bird species present in Y2, as found in Y1, with almost 27,000 individuals present in the survey area in March 2025. In November 2024, an estimated 11,659 black-legged kittiwakes were present in the survey area. For diver species and northern gannet, the corresponding estimates were 4,401 and 4,145 birds, respectively, both peaking in March 2025. The lowest numbers of diver species and black-legged kittiwakes were recorded in July 2024, while northern gannets had their lowest numbers in December 2024.

Existing data from April and May 2019 covering the entire Danish North Sea indicated the presence of an estimated 22,648 divers, primarily red-throated divers, mostly found in the southeastern parts of the Danish North Sea, with high numbers extending northwards along the west coast of Jutland (Petersen I. K., et al., 2024). Additionally, April and May 2019 data estimated populations of 46,437 northern fulmars, 31,723 northern gannets, 4,472 black-legged kittiwakes and 89,681 razorbills/common guillemots in the Danish North Sea. In the North Sea Energy Island area, situated further offshore to the northwest of the NSI area and covering ca. 60% as compared to the survey area of the NSI area, common scoters and red-throated divers were less abundant. There, bird species with a more pelagic distribution, such as razorbills/guillemots, northern fulmars and northern gannets, were more abundant. Razorbill/common guillemot abundances in the North Sea Energy Island area were estimated to count ca. 14,000 individuals in March 2023 and 25,000 birds in April 2023. Northern gannets were estimated at 2,500 to 3,800 birds in early and late April 2022 and reduced to 24 and 668 in March and April 2023 (Petersen I. K., et al., 2024).

5.2 Ship-based surveys

Another study component described the flight patterns of birds in the NSI pre-investigation area using data obtained from ship-based surveys conducted in Y1 and Y2. The ship-based approach used in this study provided high-resolution data on bird migration intensity, flight altitude, and species composition but also carries several limitations that should be considered when interpreting the results. While the standardised 1500 m transect method ensures consistency in sampling effort and directional coverage, detection probability decreases with distance, particularly for small or low-flying species under suboptimal observation conditions (e.g. glare and sea state). Although surveys were only conducted in favourable weather, visibility gradients may still have influenced detection, particularly during long blocks of effort or in cases of dense bird passage through the area.

Furthermore, flight altitude estimates, although aided by laser rangefinders, rely heavily on visual calibration and are sensitive to error, especially on a moving platform. While multiple measurements per individual were used to mitigate variability, sea motion, wave interference, and angle of view can affect both laser rangefinder returns and visual estimates. Additionally, species composition data may be affected by field identification challenges, especially among morphologically similar taxa such as gulls, terns, or auks. Although supporting equipment (e.g., telescope) enhanced identification, distant or fast-moving birds may still have been recorded at the group level, limiting resolution in some cases. Moreover, rarer species may be underrepresented due to the limited temporal window (5.4 ± 0.3 survey days) of each Y1 and Y2 survey.

Finally, ship-based surveys are inherently constrained in spatial coverage, especially compared to aerial surveys. While repeated visits to the three observation positions provided spatial balance, some areas within the pre-investigation area were not directly surveyed during the ship-based surveys. However, despite these limitations, the dataset provided a robust basis for quantifying migration patterns.

5.2.1 Migration magnitude

Diurnal bird migration through the NSI pre-investigation area was found to be seasonally structured and highly variable across survey years and observation positions. Migration intensity peaked during the autumn months (September-October), with clear peaks corresponding to known migration periods. This was primarily evident during Y2. Furthermore, Y2 recorded consistently higher migration intensity, suggesting that large-scale environmental conditions or population-level dynamics can cause substantial interannual fluctuations in passages.

Importantly, the migration intensity was not evenly distributed throughout the day. Instead, a diurnal pattern was evident during Y2, with elevated intensity right after sunrise, potentially reflecting the species' movement ecology. These findings highlight that both temporal and spatial heterogeneity in migration magnitude must be considered when assessing potential ecological impacts from offshore infrastructure.

Diurnal migration through the NSI pre-investigation area exhibited clear directional patterns during both Y1 and Y2, with most movements oriented along a North-South axis. The predominant flight direction was northbound in spring (April–June) and southbound in autumn (September - October), aligning with typical long-distance seasonal migration between breeding grounds in northern Europe and wintering areas farther south and west. However, flight direction varied notably between observation points, likely influenced by weather conditions, coastal topography, and species-specific strategies. In some of the surveys carried out in autumn, for example, a higher proportion of birds flew east-southeast or southwest, indicating possible lateral movements across the North Sea or along the Jutland coast.

5.2.1.1 Vertical radar

Radar-based monitoring during Y2 identified a peak in bird movement during October, with additional but lower levels of activity recorded in September. In 2023, peak bird movement occurred within a relatively short 24-hour window, with several thousand detections per hour. In contrast, in 2024, the peak period extended over five days, with several hundred detections per hour. In September and December, bird detections primarily occurred during daylight hours, while in October, activity peaked during the night and early morning. These changes in migratory timing across months and years may reflect underlying variations in weather conditions. Incorporating detailed meteorological data could help to clarify the environmental drivers of these patterns.

The inclusion of weather variables may also improve the performance of the computer vision algorithm (CVA). Model agreement with manual annotations was highest in months characterized by distinct weather interference, such as October and December. This suggests that the CVA may be more robust to clear, high-noise conditions than to more ambiguous ones. Improving noise classification, potentially by integrating weather metadata for use in pre-filtering, may enhance the accuracy of automated predictions.

5.2.2 Flight altitude

Most recorded diurnal flights occurred at low altitudes, with over 75% of individuals flying below 100 meters and very few exceeding 150 meters. This pattern was consistent across species, with auks, divers, and sea ducks almost exclusively flying at altitudes below 50 meters. Terns and gulls, however, displayed a broader vertical distribution and were the only groups frequently recorded above 100 meters.

5.2.2.1 Vertical radar

Spatial analyses confirmed a strong distance-dependent structure in bird density during Y2. Observers communicated that birds often clustered close to the vessel, particularly at night, likely influenced by attraction to the boat. Such an attraction may explain the high density of birds observed within a 50-100 m radius from the boat. When controlling for distance, birds were most frequently recorded at low altitudes, with detections increasing again towards high altitudes (>700 m). However, uncertainty in altitude estimates increased with distance, reflecting reduced accuracy in radar-based measurements at the edges of the scan area.

Together, these findings highlight the value of combining manual and automated radar observations with environmental data to improve our understanding of avian movement patterns and the factors shaping them.

5.2.3 Species composition

Observations from ship-based surveys also provided valuable insights into the species composition of birds that were challenging to identify from aerial surveys. Species composition varied markedly between seasons, survey years, and observation positions, reflecting the dynamic nature of migration in the North Sea. For example, spring surveys were dominated by lesser black-backed gulls, red-throated divers, and common terns, while autumn and winter were characterised by increased auk diversity, great black-backed gulls, and large numbers of common guillemots.

Across most taxonomic groups, certain species clearly dominated, but the relative proportions shifted inter-annually, indicating that community composition is influenced by year-to-year variation, e.g. in migration timing, weather conditions, or population trends. For example, razorbills were frequently observed in Y1 but were present at far lower proportions in Y2. In contrast, little gulls were observed more frequently during Y2 than Y1.

Combined, these findings underscore that several species of migratory seabirds utilise the NSI pre-investigation area, with a turnover that reflects seasonal patterns and wider ecological drivers such as for instance water depth, salinity and current conditions. As such, continued monitoring is critical for capturing long-term trends and inter-annual variation in species use, abundance, and vulnerability to marine developments.

References

BirdLife International. (2021a). *European Red List of Birds*. Publications Office of the European Union.

Buckland, S. T., Anderson, D. R., Burnham, K. P., Laake, J. L., Borchers, D. L., & and Thomas, L. (2001). *Introduction to Distance Sampling*. Oxford: Oxford University Press.

Buckland, S., Rexstad, E., Marques, T., & Oedekoven, C. (2015). *Distance sampling: methods and applications*. Switzerland: Springer International Publishing.

Dutta, A., & Zisserman, A. (2019). The VIA Annotation Sofrware for Images, Audio and Video. *Proceedings of the 27th ACM International Conference on Multimedia*, 2276-2279.

Fliessbach, K., Borkenhagen, K., Guse, N., Markones, N., Schwemmer, P., & Garthe, S. (2019). A ship traffic disturbance vulnerability index for Northwest European seabirds as a tool for marine spatial planning. *Frontiers in Marine Science, 6*, 192. doi:10.3389/fmars.2019.00192

Fox, A., & Petersen, I. (2019). Offshore wind farms and their effects on birds. *Dansk Ornitologisk Forenings Tidsskrift, 113*, 86-101. Retrieved from https://pub.dof.dk/publikationer/144

Garthe, S. &. (2004). Scaling possible adverse effects of marine wind farms on seabirds: developing and applying a vulnerability index. *J. Appl. Ecol.*, pp. 724–734. Retrieved from 10.1111/j.0021-8901.2004.00918.x

Garthe, S., Schwemmer, H., Peschko, V., Markones, N., Müller, S., Schwemmer, P., & Mercker, M. (2023). Large-scale effects of offshore wind farms on seabirds of high concervation concern. *Scientific reports*, 4779.

Garthe, S.; Hüppop, O. (2004). Scaling possible adverse effects of marine wind farms on seabirds: developing and applying a vulnerability index. *Journal of Applied Ecology, 41*, 724-734. doi:10.1111/j.0021-8901.2004.00918.x

Laursen, K., Pihl, S., Durinck, J., Hansen, M., Skov, H., Frikke, J., & Danielsen, F. (1997). Numbers and distribution of waterbirds in Denmark 1987-1989. *Danish Review of Game Biology, 14*(1), 1-184.

Leys, C., Ley, C., Klein, O., Bernard, P., & Licata, L. (2013). Detecting outliers: do not use standard deviation around the mean, use absolute deviation around the median. *Journal of Experimental Social Psychology, 49*(4), 764-766.

Lin, L. (1989). A concordance correlation coefficient to evaluate reproducibility. *Biometrics*, 255-268.

Marques, F. F., & Buckland, S. T. (2004). Covariate models for the detection function. In *Advanced Distance Sampling* (pp. 31-47). Oxford: Oxford University Press.

Marques, T. A., Thomas, L., Fancy, S. G., & Buckland, S. T. (2007). Improving estimates of bird densities using multiple covariate distance sampling. *The Auk*, 1229-1243.

Mendel, B., Schwemmer, P., Peschko, V., Müller, S., Schwemmer, H., Mercker, M., & Garthe, S. (2019). Operational offshore wind farms and associated ship traffic cause profound changes in distribution patterns of Loons (Gavia spp.). *Journal of Environmental Management, 231*, 429-438. doi:10.1016/j.jenvman.2018.10.053

Nielsen, R., & Petersen, I. (2014). *Abundance and distribution of birds and marine mammals in Jammerbugten in 2012 and 2013. Report commissioned by the Environmental Group under the Danish Environmental Monitoring Programme through contract with Vattenfall.* DCE - Danish Centre for Environment and Energy. Aarhus University.

Peschko, V., Schwemmer, H., Mercker, M., Markones, N., Borkenhagen, K., & Garthe, S. (2024). Cumulative effects of offshore wind farms on common guillemots (Uria aalge) in the southern North Sea - climate versus biodiversity? *Biodiversity and Conservation, 33*, 949-970. doi:10.1007/s10531-023-02759-9

Petersen, I. K., & Sterup, J. (2019). *Number and distribution of birds in and around two potential offshore wind farm areas in the Danish North Sea and Kattegat. Scientific report no. 327.* DCE - Danish Centre for Environment and Energy. Aarhus University.

Petersen, I. K., Mackenzie, M. L., & Scott-Hayward, L. A. (2018). *Long-term impacts on Long-tailed Duck distributions resulting from the construction of the Rødsand II and Nysted offshore wind farms, Denmark.* Aarhus, Denmark: DCE – Danish Centre for Environment and Energy, Aarhus University.

Petersen, I. K., MacKenzie, M. L., Rexsted, E., Wisz, M. S., & Fox, A. D. (2011). *Comparing pre- and post-construction distributions of long-tailed ducks Clangula hyemalis in and around the Nysted offshore wind farm, Denmark : a*

quasi-designed experiment accounting for imperfect detection, local surface features and autocorrelation. St. Andrews, UK: University of St. Andrews. Retrieved from https://hdl.handle.net/10023/2008

Petersen, I. K., Nielsen, R., & Clausen, P. (2016). *Vurdering af IBA'er (Important Bird Areas) i relation til fuglebeskyttelsesområder - med særligt henblik på marine arter og områder. Tenisk rapport nr. 202.* DCE - Nationalt Center for Miljø og Energi. Aarhus Universitet.

Petersen, I. K., Nielsen, R., & Clausen, P. (2019). *Opdateret vurdering af IBA udpegninger i relation til otte specifikke marine områder. Teknisk rapport nr. 203.* DCE - Nationalt Center for Miljø og Energi. Aarhus Universitet.

Petersen, I. K., Thomsen, H. M., Lindesay, S. H., Isojuuno, S., McKencie, M., Pedersen, C. L., . . . Sterup, J. (2024). *North Sea Energy Island, Technical Report, Birds.* Aarhus: NIRAS & Aathus University.

Petersen, I. K., Thomsen, H. M., Scott-Hayward, L., Isojuuno, S., MacKenzie, M., Alison, J., . . . Sterup, J. (2024). *Survey of Birds for Offshore Wind Farms in Danish Waters, North Sea I.* Aarhus: NIRAS & DCE, Aarhus University.

Petersen, I., Nielsen, R., & Mackenzie, M. (2014). *Post-construction evaluation of bird abundances and distributions in the Horns Rev 2 offshore wind farm area, 2011 and 2012.* Kalø, Denmark: Danish Centre for Environment and Energy, Aarhus University.

R Core Team. (2023). *R: A Language and Environment for Statistical Computing [Computer software].* R Foundation for Statistical Computing.

Scott-Hayward, L. A., Mackenzie, M. L., & Walker, C. G. (2023). MRSea R package (V1.5.0): spatially adaptive uni and bi-variate regression splines using SALSA.

Scott-Hayward, L. A., Mackenzie, M. L., Donovan, C. R., Walker, C. G., & Ashe, E. (2014). Complex Region Spatial Smoother (CReSS). *Journal of Computational and Graphical Statistics, 23*(2), 340-360.

Scott-Hayward, L., Petersen, I., Mackenzie, M., Pedersen, C., Isojunno, S., Nielsen, R., . . . Neergaard, R. (2024). *Changes in the distribution and abundance of common scoter and diver species in the Horns Rev I, II and III offshore windfarm areas, Denmark.* Aarhus: NIRAS/Aarhus University (DCE).

Skov, H., Durinck, J., Leopold, M. F., & Tasker, M. L. (1995). *Important bird areas in the North Sea, including the Channel and the Kattegat.* Cambridge: BirdLife International.

Stone, C., Webb, A., Barton, C., Ratcliffe, N., Reed, T., Tasker, M., . . . Pienkowski, M. (1995). *An atlas of seabird distribution in north-west European waters.* Peterborough: Joint Nature Conservation Committee.

Tasker, M., Webb, A., Hall, A., Pienkowski, M., & Langslow, D. (1987). *Seabirds in the North Sea.* Nature Conservancy Council.

Walker, C., Mackenzie, M., Donovan, C., & O'Sullivan, M. (2010). SALSA - a Spatially Adaptive Local Smoothing Algorithm. *Journal of Statistical Computation and Simulation, 81*(2), 179-191.

Wood, S. (2011). Fast stable restricted maximum likelihood and marginal likelihood estimation of semiparametric generalized linear models. *Journal of the Royal Statistical Society*, 73(1),3-36.

3B4BAppendix 1

Vertical radar computer vision pipeline

Executive summary of methods for Computer Vision Analysis (CVA)

Scan area detection

Inputs: one representative radar image; scan area colour parameters (determined manually).

Outputs: centre coordinates and radius of scan circle; eccentricity to convert to ellipse.

Screen grabs contain information outside of the radar scan area that is distracting for detecting birds (Figure 0-1). To isolate the scan area of images, we:

- Pixels in the image that meet specific colour criteria are selected.
- Only edge pixels using a 1-pixel erosion are selected.
- The minimum bounding circle of those pixels is found using the 'miniball' Python package.
- These are converted to an ellipse by comparing the height and width of the scan area.

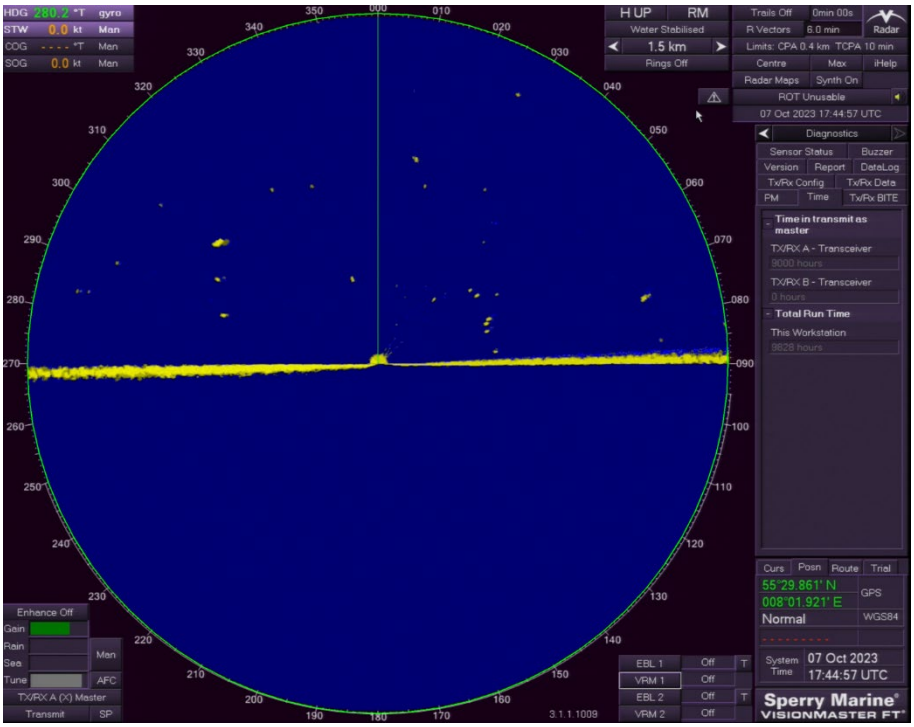

Figure 0-1 An example of a screen grab from the October session. The green line depicts the scan circle before conversion to an ellipse.

Foreground segmentation

Inputs: input image (RGB), foreground hue +/- range; minimum saturation.

Outputs: foreground mask.

To capture the yellow areas of the scan, including birds, artefacts, the water's surface, and some features of the graphical interface (Figure 0-2):

- The image is converted from RGB to HSV space.

- Pixels with hues falling within a range around a specific value are extracted, while regions of low saturation are excluded.

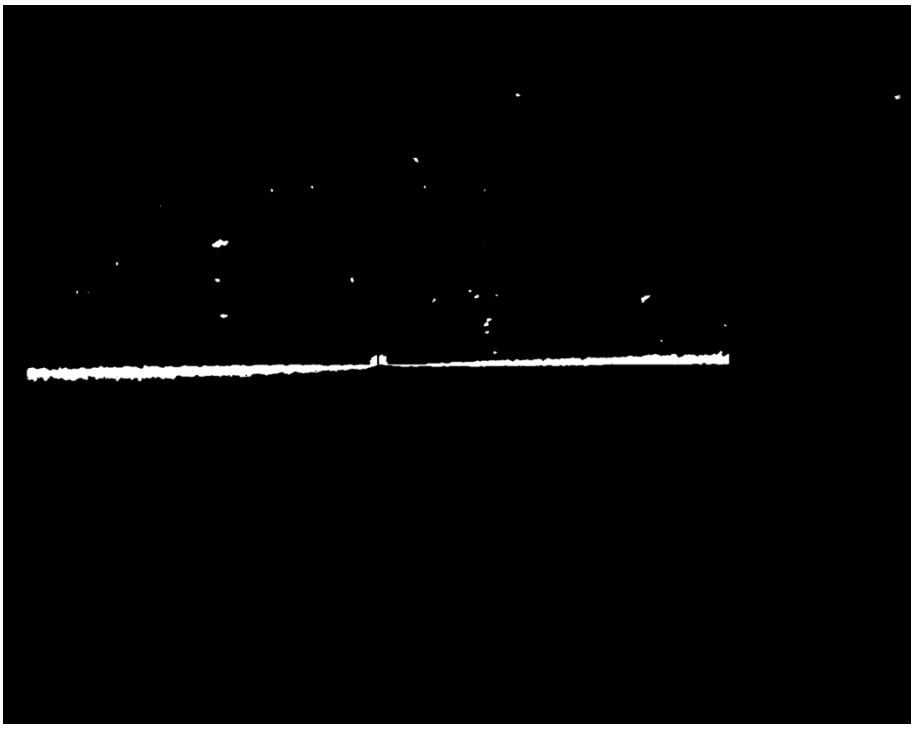

Figure 0-2 The foreground mask derived from the same image as in Figure 0-1.

Horizon detection

Inputs: scan area ellipse parameters, foreground mask, minimum horizon strength, horizon buffer angle, minimum radial artefact strength.

Outputs: Left and right horizon angles, radial artefact angles, above horizon foreground mask.

To detect the horizon lines and isolate a search area above the horizon:

- The foreground mask is cropped to the scan area.
- The average pixel value (yellowness) in the foreground mask along radial lines at 0.5-degree intervals is recorded.
- The uppermost lines with the yellowness is taken above a certain threshold on the left and right half of the ellipse as the left and right horizons, respectively (the brightest red on each side in Figure 0-3).
- The foreground mask is cropped to exclude areas within a buffer angle of each horizon line (Figure 0-4).
- The angles of those radial lines with yellowness above a certain threshold are retained to eliminate some radial artefacts.

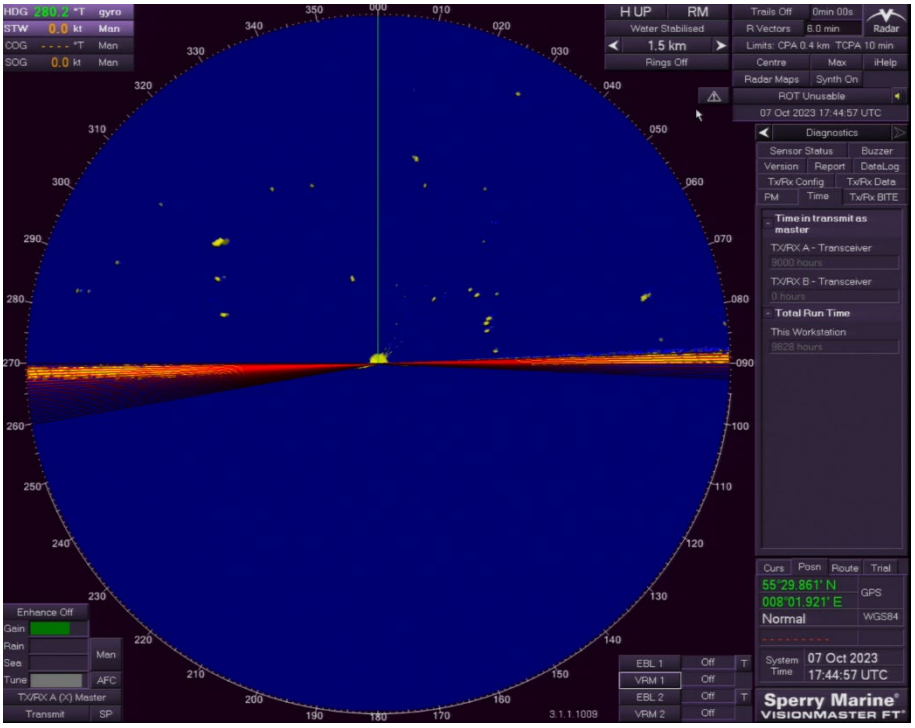

Figure 0-3 Candidate horizon lines for the image in Figure 0-1, based on the foreground mask in Figure 0-2

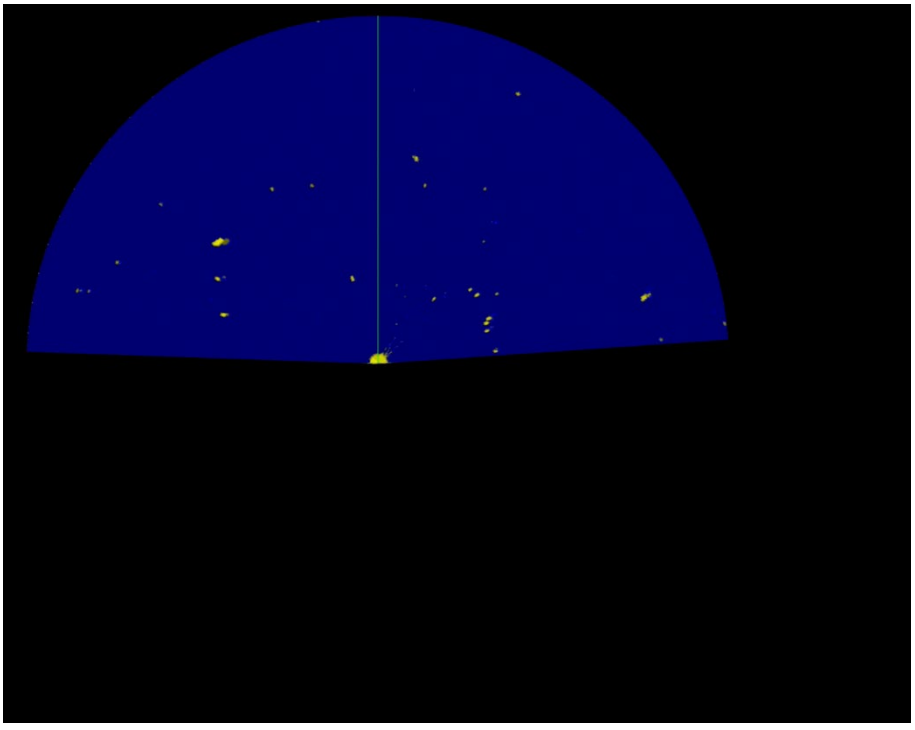

Figure 0-4 Visualisation of the image in Figure 0-1 cropped within the scan area and above a buffer around the horizon lines.

Bad weather and noise detection

Inputs: input image (RGB), scan area ellipse parameters.

Outputs: indicator of bad weather and noise in the image.

To understand the overall level of noise in the image, usually indicative of bad weather:

- The original image is cropped to the scan area above a left horizon at 290 degrees and a right horizon at 70 degrees.
- The 95 percentile of the red band within the cropped area is taken as the noise and weather indicator, for which high values indicate bad weather and/or low-quality data.

Bird filtering

Inputs: above horizon foreground mask, scan area ellipse parameters, radial artefact angles, minimum area, maximum area, minimum distance, minimum length-to-width ratio.

Outputs: coordinates of putative birds with metadata (Figure 0-5).

To extract foreground objects that are more likely to be birds:

1) Contiguous regions of the foreground mask are identified using the 'skimage' Python package.
2) Each object's locations, areas, lengths and widths are extracted.
3) The distance and angle of each object from the centre of the scan area ellipse are calculated.
4) Putative birds are filtered out based on size, shape and distance parameters.
5) Putative birds within 0.5 degrees of a radial artefact angle are excluded.

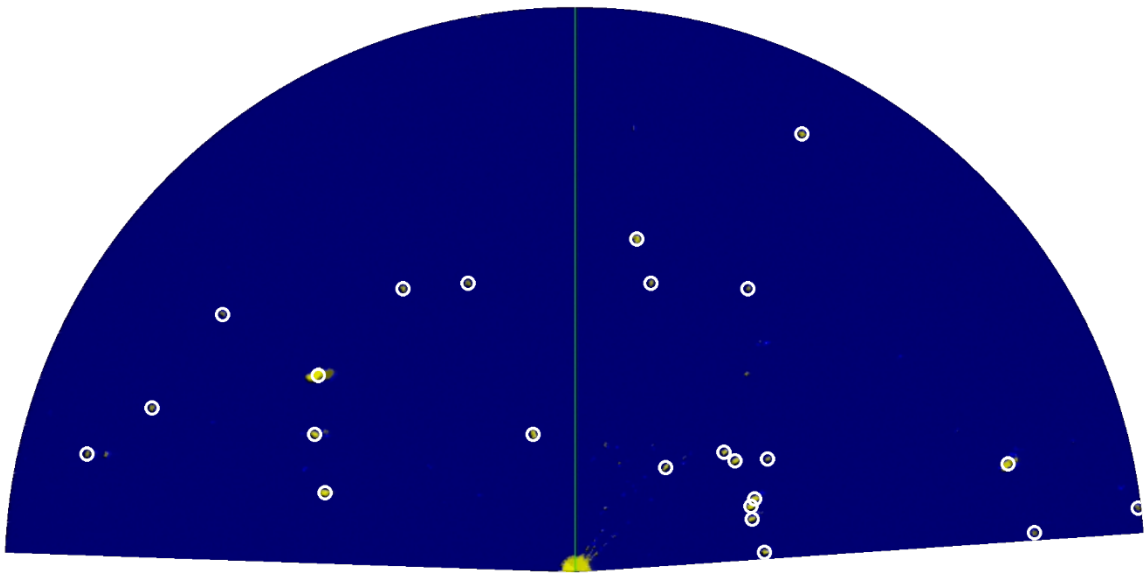

Figure 0-5 Locations of filtered putative birds (white circles) superimposed on a cropped version of the image in Figure 0-1.

3B4BAppendix 2

Aerial survey modelling methods

Detailed summary of bird density modelling methods

Distance sampling analysis

Distance sampling analyses were conducted for each species or species group by pooling the information across all surveys. When fitting detection functions, the effects of covariates, other than perpendicular distance, are incorporated into the detection function model directly (Multiple Covariate Distance Sampling, MCDS) (Marques & Buckland, 2004; Marques, Thomas, Fancy, & Buckland, 2007; Buckland, et al., 2001). In these cases, the probability of detection becomes a multivariate function, representing the probability of detection at perpendicular distance and covariates, where Q is the number of covariates. In this study, using a half-normal detection function $e^{-\left(\frac{y^2}{\sigma^2}\right)}$ the covariates were incorporated via the scale term, σ, where for sighting j, σ has the form:

$$\sigma_j = \exp\left(\beta_0 + \sum_{q=1}^{Q}(\beta_q v_{jq}\right)$$

where β_0 and β_q $(q = 1, \dots, Q)$ are parameters to be estimated (Buckland, et al., 2001). Half-normal and hazard rate detection functions were fitted with BIC (Bayesian Information Criterion) to choose between the models. The candidate variables trialled as covariates were bird group size, behaviour, observer, glare and sea state as the incorporation of these variables are often seen to improve the model (*Table 2-2*). There were too few observations for some observers, so in those cases, the observers' observations were combined with the observer with the next smallest number of observations. Observations with a sea state greater than four were removed from the analysis. Sea state is a measure of wave activity, and the more wave activity the more difficult it becomes to detect birds with increased distance away from the survey track line.

Table 0-1 Table detailing the covariates used in the detection function fitting.

Covariates	Values
Behaviour	S (sitting or diving) and F (flying or flushing)
Observer	7 Observers
Glare	1 (full sun), 2, 3 (cloudy), 9 (changeable)
Sea state	0, 0.5, 1, 1.5, 2, 2.5, 3, 3.5 (calm to rough)

Mitigating the effects of glare

Sighting conditions, such as sun glare and sea state, can influence the detection of sea birds from aerial surveys. Data to describe sighting conditions is usually collected in situ. However, when this is absent, alternative methods are required to identify (and adjust for) heterogeneity in the detection probability. Accounting for such heterogeneity is particularly important for distance sampling, where near-perfect detection at the track line is often a required assumption.

Detection information from band A was used for the left-hand and right-hand sides of the aircraft to identify transect lines with likely poor sighting conditions. For all species except flying northern gannets and black-legged kittiwakes, which are much easier to see even when glare is present, the identified transects removed observations from the affected side and reduced the coverage to one side (i.e., returning a one-sided transect).

The effects of glare and any mitigations, as a result, were approached using a dedicated analysis. The analysis was designed to quantify the extent to which directional sun glare can lead to left-hand or right-hand side bias in counts within a single transect line with the same direction of travel. Specifically, it was assumed that the proportion of left or right sightings in band A should be 0.5 and follow a binomial distribution. The proportions for each transect were then compared to a critical value calculated as the quantile of the binomial $(n, p = 0.5)$ distribution at three standard

errors greater than the mean and where n equals the number of observations on the transect. This is a common measure in extreme value theory (Leys, Ley, Klein, Bernard, & Licata, 2013). Any transects with values greater than the critical value had the observations from the smaller side removed and the coverage reduced to a single side.

Spatial analysis framework

The following sections describe the modelling methods employed for this analysis and the following outputs. For a high-level executive summary of the methods, see Appendix 2.

Model framework

The response variable for the spatial models under analysis here are bird counts in a small area (segment) corrected for detectability. This response was modelled using a Tweedie framework, which includes an estimated dispersion parameter (ϕ) and Poisson-Gamma mixing parameter (ξ) to return an appropriate mean-variance relationship in each case. The mixing parameter takes on values from 1 (equivalent to quasi-Poisson) and 2 (equivalent to Gamma). If the estimated parameter was close to 1, the models were considered quasi-Poisson.

A set of candidate explanatory variables were associated with each segment to model the signal, and in this study, each of the 12 surveys was analysed separately, including covariate selection. The candidate environmental covariates were water depth and distance from the coast (DC). As a one-dimensional term, DC was considered in each model in the unlikely case that there was compelling evidence for consistent spatial patterns with DC, which were the same in all directions. Additionally, a spatial surface was fitted to each model to account for more realistic (and localised) surface patterns potentially due to unmeasured covariates. Specifically, a two-dimensional CReSS-based (Complex Region Spatial Smoother) surface using a Gaussian radial basis function was included in the model (Scott-Hayward, Mackenzie, Donovan, Walker, & Ashe, 2014).

As an illustration, the following equation represents an example of a Tweedie model with a log link function and fitted with a one-dimensional smooth term (e.g., bathymetry) alongside a two-dimensional spatial smooth:

$$y_{ij} \sim Tw(\mu_{ij}, \phi, \xi)$$

$$\mu_{ij} = e^{\left(\beta_0 + s_1\left(\text{Bathymetry}_{ij}\right) + s_2\left(\text{XPos}_{ij}, \text{YPos}_{ij}\right)\right)}$$

where y_{ij} is the estimated count for transect i segment j and s_1 represents either a quadratic B-spline or a natural cubic spline smooth of depth. Here, s_2 is a two-dimensional smooth of space (with coordinates XPos and YPos in UTMs). Implicit in this model are also coefficients for the intercept (β_0) and any spline-based coefficients associated with the smooth terms. The effort associated with each observation varied depending on the associated segment area, so the segment area was included as an offset term (on the log scale).

A globally applicable depth or distance to the coast term and a more flexible spatial term were trialled for inclusion in each model to indicate how best to model spatial patterns in each case. In particular, this quantifies if any spatial patterns are sufficiently described by the one-dimensional covariates (which apply the same across the surface) or if a more considered approach to spatial patterns was required for each survey. For example, if the depth was selected and a two-dimensional spatial element was not deemed necessary (as determined by the model selection procedure governed by objective fit criteria), then this signals that any spatial patterns are primarily a function of the depth, regardless of the geographical location of this depth in the survey area.

If the two-dimensional spatial term was selected for inclusion in a model, then the spatial density patterns (over and above any environment-related terms) were accommodated using a spatially adaptive term which permits different amounts of flexibility across the surface in a targeted and parsimonious way. Consequently, relatively complex spatial patterns can be accommodated with few parameters.

Selection between competing models was undertaken using a 5-fold cross-validation metric while preserving any within-transect correlation via the appropriate blocking structures.

Model specification, selection and fitting

Spatially adaptive generalised additive models, with targeted flexibility, were fitted to data from each survey to allow for non-linear relationships between the one-dimensional and two-dimensional covariates and the response (Scott-Hayward, Mackenzie, Donovan, Walker, & Ashe, 2014; Scott-Hayward, Mackenzie, & Walker, 2023; Walker, Mackenzie, Donovan, & O'Sullivan, 2010).

All covariates were permitted to have a linear or nonlinear relationship with the response. When a smooth term was included in a model, it was specified to be either a quadratic (degree 2) *B*-spline (df = 3, 4, 5) or a natural cubic spline (df = 2, 3, 4). However, in cases where these degrees of freedom boundaries were reached, a broader range of parameters was trialled instead. The degrees of freedom for these terms determine the flexibility of these smooth (and nonlinear) relationships - the more degrees of freedom, the more flexible the relationship can be.

The location of this flexibility (along the x-axis) in these terms (e.g., depth) was also determined as part of the model selection process. This permitted the relationship in some areas of the covariate range to be relatively complex (e.g., in shallow waters) and in other areas (e.g., in deep waters) to be relatively simple. Both smooth types permitted a maximum of three internal knots and a specific spline number of boundary knots. An objective fit criterion determined the number and location of knots.

The spatial patterns in each analysis were based on a two-dimensional spatial term (of variable complexity). The flexibility of the spatial element constituted part of the model selection procedure and was determined for each survey using a Spatially Adaptive Local Smoothing Algorithm (SALSA). While this model selection element technically occurred between limits (df = [2, 100]), the flexibility chosen in each case was not bounded in practice by those values since the selection procedure occurred well within the bounds of the specified range.

The `MRSea` `R` package, designed to fit both CReSS- and SALSA-type models, was used for model fitting, and a five-fold cross-validation procedure was used to govern all model selection elements (Scott-Hayward, Mackenzie, & Walker, 2023). The cross-validation procedure attempts to balance the fit to data unseen by the model while minimising the number of parameters (parsimony). It was used here to select terms and the extent of their flexibility in each model. Note that this cross-validation was predicated on preserving correlated blocks of survey data (transect lines) so that any residual autocorrelation present was not disrupted when choosing folds. This was considered necessary to ensure independent sampling units under the scheme.

Parameter inference

The response data were collected along survey lines in sequence, so consecutive observations are likely to be correlated in space and time (i.e., points close together in space and/or time are likely to be more similar than points distant in time and/or space). Further, the covariates included in the model are unlikely to fully explain these patterns, so some elements will likely remain in model residuals. These patterns violate residual independence (which underpins traditional model approaches such as Generalised Additive Models). Thus, robust standard errors were routinely used in the `MRSea` modelling framework to account for residual autocorrelation.

Due to the nature of the survey procedure, uncertainty about model parameter estimates proceeded via robust standard errors. These essentially work by inflating the standard errors (normally obtained under traditional approaches) concerning the positive correlation observed within pre-specified blocks of residuals. In cases where this residual correlation is minimal, the adjustments are small, and when the correlation is more extreme, the inflation is larger.

A transect-based blocking structure was used to reflect potential correlation within blocks while independence (i.e., no correlation) between blocks was assumed. To ensure this assumption was realistic, the decay of any residual correlation to zero (i.e., independence) with the distance between points (within blocks along transects) was assessed visually. Specifically, transects in each survey were used as the blocking structure, and an Auto Correlation Function (ACF) plot was used to check the suitability of this blocking structure via a 'decay to zero trend' within blocks.

Modelling diagnostics

Diagnostic measures were used to assess the adequacy of the model fit in each case. The assumed mean-variance relationship under the model was assessed visually using plots of the model's fitted values against the residuals' variance. In this analysis, Tweedie models were employed, which assume a nonlinear mean-variance relationship

$$Var(y) = V(\mu)\phi = \mu^{\xi}\phi$$

where ϕ is the dispersion parameter. The dispersion parameter was estimated for each model, and this estimate was used in the visual assessment of the mean-variance relationship that was assumed to hold under the model. ξ is the power parameter and is estimated prior to the model fitting by using a maximum likelihood profile approach. Based on the nature of the response data, the values of ξ were permitted between 1 (Quasi-Poisson) and 2 (Gamma).

QQ plots and residuals against predicted values plots were assessed to ascertain the level of agreement between the data and the model. These plots were created using the ***DHARMa R*** package and using simulated residuals.

Regarding interpretation, the left panel is a uniform QQ plot, and the right panel shows the residuals against predicted values, with outliers highlighted in red. Given these outputs, we would expect that a correctly specified model shows:

a) A straight 1-1 line and no compelling evidence against the null hypothesis of a correct overall residual distribution, as indicated by the *p*-values for the associated tests in the QQ plot.
b) Visual homogeneity of residuals in vertical and horizontal directions in the residuals against the predictor plot.

Pearson residuals for each model were also spatially visualised to ensure no areas of consistent bias across the survey area. Clusters of negative or positive residuals in spatially similar locations would indicate this.

Residual independence was not assumed to hold under the model. Instead, model inference proceeded under robust standard errors. As described, Auto Correlation Function (ACF) plots were instead used to check the suitability of this blocking structure via a 'decay to zero' trend within blocks.

Model predictions and estimates of uncertainty

Based on each selected model, predictions of counts were made to a grid of points (each point representing a 1 km^2 grid cell) across the survey area. Additionally, abundances within the survey-based prediction region were obtained by summing the grid cell counts across the relevant areas.

The uncertainty in the detection function was reflected using a parametric bootstrap ($n = 500$) of the fitted distance sampling model. This generated new estimated numbers for each segment. The selected spatial model was then re-fitted to each of the new datasets to obtain a new set of parameter estimates for the model. The final output of this process was a parametric bootstrap procedure using the robust variance-covariance matrix from each parametric bootstrap model. These were used to calculate 500 sets of model predictions, which generated 95% percentile-based intervals and allowed for calculating a coefficient of variation for each grid cell. If it was impossible to fit a spatial model to the data, the abundance estimates for the survey were calculated from the distance analysis parametric bootstraps.

A calculation of 'persistence' was also undertaken across the two data types using the geo-referenced estimates of density (abundance/associated area) across the survey area. Persistence scores were calculated for every grid cell in the following way. Each bootstrap replicate was allocated a binary value based on whether or not the estimate in each location was above the mean estimated density (1) throughout the survey area or below this mean estimated density (0). This was performed for all 500 sets of plausible predictions in each grid cell (based on the bootstrap replicates), and the proportion of these bootstrap predictions above the mean (indicated by the value of 1) was calculated for each grid cell to give a persistence score for that location. A persistence score of 1 indicates that the density in that grid cell was estimated to be above average in every bootstrap replicate in every survey (so uniformly above the mean; high persistence), while a value of 0.1 indicates that just 10% of the estimates were above the estimated mean, and thus indicates low persistence in that location.

3B4BAppendix 3

Ship-based survey effort

Observation days

Table 0-2 Observation days spent at each observation position during the 16 ship-based surveys conducted in the NSI pre-investigation area during Y1 and Y2 (N = 87).

Survey ID	North	Southeast	Southwest
S01	0	2	2
S02	2	1	2
S03	2	2	2
S04	2	2	2
S05	3	2	2
S06	2	1	0
S07	2	2	2
S08	2	0	1
S09	2	2	2
S10	2	2	2
S11	1	2	1
S12	2	2	3
S13	2	2	2
S14	2	2	2
S15	2	2	1
S16	2	3	2
Total	30	29	28

Observation hours

Table 0-3 Observation hours spent at each observation position during the 16 ship-based surveys conducted in the NSI pre-investigation area during Y1 and Y2 (N = 1045.4).

Survey ID	North	Southeast	Southwest
S01	0	30	30.5
S02	32.8	16.5	32.8
S03	34.5	35	34.5
S04	30.5	30.5	21.6
S05	23.5	14.5	25.4
S06	22	11	0
S07	14	14	14.5
S08	10.3	0	9
S09	25.3	29.3	29
S10	32.8	32.3	32.8
S11	16.7	22.5	16.8
S12	29.8	29.8	31.3
S13	24.9	24.7	24.3
S14	19.8	18.8	23.2
S15	11.8	13.8	6.8
S16	20.1	21.9	20.3
Total	348.4	344.5	352.5

4BAppendix 4

Ship-based survey results

Observations

Table 0-4 Observations made at each observation position during the 16 ship-based surveys conducted in the NSI pre-investigation area during Y1 and Y2 (N = 7627).

Survey ID	North	Southeast	Southwest
S01	0	235	403
S02	144	58	192
S03	186	108	171
S04	185	167	141
S05	186	156	236
S06	177	115	0
S07	92	186	140
S08	101	0	67
S09	234	216	265
S10	141	122	115
S11	150	115	85
S12	345	197	156
S13	315	229	315
S14	272	398	191
S15	157	166	69
S16	156	102	202
Total	2,841	2,570	2,748

Individuals

Table 0-5 Number of individuals observed at each observation position during the 16 ship-based surveys conducted in the NSI pre-investigation area during Y1 and Y2 (N = 21,304).

Survey ID	North	Southeast	Southwest
S01	0	445	973
S02	210	93	448
S03	309	194	287
S04	755	400	334
S05	392	261	540
S06	287	146	0
S07	133	1,412	218
S08	181	0	69
S09	361	264	663
S10	220	214	251
S11	308	219	102
S12	2,714	446	233
S13	1,403	658	1,084
S14	447	676	1,408
S15	211	502	78

Survey ID	North	Southeast	Southwest
S16	285	152	318
Total	**8,216**	**6,082**	**7,006**

Species

Table 0-6 Number of species or species groups observed at each observation position during the 16 ship-based surveys conducted in the NSI pre-investigation area during Y1 and Y2 (N = 131).

Survey ID	North	Southeast	Southwest
S01	0	235	403
S02	144	58	192
S03	186	108	171
S04	185	167	141
S05	186	156	236
S06	177	115	0
S07	92	186	140
S08	101	0	67
S09	24	20	24
S10	25	29	19
S11	12	15	10
S12	22	34	22
S13	28	29	46
S14	29	29	34
S15	12	12	11
S16	16	16	15
Total	**96**	**86**	**93**

3B4BAppendix 5

Complete species list for ship-based surveys

Table 0-7 Complete list of all species observed during the 16 ship-based surveys conducted in the NSI pre-investigation area during Y1 and Y2. The table shows the number of observations, individuals, altitude records and transect counts of each species or species group.

Species group	Species	Observations	Individuals	Altitude records	Transect counts
Divers	Red-throated diver (*Gavia stellata*)	143	202	143	96
Divers	Black-throated diver (*Gavia arctica*)	1	1	1	1
Divers	Great northern diver (*Gavia immer*)	1	1	1	0
Divers	Diver sp. (*Gavia* sp.)	8	10	8	5
Petrels	Fulmar (*Fulmarus glacialis*)	406	540	368	341
Petrels	Great shearwater (*Ardenna gravis*)	1	1	1	0
Petrels	Sooty shearwater (*Ardenna grisea*)	38	48	37	16
Petrels	Manx shearwater (*Puffinus puffinus*)	3	3	2	0
Petrels	Storm petrel (*Hydrobates pelagicus*)	9	9	8	4
Petrels	Petrel sp. (*Hydrobates* sp.)	3	3	3	2
Gannets	Gannet (*Morus bassanus*)	1152	1,328	1,124	963
Gannets	Cormorant (*Phalacrocorax carbo*)	8	22	8	4
Herons	Grey heron (*Ardea cinerea*)	11	16	11	2
Geese	Pink-footed goose (*Anser brachyrhynchus*)	1	50	1	1
Geese	Greylag goose (*Anser anser*)	2	8	2	2
Geese	Barnacle goose (*Branta leucopsis*)	1	1	0	1
Dabbling ducks	Wigeon (*Mareca penelope*)	9	80	9	7
Dabbling ducks	Teal (*Anas crecca*)	18	54	18	16
Dabbling ducks	Mallard (*Anas platyrhynchos*)	3	8	3	3
Dabbling ducks	Pintail (*Anas acuta*)	6	24	6	2
Dabbling ducks	Shoveler (*Spatula clypeata*)	2	2	2	1
Dabbling ducks	Dabbling duck sp. (*Anas* sp.)	13	155	13	8
Sea ducks	Tufted duck (*Aythya fuligula*)	1	1	1	0
Sea ducks	Scaup (*Aythya marila*)	1	10	1	1
Sea ducks	Eider (*Somateria mollissima*)	1	8	1	1
Sea ducks	Common scoter (*Melanitta nigra*)	81	346	81	56
Sea ducks	Velvet scoter (*Melanitta fusca*)	1	1	1	1
Sea ducks	Goldeneye (*Bucephala clangula*)	1	2	1	1
Sea ducks	Red-breasted merganser (*Mergus serrator*)	1	1	1	1
Birds of prey	Marsh harrier (*Circus aeruginosus*)	1	1	1	1
Birds of prey	Sparrowhawk (*Accipiter nisus*)	8	10	8	6
Birds of prey	Osprey (*Pandion haliaetus*)	2	2	2	0
Birds of prey	Kestrel (*Falco tinnunculus*)	13	13	13	6
Birds of prey	Merlin (*Falco columbarius*)	12	12	10	6
Birds of prey	Falcon sp. (*Falco* sp.)	1	1	1	0
Oystercatchers	Oystercatcher (*Haematopus ostralegus*)	1	9	1	1
Plovers	Ringed plover (*Charadrius hiaticula*)	3	6	3	2
Plovers	Golden plover (*Pluvialis apricaria*)	51	234	51	34
Plovers	Grey plover (*Pluvialis squatarola*)	3	8	3	2
Sandpipers	Knot (*Calidris canutus*)	3	11	3	2
Sandpipers	Sanderling (*Calidris alba*)	3	4	3	0
Sandpipers	Dunlin (*Calidris alpina*)	24	107	23	14
Sandpipers	Snipe (*Gallinago gallinago*)	12	43	12	10
Sandpipers	Bar-tailed godwit (*Limosa lapponica*)	2	4	2	1

Species group	Species	Observations	Individuals	Altitude records	Transect counts
Sandpipers	Whimbrel (*Numenius phaeopus*)	4	5	4	2
Sandpipers	Curlew (*Numenius arquata*)	8	79	8	5
Sandpipers	Curlew sp. (*Numenius* sp.)	2	6	2	0
Sandpipers	Redshank (*Tringa totanus*)	4	9	4	2
Sandpipers	Greenshank (*Tringa nebularia*)	2	6	2	2
Sandpipers	Wood sandpiper (*Tringa glareola*)	1	3	1	1
Sandpipers	Common sandpiper (*Actitis hypoleucos*)	4	4	3	0
Sandpipers	Turnstone (*Arenaria interpres*)	6	6	6	4
Sandpipers	Wader sp. (Limicolae sp.)	26	85	26	19
Skuas	Arctic skua (*Stercorarius parasiticus*)	37	40	36	20
Skuas	Great skua (*Stercorarius skua*)	16	16	14	8
Skuas	Skua sp. (*Stercorarius* sp.)	6	6	6	1
Gulls	Mediterranean gull (*Ichthyaetus melanocephalus*)	2	2	1	1
Gulls	Little gull (*Hydrocoloeus minutus*)	200	340	200	175
Gulls	Black-headed gull (*Chroicocephalus ridibundus*)	42	68	35	23
Gulls	Common gull (*Larus canus*)	565	2,336	523	480
Gulls	Lesser black-backed gull (*Larus fuscus*)	1,336	5,336	1,190	1,018
Gulls	Herring gull (*Larus argentatus* agg.)	506	781	447	379
Gulls	Yellow-legged gull (*Larus michahellis*)	1	1	0	0
Gulls	Caspian gull (*Larus cachinnans*)	28	29	19	12
Gulls	Great black-backed gull (*Larus marinus*)	302	529	233	206
Gulls	Gull sp. (Laridae sp.)	103	167	103	94
Kittiwakes	Kittiwake (*Rissa tridactyla*)	917	1,310	894	819
Terns	Sandwich tern (*Thalasseus sandvicensis*)	32	59	32	25
Terns	Common tern (*Sterna hirundo*)	178	368	178	151
Terns	Arctic tern (*Sterna paradisaea*)	100	342	98	75
Terns	Common/Arctic tern	177	651	175	139
Terns	Black tern (*Chlidonias niger*)	2	3	2	0
Auks	Common guillemot (*Uria aalge*)	245	309	235	205
Auks	Razorbill (*Alca torda*)	81	142	80	67
Auks	Common guillemot/razorbill	284	410	284	271
Auks	Black guillemot (*Cepphus grylle*)	2	2	2	2
Auks	Little auk (*Alle alle*)	1	1	1	0
Auks	Puffin (*Fratercula arctica*)	1	1	1	1
Doves	Stock dove (*Columba oenas*)	1	1	1	1
Doves	Woodpigeon (*Columba palumbus*)	2	3	1	0
Doves	Collared dove (*Streptopelia decaocto*)	1	1	0	0
Owls	Long-eared owl (*Asio otus*)	1	1	1	0
Owls	Short-eared owl (*Asio flammeus*)	6	6	5	2
Swifts	Swift (*Apus apus*)	62	112	62	50
Kingfishers	Kingfisher (*Alcedo atthis*)	1	1	1	0
Woodpeckers	Wryneck (*Jynx torquilla*)	1	1	1	1
Passerines	Skylark (*Alauda arvensis*)	8	22	8	5
Passerines	Sand martin (*Riparia riparia*)	1	1	1	0
Passerines	Swallow (*Hirundo rustica*)	141	389	139	92
Passerines	House martin (*Delichon urbicum*)	19	38	18	13
Passerines	Swallow sp. (Hirundinidae sp.)	5	6	5	5
Passerines	Tree pipit (*Anthus trivialis*)	5	6	5	3

Species group	Species	Observations	Individuals	Altitude records	Transect counts
Passerines	Meadow pipit (*Anthus pratensis*)	352	1,907	348	226
Passerines	Rock pipit (*Anthus petrosus*)	12	12	9	7
Passerines	Yellow wagtail (*Motacilla flava*)	8	10	8	5
Passerines	Grey wagtail (*Motacilla cinerea*)	7	9	5	4
Passerines	Pied wagtail (*Motacilla alba*)	10	15	7	6
Passerines	Wren (*Troglodytes troglodytes*)	15	17	8	8
Passerines	Dunnock (*Prunella modularis*)	1	1	1	1
Passerines	Robin (*Erithacus rubecula*)	6	6	4	5
Passerines	Black redstart (*Phoenicurus ochruros*)	3	3	0	0
Passerines	Redstart (*Phoenicurus phoenicurus*)	12	12	4	2
Passerines	Whinchat (*Saxicola rubetra*)	1	1	0	0
Passerines	Wheatear (*Oenanthe oenanthe*)	7	7	7	6
Passerines	Blackbird (*Turdus merula*)	3	3	3	2
Passerines	Fieldfare (*Turdus pilaris*)	1	1	1	0
Passerines	Song thrush (*Turdus philomelos*)	4	5	4	1
Passerines	Redwing (*Turdus iliacus*)	21	96	17	13
Passerines	Mistle thrush (*Turdus viscivorus*)	1	1	1	1
Passerines	Thrush sp. (*Turdus* sp.)	1	1	1	1
Passerines	Icterine warbler (*Hippolais icterina*)	4	4	0	0
Passerines	Whitethroat (*Curruca communis*)	6	6	1	1
Passerines	Blackcap (*Sylvia atricapilla*)	6	6	4	1
Passerines	Chiffchaff (*Phylloscopus collybita*)	1	1	1	1
Passerines	Willow warbler (*Phylloscopus trochilus*)	8	10	1	1
Passerines	Warbler sp. (*Phylloscopus* sp.)	3	3	2	1
Passerines	Goldcrest (*Regulus regulus*)	6	6	4	2
Passerines	Spotted flycatcher (*Muscicapa striata*)	2	2	2	2
Passerines	Jackdaw (*Coloeus monedula*)	2	4	1	0
Passerines	Carrion crow (*Corvus corone*)	1	1	1	1
Passerines	Starling (*Sturnus vulgaris*)	25	1,161	19	15
Passerines	Chaffinch (*Fringilla coelebs*)	27	337	21	12
Passerines	Brambling (*Fringilla montifringilla*)	4	5	2	1
Passerines	Goldfinch (*Carduelis carduelis*)	1	2	1	0
Passerines	Siskin (*Spinus spinus*)	7	66	7	4
Passerines	Linnet (*Linaria cannabina*)	3	3	2	2
Passerines	Lesser redpoll (*Acanthis cabaret*)	1	1	1	1
Passerines	Hawfinch (*Coccothraustes coccothraustes*)	1	1	0	0
Passerines	Snow bunting (*Plectrophenax nivalis*)	1	3	1	1
Passerines	Reed bunting (*Emberiza schoeniclus*)	1	1	1	1
Passerines	Passerine sp. (Passeriformes sp.)	44	134	42	38